Dissertation submitted to the
Combined Faculties for the Natural Sciences and for Mathematics of the Ruperto-Carola University of Heidelberg, Germany for the degree of Doctor of Natural Sciences

Presented by
M. Sc. José Miguel Serra Lleti
Born in Valencia, Spain
Oral examination: 13/12/2018

Automated Correlative Light and Electron Microscopy using FIB-SEM as a tool to screen for ultrastructural phenotypes

Referees: Prof. Dr. Elmar Schiebel

Dr. Lars Hufnagel

Acknowledgements

This thesis is the culmination of the four years I have spent working as PhD student at EMBL, time in which I met a lot of amazing people. These friends and colleagues are, of course, just one part of all the people that helped me throughout the years and I am indebted to all of them.

First of all, and beyond doubt, I owe great thanks to my supervisor Yannick Schwab. I always could count with his support and since I consider myself to bear the engineers gloomy way to see the world (always look for the worst case scenario), his positivism and enthusiasm helped to balance my temper in critical moments and trigger good solving problem discussions. Moving to my team, even it has been changing over the years, it will be difficult for me to forget the original group formed by Anna M. Steyer, Matthia Winter-Karreman and Nicole L. Schieber. I can only thank and praise the patience and wisdom of Nicole L. Schieber, our technician, who, honestly, I wonder how she managed to train a clumsy computer scientist like me in the complex laboratory tasks that electron microscopy sample preparation requires. I am grateful also for her comments on this thesis, her infallible help during the experiments and her rational thinking and contributions during discussions. The same teaching patience goes for Anna M. Steyer, we started the FIB-SEM project together, but she was the one that showed me the way for the experimental part of it. I am grateful to have her as a colleague and I think our continuous feedback contributed to shape the project to what is today. During this four years, many other fantastic colleagues joined and/or left the group, from them I would like to thank specially Loredana Iovino, Julian Hennies and Isabella Haberbosch for their continuous discussions, help and friendship.

I would like to thank our lab interns Tom Boissonnet, Suruchi Sethi, Anna Arcon Fernandez and Tamara Lusa Agüero, which I have seen progress enormously in their computational skills during their quick period of internship. I think that the process of learning went both sides and I mainly learned how difficult is to transmit your knowledge.

I would also like to express my appreciation for all my colleagues from EMCF, specially to Rachel Mellwig, Charlotta Funaya, Martin Schorb, Paolo Ronchi and Pedro Machado. In addition of being the best colleagues I had, they always supported and helped me when I

need it. For Paolo Ronchi and Pedro Machado I am grateful for their criticism and intense discussions. Every scientific team needs people like them.

I have to thank the people from the Advanced Light Microscopy Facility (ALMF), whose kind help and skillful assistance delineated essential parts of my thesis. I learned a lot about siRNAs from Beate Neumann and I had nice discussions about high-content screening and image analysis with Christian Tischer and Volker Hilsenstein. I would also like to express my gratitude to Rainer Pepperkok and the Pepperkok lab for their discussions and feedback.

The automation of the project would have been impossible without the help of Alexandre Laguerre, David Unrau and Mike Holtstrom from *Fibics Inc.* and Heiko Steigmann and Robert Kirmse from *Carl Zeiss GmbH*. I have to thank especially Mike for his programming work and quick assistance during the darkest hours of software development.

Of course, I am also grateful to my collaborators: Matthew Raab and Matthieu Piel for the amazing week at the Institute Curie at Paris; Claudia and Jiri Lukas for their kindness and their proximity when discussing scientific topics and Ines Romero-Brey for her support and discussions about EM and potential FIB-SEM projects with the automation tool.

I would like to thank the members of my TAC committee, Prof. Elmar Schiebel, Lars Hufnagel and Wolfgang Huber for their support and valuable feedback during all these years. I would like also to thank Prof. Ralf Bartenschlager and Rainer Pepperkok for kindly accepting to be part of my defence committee.

I would like to finish dedicating this thesis to my beloved parents for their continuous encouragement and support. In every way, I would not be here without them.

Zusammenfassung

Die korrelative Licht- und Elektronenmikroskopie (Correlative Light and Electron Microscopy, CLEM) verbindet zwei Mikroskopietechniken miteinander. Auf der einen Seite Lichtmikroskopie (LM) zum lokalisieren bestimmter Regionen innerhalb der Zelle und auf der anderen Seite Elektronenmikroskopie (EM), die eine hohe Auflösung, der in der LM lokalisierten Regionen ermöglicht. Heutzutage ist CLEM die Methode der Wahl, wenn es darum geht die Anatomie von selektierten Zellen auf ultrastruktureller Ebene darzustellen. Da herkömmliche Ansätze jedoch sehr arbeits- und zeitintensiv sind, ist der Durchsatz sehr gering, sodass diese keine quantitativen oder explorativen Studien an Zellpopulationen zulassen. Die Einführung von Rasterelektronenmikroskopie mit fokussiertem Ionenstrahl (focused ion beam Scanning Microscopy, FIB-SEM) ist eine flexible Methode zur semi-automatischen Aufnahme von 3D Volumina. In dieser Arbeit habe ich an der Automatisierung eines CLEM/FIB-SEM Ansatzes gearbeitet und CLEMSite, ein Modul, das auf der Semi-automatisierung und der Navigationsmöglichkeit des FIB-SEMs basiert, entworfen. Mithilfe von CLEMSite können Volumen adhärenter Zellen automatisiert mittels FIB-SEM aufgenommen werden. Um dies zu ermöglichen wurde ein Set an Anwendungen, die auf Computer Vision und maschinellem Lernen basieren mit einer proprietären Bibliothek, die das Mikroskop steuert, kombiniert. Die proprietäre Bibliothek wurde von Fibics Inc. Im Rahmen der Kollaboration mit der Carl Zeiss GmbH zur Verfügung gestellt. Um die oben beschriebene Automatisierung zu ermöglichen wurde zwei Module implementiert. Als Erstes wurde ein korrelatives Modul entwickelt, das Referenzpunkte auf einem Gitterraster erkennt und aufnimmt. Da dasselbe Gitterraster jeweils in beiden Mikroskopieverfahren dargestellt wird, sowohl im Lichtmikroskop, als auch im Elektronenmikroskop, kann es in beiden Modalitäten auf der Kulturplatte detektiert und als Referenz verwendet werden. Als nächstes habe ich ein zweites Modul entworfen, das die jeweils gesuchten Regionen (Regions of interst, ROI), die zuvor im Lichtmikroskop identifiziert wurden, im FIB-SEM wiederfindet und somit eine automatische Aufnahme ermöglicht. Dieses neu entwickelte automatisierte CLEM-Verfahren wurde dann an verschiedenen Projekten angewandt. In einem ersten Projekt wurden Zellen mit verschiedenen siRNAs, die bei Formgebung des Golgi Apparates eine Rolle spielen, behandelt. Diese Zellen wurden anschließend mittels

des automatisierten CLEM/FIB-SEM-Verfahrens hinsichtlich ihrer ultrastrukturellen Morphologie des Golgi Apparates gescreent. Zusätzlich konnten wir an zwei weiteren Projekten unser neu entwickeltes Verfahren testen, in denen der Zusammenbruch der Kernmenbran bei unter Spannung stehenden Zellen sowie DNA-Schäden in binukleären Zellen untersucht wurden. Unsere Ergebnisse zeigen, dass hoher Durchsatz in der Elektronenmikroskopie möglich ist und somit Elektronenmikroskopie zur Entdeckung neuer biologischer Phänomene Anwendung finden kann.

Abstract

In Correlative Light and Electron Microscopy (CLEM), two imaging modalities are combined to take advantage of the localization capabilities of light microscopy (LM) to guide the capture of high-resolution details in the electron microscope (EM). However, traditional approaches have proven to be very laborious, thus yielding a too low throughput for quantitative or exploratory studies of populations. Recently, in the electron microscopy field, FIB-SEM (Focused Ion Beam -Scanning Electron Microscope) tomography has emerged as a flexible method that enables semi-automated 3D volume acquisitions. During my thesis, I developed *CLEMSite*, a tool that takes advantage of the semi-automation and scanning capabilities of the FIB-SEM to automatically acquire volumes of adherent cultured cells. *CLEMSite* is a combination of computer vision and machine learning applications with a library for controlling the microscope (product from a collaboration with *Carl Zeiss GmbH* and *Fibics Inc.*). Thanks to this, the microscope was able to automatically track, find and acquire cell regions previously identified in the light microscope. More specifically, two main modules were implemented. First, a correlation module was designed to detect and record reference points from a grid pattern present on the culture substrate in both modalities (LM and EM). Second, I designed a module that retrieves the regions of interest in the FIB-SEM and that drives the acquisition of image stacks between different targets in an unattended fashion. The automated CLEM approach is demonstrated on a project where 3D EM volumes are examined upon multiple siRNA treatments for knocking down genes involved in the morphogenesis of the Golgi apparatus. Additionally, the power of CLEM approaches using FIB-SEM is demonstrated with the detailed structural analysis of two events: the breakage of the nuclear envelope within constricted cells and an intriguing catastrophic DNA Damage Response in binucleated cells. Our results demonstrate that executing high throughput volume acquisition in electron microscopy is possible and that EM can provide incredible insights to guide new biological discoveries.

Table of contents

Introduction

"Progress in science depends on new techniques, new discoveries and new ideas, probably in that order."

– Sidney Brenner

Nowadays microscopy is, with permission of genetic tools, the central piece of instrumentation in biological research. Microscopes can image biological samples at almost any known scale and its resolution, dimensionality and quality of images keep growing every decade. However, in microscopy, scales impose a restraint: the closer we look at an organism, the more difficult it is to consider the full context. As researchers, we have to make choices: do we want to examine a full organism? Or maybe the tissue structure in one organ? What about getting inside one of the tissue cells to have a closer look at one organelle? Once we commit to a scale, we will engage in a detailed description of the phenomenon. But nature is fickle in her complexity: each time a cell divides, it is a little bit different from its predecessor. In practice, this means that more than one specimen is required to infer a general trend. The more quantitative evidence we collect of a fact, the more likely is to be a general rule and not the particular case of an individual (cell or organism).

In light microscopy, addressing cell populations has been highly exploited almost since the popularization of cell culture in the 1950´s. Questions such as, how many cancer cells survive following different drug treatments or how do cells react to diseases like microbial infections, were and still are important questions in the biomedical sciences. In the last two decades, with the advent of new technologies like fluorescent markers and automated fluorescence microscopy, cells were imaged and analyzed by the thousands.

During the 1990's, while fluorescence microscopy was becoming a workhorse tool for any cell biologist, electron microscopes were lagging behind in the quantitative world. Electron microscopy was relegated to be a qualitative technique, and in many cases, a good way to confirm what light microscopes have already discerned. The reason is a combination of several factors. Firstly, samples cannot be observed alive. They have to be fixed and embedded in resin blocks. Then, in order to image their contents, the blocks have to be cut in thin sections. All these processes are not exempt from training and expertise, and with

all, generating multiple samples is a tedious and time-consuming task. In addition, going down to the nanoscale world forces our hand to trade space for time: observing a full organ or thousands of cells simultaneously is not a possibility. Taking all of that into account, the experimenter has to select carefully his samples, usually from three to five specimens being the common deal. This thesis is presented as an attempt to increase these numbers substantially.

A total of four projects are presented, all of them centred around cell culture. During recent years, many advances have been already made on imaging multicellular organisms, especially in brain tissue or complete small organisms like *C. Elegans*. In these cases, targeting specific regions to extract useful information from electron microscopy images requires full-time dedication and expertise on a specific research field (neuroscience, development, ...). Thus, tackling full organisms or tissues is out of the scope of the present thesis.

Using cell cultures, we aim for numbers, but not blindly. We have to select a proper population corpus representative of our biological question. Chapter 1 describes how we deal with this problem using Correlative Light and Electron Microscopy (CLEM). As the word correlative indicates, the knack is to use fluorescence or light microscopy to guide us to the region that has to be imaged by EM. The chapter is a historical review of EM techniques, which, while it will not do justice to the true history of electron microscopy, will suffice to acquaint us with the basic concepts of CLEM. The chapter will close with the current state of the art in CLEM.

In chapter 2, the main instrument used in this thesis is presented in detail: the Focused Ion Beam-Scanning Electron Microscope (FIB-SEM). Hela cells trapped inside microfluidic chips lanes will be targeted to analyze their ultrastructure and to find nuclear envelope breakdown. In addition, the process of manual microscope operation for sample acquisition is described in detail.

In chapter 3, with the manual operation of the FIB-SEM microscope in mind, the automation of the microscope is presented as a solution to perform multiple acquisitions without the need of an expert. This is the most technical chapter as it will present designs, algorithms and system workflows associated with the automation of the microscope. This work represents the core volume of my thesis work.

In chapter 4 and 5, Hela cells with a Golgi fluorescent tag (GalNAc-T2) will be subjected to a CLEM workflow with full automation from the pipeline. In chapter 4, the processing of images during feedback microscopy and previous to EM will be described. In chapter 5, correlation part with EM is completed and the results of three fully automated datasets described. Thanks to the automation, we will reach numbers up to 20 cells per sample.

Chapter 5 also introduces a discussion about stereology and segmentation for quantification purposes.

In chapter 6, an intriguing problem concerning DNA catastrophic damage in U2OS binucleated cells is introduced. CLEM will be used to fetch such cells. The combination of TEM tomography with Volume SEM will help to investigate the relationship between nuclei. As a technical development, the search of the cell in the electron microscope is assisted by a plugin based on manual clicking.

For each chapter from 2 to 6, the structure will be presented similar to a scientific article. First, one short introduction and state of the art review of the biological problem at hand, followed by a comprehensive materials and methods description. It continues with a discussion of the results achieved, with the necessary methodological clarification for each result and discussion. Exceptionally, chapter 3, will be more similar to a technical white paper with explanations about algorithms. Finally, this thesis will close with a small discussion about the prospects and remaining challenges of the project and future directions for research.

1

Chapter 1: A brief history of Correlative Light and Electron Microscopy.

1.1 Introduction

Microscopy has come a long way since the seventeenth century, when Anton van Leeuwenhoek presented his works to the Royal Society. With his work, the power of microscopes in observing an uncharted microscopical world was, for the first time in history, acknowledged. Nowadays, it is amply documented, even in the most introductory biology book, that microscopes are instrumental to determine biological structure and function. Optical lenses, as calculated by Abbes law[1] , have a spatial resolution limited to hundreds of nanometres [2]. In many cases, this is not sufficient to comprehend what is happening inside the cell and therein lies the necessity to examine with more powerful instruments. At the forefront of such instruments is the Electron Microscope (EM), providing a considerable augmentation in the power of resolution . Thus, it stands to reason that combining both instruments, one could observe the same region with different resolution power, and consequently gain different pieces of information such as function and ultrastructure. Currently, these techniques are known as Correlative Light and Electron Microscopy (CLEM). This chapter attempts to summarize more than one century of electron microscopy in cell biology and its co-evolution with the light and fluorescent microscope (LM). I understand that it is impossible in few

[1] Resolution limit = $0.61 *$wavelength of monochromic light/ NA (numerical aperture of the objective lens). NA can be seen as $n * \sin\alpha$. N is the refraction index, which can be improved from 1 to 1.51 with oil immersion. α is the angle of the lens semi aperture, which can be improved using quartz lenses to be close to 90 degrees (0.93 of sin value). Using UV (150 nm wavelength), it is theoretically impossible go beyond 150 nm as a resolution limit (Abbe 1881).

[2] The discussion is centred exclusively in optical microscopes without accounting the new field of superresolution microscopy, which is a separate subject that deserves its own story.

pages to make justice to all contributions and developments in the field, especially when I will not include the ones related to material science, cryo-electron microscopy and structural biology. Nonetheless, I feel compelled to tell a small story about this amazing piece of science history; with the additional benefit of laying down some grounds to build upon most of the concepts presented in future chapters.

1.2 Early days of electron microscopy

1931 is remembered as the year when the electron microscope was invented by Ernst Ruska and Max Knoll at the Berlin Technische Hochshule. Their discovery came from unexpected developments in other branches of engineering and physics. Thirty years before, J.J. Thomson discovered the electron and its mass using an experimental set up called the Crookes-Hittorf tube (Thomson 1897). When a metal filament is heated in vacuum, similar to a light bulb but using higher voltages, it emits electrons in straight lines. From the filament, called the negative electrode or anode, rays are emitted towards the opposite side, the positive electrode or cathode. If a metal shape is placed in the middle of the trajectory, a shadow will be cast down on the glowing wall of the tube, similar to a projector (Figure 1.1-A). A modified version of this tube with the power of controlling the electron beam was created by Ferdinand Braun, which with a few modifications years later turned into a CRT (cathode-ray tube). The CRT was the precursor of the oscilloscope (an instrument used to measure voltages and intensities in analog electronic circuits), the first television tubes and the first computer monitors.

It is not by chance that CRT designs look very reminiscent of an electron microscope. Indeed, Ruska and Knoll's initial research project was on improving CRTs inside oscilloscopes. Their original idea was to replace electrostatic by electromagnetic lenses to get better performance and control of the electrons generating the beam (Ruska 1987). Ruska was attempting to reduce the spread of the electron beam by using the magnetic fields of short coils (which were originally designed by Knoll). To prove the increase in accuracy and characterize the properties of the electron beam, he borrowed a new theory from Hans Busch, a professor at Jena's Physikalisches Institut.

Busch predicted that coils on electrons could have similar behaviour as glass lenses on light. One lens, the condenser, was able to concentrate electrons into a beam, while another, the objective lens, could be used to magnify the beam into an image at the very end of the tube. The focal length could be changed by simply changing the coil current. Busch never managed to prove it experimentally but Ruska saw an opportunity on his research for developing a quality control for electron beams. He conjectured that obtaining a higher

magnification and better delineating qualities of an image projected at the bottom of the tube, would also imply a better design in the tube coils. He designed a setup were electrons passed through small apertures containing small metallic grids. The coils placed before the aperture were regulated, helping to straighten the electron beam and showing a projection of the small metal grid pattern. By modifying the properties of the coils, the properties of projected images at the end of the tube were substantially changed.

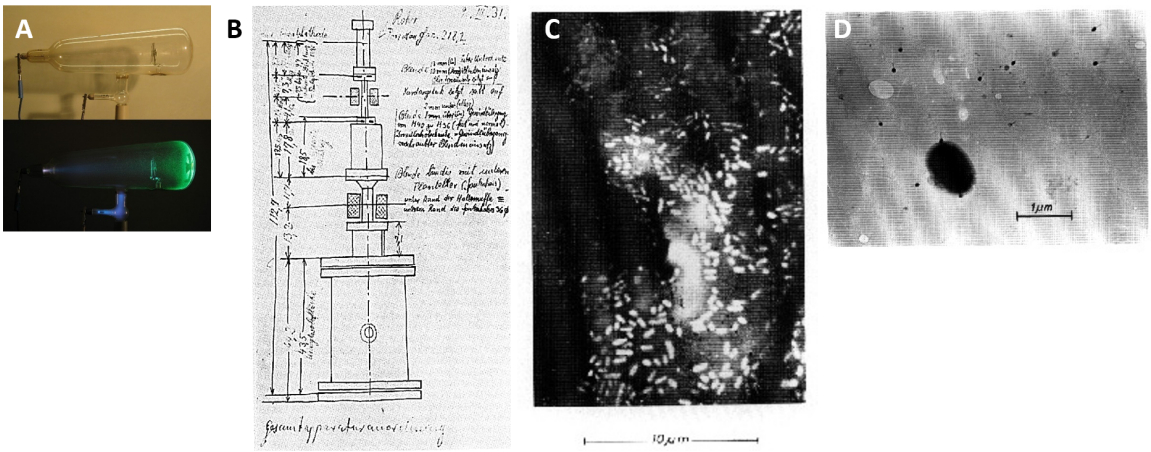

Fig. 1.1 **A.** Crookes tubes. When electrons travel from the left (cathode) to the right (anode), they cast a shadow of the Maltese cross on the glass wall of the tube. The Anode in is the electrode at the bottom (source:Wikipedia, Crookes tube). **B.** Sketch from Ruska, from 9th March 1931, the electron ray tube for testing two-stage electron-optical imaging by means of two magnetic electron lenses. (source of picture: nobelprize.org, Ruska lecture). **C.** Bacteria (culture infusion), fixed with formalin and embedded in a supporting film stained with heavy metal salt. (Krause, F.: Naturwissenschaften 25, 817-825 [1937]).(Bacteriophages. Ruska, H.: Naturwissenschaften 29, 367-368 (1941) and Arch. Ges. Virusforsch 2, 345-387 (1942)).

The first electron microscope was just 14.4 times in magnification, very far yet from the light microscopy barrier Figure 1.1-B). Could the electron beam be tightened even more? When Knoll and Ruska exposed their instrument to other colleagues, they realized its future potential to visualize objects beyond light diffraction limits. Using electrons, the wavelength of which is 100.000 times smaller than light, had to confer the power to delineate objects with the highest resolutive power of anything achieved so far. It took ten years of research (1933) to break the light microscopy barrier and in 1944, thanks to better vacuum chambers[3] and improved electromagnetic lenses, a 2 nm resolution was reached.

The first biological micrographs did not take long to come (Figure 1.1-C), including the first micrograph by the Belgium chemist Ladislaus L. Marton (Marton 1941). Ruska continued his work, especially encouraged by his brother Helmut, who was a medical doctor

[3]Electron mass is extremely small (9.109e-31 kg) and air can deflect them easily, hence there was a necessity of high vacuum and some efforts to avoid any vapor contamination in the tube.

who firmly believed in the application of technology into the medical sciences. He obtained the first images of bacteriophages in 1942 (Figure 1.1-D). There were, though, technical complications. Electrons cannot go through thick materials and when this is the case, the formed image just defines an amplified contour of the sample at the other side of the filament. Engineers also noticed that the samples were heated, which meant, they were absorbing a lot of radiation. Consequently, they started to reduce the sample size and thickness. That made difficult the study of biological samples and during the 1940s, studies were mostly limited to small particles in material science, such as pigments in colour paints and cosmetics or automobile tires. Size, shape and number of particles or cracks in a material could be quantified, but any comments about ultrastructure were always left aside as too speculative.

In 1938, the first prototype of transmission electron microscope was built at the Department of Physics in the University of Toronto under the direction of Eli F. Burton. Burton had visited Ruska's lab in 1935 in Berlin and decided to build his own EM as a proof of concept. The prototype became very successful in the academic circles and was exhibited as a recognition of the growing competence in North America's science. Soon after, while in Europe electron microscopes were stalled by the Second World War events, on the other side of the Atlantic Ocean, North America started to build its own EM industry (Reisner 1989).

Vladimir Zworykin, a scientific celebrity for being the inventor of electronic television, was the head of electronics research department position for the company *RCA* (Radio Corporation of America, posteriorly wholly owned by *General Electric*). He observed the success and growing admiration for electron microscopes and entailed it as an opportunity to find a new market in the US. To carry on his plans, he invited Marton from Europe, who was at that time building his own third generation of electron microscopes without almost any funding. He accepted and two years after (1940), the EMA (Electron Microscope A) was born at *RCA*.

Other than a complex scientific instrument, the machine was a total disaster. It was unstable and very difficult to operate, so it was clear that it could not be sold. Zworykin needed someone with a more pragmatic view, so at the end of 1940, he hired James Hillier, one of the brilliant Burton students involved in the construction of the first American prototype. After almost two years of substantial improvements, EMB (Electron Microscope B) was launched to the market. At the end of 1943, *RCA* had distributed 58 of those microscopes overall US institutions.

1.3 When Cell Biology met EM: 1950-1960

One of those few institutions that acquired an EMB was *The Research Laboratories of Interchemical Corporation* at New York. In the same city, Albert Claude, a Belgium M.D. at the Rockefeller Institute for Medical Research, was interested in finding out the virus responsible for the Rous sarcoma. At that time, medical doctors believed that all cancers were coming from viruses and the general interest was to find the virus associated with each type of cancer[4]. A common practice in cytology was to fraction cells to analyse their content by analytical ultracentrifugation (De Duve et al. 1981). Viruses were still elusive, maybe too small, but advances in the technique gave the certitude to Claude that he would eventually find the virus using centrifugation.

In one of his articles (Claude 1939) he analysed the RNA-containing fraction of the supernatant from chicken-tumour cells and noticed that there was a strange aggregate composed of small particles that he could not identify (figure 2A). Claude named them 'microsomes'. Microsomes were under the limits of traditional light microscopy and staining techniques were not revealing much more than highly refractive clumps. When Albert Gessler, the research director of Interchemical Corporation read the article in Science, he contacted Claude and suggested to use their new flamboyant electron microscope to discern the real nature of such aggregates. He put Claude in contact with Ernest Fullam, the trained specialist operator of the EMB and they get on to it.

One day, Keith Robert Porter, a research assistant at the Rockefeller Institute, went with Claude to one of his electron microscope sessions. Porter was in charge of cell cultures for studying chemical carcinogenesis. Cell culture had few standards at that time, without no conditions and no consensus about the what was a good cell culture media, so Porter had gained some name by creating new techniques and protocols for cell culture on his own. He was a curious man always ready to learn new techniques and to apply them. During that session with Claude, while observing mitochondria lysates spread on plastic over tiny metal grids, he got captivated by their level of detail. Cells were considered a simple bag of enzymes, so he wondered why the structures he was looking at were so intricate. What if he could manage to put a complete cell under the electron microscope?

Cells were too thick and when they were out of their media with the electron beam hitting them, they massively dried out, dying and shrinking in the process. To solve the thickness issue, Porter noticed some of the chicken fibroblasts in culture were highly spread in length. If the volume was going to be the same for each cell, he guessed, those stretched cells had to be thinner, maybe thin enough to be seen in the electron microscope. To prevent damage

[4] Rous sarcoma is, indeed, one of the cases were the tumour is caused by an oncogenic RNA virus.

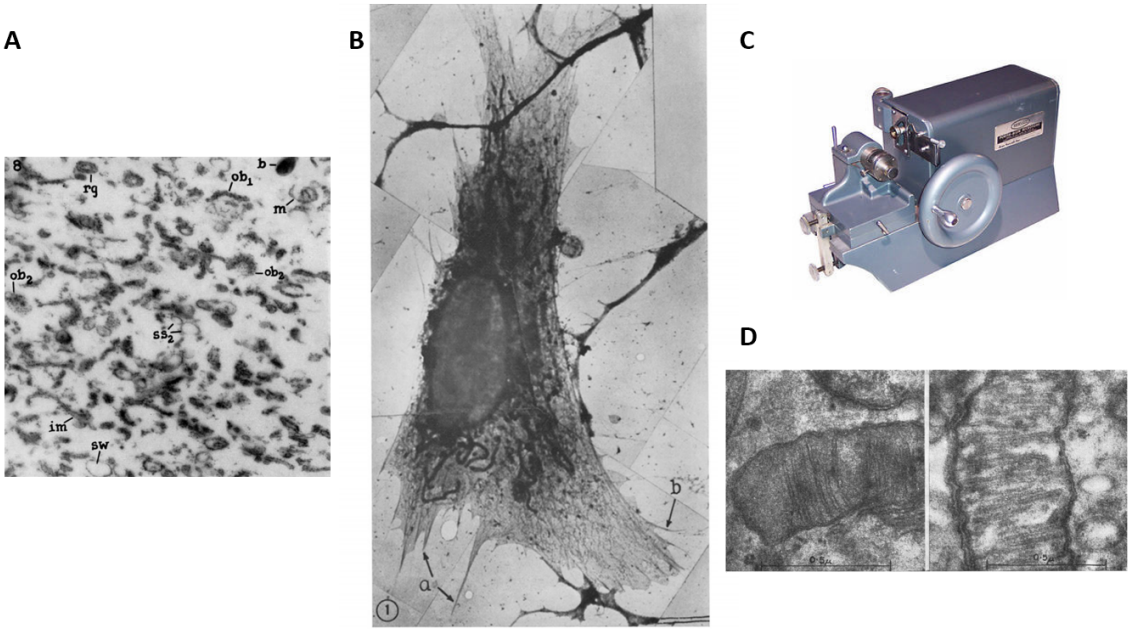

Fig. 1.2 **A.** In the picture, a picture of microsomes with ribosomes (see dots near "ob2"). Microsomes, happened to be none other than a mixture of ER endoplasmatic reticulum pieces mingled with ribosomes. Source: (Wells 2005). **B.** Electron micrograph of a "fibroblast-like cell" published in (Porter et al. 1945). 5 micrographs were stitched together to form the image. **C.** Sorval MT-1 Image from http://spwindustrial.com/sorvall-mt-1-ultra-microtome-porter-blum/ (lab equipment company). The MT1 is still sold in auctions for around 400 euros over the internet. **D.** Mitochondria micrograph by Sjöstrand as presented in Nature in 1953. The mitochondria belonged ultrathin sections of mouse kidney cells in the left and guinea pig retinal rods in the right. Double membranes and cristae were observed with detail for the first time.

upon drying, maybe the best way was to fix the cells, a well-known practice in histopathology. Porter experimented with different fixatives known in the literature of his time, like aldehydes, alcohols, acetic acid and even freezing. One typical fixation procedure used to study protozoa consisted in exposing the cells to osmium tetraoxide vapours. Porter used osmium without realizing that he was also staining the sample, and unaware that he indirectly solved another problem [5]. Membranes in biological specimens consist mainly of light atoms (H, N, C, O, P), which provide low image contrast under the microscope. Stains were fundamental to gain definition in the image.

In July 1944, Porter and Fullam examined for the first time a batch of cells in the electron microscope. After an intense afternoon search, they found one intact full cell lying over one of the openings of the metal grid carrier. It was the first micrograph of a eukaryotic

[5] From the publication (Porter et al. 1945) , he already noticed that: *"[Osmium tetraoxide] may serve also as a differential stain, for by its action some cellular structures are apparently rendered more electron-scattering than others[. . .] If not treated with osmium or another fixative of similar properties the magnitude of variation in the molecular densities which determine electron scattering and absorption may not be sufficient to outline distinctly some of the formed bodies present."*

cell (Figure 1.2-B). In their 1945 publication (Porter et al. 1945), they showed the intrinsic complexity of one single cell and a new world was opened for biology. Porter mentioned a reticular structure ranging from 30 to 150 μm in length, that he ended up calling the reticulum. He made the connection with Claude microsomes, intuition that was afterwards confirmed by other experiments. In posterior experiments, the Golgi apparatus was also hinted to, which later would draw the attention of George Emil Palade, one of Claude's student studying secretion processes also by fractionation.

Despite their success in the 1945 experiment, Claude was convinced that thinner sections of the cell would reveal the intracellular structure with much greater detail. One year before, Fullam and Gessler had been working on modifying a microtome to obtain thinner material sections. A microtome is a machine frequently used in pathology to cut thin sections of tissues embedded in paraffin for later examination under a light microscope. At that time, the general opinion was that sectioning at high speeds would compensate for thermal effects on the deformation of sections, allowing thinner sections (less than 1 micrometre) (Gessler & Fullam 1946). In 1945, Claude and Fullam collected sections from osmium-fixed liver cells on a copper mesh coated with Formvar film. The microtome was working at 49000 rpm and they had to select the most auspicious sections between a bunch of waste by using a light microscope. The published micrographs (Claude & Fullam 1946) were full of artefacts and holes with an irregular thickness between 0.3 and 0.6 μm. Regardless of the authors blaming the fixation and embedding procedures instead of the sectioning method, they acknowledged the need to introduce some modifications to current microtomes.

During the next years, several efforts were done around the world to achieve uniform thin sections of specimens (Pease & Porter 1981). Pease and Baker (Pease & Baker 1948) realized about the need to reduce the speed, for example, introducing a hand-turning wheel to have a better control. It was also found, that the conventional paraffin embedding used in histopathology was too soft (Bretschneider 1952). Hardening the sample gave better support to achieve thinner sections which eventually lead, by trial and error, to embed the sample with hard resins.

By the middle of the 50's ultramicrotomes were being developed all over the world. Curiously enough, the first commercially available ultramicrotome was the Porter-Blum MT-1, developed by Porter and the director of the instrument shop at the Rockefeller Institute for Medical Research, Joseph Blum (Porter & Blum 1953). The MT-1 was able to cut sections up to 100 nm thickness. Due to its ease of use and simple design, the MT-1 was such a success that even nowadays some laboratories keep them in use (Figure 1.2-C). Independently, in the Karolinska Institute, in Stockholm, Fritiof Sjöstrand developed another

type of ultramicrotome using polished razor blades[6]. With that, he managed to produce the first detailed micrographs of mitochondria, where for the first time, the inner and outer membranes were observed as we know them (Sjöstrand 1953), (Figure 1.2-D). In a few years, the world of science was flooded with detailed electron micrographs of every known cell type [7].

1.4 From 1960 to 1980 – EM splendour and SEM invention.

The success of the TEM lead Vladimir Zworykin to expand his research department on electron microscopy inside RCA. In 1942, he assembled a team to research a different theoretical aspect of EM . In 1935, Knoll had theorized about the possibilities of imaging secondary emission electrons (SE), but he was mostly interested in characterizing their properties. Primary electrons come directly from the beam, they are loaded with kinetic energy which is dissipated if they collide with an atom, fact that eventually happens with a sufficiently thick specimen. After the collision, some energy is transferred to other electrons and they are released. These interactions are 'inelastic' and produce low energy secondary electrons, which can be detected by placing an anode close to the surface of the sample (Figure 1.3-A).

In 1938, Manfred von Ardenne, author of more than 600 patents in radio and television technology during his life in Germany, published the theoretical principles of a "scanning microscope"[8]. An electron beam could be reduced to an extremely fine probe and then focused on the specimen's surface to collect some of the secondary electrons on that specific region, then generating an image. The reduction of the beam to a probe is achieved using a series of condenser lenses and finalized by the so-called objective lens, which focuses the

[6]One of the problem with microtomes was that steel blades are not smooth due crystallization artefacts, which beyond certain thickness can rip through the specimen. Latta and Hartman introduced in the 1950's a solution (Latta & Hartmann 1950) by replacing the blades with glass with fracture edges at the top, with no unevenness.

[7]For more information about this historical period the following assays describe in detail the rise of EM, microtomes and its impact in cell biology (Mulvey 1996; Rasmussen 1997).

[8]Von Ardenne is also known for writing the first technical book about microscopes, "Elektronen-Ubermikroskopie". After the second world war, an exemplar of this book ended up accidentally in the hands of an unemployed young Japanese military officer, Kenji Kazato. Kazato, with a bunch of friends, built a prototype of electron microscope called the DA-1, who managed to sell to Mitsubishi. Years later, he founded JEOL. The book is venerated as a relic in the headquarters of JEOL at Tokyo.

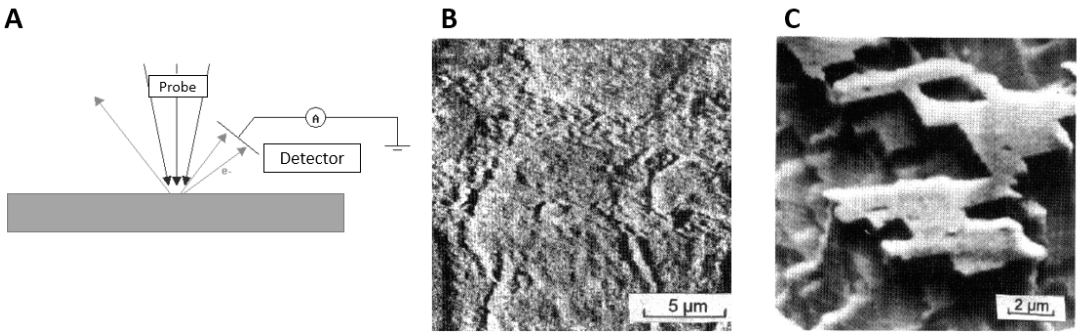

Fig. 1.3 A. Schematic of secondary electrons detection. The probe in red are the incident electrons. Secondary electrons in green are detected by a positive voltage close to the sample surface. B. A micrograph of etched brass produced by Zworykin team. C. A micrograph of etched aluminium from SEM1, the first complete SEM produced in Cambridge by Oatley's team. Images from (Smith et al. 2008)

electron beam on the surface. Von Ardenne also tried to create an experimental microscope, but he had multiple difficulties[9].

At *RCA*, they had the resources of a commercial laboratory combined with the brilliant team formed by Zworykin, James Hillier and Richard Snyder. They decided to give a push to von Ardenne's microscope idea with the following microscope design. Electrons were emitted from a tungsten filament that was passed through a grid and the current beam was chopped into pulses using a square-wave voltage signal. Following this, several magnetic and electrostatic lenses focussed the beam on to the sample, secondary electrons from the sample were attracted back to the lens and filtered towards a fluorescent screen. A photomultiplier tube enhanced the secondary electrons signal and the scanning was carried out by mechanical displacement of the object observed. The square-wave function synchronized exposure time with position and movement of the carrier. In this setup, one image took around 10 minutes to be printed. Images revealed topographic surfaces with a resolution of 50 nm (Figure1.3-B).

When the microscope was made public, many academics considered it as a simple curiosity. TEM was flourishing and there was no need for surface images of samples at a lower resolution. Zworykin thought that material scientists would look at the Scanning Electron Microscope (SEM) with different eyes: if the sample was really opaque, three-dimensional topology could help to reveal cracks and surface composition in manufacturing. However, at that time, surface replication techniques were trendy and much cheaper than the marketed SEM. It was a big commercial disaster and the project was abandoned.

A few years after (1948), in the Cavendish Laboratory, A.S. Baxter was experimenting with new improved secondary-electron multipliers. Charles Oatley, a friend of his, was a

[9]For a complete revision of the SEM and its history, it is recommended the book from (Goldstein et al. 2003).

professor of Engineering at the University of Cambridge looking for an interesting project to invest his electronics expertise (Oatley 1982). Knowing Baxter and having access to his detectors, he decided to have his students build an SEM from scratch as a mere engineering exercise. It went so well that in 1953, his first student, McMullan, published the first schematic and picture of a functional SEM (Figure 1.3-C). His second student, K.C.A. Smith, made substantial improvements to avoid aberrations, the most notable of these being the introduction of stigmators. For multiple reasons, for example material composition, non-uniform magnetic fields can create distorted images. Distortions affect the shape of the probe making it more elliptical than circular. Stigmators are electromagnetic coils placed around the microscope column which can be controlled by the user to adjust the probe to be circular.

In 1960, Everhart and Thornley, also Oatley students from the same laboratory, created the famous secondary electron detector (Everhart & Thornley 1960). The detector consisted of a grid with a low positive voltage that allowed to pass through only low energy electrons coming from the sample (less than 50 eV). Theoretically, most of these electrons are secondary. Since the signal is small, a scintillator converts them to light and a photomultiplier tube is used to amplify the signal. Technical additions kept on growing and in 1965, *Cambridge Scientific Instruments* released their *"Mark I Stereoscan"*, the first successful SEM microscope on the market.

On the other side, TEM evolution was unstoppable. Optical aberrations were reduced by improving lens design, searching for better quality materials and by developing correcting devices. It was found that generating a brighter source of electrons improved the resolution of the images, which lead during the 1960s, to the development of the lanthanum hexaboride filament (LaB_6) and the field emission guns (FEGs).

For SEM, the appearance of field emission guns (FEG) made a huge difference. In addition of being very bright, the beam source is very small (5-25 nm) in comparison to thermionic emitters (5 mm). That simplifies the demagnification lenses and reduces lens aberrations. FEGs have small energy spread, which favour imaging at low-energy (between 1 and 30 kV), a very important factor when imaging biological specimens. At present, thanks to FEGs, resolutions on the order of 1 nm can be achieved for commercial instruments, with a commercial limit of 0.4 nm[10]. A common question raised between SEM users is why the limited resolution of the instrument in comparison to TEMs. In SEMs, resolution depends on the imaged volume from where electrons escape, which means is material and energy

[10]Hitachi claims having the highest resolution SE detector resolution with his FEG-SEM SU9000. https://www.hitachi-hightech.com/eu/product_detail/?pn=em-su9000&version=

dependent. The situation is very different for TEMs where the theoretical limit is defined by electron wavelength and the energy applied to the beam[11].

1.5 TEM and its influence in Molecular Cell Biology

Starting by the early 60s, it would be a difficult task to enumerate all the discoveries made thanks to EM. It moulded our anatomic view of virus, prokaryotic and eukaryotic cells and hinted major discoveries in biology and medicine. EM was a catalyst for cell biology discoveries. For example, cell trafficking as a major subject was initiated shortly after the characterization at the ultrastructural level of the Golgi complex. In the period 1915-1945 the Golgi was a matter of controversy; some biologists claimed it only existed in certain type of cells and no one was sure about its function (Farquhar & Palade 1998). In 1954, just when the first sectioning techniques started to appear, Sjöstrand and Hanzon characterized the Golgi ultrastructure on exocrine cells of the mouse pancreas (Sjöstrand & Hanzon 1954). Also in 1954, George Emil Palade worked at the Rockefeller Institute on cell fractionation, but soon, by the influence of Claude and Porter, started to improve sample preparations of specimens for electron microscopy [12].

After gaining expertise in EM, he decided to tackle the problem of secretion. Using EM sections on pancreatic cells, radioactive leucine was tracked as it moved through the endoplasmic reticulum, then to the Golgi apparatus and finally to exocytic granules (Caro & Palade 1964). Soon after publishing, these paths were questioned and pointed that proteins could be in the cytoplasm and outside the Golgi cisternae. It took several years and additional refinement of the described autoradiography technique (Jamieson & Palade 1967a; Jamieson & Palade 1967b; Jamieson & Palade 1971), to prove the protein flow from ER to Golgi, from Golgi to vesicles and finally from vesicles to plasma membrane. At the end, evidence of a simple and good model for a basic secretory pathway was sound enough to be accepted. Additionally, many times since then, cytochemical and immunohistochemical methods revealed the location of glycosylation enzymes and the involvement of different types of enzymes in the cis- and trans- cisternae of Golgi apparatus (Mironov & Pavelka 2009). De

[11] TEMs usually operate at 200-300 kV. During the 70's some ultrahigh voltage TEM were developed, up to 3000 kV at CEMES-LOE/CNRS in Toulouse, France and at Hitachi in Tokyo and Osaka, Japan. These instruments can increase the resolution, penetrate thicker specimens and decrease chromatic aberrations caused by energy losses and scattering in the specimen. On the other side, the sample receives a lot of damage and they need extremely good vacuums.References at http://www.uhvem.osaka-u.ac.jp/en/what.html and (Fujita 1986).

[12] The Rockefeller school, with George Emil Palade at front, was without doubt, the most influential institution in cell biology. Unsatisfied with the limited quality on image reproduction of TEM images in printed journals, they created their own journal in 1955 (The Journal of Cell Biology, known at that time as The Journal of Biophysical and Biochemical Cytology). They also founded the American Society for Cell Biology. From http://www.rupress.org/content/our-history.

Duve, Claude and Palade won the Nobel Prize in 1974 for their discoveries concerning the structural and functional organization of the cell [13].

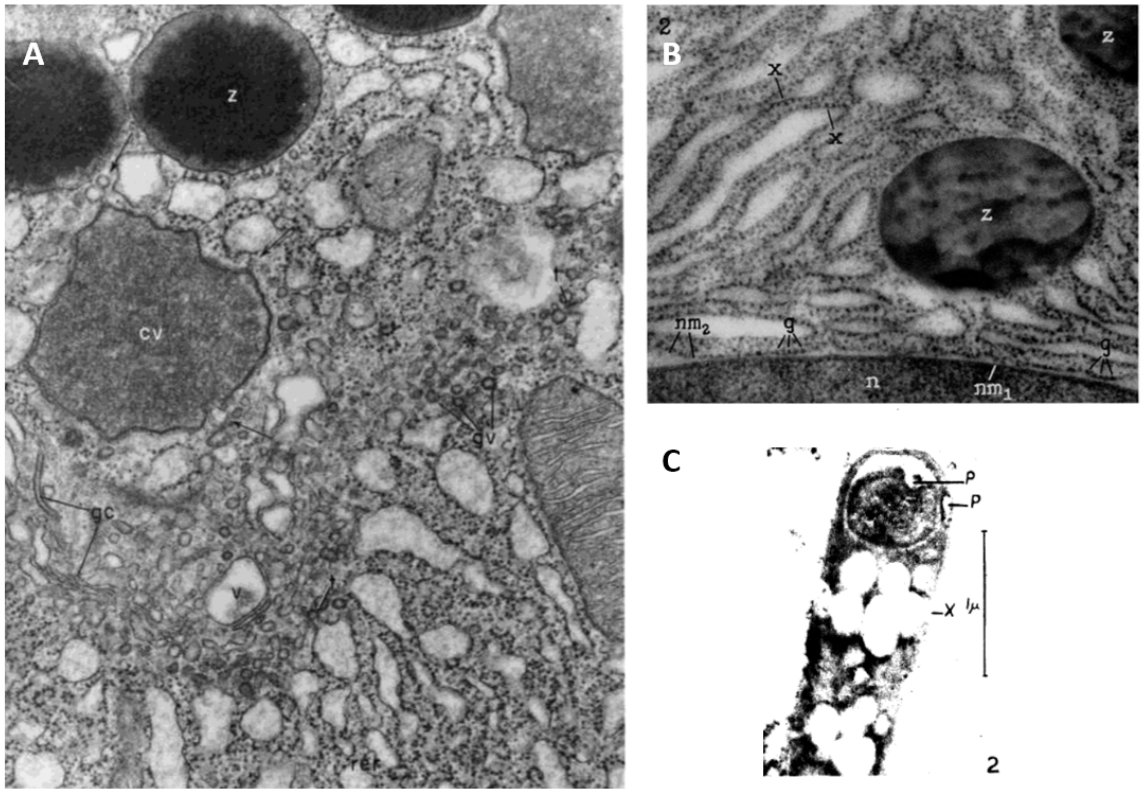

Fig. 1.4 **A.** Figure 7 of 1964 paper from Jamieson and Palade. It represents a view of the Golgi complex of a pancreatic acinar cell. At the bottom, rough ER is adjacent to the periphery of the Golgi, showing ER exocytes. In the picture, z stands for zymogen granules, cv stands for condensing vacuole, gc for golgi cisternae, v for vacuoles and gv for golgi vacuoles. Image taken at x44.000.**B.** Figure 2 from (Palade 1955) Ribosomes in acinar cell are marked with an x and g for granules. n stands for nucleus, nm for nuclear membrane and z again for zymogen granules. Magnification x74000.**C.** Bacillus megaterium section at x36.000. X are openings and P are peripheral bodies, which later became known as mesosomes (Chapman 1953).

In 1963, Ledbetter and Porter were studying the formation of cortices in plant cells (the surface layer or "skin"). The preservation with traditional methods was far from optimal, showing discontinuities of the plasma membrane and infiltration problems. The introduction of glutaraldehyde as a fixative solved the problem, but also showed a strange distribution of thin uniform filaments all over the cell, which they called "microtubules" (Ledbetter & Porter 1963). The discovery was confirmed later in all kind of eukaryotic cells and almost all microtubules have 13 protofilament subunits (Tilney et al. 1973). With the discovery of microtubules, the idea of a cell cytoskeleton was sowed.

[13] Unfairly, K.R. Porter was not even nominated.

Other major contributions were the studies of centrioles and cilia with their dynein arms (for a summary historical review check (Satir 2017)). In addition to biological research, electron microscopy examination of dynein arms is still used to diagnose immotile cilia, like in primary ciliary dyskinesia. It was not the only case where histopathology made use of EM. During the 70-80's it was heavily applied in diagnosis of renal diseases (structure of glomerulus), tumour processes, myopathies, storage disorders and infectious agents. With the advent of new tools like immuno-histochemistry (ELISA) or genetic diagnosis, EM was abandoned in pathology and nowadays is used only in few cases for diagnosis confirmation.

A big concern amongst the first community of electron microscopists was the presence of artefacts. Artefacts by stain and fixative precipitates could produce structures that were not present naturally in the samples. Palade noticed some weird granules (Figure 1.4-B), which he at the beginning mistook for precipitates. After using different fixatives, the granules were always in the cytoplasm or attached to some portions of the endoplasmatic reticulum (later identified as rough ER), and which he suspected they could be associated with Claude's microsomes. This was the first time ribosomes were observed (Palade 1955).

However, not every artefact observation ended up being a happy accident. On the contrary, artefacts had always been a core of criticism for electron microscopy and even experts can made wrong assumptions. In 1953, George B. Chapman and James Hillier, in addition to the achievement of differentiate cell wall structures of gram-positive and gram-negative bacteria, they found a new bacterial structure which they called "peripheral bodies" (Figure 1.4-C) (Chapman 1953). Renamed mesosomes later on, these structures were detected using traditional EM and freeze-fracture methods in many species. Full articles and books were written and even symposiums were made hypothesizing about its function. Many educational books and illustrations over internet still show mesosomes in their bacteria drawings. All the same, they were consequence of fixation procedures.

Ideally, a sample would be observed in the microscope in its native state, free of chemicals or another potential source of damage and artefacts. Nonetheless, we also have to consider, as discussed before, the requirements of thin sections and enough contrast of membranes - mostly composed of light elements (C, H, O, N). Because of this, previous to embedding, fixation and staining procedures via chemicals need to be applied. They can be roughly classified into two main methods. The first is known as chemical fixation and is the preferred method of this thesis. It uses a recipe of chemicals added to the sample at room temperature. Each chemical, like glutaraldehyde or osmium, is added in a series of successive steps, which fixes or stains certain parts of the cell or tissue. Chemical fixation is convenient for big samples as it allows processing in bulk. On the other side, it is a technique prone to artefacts

which affect membranes and organelles distorting their original shape or collapsing empty spaces (Korogod et al. 2015).

An alternative is high-pressure freezing (HPF) and freeze-substitution (FS) (Moor 1987; Dahl & Staehelin 1989). With this, the sample is quickly frozen under high pressure in a specifically designed machine called, obviously, high-pressure freezer. Once frozen, the sample is exposed progressively to chemicals which simultaneously fix and stain the sample whilst water is exchanged by organic solvents (such as acetone). During this process, the temperature is raised gradually until the sample is completely dehydrated, stained and then finally embedded in a resin. Being close to its native state when frozen, and with the gradual incorporation of chemicals at low temperatures, the result provides a better membrane preservation with high-quality contrast and fewer artefacts (Steinbrecht & Zierold 1987). Unfortunately, it has a limitation on size. Thick samples cannot be frozen immediately because an uneven distribution of temperature inside the specimen during freezing can cause ice damage.

A typical way of proceeding is to processes the sample by chemical fixation. If phenomena observed in chemically fixed sections need more detail or potential artefacts have to be discarded, freeze-substitution is the method of choice. It is necessary to remark that the final achievable resolution depends on the sample preparation technique and the instrument used. HPF provides better preservation, but not higher resolution. In the mesosome example, freeze-substitution observation of thin sections of bacteria, put on display serious doubts about their biological nature when compared to chemically fixed samples.

There is a third most sophisticated possibility: freeze the sample, but keep all instruments, from the ultra-microtome to the microscope at low temperature. Cryo-EM techniques (like CEMOVIS, cryoEM of vitreous sections (Al-Amoudi et al., 2004)) require expertise and a lot of labour but they have proved to be useful to solve the mesosome dilemma. Dubochet (Dubochet et al. 1983), which later would win the 2017 Nobel prize for his contributions to cryo-EM, showed that mesosomes could be artificially introduced if osmium tetraoxide was used to fix before doing cryo-EM on bacteria, but they could not be found naturally.

Cryo-EM is not only the way to solve faithfully cellular structures at high resolution. Thanks to new technological developments like the lift-out of lamellas inside cryo-stages (Mahamid et al., 2015), cryo-EM has emerged to fill the resolution gap between cell biology and structural biology. One example of it can be seen in (Mahamid et al., 2016) where a region close to the nuclear envelope is examined revealing its native organization close to molecular resolution.

1.6 Origins of Correlative microscopy

In almost all the discoveries done by EM, it was a common practice to compare EM images with transmitted light or phase contrast. For example, in his first attempt to describe the ER, Porter compared images of transmitted light microscopy and phase contrast versus electron microscopy: *"The "microscopic" components, nucleus, lipid granules, mitochondria, etc., differ from the light micrograph equivalent only in being more sharply defined."* (Porter 1943). Still, there was no correspondence between the cells imaged in the light microscope and the electron micrographs. The first paper to use clearly the word "correlative" was the work of Godman et al. (Godman et al. 1960; Morgan et al. 1960). In the article, Hela and Hep-2 cells were infected by type 5 adenovirus and its development was followed in vivo. The light microscopy images were used as a proxy to observe different infection stages, and then cells were processed to be observed by electron microscopy: *"When electron micrographs, however, are correlated with the temporal and topochemical information gathered by light microscopy, it becomes possible to reconstruct many of the events in the intranuclear development of type 5 adenovirus and to show the evolution of these changes. The most satisfactory correlation is obtained when the same cell is examined in contiguous thick and thin sections by light and electron microscopy, respectively."*

In 1987, M.A. Hayat edited a book entirely on correlative microscopy (Hayat 1987) with the collaboration of more than 40 scientists around the world. He tried to summarize all the efforts done at the time to combine the advantage of both techniques. One of the usual practices was to look at the same sections in transmitted light first and later in the electron microscope. The advantage of that was the possibility of using immuno-stain methods. The first step in immuno-techniques is to bind a specific primary monoclonal antibody to the sample section. With the immuno-peroxidase method, the antibody is tagged with a peroxidase enzyme, which catalyses a chemical reaction that generates a coloured product.

A second well-known method is immunogold labelling. First used in 1971 to identify Salmonella antigens (Page Faulk & Malcolm Taylor 1971), secondary antibodies are used to affix small particles of colloidal gold easily identifiable by the electron microscope. Using different gold particle sizes (1-20 nm) different molecules can be targeted simultaneously. During more than 30 years many proteins were identified in cellular sections by immuno-gold (Tokuyasu 1980; Geuze et al. 1984), or immuno-peroxidase methods. In Hayat's book, many of the included chapters relied on immuno-cytochemical methods.

An exception was an original chapter of the book dedicated to correlate images from confocal microscopes with EM. However, staining by fluorochromes attached to antibodies were of recent invention and it was still difficult to obtain good images. Another interesting

highlight of the book was the combination of a light and fluorescence microscope with SEM in a unique instrument. Images of critical-point dried cells could be looked in transmitted light, fluorescence and SEM (Figure 1.5-A).

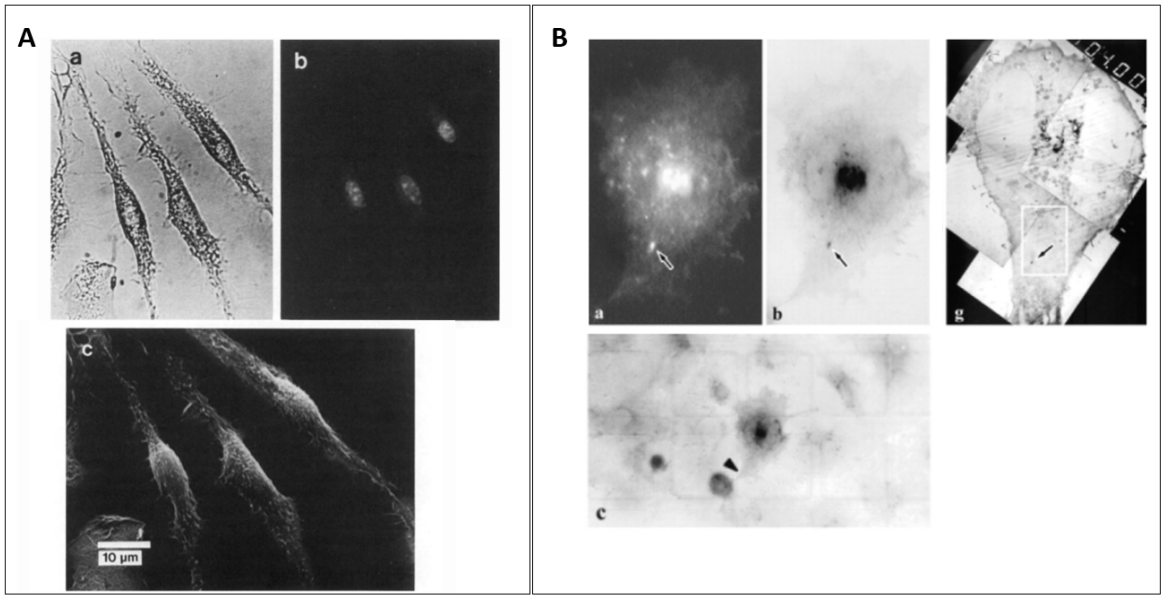

Fig. 1.5 **A.** Figure from (Hayat 1987), mouse bone marrow cultured on cover glass, transmitted light (a) and stained fluorescently for DNA (Feulgen staining) (b) and finally processed for SEM (c). Only topological information of membrane surfaces can be used to correlate cells between images. B. Figure 7 from (Polishchuk et al. 2000), Golgi apparatus VSVG-GFP (a), immuno-peroxidase (b) and montage of TEM images (g) from the same cell, as found in the CelLocate coordinates in (c). The arrow marks the same Golgi VSVG intracellular carrier.

Hayat's book was quite advanced for its time. It clearly defined the term CLEM (Correlative Light and Electron Microscopy), it emphasized the advantages of fluorescent microscopy combined with EM and the need to quantify and measure observations. Nevertheless, the excess in SEM imaging without showing clear advantages in the correlation -SEM was in the latest but cell surface topology was not a decisive source of information- and the reduced range of available antibodies (especially, for fluorescence) supported the point of CLEM as a quite shallow one.

For a few years, the progress in the field of CLEM was almost stalled. We have to wait until February 1994 when Martin Chalfie and co-workers published in Science the successful incorporation of the GFP gene into E.Coli (Chalfie et al. 1994). In less than two years, genetic tags for identification of any individual protein were possible (Heim & Tsien 1996), thenceforth, a transformation in the landscape of live-cell light microscopy. As with Palade's group 40 years before, the driving force to mix GFP with EM would be again,the intricacies

of the Golgi apparatus and the secretory pathway (Polishchuk et al. 2000; Mironov et al. 2000).

Alexandre A. Mironov and his team in Italy worked for many years on the mechanisms of intracellular transport (Mironov et al. 2000). After being transported through the Golgi cisternae, secretory proteins are confined in membranous carriers called transport intermediates (TI). TIs are then shuttled to different parts of the cell. Using GFP, they tagged the VSVG (vesicular stomatitis virus G) protein, which allowed to monitor in vivo the lifecycle of the protein from the Golgi apparatus to the plasma membrane with a time-lapse confocal microscope. They monitored several cells and when one of them was at a point of interest, it was fixed and the GFP protein immuno-peroxidase labelled. Thus, they could assess in detail the ultrastructural characteristics of the carriers. TIs differed from typical vesicles and had an unexpected tubular-saccular shape, something very difficult to differentiate at the low-resolution optical microscopy. To locate the cell of interest they used CELLocate coverslips attached to the bottom of the Petri dishes were cells were seeded (Figure 1.5-B). CELLocate coverslips were grided glass bottom dishes patented by Eppendorf-Netheler-Hinz GmbH in 1991, and used in a CLEM for the first time by (Stierhof et al. 1994)[14]. After resin embedding, they used hydrofluoric acid to dissolve the coverslip and the imprinted pattern from the coverslip remained in the resin.

All methods shown in the article were known from many years before, the achievement was to combine all of them in a comprehensible CLEM workflow. Since then, multiple articles with different variants from it have been published to any existent organelle, for example with Golgi apparatus (Brown et al. 2009; Polishchuk et al. 2004), endoplasmic reticulum (Puhka et al. 2012) or lysosomes (van Rijnsoever et al. 2008).

1.7 From 1980 to present – Automated control in Electron Microscopes

Since the very beginning, EM also grabbed the interest of structural biologists. It would be beyond the scope of this introduction to describe all the contributions in which material scientists, cell and structural biologists historically helped each other. From sample preparation to hardware progress, the boundaries between them haven always been diffuse. One particular example was in the analysis of thin material slices. Scattered electrons going through a sample can form a diffraction pattern, especially in crystals. If the sample is oriented at different degrees and the diffraction pattern gathered, this information can complement X-ray

[14] In the same way as Hayat´s book method, they used fluorescent antibodies, transmitted light and SEM.

diffraction data to solve complex structures (Cowley et al. 2006). Because of this, tilting stages were driven to a degree of accuracy and automation beyond the usual limits for TEM, converging in the development of the first fully automated control of a serial acquisition: electron tomography.

By imaging at incremental degrees of rotation around the center of a sub-cellular region of a sample, it was possible, in principle, by the Radon theorem (Radon 1917), to generate 3D reconstructions at high resolution. Computed tomography scans in medicine exploited this fact and they were a reality since the middle of the 70's. Electron tomography was also possible, but it was cumbersome, time consuming and prone to errors due to image alignment.

During the 80's, the integrated circuits industry invaded almost every research field. Stage automation and sophisticated electronic control replaced the old EM manual knobs and analogic circuitry. Structural biology pushed for automated stages with better and faster tilting capabilities. Computerized control allowed for automatic procedures like autofocus, autostigmatism, eucentricity[15], refined tilting, compensation for specimen displacements, refocusing on previous stored positions, and overall, better accuracy in positioning. In 1992, (Koster et al. 1992; Bárcena & Koster 2009), automated electron tomography became a reality and in the following years a routine for every EM laboratory .

Computerized controls enhanced all the aspects of microscopy, with the highest impact on SEM. SEM instruments were extensively used in material science and manufacturing industry to check cracks or faults on circuitry. Repairing faulty circuitry at the level of transistors in the semiconductor industry motivated the development of a new tool, the Focus Ion Beam (FIB). First reported in 1961 by Krohn as the result of research on liquid-metal ion sources for use in the aerospace industry (Wagner 1983), focused ion beam (FIB) columns produce a current of ions pulled-out into a beam by an electric field. They subsequently pass through apertures to define the size of the beam and they impact on the surface in a similar way as an electron beam. Inelastic collisions of ions can also be used to image the surface, similarly as an SEM would do. The difference is that ions are heavier and ion-atom elastic collisions can remove an atom and produce an excavation on the sample. This effect of material ablating is known as sputtering or milling. The combination of two columns, one for imaging using SEM and other for disposing of material resulted in a new type of microscope known as FIB-SEM. FIBs can remove material from a sample in the shape of thin sections. Combined with SEM imaging of the milled region, 3D volumes of materials can be acquired with a z resolution up to 4 nm in the most recent instruments. FIB-SEM was

[15]Eucentricity or eucentric height is a condition where the sample is located at the horizontal centre of the objective lens, then the sample can be tilted around its axis without shifting the image in x and y.

occasionally used as a research instrument (Orso 2005), but mostly to determine properties of biological materials or surfaces by using SEM imaging. Only after 2000, as a result of its commercial success in the materials science field, biologists drew their attention to it (Narayan & Subramaniam 2015).

Around 2005, neuroscience started to emerge as one of the largest fields in science after molecular and cell biology, physics, chemistry and medicine (Rosvall & Bergstrom 2010). In neuroscience, the structure and classification of synapses and the identification of neurons in a volume of tissue require high-resolution systems (Titze & Genoud 2016). TEM was for long the workhorse used to do this task (Harris et al. 2006), but it needs time, a dedication of laborious sectioning and imaging. A stack made of piled sections could be arranged together and boundaries segmented to form 3D models showing the disposition of cells. Resultant volumes from several sections placed in a z-stack are anisotropic (not equal in all dimensions) which can cause synapses or connections between neurons to be lost when retraced. In addition, sections can be lost, damaged or distorted by the knife of the ultramicrotome.

With the neuroscience boom , investment in gathering larger, more isotropic and quantifiable volumes of neural systems forced the development of new approaches. Together with FIB-SEM, SBF-SEM (serial block-face SEM) and ATUM-SEM techniques were developed in what would be later known in literature as Volume EM (Peddie & Collinson 2014).

In 2004, W. Denk and co-workers published the serial block-face SEM (Denk & Horstmann 2004). Conceptually very simple, consisted on introducing an autonomous ultramicrotome knife inside an SEM chamber. The face of a pre-trimmed block was imaged by the SEM using backscattered secondary electrons. In a subsequent step, a mounted knife inside the microscope chamber, sections the top of the resin block. The SEM images again and at the end of this iterative process, the full volume is imaged. SBF-SEM has several advantages over manual approaches: sectioning is automated, releasing the microscopist of hard manual labour. It is capable of imaging large field of views (0.5 by 0.5 mm2) with a z resolution between 20 and 30 nm. It also has the advantage that imaging the block face before cutting the section eliminates compression artefacts generated by knife forces.

SBF-SEM has achieved a considerable success acquiring parts of brain tissue. It has, however, some drawbacks. First, it is destructive, what is sectioned cannot be recovered for further investigation. Second, defects on the knife can affect the image or non-well cut sections can fall back on the top of the sample, losing sections in a similar way as TEM sectioning. And third and more important, it brings a serious charging problem [16]. For this reason, the material imaged has to be prepared with heavy metal staining protocols or

[16] When charging, images formed are blurred, full of distortions or just empty.This is also the reason why SEM samples of insects or pollen have to be gold-coated before imaging, then charges are compensated and a perfect image can be formed.

covered with conductive resins (Nguyen et al. 2016). In consequence, the sample becomes conductive but is also heavily extracted (outer cell membranes remain, but inner parts are diluted by the chemicals of the sample preparation, giving an impression of emptiness). This type of sample preparation is fine when tissues are nervous system and the goal is to trace neurons and synapses, but it is far from ideal for other type of biological samples.

In 2008, FIB-SEM was proposed as an alternative for brain tissue volume acquisition (Knott et al. 2008). FIB-SEM had been used in biological specimens before (Heymann et al. 2006; Drobne et al. 2005), but it was not until 2009 when it gained momentum. The imaging process is also destructive and samples also need a protective coating to avoid undesired charging on the top of the sample. The acquisition time is considerably much slower than with any other techniques. However, FIB-SEM is used when the region of imaging is smaller and the goal is to obtain isotropic volumes, for example, of 5x5x5 nm over a 50x50 µm ROI. With good sample preparation, the process of milling and imaging, also called slice and view, is fast enough (in some machines, can be even simultaneous) to get images without undesirable image distortions.

In recent years, new approaches for 3D volume based on TEM have emerged. First, increase the degree of automation in serial section TEM (Zheng et al. 2018) . This can be achieved by including an automatic exchange of sample carriers and with better cameras able to generate montages at different resolutions. Maps of regions can be generated with software assistance. Nonetheless, it still requires an operator sectioning and collecting grids. Another solution is the one presented by (Hayworth et al. 2015; Hayworth et al. 2006), called ATUM (Automatic Tape-collecting Ultra Microtome). Once a trimmed sample is arranged in a regular ultramicrotome, a conveyor belt is used to collect grids[17]. Grids are deposited on large strips of carbon-coated tape. SEM instead of TEM can be used to image sections automatically. For example, *ATLAS 5* software from *Zeiss*[18] can recognise simple patterns like the typical trapezoidal shape of sections and then focus on them to image at high resolution.

For all the Volume EM technologies , height and width cannot get below 4 nm pixel-size. What is different between the techniques is the z resolution. For ATUM and serial sections until 20 nm can be achieved. SBF-SEM has shown stacks up to 10 nm, and FIB-SEM has the record with 4 nm. That limit is about the size of an actin microfilament, which makes a hard choice of this technologies for cytoskeleton studies. Beyond that limit, TEM is the usual choice. Electron tomography can easily achieve lateral resolutions of 0.5 nanometers,

[17]https://www.rmcboeckeler.com/atumtome

[18]https://www.zeiss.com/microscopy/us/products/microscope-software/atlas.html

mostly limited by sample preparation and field of view (the real limit is about 1.4 A (Ercius et al. 2015)).

1.8 CLEM in the present

Volume EM did not take long to be combined with fluorescence microscopy reviving the interest in the field again. Different CLEM methods have been exploited with multiple variations over the last 10 years (de Boer et al. 2015). For an extensive review, the trilogy of books edited from Paul Verkade and Thomas Muller-Reichert are an excellent reference (Müller-Reichert & Verkade 2012; Müller-Reichert & Verkade 2014; Müller-Reichert & Verkade 2017).

CLEM research is mostly centered into optimize sample preparation to be the closest possible to a native state, with good contrast and without artefacts. A minimal fixation, optimal contrasting, resin selection related to specimen composition and the effect of the beam on it (e.g., need of better conductivity for SEM samples) are determinant factors to get clear images.

Another area of research is related to bi-modal probes, labels compatible with both optical and electron microscopy. We discussed immuno-gold labelling and immuno-peroxidase. These techniques have several drawbacks: cells have to be heavily permeabilized with the subsequent deterioration of membranes, they depend on the availability and specificity of primary antibodies and if antibodies target GFP, the big GFP-antibody complex can interfere with other protein complexes not giving a clear readout (Giepmans et al. 2006). Moreover, if the labelling is done per section (post-embedding labelling), the amount of manual labour is unsuitable for big specimens. On the other side, peroxidases mark the region with a dark black precipitate, but the stain hampers the visibility of the region and is limited in precision (Griffiths 1993). We also have the problem to register a 2D low-resolution image or confocal stack from the light microscope with a thin precise section of a volume in EM.

Consequently, a huge effort in the last years has been done to achieve ideal hybrid probes, visible in fluorescence microscopy and later in EM sections. In certain way, they can be seen as the technical evolution of the immuno-gold and immuno-peroxidase methods seen before. The first approach consists of introducing probes like quantum dots or nanoprobes that serve as a reference between fluorescence channels and EM sections (van Weering et al. 2010). *FluoroNanogold* are particles that can be seen as fluorescent markers (they can be conjugated with antibodies to identify the region of interest) and as gold particles in EM (Takizawa et al. 1998). In the same line, quantum dots (Giepmans et al. 2005) are nanocrystals which size allows to penetrate on membranes. Other commercial beads in the same line are *FluoSpheres*

or *TetraSpecks* both from *Thermofisher*. *TetraSpecks*, for example can be seen in fluorescence very clearly and in EM have a dark distinctive electron-dense appearance, very similar to gold nanoparticles, which allow them for a high resolution in the correlation (Kukulski et al. 2011). Unfortunately, most of these techniques, they are restricted to permeabilized cells or regions close to the extracellular side.

The other category of probes is based on the conversion of a protein with a fluorescent tag into a detectable electron dense signal[19] . Peroxidase based methods exploit the ability of peroxidases to catalyze oxidation DAB (diaminobenzidine) and generate insoluble granular precipitates. These densities are osmiophilic and can be found in the electron microscope images as black dense regions. DAB can react in the same region where fluorophores are excited and in this way are used to co-localize with fluorescence images (Maranto 1982). GRAB (GFP recognition after bleaching) used photo-oxidation to create a precipitate that could be differentiated in EM sections after bleaching the fluorescence GFP channel (Grabenbauer et al. 2005). A few years later, an improved version with increased photo-oxidation rate was released (Shu et al. 2011). Known as mini singlet-oxygen generator (miniSOG), it can be encoded genetically like GFP. The protein of interest can be double tagged, with miniSOG and GFP. When DAB is delivered in fixed cells, the protein targeted catalyzes oxidation and shows a perfect correlation with GFP. Methods like APEX (Martell et al. 2012), HRP (Li et al. 2010) or APEX2 (Lam et al. 2015) encode enzyme peroxidases which also generate densities when they react against DAB in regions where the protein of interest is located. However, multiple studies have shown that dedicated sample preparations can preserve fluorescence on sections (Nixon et al., 2009, Kukulski et al. 2012; Peddie et al. 2014; Delpiano et al. 2018). If that is the case, registration methods can deliver the same results as an encoded tag without blurring or darkening the region of interest.

Another need in research resides on the development of better software. Experimental set ups are per se very laborious, so good software can reduce the time per experiment and increase the quality of data analysis. Software packages can be used for 4 purposes: control of the microscope, correlation with other modalities, visualization and data analysis. There is some open source software freely available, but the main problem is that if developers do not get funding to continue working after a completion of their research, the software outdates and becomes obsolete. Commercial software, on the other side, is maintained as long as client portfolio is paying for it. It is usually expensive and their code is closed to experimental modifications during a research.

Microscope controllers open source like SerialEM (Mastronarde 2005), allow to control TEMs and generate maps for later acquisition of tomograms. Companies usually have

[19] A good example applied to Zebrafish in developmental biology can be found at (Ariotti et al. 2015).

programming controls delivered to the buyer under development licenses, for example, *SmartSEM* and its related set of programming APIs (*Carl Zeiss Microscopy GmbH*). For correlation, some *Fiji* (Schindelin et al. 2012) plugins or the *ec-CLEM* plugin for *Icy* (Paul-Gilloteaux et al. 2017) are open source tools that can be used for correlation. *FEI* developed *MAPS* (https://www.fei.com/software/maps/) to superimpose TEM images with fluorescence as acquired. *MAPS* is an image editor which allows registration refinement by manual clicking on spatial landmarks such as fiducial markers or cell shapes. In the same line, but more oriented to a calibrated transfer shuttle between microscopes, *Zeiss* marketed *'Shuttle & Find'*. 3 fiducial markers are used to initially calibrate the positions of the images obtained in light microscopy, and then in the electron microscope. *Shuttle & Find* has been replaced for the more sophisticated *ATLAS 5*, able to read metadata from *Zeiss* light microscopes and provide manual assisted registration between images. Finally, image analysis software needed for visualization, segmentation and measuring; open source such as *Drishti* (Limaye 2012), *Microscopy Image Browser* (*MIB*) (Belevich et al. 2016) and *Imod* (Kremer et al. 1996), or commercial like *Amira* (https://www.fei.com/software/amira-for-life-sciences) and Imaris (http://www.bitplane.com).

Software applications are in constant evolution guided by the needs of the community and the breakthroughs from the computer vision and robotics field. It is especially relevant the efforts in segmentation using deep learning (see discussion in chapter 5) and the application of registration techniques. Nowadays, the general consensus for most of them there is a lack of affordance (a concept used in design to define objects easy to use, like a doorknob or the touchpad of mobile phones), they usually have problems with image formats compatibility and they struggle managing big datasets (e.g., a single 2D image bigger than 4 Gb).

The last crucial point is the need for quantification at the level of populations. In principle, with infinite time and money, any experiment can be repeated until enough measures are available. The reality, though, constrains us to a limited amount of time and material resources. Here is when the combination of a quick and easy to reproduce sample preparation protocol, a good software to correlate fluorescence with electron microscopy, and finally, a fully automated process of data acquisition can make a difference. This is also why automation is the central topic of this dissertation.

References

Abbe, E.(1881) 'On the Estimation of Aperture', *Transactions of the Royal Society.*

Al-Amoudi, A., Chang, J.-J., Leforestier, A., McDowall, A., Salamin, L. M., Norlén, L. P. O., Richter, K., Blanc, N. S., Studer, D. and Dubochet, J. (2004) 'Cryo-electron microscopy of vitreous sections.', *The EMBO*

journal. European Molecular Biology Organization, 23(18), pp. 3583–8. doi: 10.1038/sj.emboj.7600366.

Ariotti, N., Hall, T. E., Rae, J., Ferguson, C., McMahon, K.-A., Martel, N., Webb, R. E., Webb, R. I., Teasdale, R. D. and Parton, R. G. (2015) 'Modular Detection of GFP-Labeled Proteins for Rapid Screening by Electron Microscopy in Cells and Organisms', *Developmental Cell*. Elsevier, 35(4), pp. 513–525. doi: 10.1016/j.devcel.2015.10.016.

Bárcena, M. and Koster, A. J. (2009) 'Electron tomography in life science', *Seminars in Cell & Developmental Biology*. Academic Press, 20(8), pp. 920–930. doi: 10.1016/J.SEMCDB.2009.07.008.

Belevich, I., Joensuu, M., Kumar, D., Vihinen, H. and Jokitalo, E. (2016) 'Microscopy Image Browser: A Platform for Segmentation and Analysis of Multidimensional Datasets', *PLoS Biology*, 14(1). doi: 10.1371/journal.pbio.1002340.

de Boer, P., Hoogenboom, J. P. and Giepmans, B. N. G. (2015) 'Correlated light and electron microscopy: ultrastructure lights up!', *Nature Methods*, 12(6), pp. 503–513. doi: 10.1038/nmeth.3400.

Bretschneider, L. H. (1952) 'The Fine Structure of Protoplasm', Survey of Biological Progress. Elsevier, 2, pp. 223–257. doi: 10.1016/B978-1-4832-0001-9.50010-5.

Brown, E., Mantell, J., Carter, D., Tilly, G. and Verkade, P. (2009) 'Studying intracellular transport using high-pressure freezing and Correlative Light Electron Microscopy', *Seminars in Cell & Developmental Biology*, 20(8), pp. 910–919. doi: 10.1016/j.semcdb.2009.07.006.

Caro, L. G. and Palade, G. E. (1964) 'PROTEIN SYNTHESIS, STORAGE, AND DISCHARGE IN THE PANCREATIC EXOCRINE CELL. AN AUTORADIOGRAPHIC STUDY.', *The Journal of cell biology*, 20, pp. 473–95.

Chalfie, M., Tu, Y., Euskirchen, G., Ward, W. W. and Prasher, D. C. (1994) 'Green fluorescent protein as a marker for gene expression.', *Science* (New York, N.Y.), 263(5148), pp. 802–5.

Chapman, G. B. (1953) 'ELECTRON MICROSCOPY OF ULTRA-THIN SECTIONS OF BACTERIA II. SPORULATION OF Bacillus megaterium AND Bacillus cereus'.

Claude, A. (1939) 'CHEMICAL COMPOSITION OF THE TUMOR-PRODUCING FRACTION OF CHICKEN TUMOR I.', *Science* (New York, N.Y.). American Association for the Advancement of Science, 90(2331), pp. 213–4. doi: 10.1126/science.90.2331.213.
Claude, A. and Fullam, E. F. (1946) 'THE PREPARATION OF SECTIONS OF GUINEA PIG LIVER FOR ELECTRON MICROSCOPY'.

Cowley, J. M., Goodman, P., Vainshtein, B. K., Zvyagin, B. B. and Dorset, D. L. (2006) 'Electron diffraction and electron microscopy in structure determination', in *International Tables for Crystallography*. Chester, England: International Union of Crystallography, pp. 276–345. doi: 10.1107/97809553602060000558.

Dahl, R. and Staehelin, L. A. (1989) 'High-pressure freezing for the preservation of biological structure: Theory and practice', *Journal of Electron Microscopy Technique*, 13(3), pp. 165–174. doi: 10.1002/jemt.1060130305.

Delpiano, J., Pizarro, L., Peddie, C. J., Jones, M. L., Griffin, L. D. and Collinson, L. M. (2018) 'Automated detection of fluorescent cells in in-resin fluorescence sections for integrated light and electron microscopy', *Journal of Microscopy*. doi: 10.1111/jmi.12700.

Denk, W. and Horstmann, H. (2004) 'Serial Block-Face Scanning Electron Microscopy to Reconstruct Three-Dimensional Tissue Nanostructure', *PLoS Biology*. Edited by Kristen M. Harris. Public Library of Science, 2(11), p. e329. doi: 10.1371/journal.pbio.0020329.

Drobne, D., Milani, M., Zrimec, A., Zrimec, M. B., Tatti, F. and Draslar, K. (2005) 'Focused ion beam/scanning electron microscopy studies of Porcellio scaber (Isopoda, Crustacea) digestive gland epithelium cells.', Scanning, 27(1), pp. 30–4.

Dubochet, J., McDowall, A. W., Menge, B., Schmid, E. N. and Lickfeld, K. G. (1983) 'Electron microscopy of frozen-hydrated bacteria.', Journal of bacteriology. American Society for Microbiology (ASM), 155(1), pp. 381–90.

De Duve, C., Beaufay, H. and De, C. (1981) 'A Short History of Tissue Fractionation', Journal of Cell Biology.

Ercius, P., Alaidi, O., Rames, M. J. and Ren, G. (2015) 'Electron Tomography: A Three-Dimensional Analytic Tool for Hard and Soft Materials Research.', Advanced materials (Deerfield Beach, Fla.). NIH Public Access, 27(38), pp. 5638–63. doi: 10.1002/adma.201501015.

Everhart, T. E. and Thornley, R. F. M. (1960) 'Wide-band detector for micro-microampere low-energy electron currents', Journal of Scientific Instruments. IOP Publishing, 37(7), pp. 246–248. doi: 10.1088/0950-7671/37/7/307.

Farquhar, M. G. and Palade, G. E. (1998) 'The Golgi apparatus: 100 years of progress and controversy.', Trends in cell biology, 8(1), pp. 2–10.

Fujita, H. (1986) 'Ultra-high voltage electron microscopy: Past, present, and future', Journal of Electron Microscopy Technique. Wiley-Blackwell, 3(3), pp. 243–304. doi: 10.1002/jemt.1060030303.

Gessler, A. E. and Fullam, E. F. (1946) 'Sectioning for the electron microscope accomplished by the high speed microtome.', The American journal of anatomy, 78, pp. 245–83.

Geuze, H. J., Slot, J. W., Strous, G. J. A. M., Peppard, J., von Figura, K., Hasilik, A. and Schwartz, A. L. (1984) 'Intracellular receptor sorting during endocytosis: Comparative immunoelectron microscopy of multiple receptors in rat liver', Cell. Cell Press, 37(1), pp. 195–204. doi: 10.1016/0092-8674(84)90315-5.

Giepmans, B. N. G., Adams, S. R., Ellisman, M. H. and Tsien, R. Y. (2006) 'The Fluorescent Toolbox for Assessing Protein Location and Function', *Science*, 312(5771), pp. 217–224. doi: 10.1126/science.1124618.

Giepmans, B. N. G., Deerinck, T. J., Smarr, B. L., Jones, Y. Z. and Ellisman, M. H. (2005) 'Correlated light and electron microscopic imaging of multiple endogenous proteins using Quantum dots', *Nature Methods*, 2(10), pp. 743–749. doi: 10.1038/nmeth791.

Godman, G. C., Morgan, C., Breitenfeld, P. M. and Rose, H. M. (1960) 'A correlative study by electron and light microscopy of the development of type 5 adenovirus. II. Light microscopy.', *The Journal of experimental medicine*. The Rockefeller University Press, 112(2), pp. 383–402.

Goldstein, J. I., Newbury, D. E., Echlin, P., Joy, D. C., Lyman, C. E., Lifshin, E., Sawyer, L. and Michael, J. R. (2003) *Scanning Electron Microscopy and X-ray Microanalysis*. Boston, MA: Springer US. doi: 10.1007/978-1-4615-0215-9.

Grabenbauer, M., Geerts, W. J. C., Fernadez-Rodriguez, J., Hoenger, A., Koster, A. J. and Nilsson, T. (2005) 'Correlative microscopy and electron tomography of GFP through photooxidation', Nature Methods. Nature Publishing Group, 2(11), pp. 857–862. doi: 10.1038/nmeth806.

Griffiths, G.(1993) Fine Structure Immunocytochemistry. *Springer Berlin Heidelberg.*

Harris, K. M., Perry, E., Bourne, J., Feinberg, M., Ostroff, L. and Hurlburt, J. (2006) 'Uniform serial sectioning for transmission electron microscopy.', *The Journal of neuroscience*: the official journal of the Society for Neuroscience. Society for Neuroscience, 26(47), pp. 12101–3. doi: 10.1523/JNEUROSCI.3994-06.2006.

Hayat, M.(1987), Correlative Microscopy In Biology:Instrumentation and Methods. *Elsevier Science*.

Hayworth, K. J., Xu, C. S., Lu, Z., Knott, G. W., Fetter, R. D., Tapia, J. C., Lichtman, J. W. and Hess, H. F. (2015) 'Ultrastructurally smooth thick partitioning and volume stitching for large-scale connectomics.', *Nature methods*, 12(4), pp. 319–22. doi: 10.1038/nmeth.3292.

Hayworth, K., Kasthuri, N., Schalek, R. and Lichtman, J. (2006) 'Automating the Collection of Ultrathin Serial Sections for Large Volume TEM Reconstructions', Microscopy and Microanalysis. Cambridge University Press, 12(S02), pp. 86–87. doi: 10.1017/S1431927606066268.

Heim, R. and Tsien, R. Y.(1996),'Engineering green fluorescent protein for improved brightness, longer wavelengths and fluorescence resonance energy transfer.', *Current biology*: CB, 6(2), pp. 178–82.
Heymann, J. A. W., Hayles, M., Gestmann, I., Giannuzzi, L. A., Lich, B. and Subramaniam, S. (2006) 'Site-specific 3D imaging of cells and tissues with a dual beam microscope', *Journal of Structural Biology.* Academic Press, 155(1), pp. 63–73. doi: 10.1016/J.JSB.2006.03.006.

Jamieson, J. D. and Palade, G. E. (1967a) 'Intracellular transport of secretory proteins in the pancreatic exocrine cell. I. Role of the peripheral elements of the Golgi complex.', *The Journal of cell biology*, 34(2), pp.

577–96.

Jamieson, J. D. and Palade, G. E. (1967b) 'Intracellular transport of secretory proteins in the pancreatic exocrine cell. II. Transport to condensing vacuoles and zymogen granules.', *The Journal of cell biology*, 34(2), pp. 597–615.

Jamieson, J. D. and Palade, G. E. (1971) 'Synthesis, intracellular transport, and discharge of secretory proteins in stimulated pancreatic exocrine cells.', *The Journal of cell biology*, 50(1), pp. 135–58.

Knott, G., Marchman, H., Wall, D. and Lich, B. (2008) 'Serial Section Scanning Electron Microscopy of Adult Brain Tissue Using Focused Ion Beam Milling', Journal of Neuroscience, 28(12), pp. 2959–2964. doi: 10.1523/JNEUROSCI.3189-07.2008.

Korogod, N., Petersen, C. C. and Knott, G. W. (2015) 'Ultrastructural analysis of adult mouse neocortex comparing aldehyde perfusion with cryo fixation', eLife, 4. doi: 10.7554/eLife.05793.

Koster, A. J., Chen, H., Sedat, J. W. and Agard, D. A. (1992) 'Automated microscopy for electron tomography.', Ultramicroscopy, 46(1–4), pp. 207–27.

Kremer, J. R., Mastronarde, D. N. and McIntosh, J. R. (1996) 'Computer Visualization of Three-Dimensional Image Data Using IMOD', *Journal of Structural Biology*, 116(1), pp. 71–76. doi: 10.1006/jsbi.1996.0013.

Kukulski, W., Schorb, M., Welsch, S., Picco, A., Kaksonen, M. and Briggs, J. A. G. (2011) 'Correlated fluorescence and 3D electron microscopy with high sensitivity and spatial precision.', *The Journal of cell biology*, 192(1), pp. 111–9. doi: 10.1083/jcb.201009037.

Kukulski, W., Schorb, M., Welsch, S., Picco, A., Kaksonen, M. and Briggs, J. A. G. (2012) Precise, Correlated Fluorescence Microscopy and Electron Tomography of Lowicryl Sections Using Fluorescent Fiducial Markers. Academic Press. doi: 10.1016/B978-0-12-416026-2.00013-3.

Lam, S. S., Martell, J. D., Kamer, K. J., Deerinck, T. J., Ellisman, M. H., Mootha, V. K. and Ting, A. Y. (2015) 'Directed evolution of APEX2 for electron microscopy and proximity labeling.', *Nature methods*. NIH Public Access, 12(1), pp. 51–4. doi: 10.1038/nmeth.3179.

Latta, H. and Hartmann, J. F. (1950) 'Use of a glass edge in thin sectioning for electron microscopy.', *Proceedings of the Society for Experimental Biology and Medicine.* Society for Experimental Biology and Medicine (New York, N.Y.), 74(2), pp. 436–9.

Ledbetter, M. C. and Porter, K. R. (1963) 'A *MICROTUBULE* IN PLANT CELL FINE STRUCTURE.', *The Journal of cell biology*. Rockefeller University Press, 19(1), pp. 239–50. doi: 10.1083/JCB.19.1.239.

Li, J., Wang, Y., Chiu, S.-L. and Cline, H. T. (2010) 'Membrane targeted horseradish peroxidase as a marker for correlative fluorescence and electron microscopy studies', *Frontiers in Neural Circuits*, 4, p. 6. doi:

10.3389/neuro.04.006.2010.

Limaye, A. (2012) 'Drishti: a volume exploration and presentation tool', in Stock, S. R. (ed.). *International Society for Optics and Photonics*, p. 85060X. doi: 10.1117/12.935640.

Mahamid, J., Pfeffer, S., Schaffer, M., Villa, E., Danev, R., Kuhn Cuellar, L., Forster, F., Hyman, A. A., Plitzko, J. M. and Baumeister, W. (2016) 'Visualizing the molecular sociology at the HeLa cell nuclear periphery', *Science*, 351(6276). doi: 10.1126/science.aad8857.

Mahamid, J., Schampers, R., Persoon, H., Hyman, A. A., Baumeister, W. and Plitzko, J. M. (2015) 'A focused ion beam milling and lift-out approach for site-specific preparation of frozen-hydrated lamellas from multicellular organisms', *Journal of Structural Biology*, 192(2), pp. 262–269. doi: 10.1016/j.jsb.2015.07.012.

Nixon, S. J., Webb, R. I., Floetenmeyer, M., Schieber, N., Lo, H. P. and Parton, R. G. (2009) 'A Single Method for Cryofixation and Correlative Light, Electron Microscopy and Tomography of Zebrafish Embryos', *Traffic*, 10(2), pp. 131–136. doi: 10.1111/j.1600-0854.2008.00859.x.

Maranto, A. R. (1982) 'Neuronal mapping: a photooxidation reaction makes Lucifer yellow useful for electron microscopy.', *Science* (New York, N.Y.), 217(4563), pp. 953–5.

Martell, J. D., Deerinck, T. J., Sancak, Y., Poulos, T. L., Mootha, V. K., Sosinsky, G. E., Ellisman, M. H. and Ting, A. Y. (2012) 'Engineered ascorbate peroxidase as a genetically encoded reporter for electron microscopy.', *Nature biotechnology*. NIH Public Access, 30(11), pp. 1143–8. doi: 10.1038/NBT.2375.

Marton, L. (1941) 'The Electron Microscope: A New Tool for Bacteriological Research.', Journal of bacteriology. American Society for Microbiology (ASM), 41(3), pp. 397–413.

Mastronarde, D. N. (2005) 'Automated electron microscope tomography using robust prediction of specimen movements', *Journal of Structural Biology*, 152(1), pp. 36–51. doi: 10.1016/j.jsb.2005.07.007.

Mironov, A. A. and Pavelka, M. (2009) The Golgi Apparatus. New York, NY: Springer New York. doi: 10.1007/978-0-387-74347-9_1.

Mironov, A. A., Polishchuk, R. S. and Luini, A. (2000) 'Visualizing membrane traffic in vivo by combined video fluorescence and 3D electron microscopy.', *Trends in cell biology*, 10(8), pp. 349–53.

Moor, H. (1987) 'Theory and Practice of High Pressure Freezing', in Cryotechniques in Biological Electron Microscopy. Berlin, Heidelberg:*Springer Berlin Heidelberg*, pp. 175–191. doi: 10.1007/978-3-642-72815-0_8.

Morgan, C., Godman, G. C., Breitenfeld, P. M. and Rose, H. M. (1960) 'A correlative study by electron and light microscopy of the development of type 5 adenovirus. I. Electron microscopy.', *The Journal of experimental medicine*. The Rockefeller University Press, 112(2), pp. 373–82.

Müller-Reichert, T. and Verkade, P. (2012) Correlative Light and Electron Microscopy. Academic Press.

Müller-Reichert, T. and Verkade, P. (2014) Correlative Light and Electron Microscopy II.

Müller-Reichert, T. and Verkade, P. (2017) Correlative light and electron microscopy III.

Mulvey, T. (1996) The growth of electron microscopy. Academic Press.

Narayan, K. and Subramaniam, S. (2015) 'Focused ion beams in biology', *Nature Methods*. Nature Research, 12(11), pp. 1021–1031. doi: 10.1038/nmeth.3623.

Nguyen, H. B., Thai, T. Q., Saitoh, S., Wu, B., Saitoh, Y., Shimo, S., Fujitani, H., Otobe, H. and Ohno, N. (2016) 'Conductive resins improve charging and resolution of acquired images in electron microscopic volume imaging', *Scientific Reports*. Nature Publishing Group, 6(1), p. 23721. doi: 10.1038/srep23721.

Oatley, C. W. (1982) 'The early history of the scanning electron microscope', Journal of Applied Physics, 53(2), pp. R1–R13. doi: 10.1063/1.331666.

Orso, S. (2005) 'Structural and mechanical investigations of biological materials using a Focussed Ion Beam microscope'.

Page Faulk, W. and Malcolm Taylor, G. (1971) 'Communication to the editors: An immunocolloid method for the electron microscope', Immunochemistry. Pergamon, 8(11), pp. 1081–1083. doi: 10.1016/0019-2791(71)90496-4.

Palade, G. E. (1955) 'A small particulate component of the cytoplasm.', The Journal of biophysical and biochemical cytology. Rockefeller University Press, 1(1), pp. 59–68. doi: 10.1083/JCB.1.1.59.

Paul-Gilloteaux, P., Heiligenstein, X., Belle, M., Domart, M.-C., Larijani, B., Collinson, L., Raposo, G. and Salamero, J. (2017) 'eC-CLEM: flexible multidimensional registration software for correlative microscopies', Nature Methods. Nature Publishing Group, 14(2), pp. 102–103. doi: 10.1038/nmeth.4170.

Pease, D. C. and Baker, R. F. (1948) 'Sectioning techniques for electron microscopy using a conventional microtome.', Proceedings of the Society for Experimental Biology and Medicine. Society for Experimental Biology and Medicine (New York, N.Y.), 67(4), pp. 470–4.

Pease, D. C. and Porter, K. R.(1981),'Electron Microscopy and Ultramicrotomy', 50,(20), pp. 473–477. doi: 10.1083/jcb.91.3.287s.

Peddie, C. J., Blight, K., Wilson, E., Melia, C., Marrison, J., Carzaniga, R., Domart, M.C.,O'Toole, P., Larijani, B. and Collinson, L. M.(2014) 'Correlative and integrated light and electron microscopy of in-resin GFP fluorescence, used to localise diacylglycerol in mammalian cells', *Ultramicroscopy*, 143, pp. 3–14. doi: 10.1016/j.ultramic.2014.02.001.

Peddie, C. J. and Collinson, L. M. (2014) 'Exploring the third dimension: volume electron microscopy comes of age.', *Micron* (Oxford, England: 1993), 61, pp. 9–19. doi: 10.1016/j.micron.2014.01.009.

Polishchuk, R., Pentima, A. Di and Lippincott-Schwartz, J. (2004) 'Delivery of raft-associated, GPI-anchored proteins to the apical surface of polarized MDCK cells by a transcytotic pathway', *Nature Cell Biology*. Nature Publishing Group, 6(4), pp. 297–307. doi: 10.1038/ncb1109.

Polishchuk, R. S., Polishchuk, E. V, Marra, P., Alberti, S., Buccione, R., Luini, A. and Mironov, A. A. (2000) 'Correlative light-electron microscopy reveals the tubular-saccular ultrastructure of carriers operating between Golgi apparatus and plasma membrane.', *The Journal of cell biology*. The Rockefeller University Press, 148(1), pp. 45–58.

Porter, K. R. (1943) 'OBSERVATIONS ON A SUBMICROSCOPIC BASOPHILIC COMPONENT OF CYTOPLASM'.

Porter, K. R. and Blum, J. (1953) 'A study in microtomy for electron microscopy', *The Anatomical Record*. Wiley-Blackwell, 117(4), pp. 685–709. doi: 10.1002/ar.1091170403.

Porter, K. R., Claude, A. and Fullam, E. F. (1945) 'A STUDY OF TISSUE CULTURE CELLS BY ELECTRON MICROSCOPY: METHODS AND PRELIMINARY OBSERVATIONS.', *The Journal of experimental medicine*. Rockefeller University Press, 81(3), pp. 233–46. doi: 10.1084/JEM.81.3.233.

Puhka, M., Joensuu, M., Vihinen, H., Belevich, I. and Jokitalo, E. (2012) 'Progressive sheet-to-tubule transformation is a general mechanism for endoplasmic reticulum partitioning in dividing mammalian cells.', *Molecular biology of the cell*, 23(13), pp. 2424–32. doi: 10.1091/mbc.E10-12-0950.

Radon (1917) 'Über die Bestimmung von Funktionen durch ihre Integralwerte längs gewisser Mannigfaltigkeiten', Berichte über die Verhandlungen der Königlich-Sächsischen Akademie der Wissenschaften zu Leipzig, Mathematisch-Physische Klasse, 69.

Rasmussen, N. (1997) Picture control: the electron microscope and the transformation of biology in America, 1940-1960. *Stanford University Press*.

Reisner, J. H. (1989) 'An Early History of the Electron Microscope in the United States', *Advances in Electronics and Electron Physics*. Academic Press, 73, pp. 133–231. doi: 10.1016/S0065-2539(08)60569-7.

van Rijnsoever, C., Oorschot, V. and Klumperman, J. (2008) 'Correlative light-electron microscopy (CLEM) combining live-cell imaging and immunolabeling of ultrathin cryosections', *Nature Methods*, 5(11), pp. 973–980. doi: 10.1038/nmeth.1263.

Rosvall, M. and Bergstrom, C. T. (2010) 'Mapping Change in Large Networks', *PLoS ONE*. Edited by F. Rapallo. Public Library of Science, 5(1), p. e8694. doi: 10.1371/journal.pone.0008694.

Ruska, E. (1987) 'The Development of the Electron Microscope and of Electron Microscopy(Nobel Lecture)', *Angewandte Chemie International Edition in English*. Wiley-Blackwell, 26(7), pp. 595–605. doi: 10.1002/anie.198705953.

Satir, P. (2017) 'CILIA: before and after.', Cilia. BioMed Central, 6, p. 1. doi: 10.1186/s13630-017-0046-8.

Schindelin, J., Arganda-Carreras, I., Frise, E., Kaynig, V., Longair, M., Pietzsch, T., Preibisch, S., Rueden, C., Saalfeld, S., Schmid, B., Tinevez, J.-Y., White, D. J., Hartenstein, V., Eliceiri, K., Tomancak, P. and Cardona, A. (2012) 'Fiji: an open-source platform for biological-image analysis', *Nature Methods*. Nature Publishing Group, 9(7), pp. 676–682. doi: 10.1038/nmeth.2019.

Shu, X., Lev-Ram, V., Deerinck, T. J., Qi, Y., Ramko, E. B., Davidson, M. W., Jin, Y., Ellisman, M. H. and Tsien, R. Y. (2011) 'A Genetically Encoded Tag for Correlated Light and Electron Microscopy of Intact Cells, Tissues, and Organisms', *PLoS Biology*. Edited by J. R. McIntosh. Public Library of Science, 9(4), p. e1001041. doi: 10.1371/journal.pbio.1001041.

Sjöstrand, F. (1953) 'Electron Microscopy of Mitochondria and Cytoplasmic Double Membranes: Ultra-Structure of Rod-shaped Mitochondria', *Nature*. Nature Publishing Group, 171(4340), pp. 30–31. doi: 10.1038/171030a0.

Sjöstrand, F. S. and Hanzon, V. (1954) 'Ultrastructure of golgi apparatus of exocrinecells of mouse pancreas', *Experimental Cell Research*. Academic Press, 7(2), pp. 415–429. doi: 10.1016/S0014-4827(54)80087-5.

Smith, K. C. A., Wells, O. C. and McMullan, D. (2008) 'The fiftieth anniversary of the first applications of the scanning electron microscope in materials research', Physics Procedia. Elsevier, 1(1), pp. 3–12. doi: 10.1016/J.PHPRO.2008.07.073.

Steinbrecht, R. A. and Zierold, K. (1987) Cryotechniques in Biological Electron Microscopy. Springer Berlin Heidelberg.

Stierhof, Y. D., Ilg, T., Russell, D. G., Hohenberg, H. and Overath, P. (1994) 'Characterization of polymer release from the flagellar pocket of Leishmania mexicana promastigotes.', *The Journal of cell biology*, 125(2), pp. 321–31.

Takizawa, T., Suzuki, K. and Robinson, J. M. (1998) 'Correlative Microscopy Using FluoroNanogold on Ultrathin Cryosections: Proof of Principle', *Journal of Histochemistry & Cytochemistry*. SAGE PublicationsSage CA: Los Angeles, CA, 46(10), pp. 1097–1102. doi: 10.1177/002215549804601001.

Thomson, J. J. (1897) 'Cathode rays', Philos. Mag., 44.

Tilney, L. G., Bryan, J., Bush, D. J., Fujiwara, K., Mooseker, M. S., Murphy, D. B. and Snyder, D. H. (1973) 'Microtubules: evidence for 13 protofilaments.', *The Journal of cell biology*, 59(2 Pt 1), pp. 267–75.

Titze, B. and Genoud, C. (2016) Volume scanning electron microscopy for imaging biological ultrastructure, *Biology of the Cell*. doi: 10.1111/boc.201600024.

Tokuyasu, K. T. (1980) 'Immunochemistry on ultrathin frozen sections', *The Histochemical Journal*. Kluwer Academic Publishers, 12(4), pp. 381–403. doi: 10.1007/BF01011956.

Wagner, A. (1983) 'Applications of focused ion beams', *Nuclear Instruments and Methods in Physics Research*. North-Holland, 218(1–3), pp. 355–362. doi: 10.1016/0167-5087(83)91006-2.

van Weering, J. R. T., Brown, E., Sharp, T. H., Mantell, J., Cullen, P. J. and Verkade, P. (2010) 'Intracellular membrane traffic at high resolution.', *Methods in cell biology*. Europe PMC Funders, 96, pp. 619–48. doi: 10.1016/S0091-679X(10)96026-3.

Wells, W. A. (2005) 'Microsomes are the in vitro ER', *The Journal of Cell Biology*. The Rockefeller University Press, 168(1), p. 13.2-13. doi: 10.1083/jcb1681fta4.

Zheng, Z., Lauritzen, J. S., Perlman, E., Robinson, C. G., Nichols, M., Milkie, D., Torrens, O., Price, J., Fisher, C. B., Sharifi, N., Calle-Schuler, S. A., Kmecova, L., Ali, I. J., Karsh, B., Trautman, E. T., Bogovic, J. A., Hanslovsky, P., Jefferis, G. S. X. E., Kazhdan, M., Khairy, K., Saalfeld, S., Fetter, R. D. and Bock, D. D. (2018) 'A Complete Electron Microscopy Volume of the Brain of Adult Drosophila melanogaster',*Cell*, 174(3), p. 730–743.e22. doi: 10.1016/j.cell.2018.06.019.

2

CLEM in constricted cells using FIB-SEM tomography

2.1 Introduction

Motility is one of the basic behaviours in eukaryotic cells, with many survival mechanisms depending on it, such as immunity in dendritic cells, wound healing, gamete coupling or organogenesis during embryo development. Unfortunately, tumour cells in epitheliums can also gain motility, which allows them to search for new niches in surrounding tissues and proliferate, a process known as metastasis. How they gain this movement function is still a topic of active research, but it is known that the process starts during the tumour growth. The current understanding is that cells lose their polarity and adhesion to their neighbours, and if they are in contact with the extracellular matrix, internal mechanisms trigger the production of migration associated proteins and proteases required for the cell to make its own path. Tumour cells restructure themselves in a new phenotype called mesenchymal (which resembles a developmental process known as epithelial-mesenchymal transition, EMT) (Thiery 2002; Thiam et al. 2016).

Studying metastasis by EM in a physiological environment can be very challenging (Karreman et al. 2014). The use of microscale channels patterned inside PDMS (poly-di-methyl-siloxane) blocks provides a simplified environment to study this phenomena (Le Berre et al. 2014). Inside these microchannels, cells can be easily confined so that the whole cell body is restricted within its walls (Figure 2.2). The silicon elastomer PDMS is transparent, gas permeable and biocompatible. These features allow the cell to live and migrate along the confined space of the fibronectin coated channel. Channels can be fabricated with precision down to a diameter of a few micrometers so that as cells migrate through, forces are exerted in all directions around the cell. Additionally, artificial necks (also named channel constrictions)

can be created by decreasing the diameter along the channel (Figure 2.2 B). The minimum diameter of the constriction is determined based on the cell type being studied, for example 2 µm is sufficient for epithelial cancer cells.

Channel constrictions can be used as an experimental set up to study morphological changes like cytoskeleton structure (Welch 2015; Liu et al. 2015) and nuclear deformation (Isermann & Lammerding 2017; Bell & Lammerding 2016; Denais et al. 2016; Raab et al. 2016). In studies of nuclear deformation, tumor cells demonstrated a capacity to squeeze their nucleus to fit the shape of the channel, shrinking up to 80% of the original surface area at the constriction zone. When constricted, anterior and posterior regions of the nucleus suffer high internal pressure, which eventually can lead to nuclear envelope breakdown (NEBD) (Raab et al. 2016; Denais et al. 2016). NEBDs begins as blebs, which occasionally rupture leaking the nuclear content into the cytoplasm. Leakages are sensed by ESCRT-III, a complex in the ER able to reseal the nuclear envelope (Olmos et al. 2015; Jimenez et al. 2014).

Cells under constriction have been studied intensively with light microscopy (LM). However, currently there are no publications describing the ultrastructure of a cell squeezing through the *in vitro* constriction and capturing the moment of a NEBD. In this chapter, CLEM was performed on cultured cells seeded on PDMS chips to capture this moment and to understand the ulstrastructure by 3D volume SEM, specifically focused ion beam scanning electron microscopy (FIB-SEM). Target cells were selected by LM when they moved into a constriction and were found back in the resin block after processing for EM. The correlation relied on identifying individual channels position and using local topographic cues as a navigational reference.

FIB-SEM microscopes are commonly used to acquire three-dimensional volumes that reveal the ultrastructure of the imaged region. FIB-SEM recently gained popularity with several publications where individual cell volumes were acquired (Xu et al. 2017; Hasegawa et al. 2018; Fermie et al. 2018). Two cells under constriction were acquired by FIB-SEM and their volumes are described. The first cell was prepared by our collaborator in IFOM (Milan, Italy), G.V. Beznoussenko. This dataset consists of a wild type HeLa (no phenotypes present) caught in the moment of constriction. The volume has been acquired with sagittal sections (Figure 2.6) and it will serve as an exemplary model to describe the events occurring in the cell during its migration through the channel. The second dataset, was the result of a collaboration with M.Raab and M.Piel at the Institute Curie, Paris. They provided cells transfected with a cytoplasmic component (cGAS-GFP), allowing us to find NEBD events. Approximately three quarters of the cell volume were acquired transversally, including the region under NEBD and the full constriction region.

The full ultrastructure of a cell inside a constriction channel and an event of NEBD has not been yet, to our knowledge, analysed by EM. In our results, ER and mitochondria are characterized to form an intricated meshwork, which, together with stress fibers, we suggest are instrumental for the cell to migrate across the channel. We show that NE ruffling occurs and, together with nuclear pore disruption, could be indicators of lamin changes during migration. Finally, at the region of NEBD, it stands out the vicinity of wrapping ER, which we propose could be a consequence of membrane repair. These observations, although mostly are supported by the respective cited literature, they are based merely on two 3D volumes. For this reason, results have to be limited in their interpretation and can only be used as a exploration phase to drive future and more quantitative research.

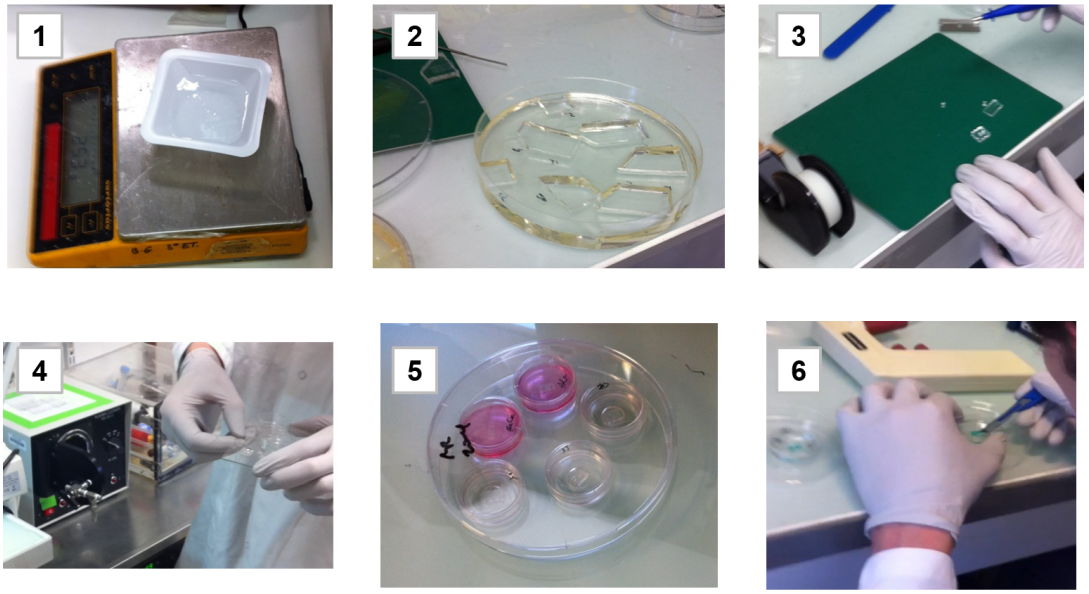

Fig. 2.1 1. PDMS components (PDMS and cross-linker) are mixed and stirred in a 10 to 1 proportion. 2. The mixture is poured into the resin mold. 3. After 24 hours, chips are removed, cut into small squares and round holes made in the channels making wells. 4. After cleaning, chips and glass bottom dishes are treated with plasma and glued together. 5. After adding fibronectin, chips are left for a few hours with media and cells are seeded in the wells. 6. After fixation with glutaraldehyde, the PDMS chip is lifted with a knife, exposing the cells attached to the glass for further sample preparation for EM.

2.2 Materials and methods

Cell line

HeLa cells were cultured in DMEM Glutamax (Gibco) supplemented with 10% FBS (GE Healthcare) and 1% penicillin and streptavidin. To locate cells during NEBD, it was used

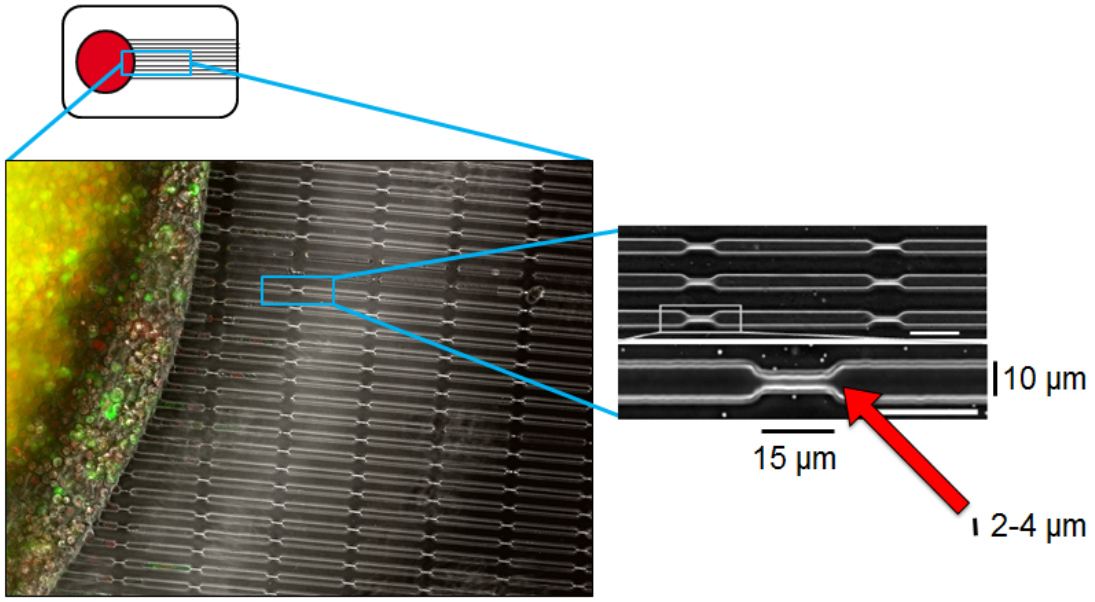

Fig. 2.2 Schematic of a single chip: the red dot is the dwell full of cells, lines represent parallel channels. When it is looked with the light microscope, constrictions can be seen. The total length of the constriction is 15 µm. The diameter is 10 µm and then constrictions of 2 or 4 µm can be found.

a stable HeLa cell line expressing histone H2B-mCherry for nucleus, and cGAS-GFP, for identification of a nuclear rupture. cGAS (Cyclic GMP-AMP synthase) (Wu et al. 2013) is an enzyme found in immune cells that binds to microbial or viral DNA. Generating endogenous cGAS protein in the cell cytosol, it becomes fluorescent when it binds to its own DNA, for example, if a nuclear rupture occurs.

Cells cultured on PDMS chips

Polydimethylsiloxane (PDMS), in a proportion 10:1, PDMS A: cross linker B (GE Silicones) was mixed, poured over hard-resin molds and left in vacuum overnight (Figure 2.1 1). The resin mold is an imprint copy from a silicon wafer chip with micro-channels carved inside (Heuzé et al. 2011) (Figure 2.1 2). The original self-made mold was supplied to us by our collaborators (M. Raab and M.Piel). Channels of 15 µm width and 5 µm height were used with constrictions of 2 and 4 µm. PDMS chips were cut out of the mold in squares. Holes were then punched in the microchannel region with a biopsy punch of 1.5 mm diameter (Figure 2.1 3). After cutting, the condition of the channels was examined, trimmed to a minimum, cleaned with ethanol, sonicated and flushed with a nitrogen gun. A MatTek glass bottom dish (35 mm dish, P35G-2-14-C) was plasma treated and the PDMS attached to the glass (Figure 2.1 4). Channels were incubated under vacuum with 15 µg/mL of

fibronectin for 30 min, then washed with PBS twice. Chips were incubated with culture medium for 4 hours before adding the cells (Figure 2.1 5). Cells were poured in chip wells at a concentration of 30 million per milliliter. With that high cell concentration, the full well gets filled and cells have a chance to insert and migrate through the micro-channels. After two hours of seeding, medium was added on top of each well.

Light microscopy and sample preparation

After approximately one day, cells inside the wells start to move into the micro-channels and a few of them try to pass through the constrictions. HeLa cells were left over night and then the channels inspected every 2 hours. If several cells were found to be close to the channels, they were left in a microscope with temperature control. For the first cell, it was enough to detect the nuclear shape by H2B-mcherry under the constriction. For the second cell, when a NEBD was detected in the GFP channel, transmitted light and fluorescence images were saved. Those images were used as a reference for finding the same region in the SEM (Figure 2.3).

In the two cells presented in this chapter, two different protocols have been followed [1] . For the first experiment, fixation and resin embedding were performed by our collaborator G.V. Beznoussenko and the protocol used can be found in (Beznoussenko & Mironov 2015).

For the second experiment, cells are fixed immediately after imaging by adding 0.5% glutaraldehyde and 4% paraformaldehyde and 0.05 % malachite green in 0.1 M PHEM buffer. Cells are left on fixative for 2 hours. Aldehydes work by crosslinking proteins and, with lesser extent, other cellular components (lipids, carbohydrates and nucleic acids) into a rigid mesh. After fixation of the cells, the PDMS chip is removed and cells remain attached to the glass bottom dish (Figure 2.1 6). One problem to be aware of when lifting PDMS is that part of the upper cell membrane, where the cell is likely to form focal adhesions, can be ripped off causing visible damage.

Sample preparation was sped up by a Ted Pella BioWave microwave following fixation. The post fixation applied was 1% Osmium Tetroxide (OsO4), 0.8% Potassium Ferricyanide ($K_3Fe(CN)_6$) in 0.1 M PHEM which after adding the solution to the sample was then processed in the microwave for 14 minutes (with an on-off 100W alternative sequence under vacuum). Following this they were washed with 0.1 M PHEM buffer. This is a secondary fixation in which osmium tetroxide oxidizes unsaturated bonds of fatty acids resulting in an enhanced contrast at the cell membranes. In the next two steps, the sample was additionally

[1] There is no advantage of one protocol over the other. At IFOM, our collaborators used the so-called OTO protocol, with two osmium steps and TCH (tetracarbohydrazide) between them. Membranes look darker in this protocol due to the double osmium stain. At EMBL we used the second one, the so-called malachite green protocol, described in the next paragraph.

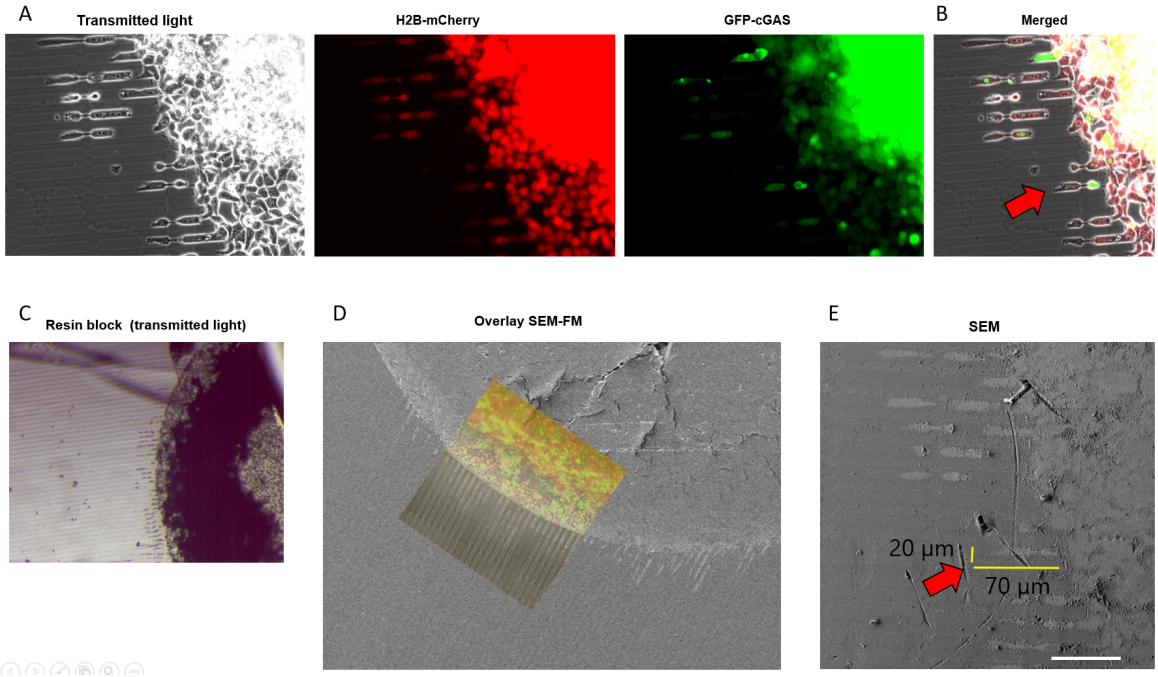

Fig. 2.3 A. Light microscopy image of cells at 20x magnification, focusing on a region close to the well border where cells are growing and moving into channels. B. Composite of transmitted light, mCherry for nuclei and GFP for nuclear envelope ruptures. The red arrow indicates the cell that has been selected to look at the NEBD, where the GFP of cGAS is easily detectable at the front and back of the cell. C. The same region after Electron Microscopy chemical processing inside the resin block. Cells are stained darker and the PDMS leaves marks that allow to identification of individual channels. D. Overlay of SEM image with composite LM image (same as B but 10x). E. Same region as image B in SEM. The red arrow again highlights the selected cell for CLEM. Scale bar 50 µm.

stained with 1% tannic acid and 1% uranyl acetate (in the microwave 100W 1 minute on-off cycles under vacuum). Then it was dehydrated in ethanol in a series of graded steps (25, 50, 75 3x100%) and embedded in Durcupan (50%, followed by 100% resin). The resin was polymerized in a 60°C oven over 48 hours, then mounted on an SEM stub, coated with gold (180s 30mA) and introduced in the FIB-SEM microscope chamber.

FIB-SEM acquisition[2]

The FIB-SEM is a dual beam instrument composed by two columns, the focused ion beam (FIB) emitter and the scanning electron microscope (SEM). Each column can be used independently, the SEM can be used in a traditional SEM mode while the FIB allows material ablation by a focused current of gallium ions. Gallium comes in the form of a reservoir which is attached to the FIB column. Inside the FIB column, the gallium is attracted by an electrostatic. The gallium is in contact with an electrode, and when heat is applied at the tip of the electrode, the gallium start to flows towards the tip. When a balance between the electrostatic force and the surface tension with the material around the tip is achieved, the gallium ionizes and starts to be ejected forming a cone shape, named the Taylor cone. The Taylor cone provides a constant flux of ions with an apex of only few nanometers in diameter which can be directed as a beam towards the sample.

Electrostatic forces are used to balance the beam (extractor and suppressor voltages), which, for Zeiss machines is achieved at a current of 2 µA. After the ion beam starts, an aperture is used to adapt the energy of the incidental beam onto the final sample. Ions coming from the beam bombard the surface of the sample with enough energy to pull up atoms exposing the material below (Figure 2.4). Smaller apertures allow better definition of beam spots, achieving nanometer precision for nano-patterning, and thinner slices in volume EM.

The SEM column, used only for imaging, has three types of detectors. In the origins of SEM, there were only two types of detectors, secondary or backscattered electrons (BSE). In present day instruments, we have a secondary electron detector able to detect secondary electrons and secondary ions (SE or SESI if also detects secondary ions) able to distinguish topographical information. Another detector called InLens is mounted inside the SEM column. The InLens detector can detect backscattered electrons at small working distances (close to the 5 mm) and give more information about the sample surface and its composition and less about topography. For backscattered electrons, which have a narrower band of energy than secondary electrons, the Energy Selective Backscattered (EsB) detector is mounted above Inlens. EsB uses a filtering grid to select a band of SE, which for biological samples in

[2]The following paragraph is longer and more detailed than corresponds to a methods section. The reason is that many technical concepts regarding FIB-SEM are detailed here.

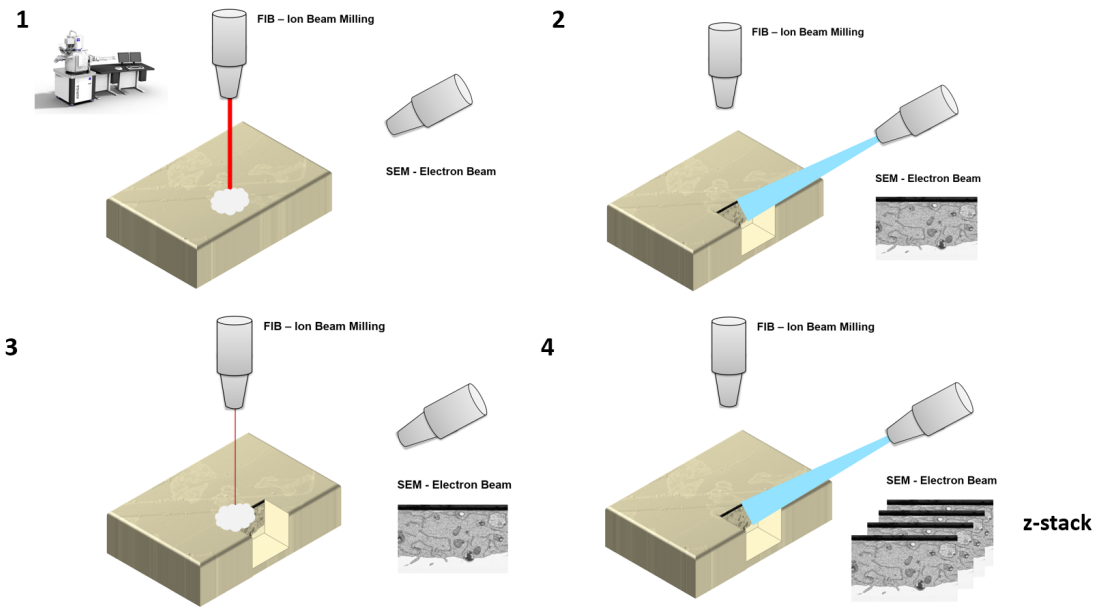

Fig. 2.4 A representation of a resin block and the two column beams of FIB-SEM. In 1, the focus ion beam applies a heavy current in the sample surface, which will expose the underlying tissue or cell. In 2, the electron beam is scanning the exposed face, generating an image (back-scattered electrons) of the block face. In 3, the ion beam is regulated with a lower energy, enabling control of the thickness of ablated material to few nanometers. In 4, when the material is removed by the ion beam it can be imaged again. By iterations of this process (3 and 4), a z-stack is generated through the depth of the targeted cell or tissue.

our instrument proved to have a good signal to noise ration (SNR) with 1100 volts for the filtering grid (Garitagoitia Cid et al. 2016).

For SEM, it is important to decide the right accelerating voltage (kV) for imaging. Accelerating voltage is the voltage difference between the filament and the anode, which determines the acceleration of the electron beam towards the anode. Typical SEM ranges from 0 to 30 kV. The greater the kV, the greater the power of penetration by the beam into the sample and the subsequent interaction volume. This effect has major consequences on the election of the accelerating voltage since the thickness of milled sections has to be accounted for in relation to the penetration depth of the electrons. For example, imaging at 5 kV will generate an interaction volume deeper than several nanometers. Therefore sectioning at 1 nm implies collecting the same information over a few sections. In (Piños et al. 2017) several simulations and formulations tested the electron depth for BSE under different kV, however, no similar publications are found for embedded biological samples.

Additionally, using higher kV does not improve the quality of the image because the number of backscattered electrons from deeper regions degrades the final SNR and produces radiations that damage the sample. Reduction of kV to a lower value is thus important. For

biological specimens, there is a general consensus in the literature (and also in agreement with our own experience) to acquire between 0.9 and 3 kV.

In this chapter, the SEM beam was increased to 5 kV for localizing an area where micro-channels could be seen at the surface of the resin block. Imaging with such a higher kV gives more penetration when using the SESI detector, which allows observation of cell shapes. The correlation of the region of interest between SEM images and LM images can be established by overlaying both with any image editor (Figure 2.3). After this, for imaging the cross-section face, SEM is set up to image at 1.5 kV with a probe size of 700 pA. Focus, stigmators and wobbler are adjusted until images with 4 nanometer pixel-size are perfectly defined.

Samples are glued to a metal stub and introduced inside the microscope chamber. Then, the microscope operator moves to the center of the sample and sets up the eucentric height. The eucentric height is an additional plane on the stage which allows movement in x and y without moving in z when tilted at 54 degrees. Imaging of the sample is done by SESI detector, which provides topographic information of the surface. Under low currents (usually 50 pA), the FIB also can be used for imaging without excessive damage of the sample's surface. The distance between the sample surface and the SEM or FIB lens, when the sample is in focus, is called the working distance (when the image is in focus, the focal distance and the working distance are the same), which in the Zeiss systems is usually 5 mm for SEM and 16.5 mm in FIB.

In order to perform slicing and imaging simultaneously, both beams must be aligned. This is achieved manually by finding a common feature at the surface of the sample that can be seen in both SEM and FIB (for example an indent at the surface of the resin block). The user first centers the feature in SEM, then switches to FIB imaging. In FIB mode, Z is moved manually until the feature is centered again. Switching back to SEM mode, the centering is finalized using the SEM beam shift. As a result, both beams are pointing at the same position (Figure 2.5).

Up to this point, all operations can be done in the microscope using *SmartSEM* from Zeiss, the default microscope software. The next steps are performed using *ATLAS 3D Fibics* software. *ATLAS 3D* shows an accordion of buttons and options to be modified sequentially until the slice and view starts. In our experiments, we selected an area of 70x20 µm in one case and 20x70 µm for the other experiment. The area should be slightly larger than our fluorescently targeted ROI. The CLEM experiment was acquired before the wild type, and it was observed that coronal cuts had a disadvantage respect to sagittal cuts. Since the number of slices is almost 3 times as larger in coronal sections, the stability of the microscope is a more sensitive issue (drifting and artifact problems).

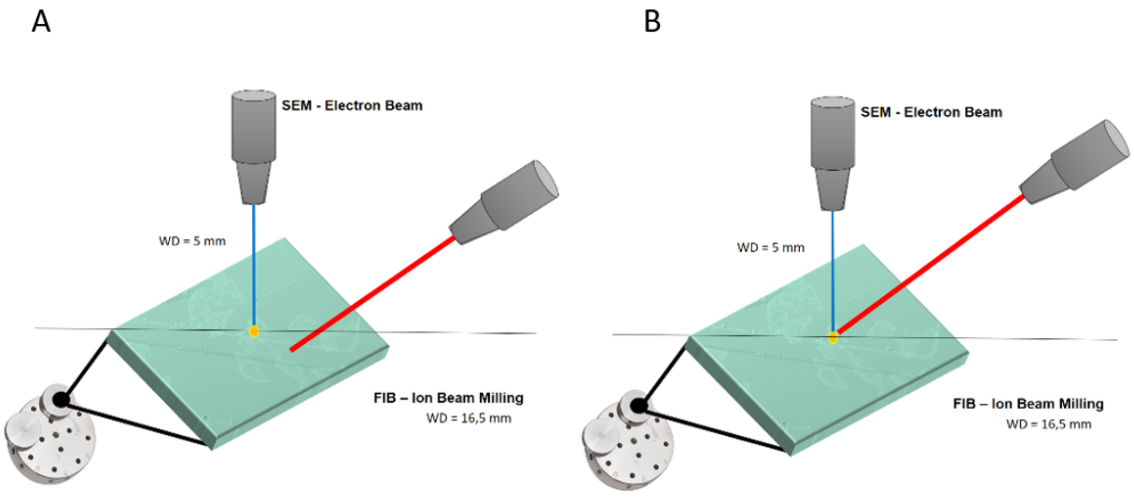

Fig. 2.5 A. A stub representation depicting the misalignment of the two beams, SEM blue, FIB in red. B. When the coincidence point is calculated, both beams point to the same position. Since both working distances (WD) have to be maintained, the sample is move in the Z axis to centre with the FIB and by beam shift with the SEM to achieve coincidence.

As shown Figure 2.6 A, a box highlighting the region of interest is automatically shown when selected by the user on an image from the surface. The user must define the area of acquisition, and for each shape, which FIB current will be in use. For the milling steps, the FIB milling current will dictate the quality of the cut face and the time required to mill the selected volume.

The first step is a platinum deposition to protect the area of acquisition. A gas delivery arm (called GIS, gas injection system) with a reservoir containing coating materials, like platinum, insulator (SiO_2) or carbon is used to apply this deposition. When the arm is inserted close to the sample surface at the region of interest (ROI), material is released from the needle at the tip of its arm while the FIB beam moves across the sample in a sequential scan. Materials are combined in a gas form called precursor. When secondary electrons and ions collide with the gas molecules of the precursor, they break the weak chemical bounds and separate them into two components. One remains volatile and the other is deposited onto the surface, and with time the deposited material is forming a surface pad which can generate a protective coating of a desired thickness, usually around 1 µm (Figure 2.6 B-1 to B-3). For the deposition steps, the precursor material and the FIB current are indicated.

After deposition, five-line patterns are milled on top of the deposited layer of platinum. From the five, two lines form 45 degrees with a center line positioned at the center of the deposition layer. Thus, change in distance between the center line and the lines at an angle

are equal and can be used to calculate the slice thickness as the acquisition progresses. With 45 degrees lines, they will move towards the center and the distance will be geometrically proportional to the slice thickness. These lines are used by the software for tracking purposes.

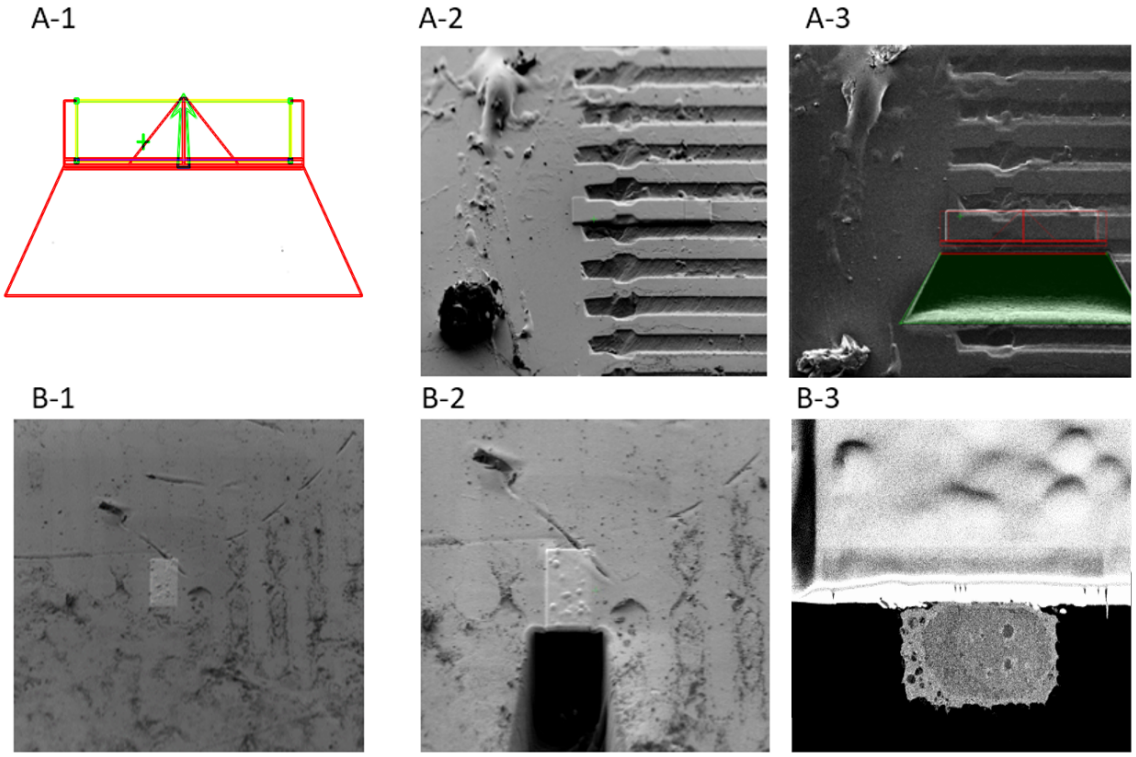

Fig. 2.6 A. Images correspond to the first experiment, where the cell is acquired with sagittal sections. B images correspond to the second experiment, where the cell was acquired transversally. A-1. Example of geometrical shape shown in *ATLAS 3D* before all preparation steps previous to acquisition. The red trapezoid in the bottom is the trench region milled to expose a cross-section of the cell (A-3 and B-2). On top of the trapezoid, the green rectangle indicates the acquisition area. This area is split in a small bottom part (for polishing) and upper part (for acquisition). The middle rectangle defines the region of deposition (A-2 and B-1). Red lines forming a triangle are the tracking pattern. The middle line situated at the center is composed by three lines. The pattern can be observed in the deposition pattern on the top of the exposed cross-section of the cell in B-3.

Additionally, two more lines are carved at 2 µm distance parallel to the center one. The lines are milled three dimensionally as a prism so they look as spikes in a cross-section. The three center spikes are used by the auto-focus and auto-stigmation algorithm as references. To achieve a perfect spiked shape, the user must tune a fine focus and stigmation of the FIB beam before starting. Once the line patterns are milled at the top of the deposition, they are covered by a layer of insulator, for contrast purposes and by an additional layer of platinum for protection of the shapes. Depending on how thick the deposition layer is, the full process can take one to two hours.

The next steps consist of two milling operations. First, a large trench in the shape of a trapezium is performed to expose the cross-section and to leave space for waste material generated during the acquisition. A high FIB current of 15 nA is used to mill a trapezium the size of which is calculated automatically by the application. The depth of the trapezium and all the other shapes (polishing and acquisition) is set by the user before starting, in our experiments it was set to 30 µm depth. The second step is used to fine polish the exposed surface. Defined by a shape of a small rectangle of a few micrometers, it is executed with a FIB current of 1.5 nA. When both trenches are ready, the user changes to ESB detector for imaging.

To now set up the microscope for acquisition the user will need to adjust many parameters. After a correct brightness and contrast for the ESB detector, the user must tune focus, stigmation and repeat the coincidence point. The dwell time (time spent per scanning spot) is set, in our case this was 10 µs with line averaging of 1 [3]. Next, the resolution and thickness are decided, this was 8x8x16 nm voxel size for the sagittal dataset and 8x8x8 nm in the coronal dataset. The imaging field of view (FOV) has to be defined in the cross-section face. In *ATLAS 3D*, a FOV is first defined as a bigger region typically with lower resolution, called the keyframe. Within it, is possible to select multiple smaller ROIs with high resolution. This flexibility not only provides some context, but allows to adapt to change the ROIs position if required (Figure 2.6 B-3). The ROI was set to 30 x 15 µm in the coronal data and 50 x 15 µm in the sagittal data. In case of changing conditions, this region was modified manually during the acquisition.

For the auto-tune functions, the so-called Autotune box has to be placed in the central marks of the deposition layer and another two small boxes on the lateral marks for tracking. This is done via the GUI in which a rectangle is placed on regions containing the marks, which are then automatically registered. After this, the acquisition can be started. When the acquisition is started, the software will first mill in search mode until the user sees that the cross-section surface is being milled and then will command that images are saved. After this, the software increases progressively the dwell time (which is called stabilization period), so a balance between the ion and the electron beam is achieved smoothly. Starting with high dwell times can generate artefacts like walls (curtains in the image caused of uneven cutting of material by the FIB). In Figure 2.7, a summary of all the steps is listed.

A few additional notes have to be considered before acquisition. First, FIB currents must be aligned with the apertures. Aligning a current means to fix the beam on the optical axis

[3]Line averaging repeats the same scan at certain dwell time and then averages per pixel. Line averaging smooths the noise but increases the time of image acquisition. For biological samples, the SNR is usually good enough that increasing dwell time has the same effect as line averaging (i.e. SEM image taken at line average 2, dwell time 4, gives similar quality as one taken with dwell time 8).

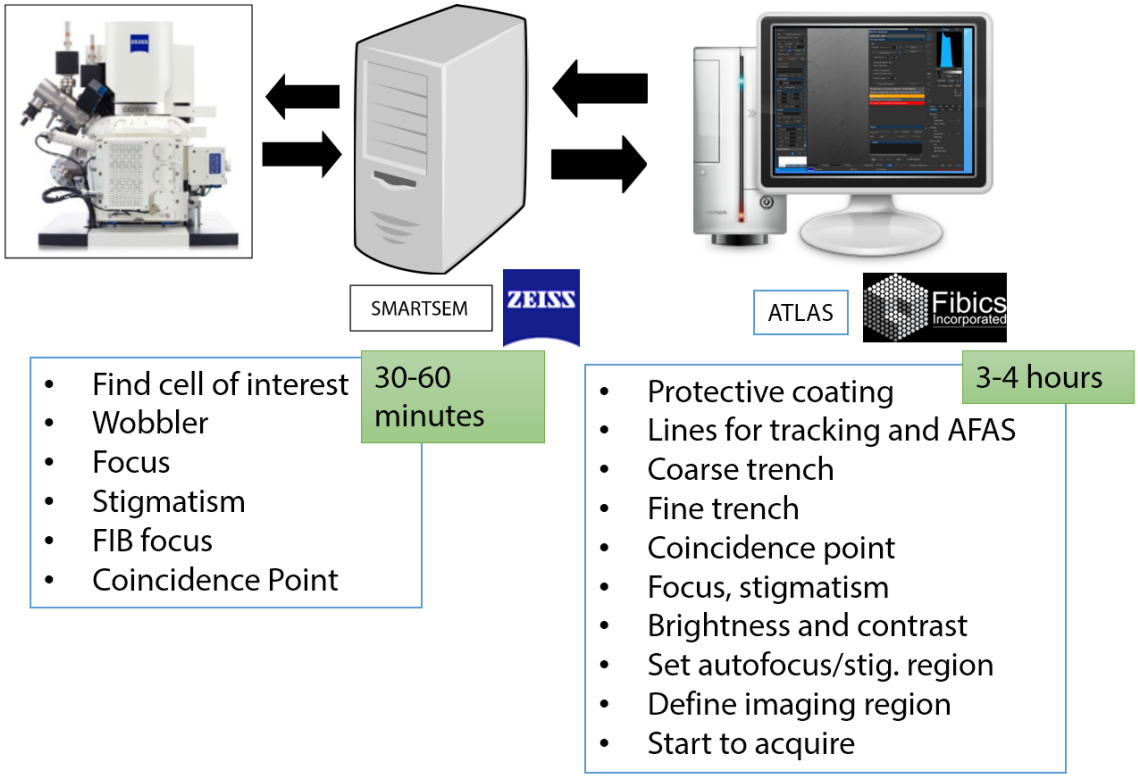

Fig. 2.7 Operating FIB-SEM using *SmartSEM* (*Zeiss*) and *ATLAS 3D* (Fibics). *Zeiss* FIB-SEM Microscope communicates with *SmartSEM* software and *SmartSEM* computer communicates with ATLAS software from Fibics Inc.. The common steps in the acquisition workflow are summarized in the two tables with the time need to complete all steps, including waiting times for deposition and milling. Table 1 operations are done with *SmartSEM*, table 2 with *ATLAS 3D*. AFAS stands for Autofocus and Autostigmatism.

and adjust the voltages to have the right current values for each aperture. Due to continuous imaging, currents tend to misalign and proper calibration is needed every 2-3 weeks.

Second, internally, there is a balance between inner voltages of the FIB column to achieve a constant flow of ions. When impurities accumulate at the tip of the Gallium source or the range of the suppressor voltage used to compensate is not enough to yield a beam current, the source must be re-heated. This can interrupt the acquisition for several hours while the ion current stabilizes again. Subsequently, a few sections can be lost because of the new stabilization period and necessary readjustments of the acquisition region (thermal drift can move away from the cross-section after several hours).

During the acquisition of the datasets, the microscope is monitored every 3 or 4 hours to prevent any drifting or to adjust dwell time if uneven milling is detected in order to prevent a wall forming. After the acquisition, datasets were cropped, smoothed with a Gaussian filter of standard deviation of 1.5 with Fiji (Schindelin et al. 2012) and aligned using TrakEM2 (Car-

dona et al. 2012). For 3D visualization, segmentation of the datasets was performed using Drishti (Limaye 2012) for the first cell (sagittal) and IMOD (http://bio3d.colorado.edu/imod/) and Amira (https://www.fei.com/software/amira-for-life-sciences/) for the second cell (coronal).

2.3 Results and discussion

ER and mitochondria form an entangled meshwork in the anterior part of the cell

From the two volumes acquired, a massive rearrangement of the usual distribution of organelles with respect a resting Hela cell could be observed. The time a cell spends to cross through a full constriction takes around 6 hours, during which the cell restructures itself morphologically. Each cell was fixed in light microscopy at different times, first cell 3 hours after the leading edge entered the constriction, second cell after 5 hours.

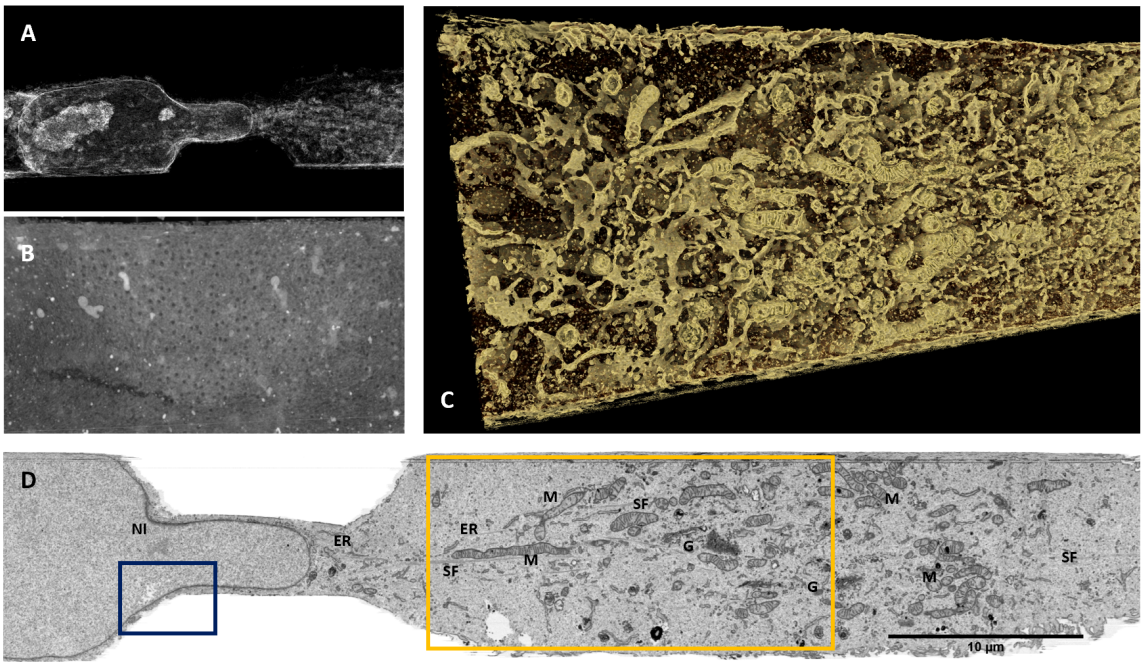

Fig. 2.8 A. Three-dimensional visualization of experiment 1 in gray values, emphasizing nuclear envelope, nucleolus and internal distribution of organelles. Direction of migration from left to right. B. Inner face of nuclear envelope (blue rectangle in D), showing the nuclear pore distribution, each black dot is a nuclear pore. C. Three-dimensional visualization of mitochondria and endoplasmic reticulum at the right side of the constriction, marked in a yellow square in D. ER sheets can be seen together with a complex mitochondrial network. D. One transversal section in EM. M, mitochondria, SF, stress fibers, NI, nuclear invagination, ER, endoplasmic reticulum, G, Golgi apparatus.

For both, it looks like the majority of organelles are pushed through the channels before the nucleus. Golgi apparatus, lysosomes and most of the mitochondrial network and associated ER are consistently located in the front region, which given the cell direction movement, could be considered as the anterior region or leading edge. Mitochondria concentrate along the central axis of the movement, together with an intercalated network of ER (Figure 2.8-C). The same network can be observed in a smaller scale at the posterior side before the constriction and close to the nucleus. These observations have been confirmed in literature for migrating cancer cells in (Zhao et al. 2013; Desai et al. 2013), with special emphasis in the mitochondrial network. Additionally, it has been confirmed in TEM sections of other cells (unpublished material) by our collaborator G.V. Beznoussenko.

ER and mitochondrial networks seem to be entangled between the formed cytoskeleton. ER forms wrapping sheets as is shown in the 3D reconstruction of Figure 2.8-C. As suggested in (Rowland & Voeltz 2012; Phillips & Voeltz 2016), the ER provides the necessary amount of synthetized factors that help to generate a robust pulling actin network and to assist in mitochondria proliferation. Mitochondria, in exchange, produce enough energy in the form of ATP to assist the pushing movement by motor-proteins (like myosin) and actin polymerization. To sustain the high energetic demand, internal feedback loops force ER to split mitochondria and proliferate by Drp1 cleavage (Friedman et al. 2011). Still, more studies are needed on how mitochondrial and ER dynamics are regulated in cell motility, and which are the precise stimuli that direct their redistribution during migration under confined spaces.

Stress fibers wrap the nuclear envelope and form rails from side to side of the constriction

Along the ER and mitochondria, actin bundles and stress fibers can be observed following the central axis of movement. Their thickness increases especially close to the nuclear envelope, where actin bundles form a web that grows to thick stress fibers, like a branching tree (Figure 2.9 A-1). Stress fibers inside the constriction cross to the other side, connecting the cytoplasm (Figure 2.9, A-2 and A-3). Fibers can be tracked to the membrane walls and they are especially abundant at the bottom of the cell, attached to the glass substrate (coated with fibronectin). They likely also form focal adhesions to the PDMS walls [4]. It is possible that cells attach to the substrate using focal adhesions and then produce actin bundle

[4] As an indirect evidence of the presence of focal adhesions, when the chip is lifted off for sample processing it always rips the contacting plasma membrane, even to the point that several samples were destroyed during the chip removal. For the two cells shown in this chapter the plasma membrane is mostly ripped off in the contact regions with PDMS.

filaments that connect to the nuclear cortex. These findings suggest that they create a massive rail system which can pull the cell along the constriction using contractile forces.

It has been well established that cells migrating on a flat surface (not confined) move by forming actin-rich lamellipodia at their leading edge and by pulling themselves along in the rear using contractile forces with stress fibers. Protrusions are actin driven and generate focal adhesions, which in turn use the substrate to exert forces that push the cell in a determined direction (Lämmermann et al., 2008; Diz-Muñoz et al., 2010). However, when cells are confined in a three-dimensional environment, they can display a movement more similar to an amoeba. Ameboid movement for these cells is characterized by no adhesions and a flowing cortex with strong polarity (Poincloux et al., 2011). There is evidence that the difference between mesenchymal and ameboid type migration are just an adaptation of the cell to the surrounding environment (Liu et al., 2015), supporting that cells under confinement use an ameboid type of migration with less attachment and less focal adhesions. With the current experiments we do not have evidence to support one or the other models (it would require quantification of focal adhesions and recording dynamics by time lapse), but the amount of stress fibers found is indicative of a mesenchymal mode of migration.

Nuclear envelope suffers massive deformation and ruffling

In the first cell, the nuclear envelope starts to deform close to the constriction and fibers are more abundant towards the anterior part of the constriction. In the second cell, which is in a more advanced state of crossing the constriction than the first, a higher abundance of stress fibers are observed along the constriction. A massive convolution of the nuclear envelope along the constriction axis occurs, particularly close to the constriction (Figure 2.9 B). This ruffling of the nuclear envelope has been observed experimentally by our collaborators in the same type of cells tagged with fluorescent Lamin A (Figure 2.9 B-3). Lamins are dynamic proteins which control the stiffness of the nucleus. They form a filamentous meshwork beneath the inner nuclear membrane of the nuclear envelope and they can be regulated by phosphorylation (e.g. during mitosis). This hints towards a possible relationship between Lamin changes and different stages of the nucleus migration through the constriction. It is unknown which mechanisms are used for lamina self-regulation during the movement through constrictions.

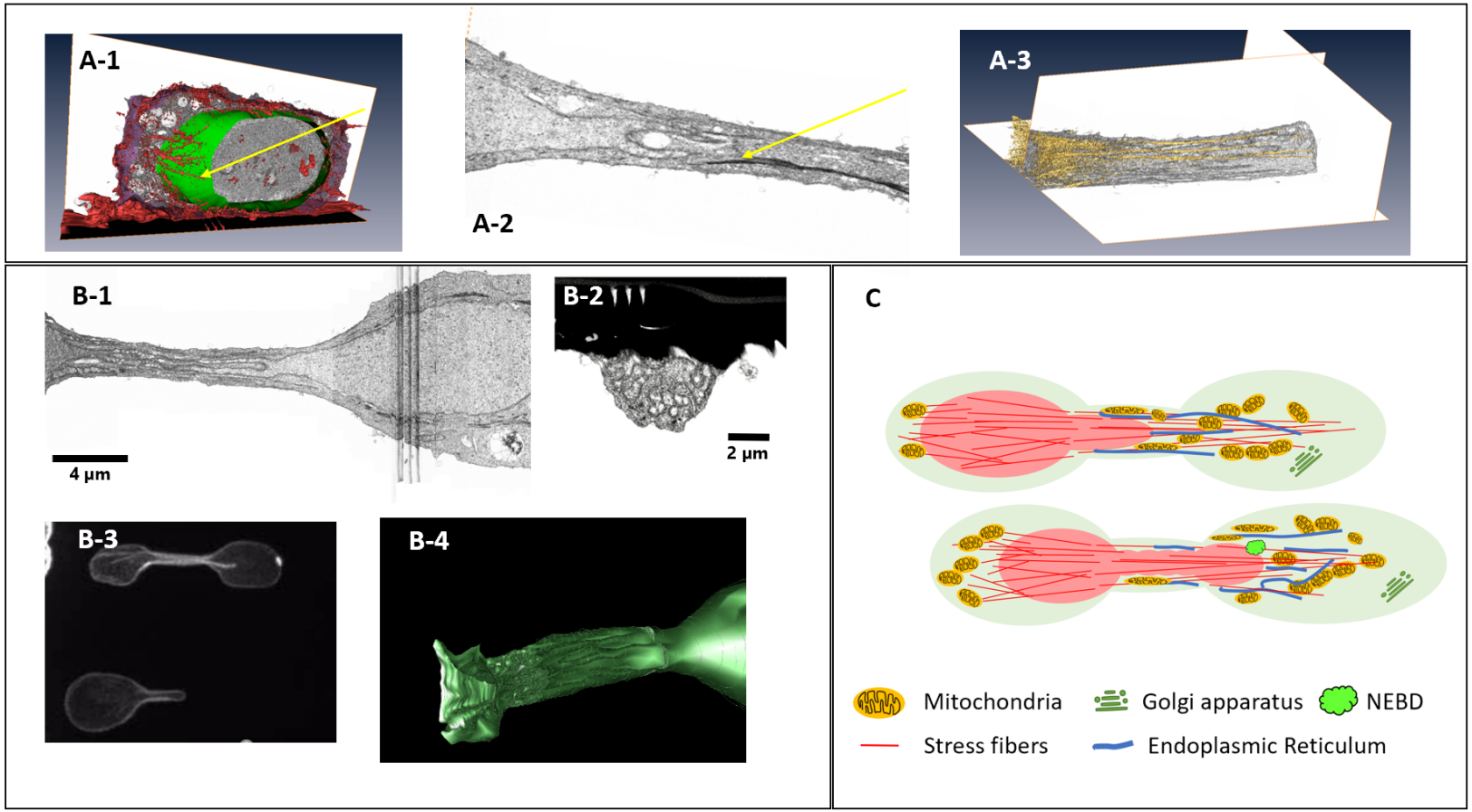

Fig. 2.9 A. Visualization of stress fibers. A-1. Segmented stress fibers in red by isosurfaces (yellow arrow), around the nuclear envelope in green, manually segmented. A-2, section of the constriction with a stress fiber along the constriction axis (yellow arrow). In A-3, in the same segmented stress fibers segmented by isosurface in yellow-gold. B. Deformation of nuclear envelope. B-1 and B-2. Coronal and transversal sections of the cell in EM . B-3 . Lamin A GFP expression of cell. Image kindly provided by M.Raab. Ruffling of Lamin A during constriction matches with the model of the nuclear envelope from the EM volume, B-4. C. Sketch model that represents the two experiments observed and their differences in ER, mitochondria, stress fibers and nuclear deformation.

When the leading edge crosses the constriction and starts to pull the nucleus inside the constriction mouth, there must exist a signal to the nucleus to change its elasticity. I suggest that when the nucleus starts to get close to the constriction, the structure of the cytoskeleton close to the constriction is able to detect pressure changes . If stress fibers pull, a mechano-sensing system signals to the nuclear cortex (Isermann and Lammerding, 2017) which leads type A lamins to relax close to the high pressure areas. The nuclear envelope is less stiff and stress fibers start to pull the nuclear envelope inside the constriction. If that model is correct, lamin changes in the NE should be bigger than at the posterior side of the constriction. Indications of this are in Figures 2.9 B-3 and B-4, where the nuclear envelope ruffles inside the constriction.

CLEM on cell under NEBD

In the second experiment, the goal was to capture a cell in the precise moment of NEBD and to obtain a corresponding high-resolution view of its ultrastructure at the nuclear envelope. NEBD usually appears in both posterior and anterior edges of the NE, being most frequently at the leading edge. When the tip reaches maximum pressure, it breaks leaking nuclear content inside the cytoplasm. Leakage is detected and ESCRT III complexes recruited, leading to rapid sealing of the nuclear envelope (Raab et al., 2016). Interestingly, we observed that endoplasmic reticulum seems to form an extended sheet that wraps the nuclear envelope at the site of the breakage (Figure 2.10 10). ER wrapping could be a consequence of the membrane repair mechanism (Hampoelz et al., 2016), but it is also possible that ER sheets are constantly forming around the nuclear envelope during cell migration. Whether this distribution of ER lamina is randomly sparse or it increases especially in regions were lamina is weakened and annular fusion of membranes is required, still needs further research.

In Figure 2.10-B, the common distribution of nuclear pores in one side of the constriction does not seem to be altered. However, with the same model at the leading tip, it was not possible to obtain clear images of the nuclear pore distribution. It was showing instead a really thin and almost transparent layer of nuclear envelope with a disarranged distribution of nuclear pores. The generally accepted model of NEBD is that, as the nuclear envelope with a weakened lamina moves into the constriction, the cytoskeleton exerts forces which increase nuclear membrane surface tension. In addition, it has been suggested that there is an increase in intranuclear pressure generated by chromatin compaction (Denais et al., 2016; Hatch and Hetzer, 2016). In (Raab et al., 2016), they propose a model in which inner and outer nuclear envelope membranes separate as a consequence of this pressure. If that were true, it would imply a loss of nuclear lamina and changes in the nuclear pore distribution with our observations in agreement with their model.

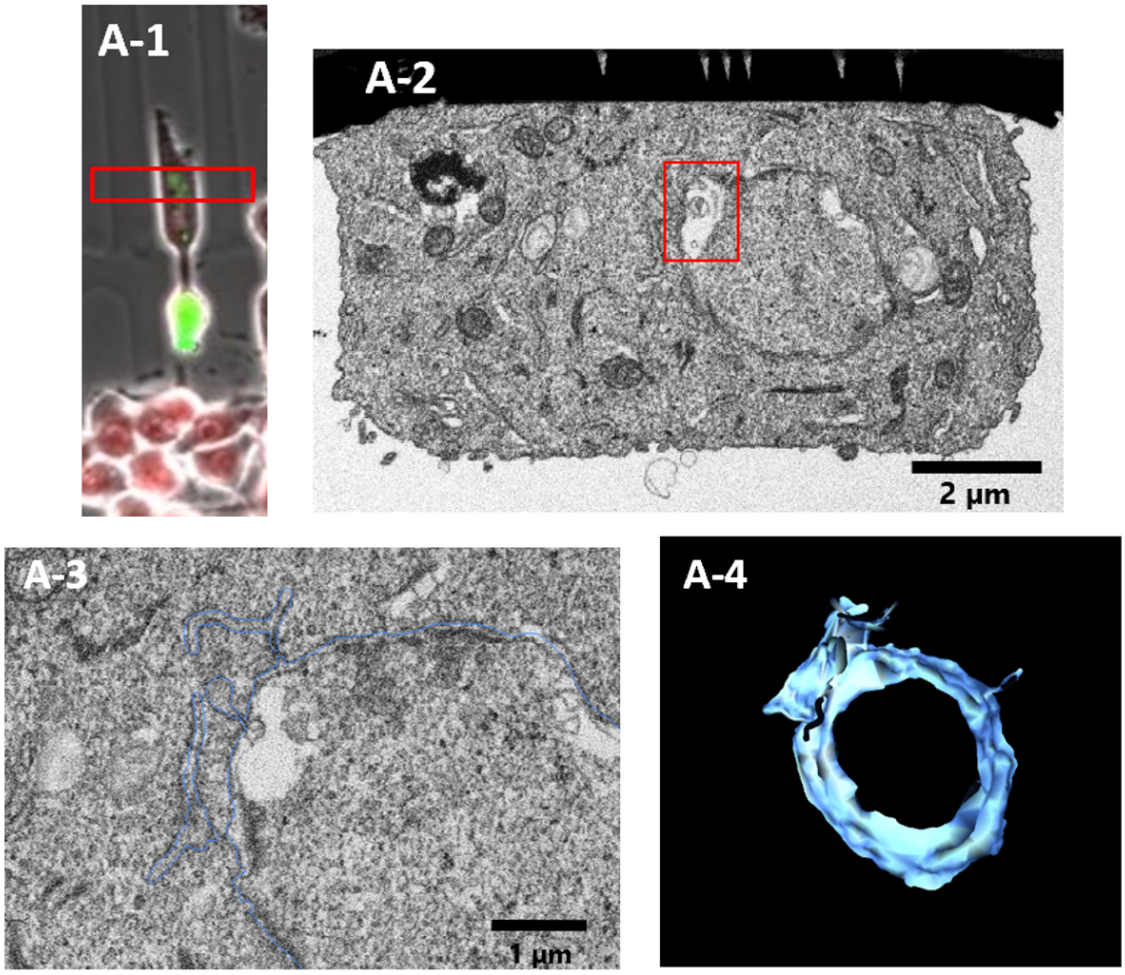

Fig. 2.10 NEBD. A-1, cGas-GFP, H2B-mCherry and transmitted light of selected cell. The square marks the region where in the front, a fluorescent spot marking a breakage was found. A-2 shows a cross-section in the middle of the breakdown. A-3 shows another cross-section with the ER enhanced marked for segmentation, in A-4. A-4 shows the segmentation of the region of the nuclear envelope and the connected ER in the breakage area.

2.4 Outlook

During migration, the complex cytoskeleton network composed of stress fibres, actin bundles, microtubules and intermediate filaments plays an important role. Some components bind to the nuclear envelope (e.g. via nesprins) and form a big complex known as LINC (Linker of Nucleoskeleton and Cytoskeleton) complex (Wilson and Berk, 2010). LINC is the nexus between force transmission of the cytoskeleton and nuclear lamina. The involvement of cytoskeletal structures during nuclear constriction and migration has not been studied in depth (like a possible involvement of MTOC during migration). In our research, due to the limited resolution of the FIB-SEM and the generalized sample preparation by chemical fixation, fine cytoskeleton components could not be observed. FIB-SEM provided a general volume context of all the involved organelles, but only the use of electron tomography by TEM or even cryo-electron tomography could help to visualize other cytoskeletal structures (Mahamid et al., 2016).

Additionally, nuclear lamina is associated with a variety of inner nuclear membrane (INM) proteins and provides anchoring sites for chromatin domains inside the nucleus. Chromatin changes and signaling during migration is another point that requires further research (Kumar et al., 2014). With multiple cells acquired, different chromatin densities (euchromatin and heterochromatin regions) under pressure regions of the nuclear envelope could be statistically confirmed by image analysis (Hoang et al., 2017). Thus, correlations between debilitated nuclear lamina and heterochromatin changes could be found.

Technical challenges

The aim of this chapter was to demonstrate the application of FIB-SEM for revealing three-dimensional features of HeLa cells under specific conditions. By CLEM, it is possible to study single cells at a desired time point migrating through a constriction channel and generate a volume by EM. In the two cells that were analyzed, FIB-SEM proved to be efficient for visualizing the ultrastructure of migrating cells and their cytoplasmic processes. Nevertheless, these experiments where exploratory, more cells are needed to confirm current observations and to possibly quantify them. With more data it would be possible to measure differences during various time points of nuclear constriction, such as envelope thickness, density of the surrounding chromatin, lamina disruption and cytoskeletal elements arrangement.

On a technical point of view, this project was bearing great interest because it had specific implications for the use of the FIB-SEM in a CLEM experiment. Whilst the workflow was proven efficient, we think some adjustments could address some issues related to the sample preparation. One possibility is to increase the preservation of organelles by switching from

chemical fixation to high pressure freezing. With the current setup this is not possible and very challenging technically. Smaller PDMS chips would be required to fit inside the HPF machine (so they can freeze uniformly), which makes the process very difficult for their preparation and manipulation. Another technical drawback to improve is the removal of PDMS attached to the glass, since it becomes extremely charged under SEM, preventing good imaging.

If we aim to reproduce the experiment enough times to quantify observations, better tools and an optimization of the current workflow are required. For example, correlating the position of the fluorescence breakage with the same position found in EM images could be performed in a high throughput manner. In commercially available light microscopes it is possible to program them to monitor several cells simultaneously in a time lapse manner within the same PDMS chip. Each chip could then provide a cell at different time points of the nuclear constriction process. Thus, a system for detecting channels in the SEM surface images could be implemented without much effort. By using computer vision techniques and by knowing the chip measurements, channels could be identified individually. Then, a registration with light microscopy images could define where exactly each cell is located.

Our efforts to improve the throughput in CLEM experiments will be described in the following chapters. This experiment represents a good example that justifies the need for an increased degree of automation in a complex workflow such as this one.

Acknowledgments and contributions

Yannick Schwab[1], my supervisor, initiated the project by contacting Matthieu Piel[2] at the Institut Curie and Marco Foiani[3] at IFOM. Matthieu Piel[2] provided the cells for the experiment.

Galina V. Beznoussenko[3] prepared the sample with cell 1. Nicole L. Schieber[1] and José Miguel Serra Lleti[1] did the FIB-SEM acquisition of cell 1. José Miguel Serra Lleti performed data post-processing and analysis. Matthew Raab[2] and José Miguel Serra Lleti elaborated the PDMS chips and did the light microscopy for cell 2. José Miguel Serra Lleti did the sample preparation of cell 2, FIB-SEM acquisition, data post-processing and analysis, including alignments and segmentation.

M.Raab contributed to discussions in relation to NEBD and lamin involvement. Galina V. Beznoussenko contributed to discussions in relation to organelle positioning and to point the similarity of the presented observations with her TEM data. Galina V. Beznoussenko, Yannick Schwab and Nicole L. Schieber contributed to discussions over sample preparation and technical details.

Affiliations

(1) Cell Biology and Biophysics Unit, European Molecular Biology Laboratory, 69117 Heidelberg, Germany

(2) Institut Curie, PSL Research University, CNRS, UMR 144, F-75005 Paris, France.

(3) IFOM, Istituto FIRC di Oncologia Molecolare, Milan, Italy

References

Bell, E. S. and Lammerding, J. (2016) 'Causes and consequences of nuclear envelope alterations in tumour progression.', *European journal of cell biology*. NIH Public Access, 95(11), pp. 449–464. doi: 10.1016/j.ejcb.2016.06.007.

Le Berre, M., Zlotek-Zlotkiewicz, E., Bonazzi, D., Lautenschlaeger, F. and Piel, M. (2014) 'Methods for two-dimensional cell confinement.', *Methods in cell biology*, 121, pp. 213–29. doi: 10.1016/B978-0-12-800281-0.00014-2.

Beznoussenko, G. V. and Mironov, A. A. (2015) 'Correlative Video-Light–Electron Microscopy of Mobile Organelles', *in Methods in molecular biology* (Clifton, N.J.), pp. 321–346. doi: 10.1007/978-1-4939-2309-0_23.

Cardona, A., Saalfeld, S., Schindelin, J., Arganda-Carreras, I., Preibisch, S., Longair, M., Tomancak, P., Hartenstein, V. and Douglas, R. J. (2012) 'TrakEM2 Software for Neural Circuit Reconstruction', *PLoS ONE*. Edited by A. Samuel. Public Library of Science, 7(6), p. e38011. doi: 10.1371/journal.pone.0038011.

Denais, C. M., Gilbert, R. M., Isermann, P., McGregor, A. L., te Lindert, M., Weigelin, B., Davidson, P. M., Friedl, P., Wolf, K. and Lammerding, J. (2016) 'Nuclear envelope rupture and repair during cancer cell migration', *Science, 352(6283)*, pp. 353–358. doi: 10.1126/science.aad7297.

Desai, S. P., Bhatia, S. N., Toner, M. and Irimia, D. (2013) 'Mitochondrial localization and the persistent migration of epithelial cancer cells.', *Biophysical journal. The Biophysical Society*, 104(9), pp. 2077–88. doi: 10.1016/j.bpj.2013.03.025.

Diz-Muñoz, A., Krieg, M., Bergert, M., Ibarlucea-Benitez, I., Muller, D. J., Paluch, E. and Heisenberg, C.-P. (2010) 'Control of Directed Cell Migration In Vivo by Membrane-to-Cortex Attachment', *PLoS Biology*. Edited by W. A. Harris. Public Library of Science, 8(11), p. e1000544. doi: 10.1371/journal.pbio.1000544.

Fermie, J., Liv, N., ten Brink, C., van Donselaar, E. G., Müller, W. H., Schieber, N. L., Schwab, Y., Gerritsen, H. C. and Klumperman, J. (2018) 'Single organelle dynamics linked to 3D structure by correlative live-cell imaging and 3D electron microscopy', *Traffic*. Wiley/Blackwell (10.1111), 19(5), pp. 354–369. doi: 10.1111/tra.12557.

Friedman, J. R., Lackner, L. L., West, M., DiBenedetto, J. R., Nunnari, J. and Voeltz, G. K. (2011) 'ER Tubules Mark Sites of Mitochondrial Division', *Science*, 334(6054), pp. 358–362. doi: 10.1126/sci-

ence.1207385.

Garitagoitia Cid, A., Rosenkranz, R. and Zschech, E. (2016) 'Optimization of the SEM Working Conditions: EsB Detector at Low Voltage', *Advanced Engineering Materials*. Wiley-Blackwell, 18(2), pp. 185–193. doi: 10.1002/adem.201500161.

Hampoelz, B., Mackmull, M.-T., Machado, P., Ronchi, P., Bui, K. H., Schieber, N., Santarella-Mellwig, R., Necakov, A., Andrés-Pons, A., Philippe, J. M., Lecuit, T., Schwab, Y. and Beck, M. (2016) 'Pre-assembled Nuclear Pores Insert into the Nuclear Envelope during Early Development.', *Cell. Elsevier, 166(3), pp. 664–678*. doi: 10.1016/j.cell.2016.06.015.

Hasegawa, T., Yamamoto, T., Hongo, H., Qiu, Z., Abe, M., Kanesaki, T., Tanaka, K., Endo, T., de Freitas, P. H. L., Li, M. and Amizuka, N. (2018) 'Three-dimensional ultrastructure of osteocytes assessed by focused ion beam-scanning electron microscopy (FIB-SEM)', *Histochemistry and Cell Biology*. Springer Berlin Heidelberg, 149(4), pp. 423–432. doi: 10.1007/s00418-018-1645-1.

Hatch, E. M. and Hetzer, M. W. (2016) 'Nuclear envelope rupture is induced by actin-based nucleus confinement.', *The Journal of cell biology*. Rockefeller University Press, 215(1), pp. 27–36. doi: 10.1083/jcb.201603053.

Heuzé, M. L., Collin, O., Terriac, E., Lennon-Duménil, A.-M. and Piel, M. (2011) 'Cell Migration in Confinement: A Micro-Channel-Based Assay', *Humana Press*, pp. 415–434. doi: 10.1007/978-1-61779-207-6_28.

Hoang, T. V., Kizilyaprak, C., Spehner, D., Humbel, B. M. and Schultz, P. (2017) 'Automatic segmentation of high pressure frozen and freeze-substituted mouse retina nuclei from FIB-SEM tomograms', *Journal of Structural Biology*, 197(2), pp. 123–134. doi: 10.1016/j.jsb.2016.10.005.

Isermann, P. and Lammerding, J. (2017) 'Consequences of a tight squeeze: Nuclear envelope rupture and repair', *Nucleus*, 8(3), pp. 268–274. doi: 10.1080/19491034.2017.1292191.

Jimenez, A. J., Maiuri, P., Lafaurie-Janvore, J., Divoux, S., Piel, M. and Perez, F. (2014) 'ESCRT Machinery Is Required for Plasma Membrane Repair', *Science*, 343(6174), pp. 1247136–1247136. doi: 10.1126/science.1247136.

Karreman, M. A., Mercier, L., Schieber, N. L., Shibue, T., Schwab, Y. and Goetz, J. G. (2014) 'Correlating Intravital Multi-Photon Microscopy to 3D Electron Microscopy of Invading Tumor Cells Using Anatomical Reference Points', *PLoS ONE*. Edited by J. A. Coles. Public Library of Science, 9(12), p. e114448. doi: 10.1371/journal.pone.0114448.

Kumar, A., Mazzanti, M., Mistrik, M., Kosar, M., Beznoussenko, G. V., Mironov, A. A., Garrè, M., Parazzoli, D., Shivashankar, G. V., Scita, G., Bartek, J. and Foiani, M. (2014) 'ATR Mediates a Checkpoint at the Nuclear Envelope in Response to Mechanical Stress', *Cell*, 158(3), pp. 633–646. doi: 10.1016/j.cell.2014.05.046.

Lämmermann, T., Bader, B. L., Monkley, S. J., Worbs, T., Wedlich-Söldner, R., Hirsch, K., Keller, M., Förster, R., Critchley, D. R., Fässler, R. and Sixt, M. (2008) 'Rapid leukocyte migration by integrin-

independent flowing and squeezing', *Nature*. Nature Publishing Group, 453(7191), pp. 51–55. doi: 10.1038/nature06887.

Limaye, A.(2012) 'Drishti: a volume exploration and presentation tool',*Stock, S. R. (ed.). International Society for Optics and Photonics*, p. 85060X. doi: 10.1117/12.935640.

Liu, Y.-J., Le Berre, M., Lautenschlaeger, F., Maiuri, P., Callan-Jones, A., Heuzé, M., Takaki, T., Voituriez, R. and Piel, M. (2015) 'Confinement and Low Adhesion Induce Fast Amoeboid Migration of Slow Mesenchymal Cells', *Cell*, 160(4), pp. 659–672. doi: 10.1016/j.cell.2015.01.007.

Mahamid, J., Pfeffer, S., Schaffer, M., Villa, E., Danev, R., Kuhn Cuellar, L., Forster, F., Hyman, A. A., Plitzko, J. M. and Baumeister, W. (2016) 'Visualizing the molecular sociology at the HeLa cell nuclear periphery', *Science*, 351(6276). doi: 10.1126/science.aad8857.

Olmos, Y., Hodgson, L., Mantell, J., Verkade, P. and Carlton, J. G. (2015) 'ESCRT-III controls nuclear envelope reformation', *Nature*. Nature Publishing Group, 522(7555), pp. 236–239. doi: 10.1038/nature14503.

Phillips, M. J. and Voeltz, G. K. (2016) 'Structure and function of ER membrane contact sites with other organelles.', *Nature reviews. Molecular cell biology*. NIH Public Access, 17(2), pp. 69–82. doi: 10.1038/nrm.2015.8.

Piños, J., Mikmeková, Š. and Frank, L. (2017) 'About the information depth of backscattered electron imaging', *Journal of Microscopy*. Wiley/Blackwell (10.1111), 266(3), pp. 335–342. doi: 10.1111/jmi.12542.

Poincloux, R., Collin, O., Lizárraga, F., Romao, M., Debray, M., Piel, M. and Chavrier, P. (2011) 'Contractility of the cell rear drives invasion of breast tumor cells in 3D Matrigel.', *Proceedings of the National Academy of Sciences of the United States of America*. National Academy of Sciences, 108(5), pp. 1943–8. doi: 10.1073/pnas.1010396108.

Raab, M., Gentili, M., de Belly, H., Thiam, H.-R., Vargas, P., Jimenez, A. J., Lautenschlaeger, F., Voituriez, R., Lennon-Dumenil, A.-M., Manel, N. and Piel, M. (2016) 'ESCRT III repairs nuclear envelope ruptures during cell migration to limit DNA damage and cell death', *Science*, 352(6283), pp. 359–362. doi: 10.1126/science.aad7611.

Rowland, A. A. and Voeltz, G. K. (2012) 'Endoplasmic reticulum-mitochondria contacts: function of the junction.', *Nature reviews. Molecular cell biology*. NIH Public Access, 13(10), pp. 607–25. doi: 10.1038/nrm3440.

Schindelin, J., Arganda-Carreras, I., Frise, E., Kaynig, V., Longair, M., Pietzsch, T., Preibisch, S., Rueden, C., Saalfeld, S., Schmid, B., Tinevez, J.-Y., White, D. J., Hartenstein, V., Eliceiri, K., Tomancak, P. and Cardona, A. (2012) 'Fiji: an open-source platform for biological-image analysis', *Nature Methods*. Nature Publishing Group, 9(7), pp. 676–682. doi: 10.1038/nmeth.2019.

Thiam, H.-R., Vargas, P., Carpi, N., Crespo, C. L., Raab, M., Terriac, E., King, M. C., Jacobelli, J., Alberts, A. S., Stradal, T., Lennon-Dumenil, A.-M. and Piel, M. (2016) 'Perinuclear Arp2/3-driven actin

polymerization enables nuclear deformation to facilitate cell migration through complex environments', *Nature Communications*, 7, p. 10997. doi: 10.1038/ncomms10997.

Thiery, J. P. (2002) 'Epithelial–mesenchymal transitions in tumour progression', *Nature Reviews Cancer*, 2(6), pp. 442–454. doi: 10.1038/nrc822.

Welch, M. D. (2015) 'Cell Migration, Freshly Squeezed', *Cell*, 160(4), pp. 581–582. doi: 10.1016/j.cell.2015.01.053.

Wilson, K. L. and Berk, J. M. (2010) 'The nuclear envelope at a glance', *Journal of Cell Science*, 123(12), pp. 1973–1978. doi: 10.1242/jcs.019042.

Wu, J., Sun, L., Chen, X., Du, F., Shi, H., Chen, C. and Chen, Z. J. (2013) 'Cyclic GMP-AMP Is an Endogenous Second Messenger in Innate Immune Signaling by Cytosolic DNA', *Science*, 339(6121), pp. 826–830. doi: 10.1126/science.1229963.

Xu, C. S., Hayworth, K. J., Lu, Z., Grob, P., Hassan, A. M., García-Cerdán, J. G., Niyogi, K. K., Nogales, E., Weinberg, R. J. and Hess, H. F. (2017) 'Enhanced FIB-SEM systems for large-volume 3D imaging.', *eLife*. eLife Sciences Publications, Ltd, 6. doi: 10.7554/eLife.25916.

Zhao, J., Zhang, J., Yu, M., Xie, Y., Huang, Y., Wolff, D. W., Abel, P. W. and Tu, Y. (2013) 'Mitochondrial dynamics regulates migration and invasion of breast cancer cells', *Oncogene*. Nature Publishing Group, 32(40), pp. 4814–4824. doi: 10.1038/onc.2012.494.

3

Automation of FIB-SEM for cell volume acquisitions

3.1 Introduction

In chapter 1, FIB-SEM was classified as a new generation of microscopes highly automatized. But as it has been shown in chapter 2, targeting a cell and starting an acquisition requires several manual steps to be applied by an expert operator. During my thesis, I developed *CLEMSite*, a software solution that automate many of the manual steps of a CLEM workflow using FIB-SEM. At the user level, *CLEMSite* can be divided in two major parts: correlation and acquisition. During the correlation, cell positions previously defined by light microscopy are accurately retrieved in the SEM. After that, during acquisition, 3D volume collection by slice and view is triggered at the corresponding positions. This process can be repeated iteratively, thus enabling automated acquisition of dozens of cells.

Unlike for TEMs where open source libraries are freely available, FIB-SEM controllers are proprietary and any access to microscope control must be licensed. Thus, a collaboration with *Carl Zeiss Microscopy GmbH* (*Zeiss*) was established. Our model, a Crossbeam 540 is by default controlled by SmartSEM, a software package from *Zeiss*. In addition, *Fibics Inc.* is a third-party company of *Zeiss* who created their own hardware and software to control the FIB-SEM (*ATLAS 3D*), which in many ways excels the default machine software. This project was possible thanks to a license granted by *Fibics Inc.* and their continuous support for the extra functionality provided by their software libraries.

3.2 Introduction to the software instrument, *Zeiss Crossbeam 540*

A server is a program able to accept requests from other programs called clients via the internet. Similar to a telephone number, a client knows the address of the server. A client can connect to the server by sending a request. If the request is granted, both programs can start to communicate data between them. *SmartSEM* is an application from *Zeiss* that connects as a client to another program called the *EMServer*, also from *Zeiss*. *SmartSEM* sends bursts of commands and the EMServer translates them to instructions to the hardware and electronics of the FIB-SEM.

ATLAS 5 from *Fibics Inc.* comprises two different software packages: *ATLAS 5*, which is a viewer and project manager, also containing registration software for ATUM or 3D fluorescent stacks, and *ATLAS Engine*, containing *ATLAS 3D* wizard, nanopatterning wizard and other tools integrated in a single GUI. *ATLAS* does not communicate directly to the *EMServer*. They use another program as bridge, *FibicsServer*, which connects *ATLAS* Engine, the core of their *ATLAS* package , via local networking. The *ATLAS* software package is usually placed on a different computer from SmartSEM and is used to control the microscope via a GUI (Figure 3.1).

ATLAS 5 is a combination of software and hardware. Their hardware consists in a FPGA able to read the inputs from SEM and FIB sensors at a higher rate than the default software is capable. This allows for better synchronization, with the possibility of milling and imaging simultaneously, generating full montages of SEM images at different resolutions and controlling of the nanopatterning to be rasterized in any desired shape.

3.3 *CLEMSite* modules

CLEMSite is an application composed of multiple modules, that have their own set of scripts and graphic user interface (GUI). We have opted for this modular architecture to allow for efficient updating and independent testing during the development phase. Modules are enumerated and their function summarized in Figure 3.2.

Light Microscopy (LM) map builder and the Navigator are modules executed during the correlation part of the workflow. These two modules can be easily adapted to any type of light or electron microscope. For light microscopy, the format of provided images and metadata header has to be adapted. Nowadays this is not a difficult task if the light microscope follows

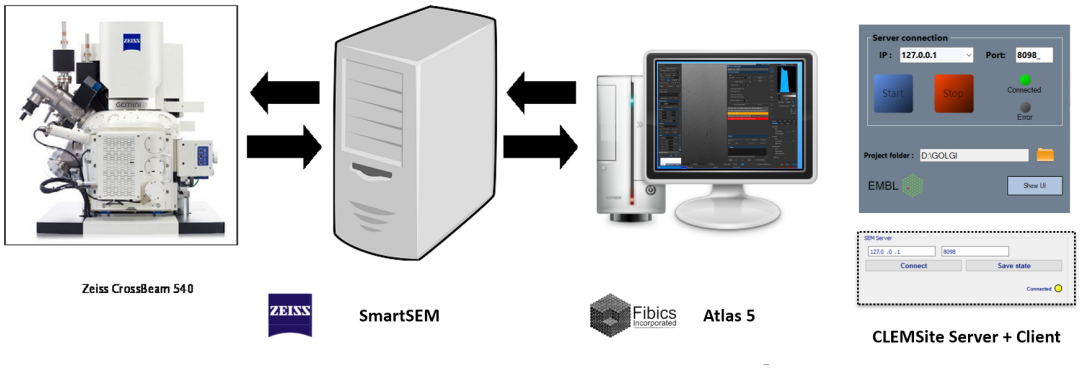

Fig. 3.1 From left to right, The *Zeiss Crossbeam 540* is connected to a computer which runs the SmartSEM. SmartSEM communicates with another computer that contains *ATLAS* Engine via the *Fibics Server*. In the final step, *ATLAS Engine* is connected to our software, *CLEMSite* via the *CLEMSiteServerServer*. *CLEMSiteServer* functionality is reduced to the minimum with only Start and Stop and the project folder where data acquired will be stored.

the standard OME format[1]. For electron microscopes, the minimum requirements needed for adaptation are usually provided by all microscopy companies and would consist in getting access to only a few functions: moving the stage, querying the stage and beam positions and grabbing images at different magnifications.

Multisite is a module used for the autonomous acquisition. *CLEMSiteServer* was developed with C# and wraps .NET components from the *FibicsVE* API functionality able to command the microscope. Navigator and Multisite are both clients of *CLEMSiteServer*, which contains a server able to execute sequences of functions sent from clients. Clients can send messages but they are not allowed to interfere with major microscope operations, for example, to interrupt an imaging session. To enforce this constraint, the server replies asynchronously, which means it will reply after finishing any important operation and not immediately. Only in a few exceptional situations (e.g. when input is needed from the user), the server does pause actively, waiting for a client's answer.

To explain this in more detail, a client of *CLEMSiteServer* can send the order 'mill a trench'. *CLEMSiteServer* receives the command and executes a set of functions from the *ATLAS Engine*, such as setup a shape and call a feedback loop control to recognize when the operation has finished. *ATLAS Engine* will communicate with *FibicsServer* sending several hundreds of instructions to execute the order, and the *FibicsServer* will translate even in more basic instructions to the *EMServer*. Because *ATLAS 5* is only available for Windows OS,

[1] https://www.openmicroscopy.org/bio-formats/

CLEMSiteServer can only be used in Windows machines. Alternatively, all clients connected to the *CLEMSiteServer* are using python and Qt5 libraries, which are independent of the OS.

Finally, RunChecker executes several python scripts in parallel as independent processes when an acquisition (also known as run) is on-going. It provides additional functionality and, when possible, feedback, such as the current status (focus, drifting, potential errors) of acquired images.

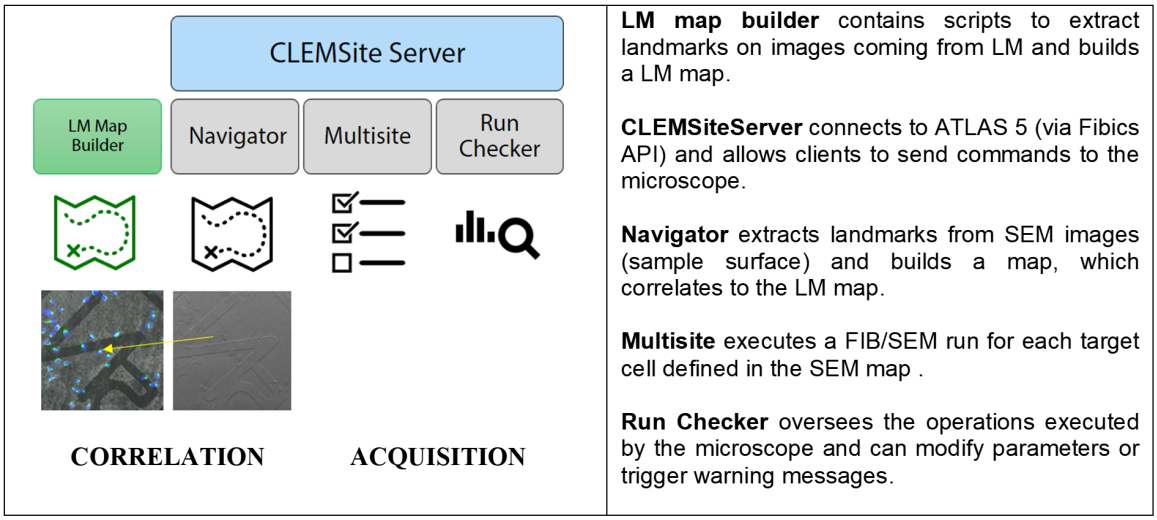

Fig. 3.2 *CLEMSite* architecture and main functionality of modules.

To summarize this section, *CLEMSite* is a software package developed for automation. It has two major functions, to establish correlation between targets in fluorescence and electron microscopy and to automatize the acquisition of 3D volumes. This is achieved by using a total of 4 modules, (1) to process light microscope images of cell targets, (2) to drive the SEM microscope to the targets, (3) to automatically acquire the volume of each target and (4) to make sure that this process is executed properly. A module can send commands to the electron microscope via connection to a server (*CLEMSiteServer*). The first two modules are microscope independent, the last two have been developed in collaboration with *Carl Zeiss GmbH* and depend on a license for their software (*ATLAS 5*).

In the rest of the chapter, I will present in detail the automation of the acquisition, which is common for the remaining of the experiments of this thesis. With this in mind, in chapters from 4 to 6, software description will be focused around the correlation workflows that employ the LM map builder and the Navigator.

3.4 Preconditions and set up for automatic acquisition

Initialization steps

ATLAS Engine contains an index of all available FIB currents and their configuration (such as the scanning pattern). It also indexes the gas injection system (GIS) materials used for deposition. Before any operation, an expert user must define a material (Epon or Durcupan resin for our samples) and calculate and adequate milling rate (ion dose per squared nanometer). This value can be used to calculate milling times and dosages in milled shapes like trapezoids or squares. All this information is usually saved in a file called recipe. A typical recipe saves the measurements of a shape as is shown in Figure 3.3 with the additional currents and dosages needed for proper milling.

ATLAS 3D is a wizard utilized to define an acquisition recipe, but also the imaging parameters for an acquisition. A setup file contains the ROI target and trench depth to be acquired, brightness and contrast of all detectors, SEM dwell time, auto-focus and auto-stigmatism parameters, currents used by the FIB, section thickness and keyframe[2] preferences. After this, *ATLAS* can be closed and the *CLEMSiteServer* can be started. *CLEMSiteServer* will start *ATLAS* again and wait for incoming client connection.

Communication Scheme

CLEMSiteServer is a TCP application listening to the port 8098 that follows its own communication protocol. It has a thread constantly listening to client requests. When a connection is accepted, data frames are sent by the client. The frames are information packets composed by 32 bytes header plus an additional body of information, the payload. Frames follow a special format adapted from RFC6455 (Asynchronous Websockets) [3].

In the payload, all data is passed as JSON[4]. Once the JSON is decoded, the name of a command is searched on a dictionary list and executed with its corresponding arguments (also decoded from the JSON parsed file). Thus, each function available in *CLEMSiteServer* is encapsulated with a launcher method (Figure 3.4). The advantage of this architecture is that it simplifies the process of creating new functions.

In everyday use of the software package, this process is hidden to the user. The user just needs to push a button to connect the client to the server. Upon connection, pending starting conditions have been defined (Table 2), the user pushes “Save state” button to store

[2] Keyframes are SEM images taken periodically during the run at low resolution with a big field of view. They help to monitor the acquisition.

[3] https://tools.ietf.org/html/rfc6455

[4] https://www.json.org

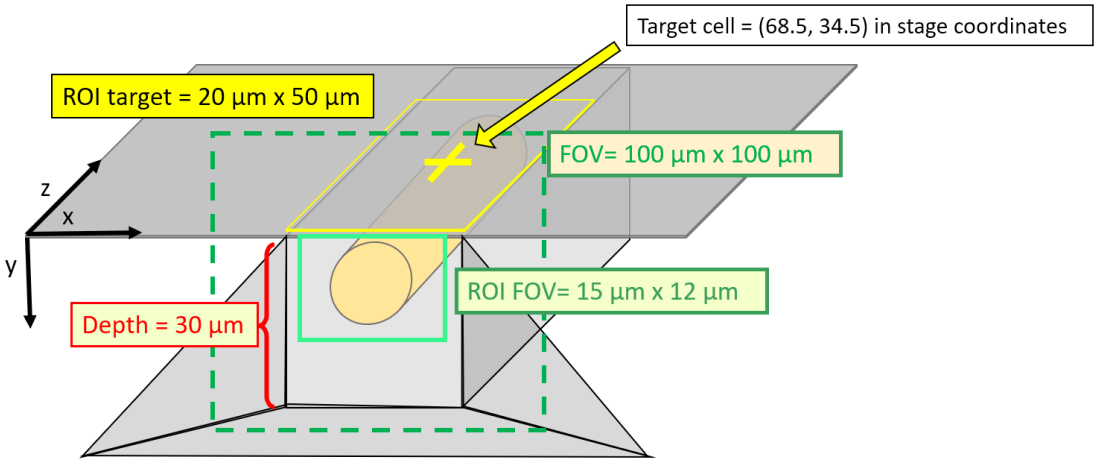

Fig. 3.3 Definition of ROI. Schematic representing a cell (cylinder) to be acquired by FIB-SEM. The volume of acquisition is illustrated by the rectangular prism surrounding the cylinder. The yellow cross marks the center of the target cell projected onto the x/z plane and parallel to the surface of the sample. Centre position is indicated using stage coordinates. This position can be used to define a 3D bounding box, the ROI target which is outlined in yellow (20 x 50 µm, depth 30 µm), and is the total volume to be acquired. The trapezium is milled to expose the face of the rectangular prism that becomes the cross-section face to be imaged (light green). Once the imaging surface is exposed, the user can define two regions: first, the Field Of View (FOV), and second, the ROI FOV, which is a portion of the FOV where the cross-section is imaged at final resolution, defined by width and height, in this example 15 x 12 µm (x/y).

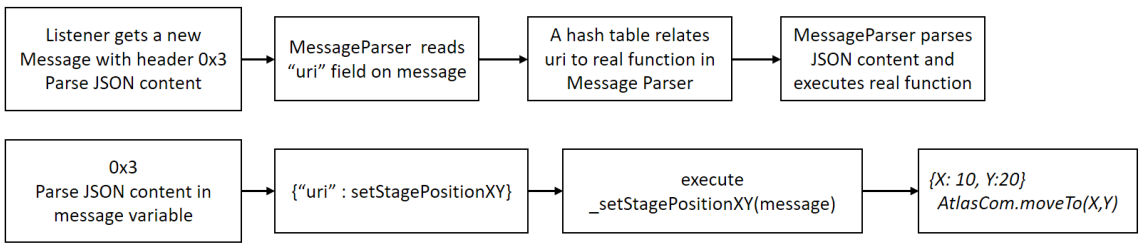

Fig. 3.4 Example of sequence of instructions as processed from client to server. Upper part indicates a description, bottom a call like it is written in code. Translated in plain text, when setStagePositionXY has to be executed, the string "setStagePositionXY" is sent together with the X and Y coordinates. All three fields are obtained from the decoded JSON. Then, a real function setStagePositionXY, which internally calls the *FibicsVE* API, is executed

all the initial conditions in the server. This step is of the utmost importance since each time an acquisition is started, the server will push all saved values for imaging in this moment. Certain microscope status conditions have to be stored before starting: 54 degrees stage tilt, original values of beam shift x and y, focus, stigmatism, brightness and contrast for all detectors in use (both with SEM and FIB imaging conditions) and FIB imaging probe.

1. SMART SEM is connected
2. Column chamber valve is open, EHT is on at 1.5 kV or to the kV decided for data acquisition.
3. FIB valve is open and FIB gun is on with the appropriate emission current and target (current, extractor and suppressor voltages operative)
4. Sample is in position with the following conditions properly set up:
   (a) Eucentric height at 54° stage tilt
   (b) WD at 5 mm
   (c) FIB at 50 pA imaging, with good focus
   (d) Focus, stigmatism and wobbler adjusted in SEM
   (e) B&C for SESI (FIB and SEM) and for ESB (SEM only).
   (f) Coincidence point done by user in the middle of the sample
5. Atlas Engine computer is properly configured and connected to SmartSEM and to the “white box” provided by *Fibics*.

3.5 *Multisite* Client

After starting the client and connecting to the *CLEMSiteServer*, the user must provide a list of coordinates. Coordinates correspond to a stage position where the cell centers (or organelle centers) are located, as defined by light microscopy. From now on, we will refer to each of those stage positions as a target cell.

By default, some general settings are applied to each target cell. This includes a setup file, a region of interest field of view (ROI FOV, as described in Figure 3.3), the order of acquisition and if it will be acquired or not. Optionally, each target cell can be configured with a different setup file and ROI FOV. Configuring each cell target separately can be useful when different phenotypes are present with varying shape requirements. It is also possible to acquire with different slice thicknesses (e.g. 20 nm for 5 cells and 100 nm for another 15 cells).

When the list of target cells is loaded, positions are sorted from regions of high to low spatial density. The reason for this is related to the determination of the coincidence point and the initial focus conditions. When the microscope moves from one target to another, all initial parameters have to be adjusted. If the next target is close in space, parameters have closer values and automatic adjustments are less prone to fail. The algorithm of sorting uses a kd-tree to sort positions. The spatial density map is computed by considering densities over 100 µm (when two cells are closer than 100 µm, it reaches its maximum). Cells are sorted by spatial density and if two are closer than 200 µm they are marked with a warning. When two cells are too close, the user has to decide whether they should both be included in the run or select only one of them. As we have seen in chapter 2, a trench has to be milled to expose the cell cross-section before slicing thin sections. When cells are within 200 µm of each other, it is likely that one of the trenches will also mill a part of the other. Additionally, it is possible to manually decide the order of acquisition in the list.

Following these initial setup steps, the application can be started by clicking on the play button (Figure 3.5). When the user clicks on start, the server is then blocked for other potential client requests and it will work exclusively with *Multisite*. The microscope cannot carry on other commands when a run is performed because it could end in a catastrophic failure (such as asking the microscope to move to a new ROI while it is milling a trench). As part of the software driven acquisition, first an automatic coincidence point and trench milling are carried out, which usually takes 25 minutes. After the trench is milled, the user is prompted twice to adjust brightness and contrast. The first time is the brightness and contrast (B&C) typical for image acquisition, the second is for the auto-focus and auto-stigmation algorithm. Originally the image B&C was set automatically by finding a balanced image

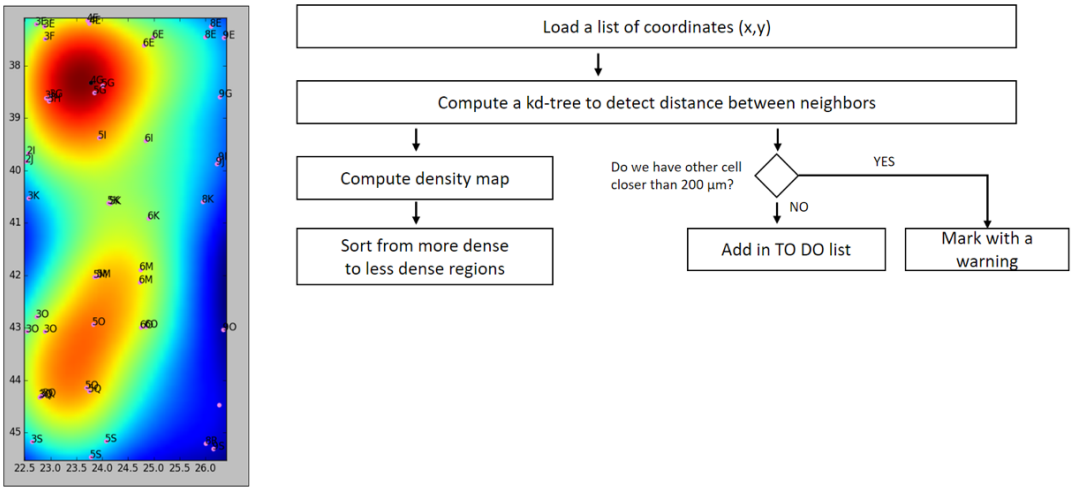

Fig. 3.5 Left, shows a computed spatial density map, each target cell is shown as a point. Red shows areas of high density, blue shows low density. The density is relative to the amount of points per area. Right, in the workflow, a 2 dimensional kd-tree implementation is used to sort points and calculate the distances between them. This information is used to compute the spatial density map, and also to spot points that are within a given threshold (200 µm).

histogram. In computer vision, balanced histograms reflect the maximum dynamic range available. Ideally, the gray scale image looks similar to the values that the same specimen would have in a well-adjusted cross-section from a TEM microscope. However, when including the top surface of the block in the FOV, the gold coating of the surface tends to saturate towards white values. These have to be ignored for a proper B&C balance in the image of the cross-section and can change with different coat thickness. Moreover, experience shows that different users and sample preparations tend to differ from what a computer considers a nice histogram.

Fibics developed an algorithm for auto-focus and auto-stigmatism (AFAS). This algorithm was designed to work with marks that are milled into a deposition layer and then filled with a contrasting material (insulator). *Fibics* auto-focus algorithm requires a more balanced histogram (with the best possible dynamic range to differentiate high frequencies) in the full FOV (not only in the cross-section), avoiding saturation towards white or black. In many occasions, when the sample preparation is excellent and membranes are well differentiated in the biological specimen, the distinction of B&C values for auto-focus and for imaging are irrelevant. In this case it is recommended to get the best possible dynamic range in the regions where the cell is imaged, or if the cell is not present yet, at the interface region between the protective coat and the resin. These values of B&C will be used again for all subsequent cells acquired in the sample.

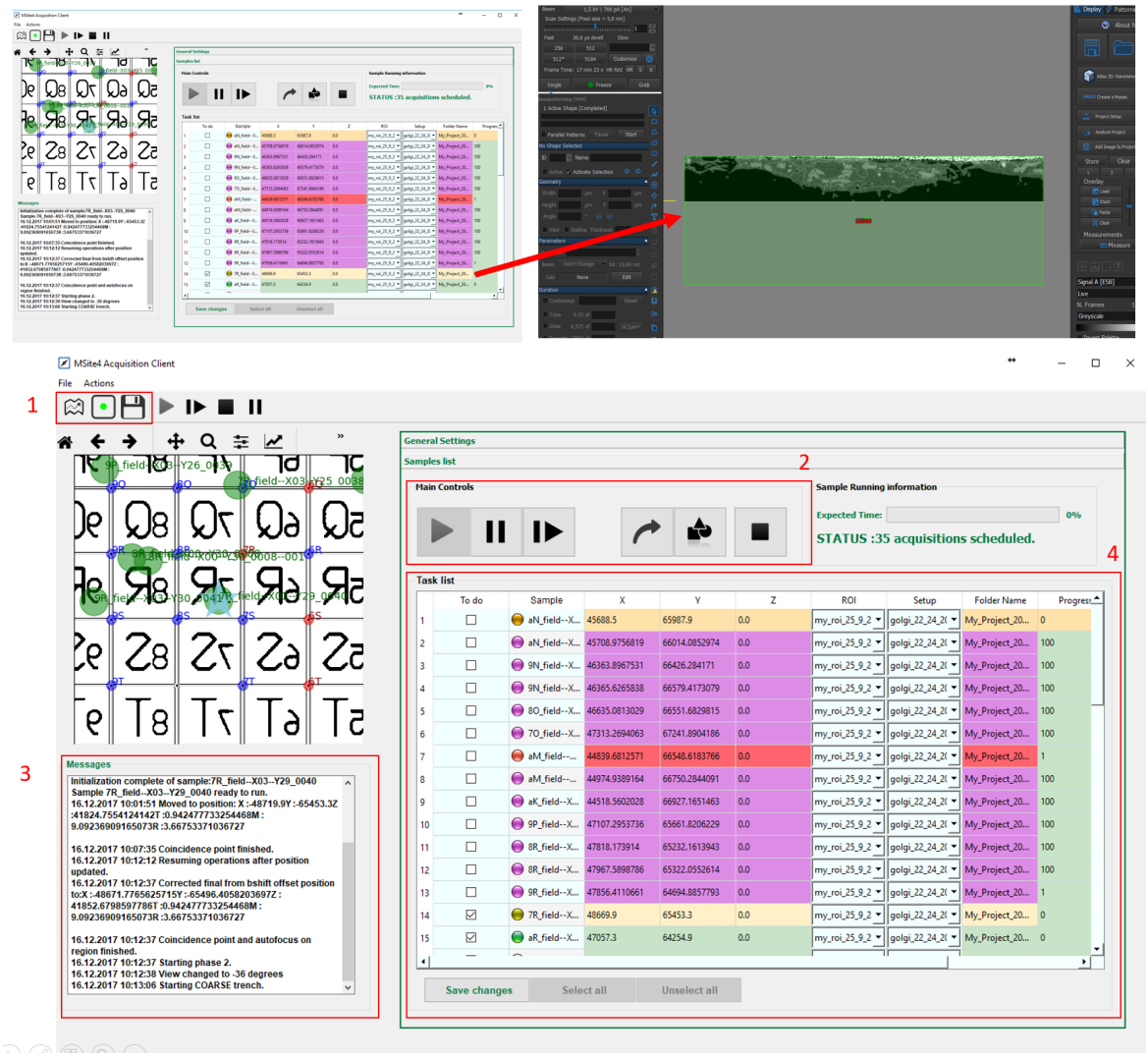

Fig. 3.6 *CLEMSite Multisite* GUI. Upper part, snapshot from the client GUI, with the arrow pointing to the current cell and how acquisition is displayed in *ATLAS* Engine. Bottom part, in the GUI: Box 1. User gives a session map (icon map) or a list of positions (square with green dot). Box 2. Main controls to operate the acquisition (from left to right): start, pause, resume acquisition after pause, move to the next target, show folder with acquired images, stop. Box 3. Messages sent by *CLEMSiteServer* to the client showing the status of the current acquisition (e.g. slice number, auto-focus executed, paused). Box 4. List of targets, magnified in B, here each row corresponds to a target cell and is color coded depending on its status. Green is the status before starting; orange warns that the cell can be acquired but is very close to another one; purple means that the target cell volume has been already acquired; red means there was a failure or that the user decided to skip or cancel the acquisition of that particular cell; yellow means that it is being acquired. Each row also contains: the sample name; X, Y, Z stage coordinates in the SEM, FOV size to be acquired, recipe that will be used (setup file) and the folder name where data will be stored.

From this point forward, the software will run the microscope automatically without user intervention. During the acquisition, the user will only be required to check two or three times per day to be sure nothing has gone wrong. A list of problems and potential fixes will be described in the monitoring section. In the event of a critical problem which stops the microscope, acquisitions can easily be resumed in a matter of minutes as the application saves automatically the project status of acquisitions on the fly.

3.5.1 Detailed computational workflow

So far, *Multisite* has been described from the point of view of an external user. This section is centered on a description of the computational workflow of the automation (Figure 3.7). An acquisition can be divided into three parts. First, is the movement and refinement of the stage position for the target cell, described in chapter 5. Second, is the preparation steps before slice & view (i.e. milling and imaging cross-sections). There are several critical steps which need computer vision assistance to replace a manual operator. Here, the goal is to center the field of view and obtain an image of the cross section with crisp focus. Finally, when the slice & view starts, monitoring is crucial.

3.5.2 Step 1: Positioning and Automatic Coincidence Point.

The first task of the client after pressing the start button is to send the setup file, ROI FOV and target cell position to *CLEMSiteServer*. Received files are assessed for correctness, and then the stage is positioned at the target cell. As explained in chapter 2, coincidence between beams is usually done manually by pointing to the same feature in the SEM beam and then adjusting the z height for the FIB beam. To automatize this procedure, the initial proposal was to create a linear model to super impose a plane over the surface of the sample, so z could be updated based on the position of the sample. To test this initial solution, several points were manually gathered across 4 different samples. A total of 9 points following the surface of the sample were taken and the coincidence point was calculated for each position. This covered almost the complete surface of the sample (around 800 mm^2) (Figure 3.8). While in theory the linear model should account for sample tilting, local variations on the sample topology had drastic effects on the calculation. For this reason, a different and better strategy is to consider only the vicinity of each region.

The solution which was successfully implemented in the workflow uses the algorithm following the pseudo-code shown in Figure 3.9. An auto-focus operation is performed on the surface of the sample. The difference between the previous focus distance and the new working one, gives the change in the z axis across the surface. If we surmise that the ion

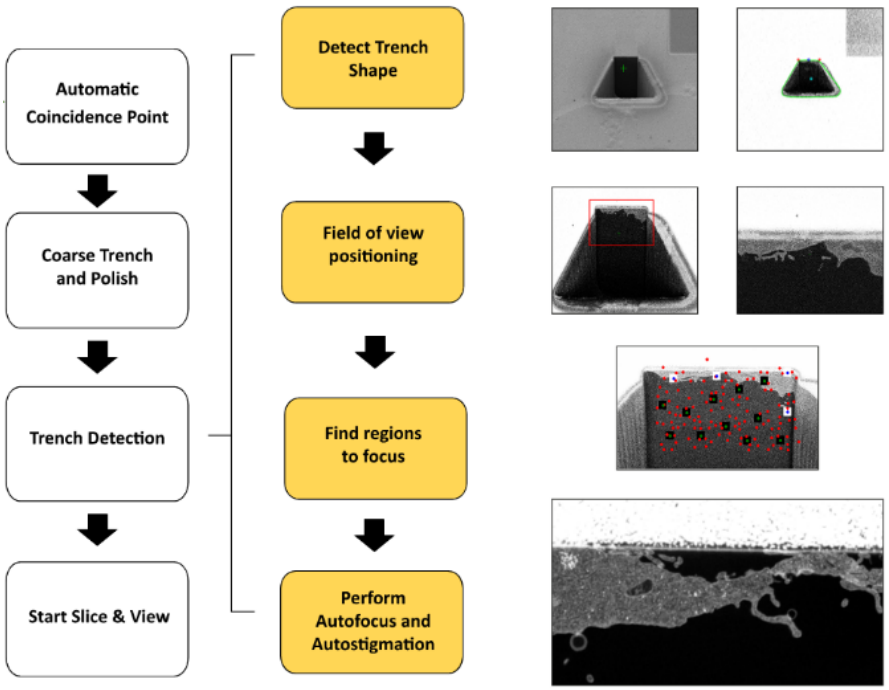

Fig. 3.7 After clicking on start, a series of automatic steps drive the microscope until it starts the slice and view (milling and then imaging). These steps are: automatic coincidence point, coarse trench and cross-section polish, trench detection and slice & view. **Trench detection** involves detecting a trench shape by computer vision algorithms (a trench is shown before and after detection of its contour), **positioning the field of view** in the trench (ROI field of view marked in red and magnified in second image), detecting high contrast **regions to focus** on (image shows a cross-section face where red points are candidates, blue points are selected points) and **perform autofocus and autostigmatism** on them (image presents a cross-section after autofocus and autostigmatism). Images taken with ESB detector at 1.5 kV.

beam has not moved, this distance can be added to the Z axis, so the sample is positioned where the ion beam and the electron beam are coincident.

In a second step of refinement, a square is burned onto the surface of the sample by imaging a small area of the surface with a 3 nA FIB current. An SEM image in a FOV of 350 µm2 is taken. The square in the image indicates the position of the ion beam. Then, the detection of the square consists of: background subtraction to remove noise, thresholding to segment the area, connected components for labelling all white objects in a binary image and finally shape detection by area size or square proportions. Traditional thresholding like Otsu (Otsu 1979) had to be replaced by *SLIC* thresholding, algorithm that I developed to circumvent the problem of bimodal histograms (Appendix 2, Algorithm 1). *SLIC* thresholding splits the image in 3 equidistant ranges. Then, gray values can be assigned to background, in our case, black. The contour accuracy of the algorithm depends on the amount of superpixels

computed by *SLIC* (Achanta et al. 2010). *kMeans*, *enhanceContrastPercentile* and *SLIC* are functions present in scikit package from python (Pedregosa et al. 2011).

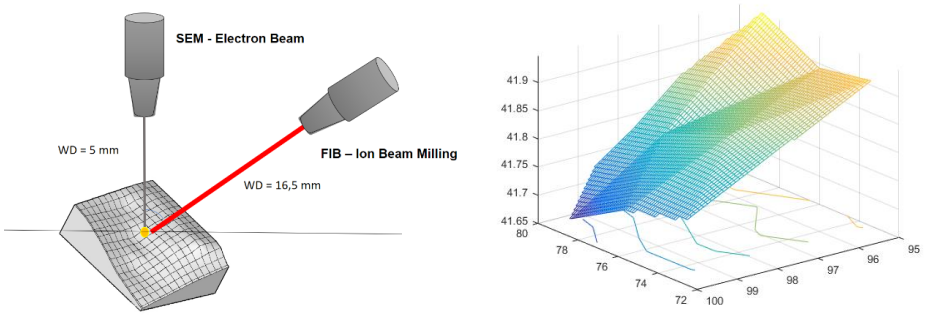

(a) (b)

Fig. 3.8 A representation of a sample and coincidence point is shown on (a). Local variations in sample topology can affect the calculation of the coincidence point. In the right plot (b), a total of 9 measures in Z along the full surface of the sample were taken. At each position the coincidence point was performed by an operator. Ideally, the 9 points should be in the same plane, but in the plot there were changes in the range of 250 µm in Z and a tilt variation of 2.85° respect the nominal sample (54°).

The centroid of the square is found in stage coordinates and used as a reference. If it is not in the center, the z axis is moved based on the geometrical relation between the SEM position (center of the image) and the FIB beam (center of the square). In a final step of refinement, images with FIB and SEM are taken and the position of the square is compared again. To detect the squares in both FIB and SEM, the original mark is cropped and cross correlation is used to find the location of the square in both images. Again, the center of the square indicates the position of each beam, then, the SEM beam is moved to the center of the FIB image by beam shift.

3.5.3 Step 2: Trench, polish and automatic detection of trench

After the coincidence point is determined, with the FIB pointing at the same stage coordinates as the SEM, we proceed with milling a trench and polish the exposed surface . The trench uses a high current to expose the cross section of the target cell. It has a trapezoidal shape to favor the accumulation of milled material to its side walls. Right after the trench, a lower FIB current mills a small rectangle at the cross-section face. This step is recommended to achieve better initial auto-focus and to clean the surface from charging ions generated by the use of high FIB currents. Trench and polish are performed using the *FibicsVE* API with the parameters defined initially in the *ATLAS* setup files.

Next, a low magnification image is performed using the EsB detector (Figure 3.10-2). The image is thresholded (Figure 3.10-3), and the top corner and centroid of the trapezoid

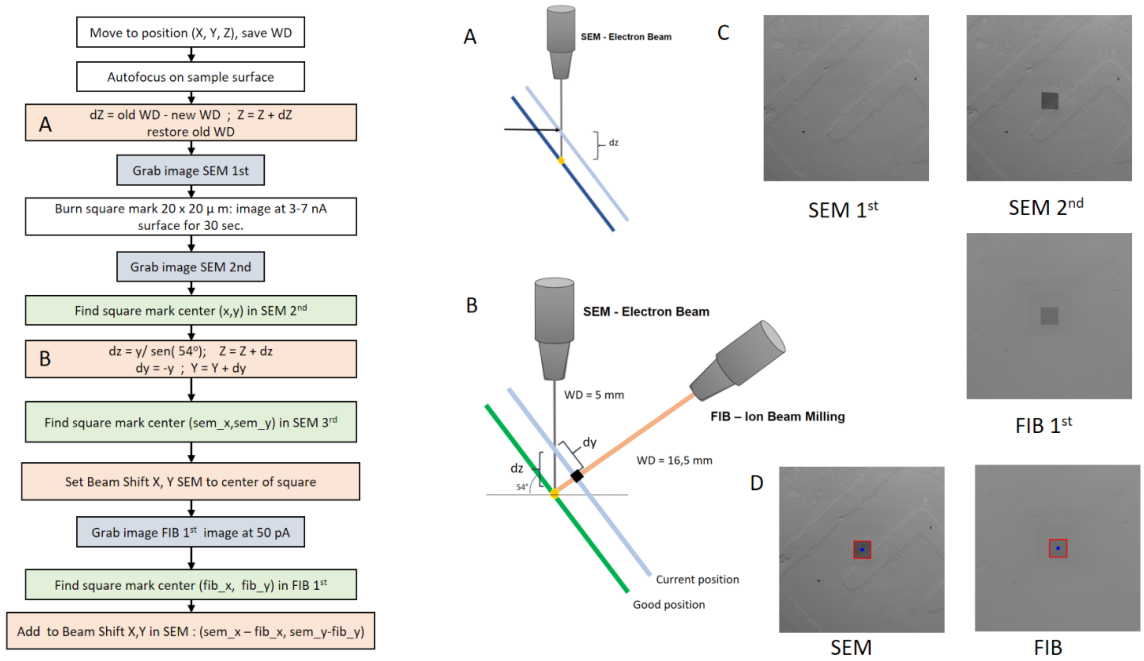

Fig. 3.9 **Detailed workflow for the automatic coincidence point.** Left figure, schematic of the algorithm. Orange boxes represent calculations carried on the stage coordinates or beam shift in micrometers. Image A, depicts the electron beam and a side view of the sample surface, where dz is the difference between the SEM Z position (arrow) and the ideal position of coincidence (orange dot on the dark blue line). The FIB beam could be really far, so this movement in Z direction is a coarse approach. B, depicts the relation with the SEM beam and the FIB beam. The blue plane is the current position, and the green plane is the ideal position. C, shows different images taken with SESI detector at the different stages of the algorithm (names correspond to the algorithm boxes in gray). For each image taken, the center of the image is the position of the current beam center (focal point of beam). D, shows the final result with the SEM and FIB aligned. Green boxes represent object detection scripts. The scripts use two techniques to find the square mark: first, subtraction of the background and object detection by thresholding, and once the mark is found, it follows with cross correlation of the marked square.

in the image are found in order to position the center of the field of view in the exposed cross-section using beam shift.

3.5.4 Step 3: EsB brightness and contrast, autotune box positioning and AFAS

The next step consists of magnifying and centering the FOV in the centroid of the trapezoid. At this point, but for the first cell only, fine adjustments are manually performed for brightness & contrast, astigmatism and focus for high resolution imaging. The set of functions called to obtain good focus and stigmation values automatically are AutoFocusAutoStigmation (AFAS) and autotune functions by *Fibics Inc.*.

Auto-focus refers to an algorithmic technique in which consecutive images are taken at different stage heights. The image which has a better measure of sharpness (or less

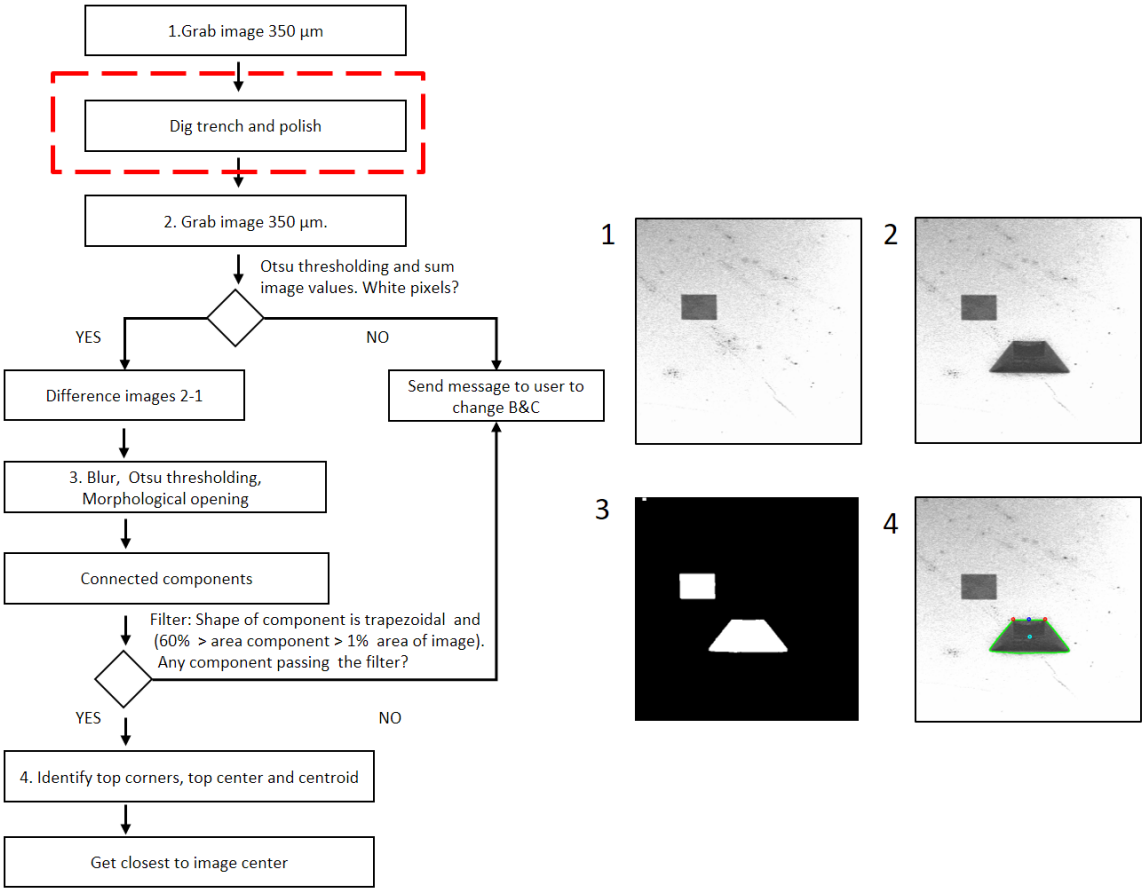

Fig. 3.10 **Algorithmic sequence to detect trench.** The red box indicates a call done to *FibicsVE* API functions for milling a trench and polish. Images are taken before and after the milling to quickly facilitate finding the newly milled elements by the difference between both images. With the image of the difference, auto thresholding is applied to find darker components (milled shapes). Since detection is based on thresholding, the user needs to balance properly B&C of the ESB detector before starting. After segmentation using connected components (labeling individual objects), a polynomial is fit to the contour of each object to find the top and bottom corners of the trapezoid. Then, the centroid of the figure is obtained. If the contour geometrically fits to be a trapezoid and its area is in an acceptable range, the object is stored as potential trapezoid. From the list of trapezoid candidates, the selected trapezoid is always the closest to the image center.

blurriness) is selected. Mathematically this can be converted to an optimization problem where the goal is to find the minimum (or maximum) of a sharpness measure, called metric. This is not difficult for objects with defined edges but can be challenging for real images. Here is when the metric used for convergence is essential. Metrics are usually based on convolutional filters that apply blurriness or gradients to obtain a score per image (Shen et al. 2006; Bravo-Zanoguera et al. 1998; Pertuz et al. 2012). Scores can then be compared across the sequence of images. Another possibility is to use the spectral domain of images to compare the middle and higher frequencies. These methods are usually based on DCT

or pass band filters (Zhang et al. 2018; Harada et al. 2017). And finally, some methods are based on histogram sharpness.

In SEM, another condition is required when choosing auto-focus algorithms: the number of frames obtained by the camera must be minimum (Cui et al. 2015; Rudnaya et al. 2010) in order to minimize the radiation damages. Because of this, SEM algorithms always have to work in specific ranges. Given the sample, the user has to specify the variation allowed by the algorithm. An example could be to move the focal length in 20 discrete steps over 1 µm using a FOV of 100x100 µm. That means an image will be taken at the desired magnification every 50 nm in z. During the slice & view process, the focal distance of the SEM is changing upon progression of the run, since the surface is progressively milled away. As a consequence, the autofocus functions have to be triggered periodically to maintain images quality, typically every one or two hours.

FibicsVE API gives access to *Fibics* proprietary algorithm for AFAS. These functions can result in a SUCCESS or FAIL state. If they succeed, the AFAS values are updated and stored, otherwise, initial values are kept. Parameters for the auto-focus had to be specified before the run, which means they will operate on stored ranges that can fail when breached (e.g. we set up 1 µm range, but the good focal distance is in the range of 2 µm). The metric (unknown)[5] works very well when defining the correct ranges. Hence, it is essential to provide a good initial focus of the cross-section before starting the slice and view process. However, it is nearly impossible to obtain a good initial focus by applying just one range. Because of this, I decided to iteratively apply the auto-focus from wide (0.2 µm steps in a space of 2 µm) to very narrow (0.01 µm steps in a space of 0.1 µm) ranges using binary searches. Each time, the optimal focus is closer. This procedure proved to obtain high quality initial focus values.

The same ideas are applied for correcting the beam astigmatism, except that astigmatism has one more dimension than for the focus (direction x and direction y). Optimal astigmatism is more difficult to find because it requires that the search is expanded in a bi-dimensional space and is also dependent on a relatively good focus. To solve this, typically AFAS is executed following the sequence auto-focus -> auto-stigmation -> auto-focus.

Additionally, AFAS functions cannot be executed anywhere on the cross-section. An AFAS is executed in a small window within the FOV (corresponding to 20-30% of its width and height) called Autotune box. In the manual workflow, the user positions the box on a series of marks (autotune marks) present at the block surface.(Jones et al. 2014). Autotune marks in the deposition layer are done with contrasting materials and they are very sharp (high frequency elements and with high contrast) (Figure 3.16). In the current automated workflow, and for the sake of simplicity, we decided to replace this step by a pure computer

[5] *Fibics Inc.* does not want to reveal which metric or metrics is using to measure quality of AFAS

vision software approach. Marks are not milled and an algorithm (Appendix 2, algorithm 2) searches maximum variation of intensity on the cross-section itself. When one of these regions is found, it is selected as a region to apply the auto functions.

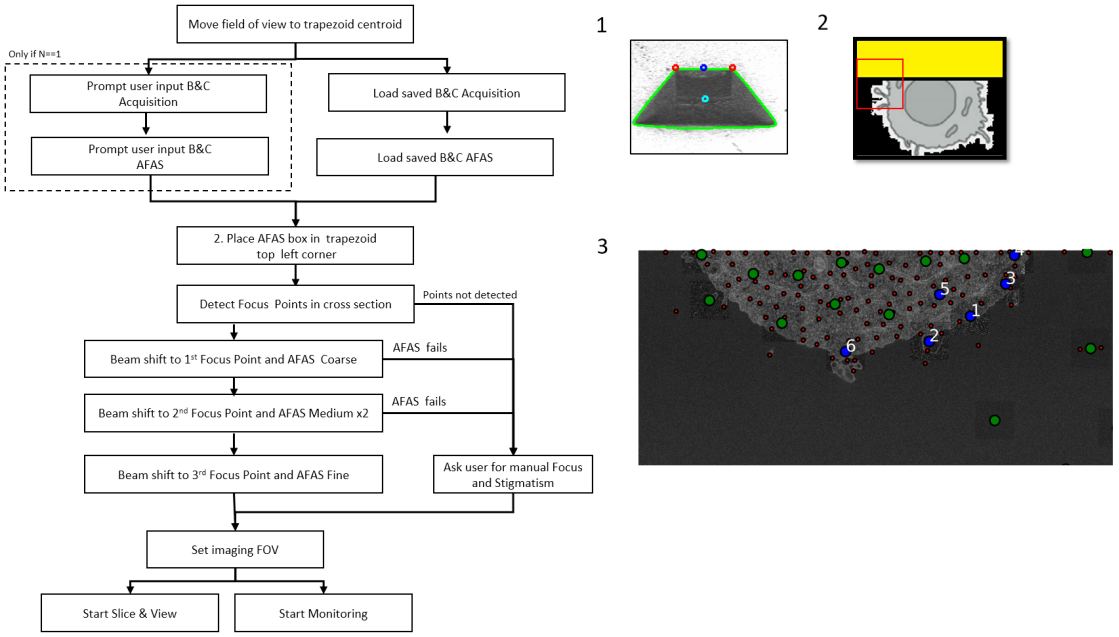

Fig. 3.11 **Algorithmic sequence to B&C and AFAS.** Boxes within the dotted line box will only happen once at the beginning of the run. 1, The trapezoid is labelled to mark its center (light blue dot), middle (dark blue dot) and upper corners (red dots). The upper left corner (red) is used to initialize the AFAS box for Autotune, as shown on 2. Image 3 shows the FOV after digging the trench, and points 1 to 6 in blue are selected for AFAS, based on maximum contrast variation (green dots are other candidate positions that were discarded); red points are the surrounding small local variations.

Maximum variation regions can be computed as follows. Images are converted to 8 bits, Hessian values (second order partial derivatives of the image, which can be used to find curvature) are calculated, then the maxima are found using a window of 20x20 pixels. Equivalent results were obtained using corner detectors, like Harris corner detector, which works efficiently, but is slower in practice (Harris & Stephens 1988). The maximums are clustered and 25 clusters around the image are selected using k-Means algorithm. From them, at each point, the variance is computed in a 50 by 50 patch. When the standard error lowers by 20 (gray value variation), the patch is too homogeneous and the corresponding point is deleted. After this pre-selection, the 6 points closer to the center of the image in x, and positioned at the upper part in y are selected. From the upper part of the image, the function stop_point is used to detect the boundary with the gold coating. The part of the image belonging to the gold coat cannot be considered for focusing because it is a perspective

projection of the surface, thus, the focus cannot be done in this region without the risk of focusing away from the cross-section.

This list of coordinates (6 points) is used to center the AFAS window and avoid too much radiation damage in the same region during the calculation of the initial focus. With a sharp focus and the ROI FOV centered in the cross-section face, the process of slice & view starts.

3.5.5 Runchecker: Monitoring the status of the current acquisition

Once *Multisite* orders to acquire images, two passive threads are started (Figure 3.11). The first thread sends continuous messages to the client about the acquisition progress. In case of a problem a message is sent to the client application and the run is stopped. At the time of volume completion, the client application is informed to proceed and sends instructions (position, setup file, cross-section ROI) for the next acquisition. Additionally, in an active way, users can cancel the ongoing acquisition if they detect any problem, e.g. the targeted region is not correct. During the run, users can pause, which will stop imaging (not milling though) until further orders; stop the current project, which finalizes any communication with the microscope; or skip current target, which moves to the next target location, starting a new process of acquisition.

A second thread is in charge of monitoring the folder where images are stored. This program is called RunChecker and works with several python scripts that provide extra functionalities to the acquisition process using python and OpenCV functions. Runcheck works synchronously with an event triggered after an image acquisition. When a new image is stored in the folder, it reads the image and calculates the relative displacement between the current image and the previous one. In case of a drift, the vertical translation that has to be moved in micrometers is calculated (see next section Tracking). Its other main function is to find when was the last time an autofocus was triggered. For that, usually *ATLAS Engine* logs are read and a timer is triggered to compute new AFAS regions at least 2 minutes before an AFAS operation is executed. All this information is sent back to *CLEMSiteServer* to correct the next acquisition or to move the autotune region to a different point (next paragraph, Autotune Box positioning).

Autotune Box positioning

Previously, it was described how AFAS functions are required to maintain a good image quality throughout the full volume acquisition. The AFAS cannot be done in the full FOV because radiation damages would affect the sample surface, thus the image quality. The solution provided by *ATLAS 5* is to position a small box in a region where AFAS will be applied every 30 or 45 minutes, the Autotune box.

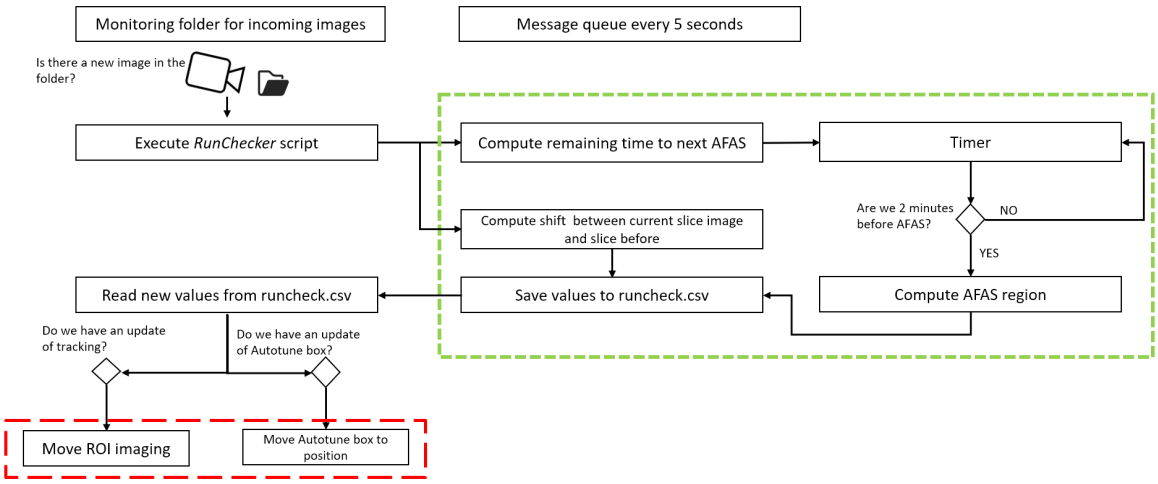

Fig. 3.12 Two threads are launched when an acquisition starts: one for messaging (a message queue that stores a new message every 5 seconds) and the other to monitor the folder where images are being stored. Checking is performed by an independent process called RunChecker which is executed in two main steps: first, analysis on current data is performed (green box), second, this information is stored in a file called runcheck.csv, which is read by the server and executed using the corresponding functions (red boxes which indicate calls to *FibicsVE* API).

The interface is the region between a thick layer of gold (or other metal coat to protect the sample) deposited on the surface of the sample and the cross-section face imaged. Usually the interface at the sample surface gives enough contrast and high frequency details to achieve good focus and stigmation values using the AFAS functions. However, progression by milling over the sample eventually will move the interface away from the box (Figure 3.12-A). The result can be catastrophic, leading to many out of focus images. For this reason, Algorithm 2 was applied to find regions where to focus and the Autotune Box is placed there just before a scheduled AFAS occurs (Figure 3.12-A).

Tracking

As described in literature (Jones et al. 2014), fiducial lines milled in layers with high contrast (also known as surface marks or fiducial marks) are used by *ATLAS* to track each section and continually move the FOV as milling progresses. In addition, the FOV can suddenly shift due to instabilities in the ion beam source, stage movements, thermal drifts in the room or errors in calibration. In Figure 3.13-B we illustrate the two possible outcomes of drifting (up or down).

Without the milled marks, another possibility is to rely on computer vision algorithms used for tracking. To our best knowledge and with the exception of cross-correlation (MacSleyne et al. 2009), no attempts at online (while the microscope works) tracking

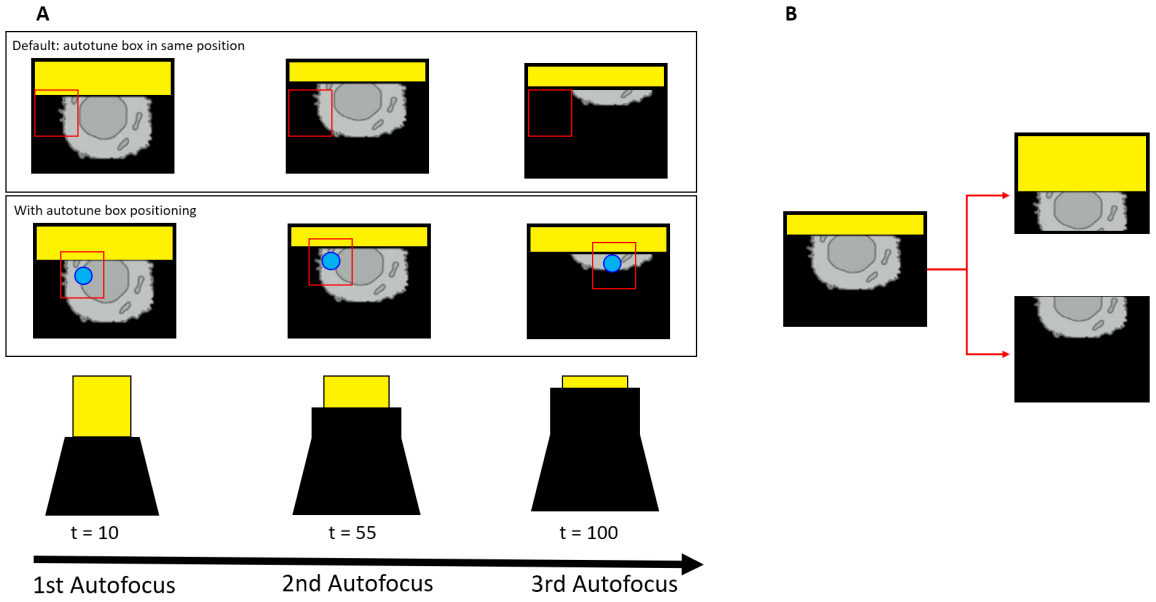

Fig. 3.13 Illustration of the two problems that require monitoring. In A, the black arrow at the bottom represents a temporal evolution of the acquisition in minutes. At different time points, an autofocus is executed. If the Autotune box is positioned always in the same position (**Default**), is very likely that at one point (e.g. at t=100), there will be an insufficient number of features to achieve good focus and stigmation. Thus, the box has to be relocated to optimal regions (**With Autotune box positioning**). In B, illustration of the two most often outcomes of stage drifting (up or down).

algorithms have been described in literature for FIB-SEM acquisition. The main reasons are that tracking marks allow the prediction and correction of slice thickness, and that tracking algorithms are too specific for certain types of data.

For this reason, sections are usually aligned a posteriori using specialized software. Let's consider the simplest way of assessing drift between two consecutive sections, by cross-correlation. In cross correlation, two signals are convolved in space to produce a third one where the highest value will point the region of maximum overlap. Cross-correlation works well when computing alignments between consecutive isotropic sections. However, when sections differ a lot from one to the next (slice thickness bigger than 10 nm), cross-correlation signal is likely to deliver poor accuracy. This image difference is avoided when there is a similar common feature in the images, for example, the milled fiducial lines that allow online tracking.

Another approach is based on features that can be abstracted to higher levels, like geometrical shapes, patches that remain almost the same between images. The first step is to locate these common features in both types of images. These features are then compared and associated with each other. When a certain degree of confidence is achieved, a transform can

be computed and used to find a relative shift between the images. This is used to generate alignments in TrakEM2 (Cardona et al. 2012) by computing SIFT features (Lowe 2004).

In my online tracking algorithm (Appendix 2, Algorithm 3), two main methods are followed. For sections bigger than 50 nm or when the acquisition is starting, the stop_point algorithm is used to keep the FOV at the center. The beginning of the acquisition is more unstable and tends to register bigger drifts until it stabilizes. The stop_point algorithm detects the boundary between the coated surface of the block and the cell profile at the cross-section. The boundary usually is the most prominent edge and can be found by the maximum gradient signal (maximum change from white to black). But if the coat is not present in the image, this condition doesn't hold anymore. In this case, we use the entropy of the upper part of the image. Entropy can be computed as:

$$H = -\sum_{k} p_k log_2(p_k) \tag{3.1}$$

Where p_k is the probability of a gray value pixel. The probability of this gray value can be obtained from the image histogram. Therefore, computing the entropy on the image rows can tell us if one row is occupied by cell (high entropy) or is totally uniform (coat or resin) (low entropy) (Figure 3.14). In case no cell would be present, the boundary would be the one calculated by the gradient.

For sections below 50 nm, ASIFT is used to keep track of the shift (Yu & Morel 2011). ASIFT is similar to SIFT except that it computes several affine transformations on the images to remove potential false positive features. The final algorithm, shown in pseudo code below as Tracking, has been tested with section thickness changing from 5 nm to 200 nm. After 50 nm thickness, there is usually not enough similarity between sections which can lead to potential miscalculations. Parameters beta and gap are used to control SIFT. A gap value of 0.5 is equivalent to specifying that if a shift bigger than 0.5 is computed by SIFT, it will be ignored. Beta is the parameter of a moving average used to control how much of the computed shift is added to the old one. Beta restrains the computed increment with respect to the previous section, which avoids abrupt changes or progressive increments.

In short, I have developed here an algorithm to detect and correct the drift in the y direction. This algorithm is based on detecting the region between the coat and sample (stop point), or with features from section to section (using ASIFT). Still, there are potential superior algorithms to be investigated. In them, sections could be considered as an object that is continuously moving over time, then authentic tracking algorithms can be applied, e.g. based on filtering (Chen 2003), like Kalman or particle filters, optical flow (Tao et al. 2012) or machine learning on features over sections (Feng et al. 2016).

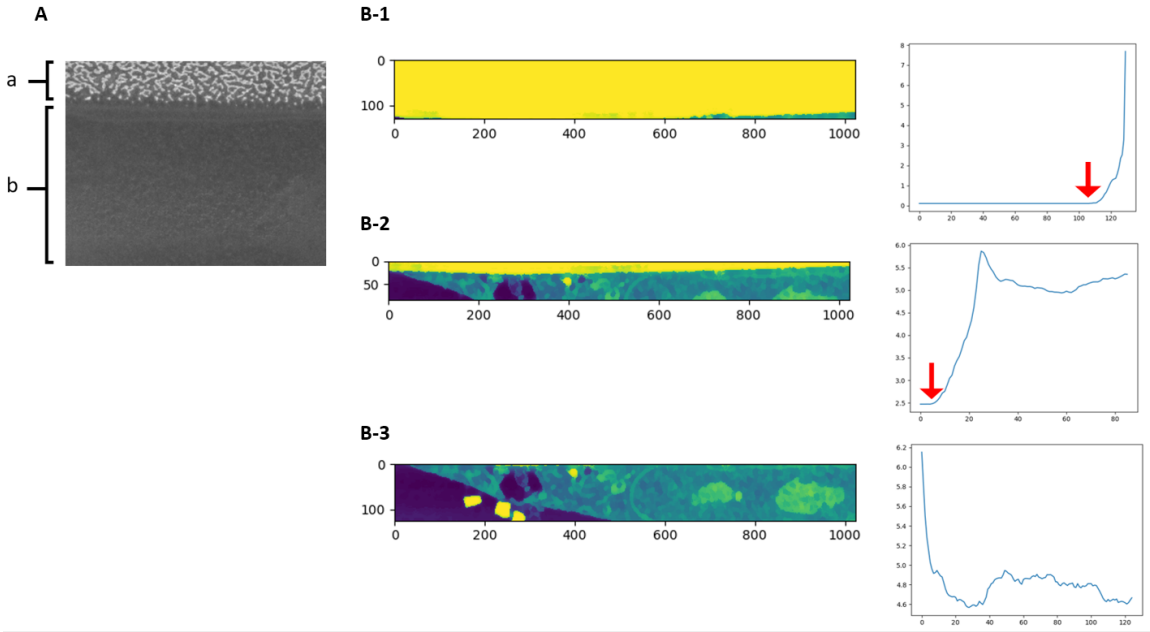

Fig. 3.14 A, a window of the FOV where the Autotune box is placed. The region covers a part of the so-called interface, usually covered by a thick layer of gold over the surface of 15 nm (A-a). In the algorithm (Appendix 2, algorithm 4) we define the stop point as the boundary line between A-a and -b. B, the plots represent the entropy calculated for each image of a cross-section. The stop point is when the entropy value starts to grow (red arrow). To find if there is cell present in the image and there is no coat, superior values of entropy indicate the presence of complex structures.

Cancel if imaging black regions

It is a waste of time and resources (gallium source) to keep acquiring images if the target cell has ended. If more than 80% of the target cell has been acquired, it is possible to detect if there is more remaining. Avoiding the last 20% is a gain in time when we are doing 50 targets. After detecting the stop point, if we add a safe margin, the resultant image should have a bilobed image histogram, one for grays belonging to the cell, and one for the background, ranging in values between 0-50 if the image is 8 bits. However, illumination changes, artifacts and noise can alter this variation. We used a strategy similar to the one used for the stop point detecting the entropy by rows, but this time, we also count how many points with high variation are present in the image. If less than 5 points and normalized entropy below 3, the image is considered black.

3.6 Potential problems during acquisition

In general, three type of technical problems can prevent a successful run:

Sample limitations. If the sample is physically in two separate parts or the quality of the imaging is insufficient due to inadequate sample preparation, the acquisition has to be stopped.

Software bugs. Software limitations can be solved by debugging or improving current algorithms. A bug is a mistake in coding where the logic of the software failed to produce expected results. For example, *CLEMSite* collapsed at one point during the acquisition when the routine for trench detection identified other objects in the image that where different from a trench. Software limitations can be solved once detected and are common in the life cycle of software. Their rate of failure is expected to drop down with more practical executions of the software. Alas, there is a risk when working in dependence with commercial software like *ATLAS 5*, because they are not free of bugs. Failures from commercial software are difficult to reproduce without the help of company software developers and their customized tools like logs and debuggers. If a bug is detected, one has to wait for the associated company to deliver a new version without the current bug, stopping the process of development.

Maintenance and electronic failures. If the microscope has to be stopped for maintenance (out of suppressor), the system has to be stopped without exception. In the FIB-SEM, common maintenance has to be done every two or three months for replacing the Gallium source and worn out apertures. Also, even if they do not happen often, electronic failures have to be taken into account.

Even so, the results were satisfactory for a prototype and the failure rate in future screenings is expected to be reduced at each iteration until only maintenance and electronic failures can pose a threat to the normal operation of the microscope.

One major reason that causes a run to be stopped is the FIB heating. The FIB column is continuously readjusting the ion source by using two voltages, the suppressor and the extractor. Usually the extractor is fixed, and the suppressor is regulated to guarantee a continuous flux of gallium ions. But this continuous pushing of voltage has a limit which has to be reset after a certain time, which is performed by heating the Gallium source. A common FIB gallium source requires reheat every 3 days.

Another potential interruption is the depletion of the gallium source, but usually they have a lifetime of 3000 hours which can thus be anticipated. In (Xu et al. 2017), in Janelia campus, they have engineered their own FIB-SEM to prevent interruptions by automatically stopping when fluctuations in the FIB milling rate are detected and then it will automatically re-heat if needed and resume the acquisition. This is done by a tailored combination of software and hardware modifications and unfortunately is not a commercially available solution yet.

Another potential source of improvement is in resuming failed acquisitions. This is possible by programming a similar pipeline like the one proposed in this chapter but able to resume in the same conditions after a problem has stopped the acquisition. In (Xu et al. 2017) they propose a continuous monitoring and changing of focus and astigmatism based on a focus metric proposed by (Binding et al. 2013).

Unfortunately, this technique cannot be applied during *ATLAS* slice & view because auto-focus and auto-stigmatism is internally triggered and it cannot be modified on the fly. I suggest the following scheme as a potential improvement. First, auto-focus and auto-stigmation have to be applied after a set period of time. When the next section is acquired, the following secondary metrics can be extracted from the image: Gaussian Derivative (GDER), Vollath's autocorrelation (VOLA), Gray Level Variance (GLVA) and Shifted Frequency (SFREQ). I tested these metrics against all the ones present in (Pertuz et al. 2012) and (Crete et al. 2008), and they show a good performance to detect changes in focus and stigmatism quality, with Vollath's autocorrelation (Vollath 1987) performing best (Figure 3.15). The initial focus can be used as reference, and if the secondary metrics detect that the image quality drifts below a certain threshold after AFAS, they can trigger another AFAS but with an extended range. In case of failure, the range can be changed and the AFAS repeated every 5 or 10 sections to avoid damage until both, primary and secondary metrics are satisfied.

One of the setbacks with EM imaging in the current workflow configuration is the absence of a protection pad. In a common workflow, a deposition step is required. A layer of platinum is deposited on the top of a region to protect the sample from continuous radiation exposure on the surface from imaging and milling. It also acts to provide stability to ion beam milling as well as being the location of the marks used for tracking the actual section thickness, as discussed before. In our experience, these marks can be omitted for biological samples. Biological samples in resin display enough variation to provide good features to apply AFAS. They also have enough hardness to provide beam stability and it is possible to use tracking algorithms to maintain the FOV. Moreover, doing a deposition of 1 µm of platinum adds around one hour per cell in the workflow (using a 35 by 35 µm region as reference) and necessitates accounting for displacements caused by insertion and removal of the nozzle and for material reservoir heating.

We decided, in a first approach, to replace the deposition layer using a very thick gold coat (150 nm thickness) on the full surface sample. Such deposition is performed in a dedicated sputterer, before loading the sample in the FIBSEM. Whilst this procedure is a very good solution to gain significant time over the acquisition of multiple cells, it is important to make sure that sections milled are spaced more than 50 nm, otherwise the gold coating can be sputtered away upon imaging (Figure 3.16). In addition to an aesthetically bad effect, it

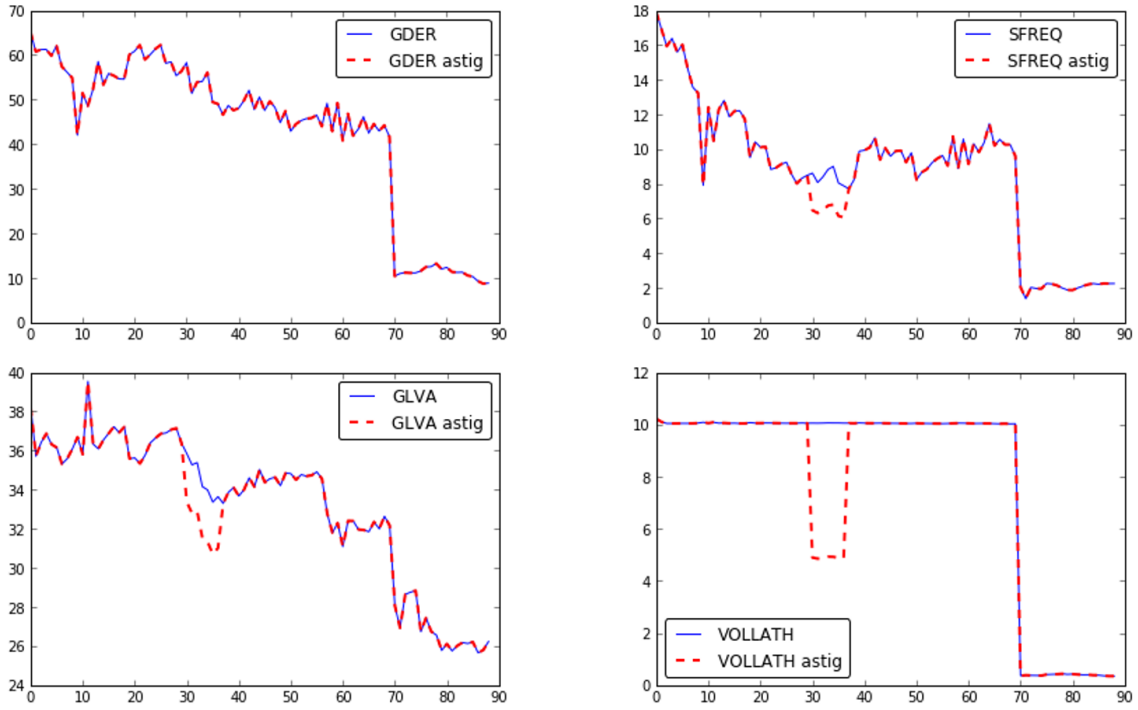

Fig. 3.15 Each plot shows the same metric over 90 sections. The original dataset is in good quality for focus. In dataset 1 (blue) the first 70 sections are in focus, from 70 to 90 an artificial gaussian blur has been applied. GDER, SFREQ and VOLLATH provide a consistent drop in quality. In dataset 2 (red), sections from 31 to 37 have been artificially astigmated. GLVA and VOLLATH, and with less measure SFREQ are sensitive to astigmatism changes.

compromises the quality of the tracking mechanism which is based on finding the interface between the coat and cell.

I suggest, that a thin deposition coat of 200 nm platinum on top the already existent gold coat would be enough to avoid this problem. Even if not tested thoroughly yet, here is a possible procedure to automate the precursor deposition. Such a process would be performed right after having set the coincidence point:

1. GIS conditions are checked by the system: pressure, levels of precursors (platinum, insulator) Outgassing has to be done automatically by a routine. FIB and SEM valves have to be closed for outgassing and reopened after.

2. If FIB and GIS conditions are satisfied, the system proceeds by inserting the nozzle.

3. At this point, it has been suggested by experimented operators that the coincidence point has to be calculated again due to a possible drift on the original position caused by an “antenna” effect from the nozzle. Further checks are needed to measure the actual effects of this drift in the final deposition respect the original position.

4. After an initial deposition, it has to be checked if the deposition is working (to be sure that it is not milling but is actually depositing) and if the right thickness is achieved. This can be performed taking images and measuring the thickness of the deposition coat by a computer vision algorithm.

5. Retract nozzle and restore conditions before deposition (coincidence point).

In order to allow automated deposition as described above, a specific API from the manufacturer for GIS management would be necessary.

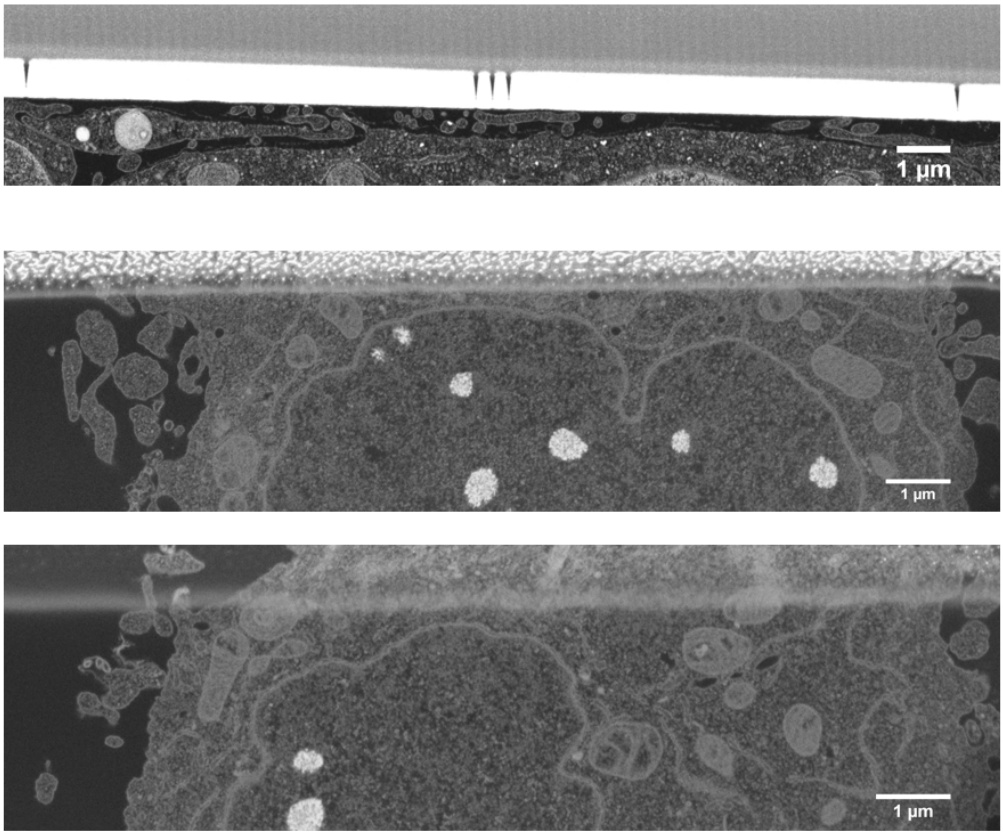

Fig. 3.16 A, typical deposition on top of a cell, with marks for tracking (left and right) and autotune (three spikes in the center). Thickness of deposition is close to 1 µm. B-C two sections from the same acquisition with a slice thickness of 50 nm. B, section number 30 and C, section number 50 where it can be seen the loss of gold coating.

Finally, failures regarding accuracy in targeting will be discussed in the next chapters. Other failures are beyond any possible improvement of *CLEMSite*. Samples can be broken

and scratched resulting in the loss of cell targets. Electronic problems with detectors or pumps, beam instability or crashes in *Zeiss* or *Fibics* software without apparent cause (non-reproducible bugs) are some of potential risks during a run. Luckily, hardware failures are not common, and if the microscope is well tuned and calibrated, long term acquisitions can be expected without interruption.

3.7 Conclusion

During this chapter, a software solution for automated acquisition of 3D volumes has been introduced. I have also pointed out some weaknesses (no deposition, tracking) and several potential amendments. The current system can work very well for one to two weeks uninterrupted and acquire volumes of multiple cells (up to 20 cells at the moment).

Acquisition time depends on multiple factors, but the most determining is the SEM imaging. SEM takes longer to acquire than a TEM image because of its scanning nature. In SEM, the detector receives a weak signal in the form of secondary or back scattered electrons from each point of the electron beam probe, this is translated into pixels that average over time, known as dwell time. To achieve a good signal to noise ratio (SNR) a higher dwell time is required, but as a consequence there will be a slower acquisition time. When imaging sections, such as in TEM or array tomography, contrast is enhanced by post-staining the sections with heavy metals, which increase dramatically the SNR and enable short dwell times. This is not possible for FIB-SEM (Wanner et al. 2015), as the block surface is sequentially exposed within the chamber of the SEM, with no possibility for post-staining.

The time taken to acquire a full cell volume will mostly dependent on the pixel size and the milling depth. Typically, when imaging adherent cells prepared by chemical fixation of high-pressure freezing / freeze substitution, the minimum pixel size that can be imaged is around 5 nanometers (yielding a good compromise between SNR and dwell time). With a milling depth of 200 nm, imaging a volume of 30x30x15 µm would take about 2.5 hours (1 minute per section). Changing to 100 nm slice thickness will take about 5 hours, 50 nm about 10 hours per cell, and finally, with 5 nm per section, the volume would take 4 days. This numbers can oscillate up and down depending on the FIB current and dwell time conditions.

Whilst isotropic acquisition is a powerful tool to describe in details the complexity of the sub-cellular architecture (cytoskeleton, membrane contact sites, fine organelle reticulations etc) thick sections can also be used for screening. Many phenomena at the cellular level can be visualized this way, the bonus here being that one can then increase the numbers of cells and therefore access to information about the cell population as opposed to the individual. For pixel sizes of 5 to 8 nm in x/y, the milling thickness would depend on the structure of

interest and the question at hand. For example, counting contact sites between mitochondria and ER, given the relative size of both organelles, the size of a contact site (around 15 nm) and their density across the cell volume, would require sections of 10 nm to be efficiently probed. In comparison, simply counting mitochondria or vacuoles in Hela cells can be done with 100 nm slice thickness.

To examine exceptional organelles like centrioles, if the rest of the cell is of no interest, the total volume of the cell can be reduced to focus only on the volume of interest. Other strategies are possible, as it will be shown in chapter 5, like using a bigger thickness to apply stereological measurements (Ferguson et al. 2017).

Currently, there is no solution for long acquisition times except to wait for more research on FIB-SEM technology. So far, FIB-SEM is mostly used for particular applications that do not require more than a few hours of manual operation to analyze a cross-section of a material. Long acquisitions are more specific to the field of biology. I hope this project or similar ones trigger enough interest from the community and the enthusiasm could eventually reach to companies and FIB-SEM engineers to develop more stable instruments with faster and durable ion sources.

3.8 Acknowledgments and contributions

Yannick Schwab[1], my supervisor, was the main promoter of the project. He negotiated a collaboration with *Carl Zeiss GmbH* and he was actively involved discussing each step of the project. Robert Kirmse[2] was the link with *Carl Zeiss GmbH* and he also participated in many of the project discussions. Nicole L. Schieber[1] and Anna M.Steyer[1] were active members of the project and thanks to their expertise using the FIB-SEM it was possible to take valuable advices for the software development.

Mike Holtstrom[3] was the main contact at *Fibics Inc.* He was actively answering any question regarding *ATLAS Engine* and debugging the API when a problem appeared. Alexandre Laguerre[3], Ken Lagarec[3] and David Unrau[3] participated in many discussions and assisted in many technical problems from the software and the instrument. José Miguel Serra Lleti[1] fully designed, developed and tested the CLEMSite software and tested the functions from the *FibicsVE* API.

Affiliations

(1) Cell Biology and Biophysics Unit, European Molecular Biology Laboratory, 69117 Heidelberg, Germany

(2) Carl Zeiss Microscopy GmbH, Germany.

(3) Fibics Inc., Ottawa, Canada.

References

Achanta, R., Shaji, A., Smith, K., Lucchi, A., Fua, P. and Süsstrunk, S. (2010) 'SLIC Superpixels', *EPFL Technical Report 149300*.

Binding, J., Mikula, S. and Denk, W. (2013) 'Low-Dosage Maximum-A-Posteriori Focusing and Stigmation', *Microscopy and Microanalysis*, 19(01), pp. 38–55. doi: 10.1017/S1431927612013852.

Bravo-Zanoguera, M., v. Massenbach, B., Kellner, A. L. and Price, J. H. (1998) 'High-performance autofocus circuit for biological microscopy', *Review of Scientific Instruments*, 69(11), pp. 3966–3977. doi: 10.1063/1.1149207.

Cardona, A., Saalfeld, S., Schindelin, J., Arganda-Carreras, I., Preibisch, S., Longair, M., Tomancak, P., Hartenstein, V. and Douglas, R. J. (2012) 'TrakEM2 Software for Neural Circuit Reconstruction', *PLoS ONE*. Edited by A. Samuel. Public Library of Science, 7(6), p. e38011. doi: 10.1371/journal.pone.0038011.

Chen, Z. (2003) 'Bayesian Filtering: From Kalman Filters to Particle Filters, and Beyond'.

Crete, F., Dolmiere, T., Ladret, P. and Nicolas, M. (2008) 'The Blur Effect: Perception and Estimation with a New No-Reference Perceptual Blur Metric', *SPIE Electronic Imaging Symposium Conf Human Vision and Electronic Imaging*.

Cui, L., Marturi, N., Marchand, E., Dembélé, S. and Piat, N. (2015) 'Closed-Loop Autofocus Scheme for Scanning Electron Mi- croscope', *Int. Symp. of Optomechatronics Technology*, ISOT 2015.

Feng, X., Mei, W. and Hu, D. (2016) 'A Review of Visual Tracking with Deep Learning'.

Ferguson, S., Steyer, A. M., Mayhew, T. M., Schwab, Y. and Lucocq, J. M. (2017) 'Quantifying Golgi structure using EM: combining volume-SEM and stereology for higher throughput', *Histochemistry and Cell Biology*, 147(6), pp. 653–669. doi: 10.1007/s00418-017-1564-6.

Harada, M., Obara, K. and Nakamae, K. (2017) 'A robust SEM auto-focus algorithm using multiple band-pass filters', *Measurement Science and Technology*, 28(1), p. 015403. doi: 10.1088/1361-6501/28/1/015403.

Harris, C. and Stephens, M. (1988) 'A COMBINED CORNER AND EDGE DETECTOR', *Alvey Vision Conference*. doi: 10.5244/C.2.23.

Jones, H. G., Mingard, K. P. and Cox, D. C. (2014) 'Investigation of slice thickness and shape milled by a focused ion beam for three-dimensional reconstruction of microstructures', *Ultramicroscopy*, 139, pp. 20–28. doi: 10.1016/j.ultramic.2014.01.003.

Lowe, D. G. (2004) 'Distinctive Image Features from Scale-Invariant Keypoints', *International Journal of Computer Vision*.

MacSleyne, J., Uchic, M. D., Simmons, J. P. and De Graef, M. (2009) 'Three-dimensional analysis of secondary gamma precipitates in Rene-88 DT and UMF-20 superalloys', *Acta Materialia*, 57(20), pp. 6251–6267. doi: 10.1016/j.actamat.2009.08.053.

Otsu, N. (1979) 'A Threshold Selection Method from Gray-Level Histograms', *IEEE Transactions on Systems, Man, and Cybernetics*, 9(1), pp. 62–66. doi: 10.1109/TSMC.1979.4310076.

Pedregosa, F., Varoquaux, G., Gramfort, A., Michel, V., Thirion, B., Grisel, O., Blondel, M., Prettenhofer, P., Weiss, R., Dubourg, V., Vanderplas, J., Passos, A., Cournapeau, D., Brucher, M., Perrot, M. and Duchesnay, É. (2011) 'Scikit-learn: Machine Learning in Python', *Journal of Machine Learning Research*, 12(Oct), pp. 2825–2830.

Pertuz, S., Puig, D. and Garcia, M. A. (2012) 'Analysis of focus measure operators for shape - from - focus'. doi: 10.1016/j.patcog.2012.11.011.

Rudnaya, M. E., Mattheij, R. M. M. and Maubach, J. M. L. (2010) 'Evaluating sharpness functions for automated scanning electron microscopy', *Journal of Microscopy.* Wiley/Blackwell (10.1111), 240(1), pp. 38–49. doi: 10.1111/j.1365-2818.2010.03383.x.

Shen, F., Hodgson, L. and Hahn, K. (2006) 'Digital Autofocus Methods for Automated Microscopy', in, pp. 620–632. doi: 10.1016/S0076-6879(06)14032-X.

Tao, M., Bai, J., Kohli, P. and Paris, S. (2012) 'SimpleFlow: A Non-iterative, Sublinear Optical Flow Algorithm', 31(2).

Vollath, D. (1987) 'Automatic focusing by correlative methods', *Journal of Microscopy.* Wiley/Blackwell (10.1111), 147(3), pp. 279–288. doi: 10.1111/j.1365-2818.1987.tb02839.x.

Wanner, A. A., Kirschmann, M. A. and Genoud, C. (2015) 'Challenges of microtome-based serial blockface scanning electron microscopy in neuroscience', *Journal of Microscopy*, 259(2), pp. 137–142. doi: 10.1111/jmi.12244.

Xu, C. S., Hayworth, K. J., Lu, Z., Grob, P., Hassan, A. M., García-Cerdán, J. G., Niyogi, K. K., Nogales, E., Weinberg, R. J. and Hess, H. F. (2017) 'Enhanced FIB-SEM systems for large-volume 3D imaging.', *eLife*. eLife Sciences Publications, Ltd, 6. doi: 10.7554/eLife.25916.

Yu, G. and Morel, J.-M. (2011) 'ASIFT: An Algorithm for Fully Affine Invariant Comparison', *Image Processing On Line*, 1, pp. 11–38. doi: 10.5201/ipol.2011.my-asift.

Zhang, Z., Liu, Y., Xiong, Z., Li, J. and Zhang, M. (2018) 'Focus and Blurriness Measure Using Reorganized DCT Coefficients for an Autofocus Application', *IEEE Transactions on Circuits and Systems for Video Technology*, 28(1), pp. 15–30. doi: 10.1109/TCSVT.2016.2602308.

4

Automated CLEM as a screening tool using the Golgi apparatus as example (I:LM)

4.1 Introduction

The Golgi apparatus (GA) and the discovery of its functions has an intimate history with Electron Microscopy (EM). First noticed by Camillo Golgi in 1898, was not acknowledged as de facto organelle until the period between 1954-1963 (Farquhar & Palade 1981). The electron microscope revealed an intricate structure formed by smooth cisternae (flattened membranes, stretched at the center and with dilated rims), tubules and vesicles, for which the term Golgi 'complex' was coined. The GA is a polarized organelle: it receives vesicles coming from the ER at its *cis* side and produces secretory cargo directed to the plasma membrane or other intracellular organelles at the *trans* side. Despite these key features, depending on the cell type and organism, morphology and cytoplasmic disposition can change dramatically (Rios & Bornens 2003).

Under the heavy scrutiny of electron microscopists, the Golgi was found to be associated with coated vesicles, lysosomes, centrosomes and microtubules, which later proved to entail functional relationships critical for intracellular membrane trafficking and mitosis. Golgi stacks contain between four to eight cisternae and can be found in most cell types in perinuclear regions. The MTOC (MicroTubule Organizing Center) links multiple Golgi cisternae and help to distribute vesicles and connect tubules all over the cell (Chabin-Brion et al. 2001). Organelles around the Golgi (like ribosomes, mitochondria and ER) are kept out from the stacks region in an exclusion zone formed by a dense cytoplasm region. This region

was found to be formed by a combination of microtubule cytoskeleton and Golgi matrix proteins (like golgins) that are organized close to the centriole (Sütterlin & Colanzi 2010).

In the years following its ultrastructural description, cytochemistry techniques started to unveil the importance of the GA as a chemical factory. It is well established that proteins coming from the ER undergo PTMs (post-translational modifications) like glycosylation and then then they are wrapped for secretion (Palade 1975). The Golgi apparatus is also involved in lysosome formation, membrane biogenesis and recycling (Klumperman 2011). As the main center for secretion and chemical factory it has been shown to be a very dynamic organelle. For example, under mitosis, it experiences massive structural changes (Zaal et al. 1999; Altan-Bonnet et al. 2003; Lucocq et al. 1989). Mitotic protein kinases phosphorylate the Golgi matrix proteins, which cause unstacking and vesiculation. Vesicles diffuse in the cytoplasm, some proteins are absorbed by the ER and others are involved in spindle formation or even mitosis (Yadav et al. 2009; Ayala & Colanzi 2017). After cytokinesis, cisternae stack up and become linked to the MTOC again and the GA ribbon reassembles in early interphase.

It is known that altering mitotic regulators can affect GA structure and present different phenotypes. For instance, siRNA knockdown of kinase VRK1 led to a fragmented phenotype (López-Sánchez et al. 2009) or overexpression of Aurora A displayed a condensed, tightly packed GA during interphase (Kimura et al. 2018). Nonetheless, the relationship between GA phenotypic structure and function is not limited to the cell cycle. Changes in GA structure had been also observed under diseased cells (Huang & Wang 2017), like AML (amyotrophic lateral syndrome) or Alzheimer disease, displaying a fragmented GA or incomplete stacks under the microscope (Fujita & Okamoto 2005; Joshi et al. 2014).

The understanding of Golgi dynamics guided some laboratories on the search of possible master regulators via siRNA screenings (Farhan et al. 2010; Gordon et al. 2010; Simpson et al. 2012). In (Simpson et al. 2012) connections with pathways far from the well-known intracellular trafficking were explored. They showed that knockdown (KD) of some non-trafficking related genes resulted in morphological changes of the GA. Immunolabeling of GM130[1] displayed different morphologies for each gene KD: diffuse, condensed, fragmented, disorganized and dispersed.

Although light microscopy images provided a substantial source of information about the phenotypes, EM could complement the information of the screening as follows:

[1] GM130 is a golgin involved in maintaining structure, capturing and tethering of vesicles. Additionally COPI subunit COPB2 and COPII subunit SEC13(vesicular coat protein complex COPI and COPII) were imnunolabeled and imaged.

1. Some protein knockdowns could affect the Golgi ribbon structure, fragmenting it into multiple stacks dispersed around the cell, but keeping trafficking intact. By EM should be possible to count the number of stacks.

2. The number of vesicles around the GA can be counted, which, if different from controls, could identify a key regulator in vesicle budding.

3. The number and length of cisternae, if different from controls, could reveal the involvement of one gene in protein maturation or vesicle budding. It would be interesting to search for correlations between the number of vesicles and tubes in one side and some morphological variations of cisternae on the other side. (e.g. more vesicles but a less average length of cisternae).

4. Ministacks are usually connected by microtubules (centrosomal or by non-centrosomal microtubules (Nishita et al. 2017)). Changes in morphology could indicate an effect on the cytoskeleton network, which could be observed by EM potentially revealing changes in the amount and distribution of microtubules within the Golgi network or variations in the position of the centrosome in the cell relative to the GA.

5. Some phenotypes could display where a certain degree of unstacking in cisternae. This separation between cisternae could involve a direct effect on Golgi membrane proteins, like has been previously shown for GRASPs (Wang et al. 2008; Zhang & Wang 2016).

6. Other unexpected effects in GA morphology, like swelling of cisternae or appearance of interconnections between cisternae, conditions only observed so far under hyperstimulation of secretory cells (Marsh et al. 2004).

7. Relationships with other organelles, like ER, lysosomal production and mitochondria, and if they are interfering with the exclusion zone, indicating a GA structural defect.

   In this chapter, EM combined with fluorescence microscopy (CLEM) is proposed as a tool to first screen heterogeneous populations with light microscopy (LM), and then, direct the resolutive power of EM to a sub-population of interest. An array of solid phase transfection (Erfle et al. 2008) was arranged inside a glass bottom dish. Gelatin spots containing siRNA were seeded in the dishes and then Hela cells expressing GalNAc-T2-GFP (a transferase found in the GA membranes) cultured on top. Thus, a localized transfection was achieved in a region of 500 μm^2. Thus, a selection of 14 genes from the ones presented in (Simpson et al. 2012), plus two positive controls and one negative control could be fitted for screening at the EM level. With the cells

imaged by light microscopy, we present a workflow where it is possible to acquire multiple EM volumes of the phenotypes.

With this method, questions 1, 2 and 3 of the proposed list could be answered quantitatively by stereology (Ferguson et al. 2017). Questions 4, 5, 6 and 7 can be assessed qualitatively, and if that is the case additional experiments or secondary screenings can be scheduled. For example, in question 4, changes in the cytoskeleton distribution could be observed by electron tomography.

This chapter presents the light microscopy (LM) part of the CLEM workflow, divided in two parts. The first part consists of imaging by feedback microscopy, analysis of fluorescence images for feature extraction and the final selection of the cells of interest based on their individual phenotypes. In the second part, I explain the software that I developed to detect the patterns of the gridded coverslip from light microscopy images. Such landmarks are essential for our correlation strategy, as they link both LM and EM. With these experiments, an efficient process of phenotype finding and selection has been achieved.

4.2 Materials and methods

Cell culture

HeLa Kyoto cells stably expressing GalNAc-T2-GFP were cultured using DMEM (Dulbeccos Modified Eagles Medium Sigma Aldrich) with 10% fetal calf serum, 1% streptomycin and penicillin, and 1% L-Glutamine , incubated at 37°C at 5% CO2. Cell selection was applied using 100 µl of geneticin at every passage (G-418 sulfate, Gibco Life Technologies). Cells were seeded in MatTek dishes (P35G-2-14-C-GRID) at 70.000 cells/ml per dish.

siRNA selection and transfection

Solid-transfection array in glass bottom dishes.

From an initial genome-wide screen for proteins affecting the secretroy pathway (Simpson et al., 2012), 143 siRNAs were identified as affecting the morphology of the COP coated vesicles and/or the morphology of the Golgi apparatus. From them, my colleague Anna Steyer selected 79 of the strongest phenotypes from the original

study. Since the cell line was fluorescent for GalNAc-T2 and not for GM130 or beta COPs as in the original paper, liquid transfection of the 79 candidates had to be repeated in 96 well plates. Each siRNA treatment was imaged for GalNAc-T2-GFP cells. Information about selected siRNA, like ID and manufacturers can be found in the published supplementary data of (Simpson et al., 2012).

Light microscopy images of candidates were acquired at 20x (DAPI nucleus, GalNAc-T2-GFP). Christian Tischer developed a CellProfiler pipeline (Jones et al., 2008), in which he defined different morphologies as quantifiable features as follows (Figure 4.1-A):

Diffuse : fluorescence is sparse over the cell cytoplasm, showing a visible difference in intensity over the background. It can be quantified as the relative intensity of the cytoplasm (segmented GFP signal of cell body) respect to the background.

Fragmented: the Golgi apparatus is split in many pieces of variable size, with the biggest pieces being much smaller than a typical Golgi shape that would be observed in the negative control. In Simpson et al., fragmentation is divided into mild and severe. Here, both categories are merged. Fragmentation can be calculated by counting the number of separated components using a top hat morphological transform and Otsu thresholding (Otsu, 1979).

Tubular: scribed as "enlarged" in Simpson et al., the Golgi apparatus have elongated cisternae running along the cytoplasm. Elongation can be calculated by applying directional line filters on the segmented cell. The difference between orientations that yielded maximum and minimum results of the filter where saved for each pixel. After this, the total value of elongation was computed as the sum of all values divided by the sum of the GFP intensity value for each cell.

Condensed: the Golgi is condensed in a smaller area, looking almost circular at the fluorescent microscope. Condensation was measured by the form factor, which can be calculated using the formula $\frac{4\pi area}{perimeter}$. When the shape is a perfect circle, the maximum of value 1 is achieved.

Candidates selection was based on morphology. A phenotype was considered as strong if a standard deviation from the negative control was bigger than three (Figure 4.1-B). Appendix A Table 1, shows the total of 14 genes selected, in addition to 3 positive controls and 1 negative control.

After gene selection, and in favor of EM where there are further restrictions to sample size, solid phase transfection was adapted from (Simpson et al., 2007) to a small glass

bottom MatTek dishes (0.8 cm^2) with a coordinate pattern . Dishes were with 16 different treatments distributed over 32 spots (using 2 biological replicates per gene and control) and cells were seeded 72 hours before imaging. The observed transfection efficiency oscillates between 30 to 60% within the spots.

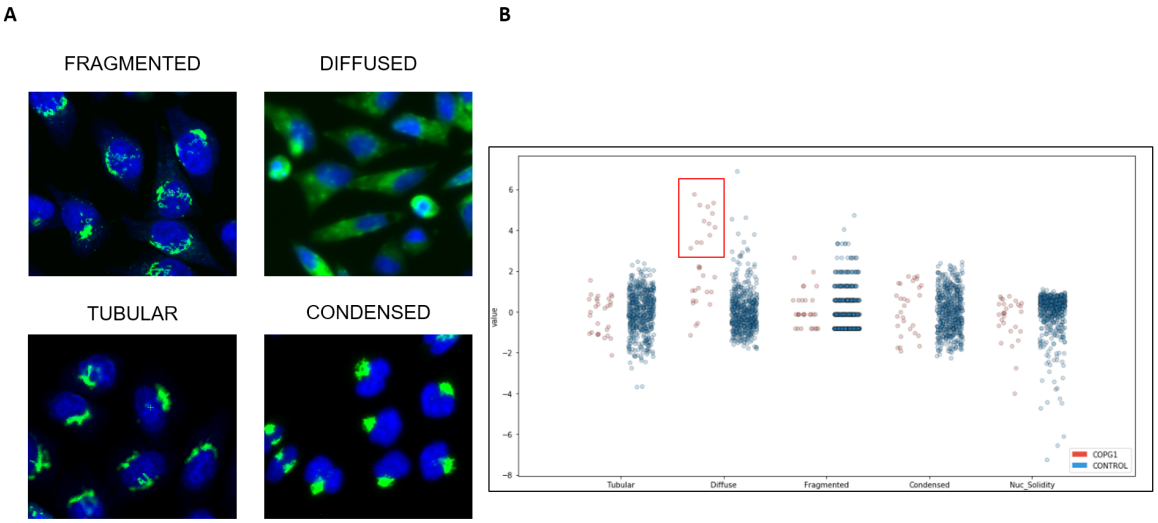

Fig. 4.1 A. Cells showing the different morphologies used to classify phenotypes. Images from liquid transfection of DNM1 for fragmented, COPB2 for diffuse, IPO8 for tubular and ACTR3 for condensed, GFP for GalNAc-T2-GFP , and DAPI in the blue channel. B. In the Y axis, feature values normalized against negative control, each column of the X axis represents a feature that describes phenotype. In this case, gene COPG1 feature values in red are plotted against negative control in blue. The red square shows a region with high diffusivity in a subpopulation (red square).

Light fixation of cells.

72 hours post-transfection, cells were fixed with a mixture of 4% formaldehyde from a stock of 16% in H20 and 0.5% glutaraldehyde from a stock of 25% in H2O (both from Sigma-Aldrich) in 0.1M PHEM Buffer (240 mM PIPES, 100 mM HEPES, 8 mM MgCl2, 40 mM EGTA in H2O, pH 6.9). A Ted Pella BioWave microwave was used to accelerate the process to 15 minutes. DAPI was applied to cells in a proportion 1:1000 from a stock solution of 1 mg/ml (in 0.1M PHEM) to stain the nucleus for a total of 10 minutes. To quench glutaraldehyde auto-fluorescence, cells were rinsed with 150 nM glycine in PHEM buffer. Cells are left in PHEM buffer for imaging.

4.3 Feedback microscopy.

Prior to imaging, cultured Hela cells expressing GalNAc-T2-GFP were transfected in glass bottom dishes and fixed (see *Materials and methods*). Cells were mounted in a Leica SP5 confocal microscope (Leica Mikrosysteme Vertrieb GmbH) in which previously two collections of imaging routines were set up. We named the first *prescan* imaging or acquisition. It consists of a collection of cell images from the dish, stored for further analysis. After the prescan is finished, cells are screened and individually selected. Each analyzed cell keeps its original stage coordinates, which are used to trigger a second job on them, which We named this collection of imaging routines *High resolution*, consisting of a confocal stack from the GFP channel and contextual images used for correlation. The following subsections describe this part with detail.

Prescan imaging.

Independently of the microscope used for this task, a program has to determine an array of positions for sampling. For each position, images were collected with a 10x objective at a zoom factor of 5 (FOV 258 by 258 μm) with two channels, DAPI for nuclear staining (excitation light of 405 nm) and GFP for the Golgi apparatus (excitation light of 488 nm). These imaging conditions were chosen to speed up the process of image acquisition and provide enough quality to differentiate the morphology of the Golgi apparatus. The conditions would change depending on the selected organelle and the objectives available on the microscope.

To define the array of positions, a software script was developed by Volker Hilsenstein. The user must click on four corners of the glass dish forming a rectangle and a submatrix of 32 positions is automatically generated. For each position, two side by side frames are acquired. The script generates a file with stage coordinates of the 32 spots that can be fed into the microscope software. Then, each position will be imaged with the conditions described above, taking a total of 4 images per spot.

Software for cell selection after prescan

Independently of the software application, a typical processing pipeline can be divided into five conceptual steps:

Image and metadata extraction. By using regular expressions and reading image headers, information about the experiment and its structure can be extracted. Particularly useful are bio-formats, a set of libraries for metadata extraction.

Pre-processing and segmentation. Most pipelines require noise cleaning by filtering, background subtraction and illumination correction. After this step, images are segmented for each channel independently.

Feature extraction. Features are extracted from the segmented regions. Features can be numerical (counts), geometrical (shape), descriptive (texture) or contextual (number of neighbors).

Quality control and data exploration. Before classification, it is important to remove possible artefacts or undesired effects like dividing cells or cells too dim to be properly classified. Along the same lines, it is useful to explore the results by analyzing the quality of the controls and by extracting basic statistics of features to find outliers.

Classification. Phenotypes are classified and ranked, this is generally based on applying machine learning on features.

These five steps are modified and adapted depending on the application. In deep learning frameworks, for example, segmentation, feature extraction and classification are done simultaneously by a trained network. In the presented pipeline, *CellProfiler* (v. 2.2) is used for the first three steps. The same *CellProfiler* project created for liquid transfection in 96 dwell-plates was applied for prescan images. This *CellProfiler* pipeline was prepared by Christian Tischer and extracts features from both Golgi, in GFP, green channel and for nuclei in DAPI, blue channel. Cell position in the images is determined by nucleus segmentation, thus, the center of gravity of the nucleus defines the center of each cell. Additionally, each nucleus is associated with its corresponding Golgi by proximity. Features are extracted as explained in the siRNA selection.

Christian Tischer also developed the initial quality control by using HTM explorer (R package software). *HTM explorer* had excellent capabilities for quality control, but continuous changes in the workflow proved difficult to adapt (e.g. changing cell selection criteria), so I decided to migrate the selection process to a *Jupyter Notebook* (Kluiver et al. 2016).

A *Jupyter Notebook* is a web application with code execution capabilities. It is divided in small cells , where Python functions can be called and executed on a cell by cell basis. Results are stored in memory and can be displayed as plots or explored. The

linear conception fits perfectly with the step by step analysis performed during quality control and data exploration. Additionally, comments and pictures can be added to document each step.

The *CellProfiler* software extracts the information in form of comma separated values. The main packages used together with the *Jupyter* environment are *Pandas* and *Bokeh*. Pandas is able to read data files and format them in tables. Tables are inclined to being queried by column and data is easily extracted for plotting. *Bokeh* allows insertion of *Javascript* commands inside *Jupyter Notebooks*, which results in interactive plots. The following subsections describe each one of the pipeline execution steps for quality control and cell selection.

Step 1 Quality control. Each cell in the image goes through the following procedure for quality control (QC). Values for each QC have to be decided by looking at the images of the experiment (Figure 4.3 A and B):

PowerLogLogSlope of DNA Removing cells out of focus. Based on metrics from (Bray et al., 2012), this feature is present on CellProfiler to remove potentially out of focus cells[2]. The common reference value is -2.2, oscillating between -2.5 and -2.0. Cells with values below the selected value are removed.

Mean Nuclei Coefficient of Variation Coefficient of variation of nuclear intensity. Mitotic cells possess higher values due to chromosome condensation. Typical values range from 0.3 to 0.5. Values higher than the selected value are removed.

Integrated Intensity of Golgi background Images which have correlation values close to the background are too dim and have to be removed. A typical value range is from 10 to 50. Anything smaller than the selected value is removed.

After the quality control filter, usually 20 % of cells are rejected and typically between 2000 and 3000 cells remain.

Step 2 :Positive control check. Images of positive controls are shown for qualitative assessment, and the experiment is continued if the three positive controls show visible effects. For the current set of experiments, AURKB, KIF11 and COPB1 were checked to assess siRNA transfection.

Step 3: Feature normalization and data exploration. For each gene, all values are normalized via z-score (each value minus the mean divided by standard deviation) using the mean and standard deviation of all experiments. This is done for each

[2]http://cellprofiler.org/manuals/current/MeasureImageQuality.html

feature individually (Tubular, Fragmented, Diffuse and Condensed, and with Nuclear Solidity). Mean and standard error of the mean respect to the negative control are calculated for each individual gene and plotted (Figure 4.1-B). These plots can be used to check differences against the negative control of each feature. For example, COPB1 should show a sub-population with high values in diffusion. Nuclear solidity is another measure that calculates the area divided by the convex area. A solid nucleus has a value close to 1, then, values close to 0 are cells that are in the process of apoptosis or cell division. Features can be used for quality control on individual treatments.

Step 4: Cell selection. The selection of cells is integrated after the quality control in a series of interactive plots that allow cells to be selected individually. When the phenotype can be distinguished by one of the main features (e.g. COPB1 by diffusion), cells can be selected inside a jittering plot based on its feature value (Figure 4.3-C). However, some phenotypes can manifest synergy in the feature space, for example those that show fragmented and tubular in combination. By plotting individual features, this synergy is lost and the real phenotype subpopulation is missed. For this reason, t-SNE (van der Maaten, 2013) can be used to cluster populations naturally (Figure 4.3-D).

After the fine selection all subpopulations for each gene are shown and 42 cells are picked (3 per treatment, the 2 positive controls are excluded) for CLEM (Figure 4.3-D). The selected stage coordinates of the cell are saved and given as input to microscope for high resolution imaging.

High resolution imaging

Since stage coordinates were stored for each of the cells selected in the previous step, they can be sequentially re-acquired. This will permit to obtain, first a high resolution confocal stack and second a cell-centered set of images used to provide context with CLEM. The following collecting pattern was executed for each cell: (1) 40x air objective high resolution confocal stack of Golgi (9 slices, 10.1 µm range), at FOV of 77.5 µm by 77.5 µm, (2) contextual information was given by 10x air objective following a sequence of fluorescent channels 405 nm for DAPI, 488 nm for GFP, 594 nm for Alexa 594 of siRNA spots, transmitted light and reflected light (Figure 4.3-A), all images with a resolution of 1024x1024 pixel, FOV 1.29 mm x 1.29 mm. Reflected light images are 80% transmitted light and 20% laser reflection. This setting, defined for the microscope Leica SP5, but also possible for any confocal microscope, enables clear visualization of the coordinate patterned on the coverslip with at least

one full square fitting within a single FOV, which will be important for the automatic recognition in later steps. In addition, overlaying the RFP signal of the siRNA gelatin spot with the GFP channel of cells at low magnification (10x), can be used as an extra quality control to check if the cell selected is inside the spot.

Communication of stage coordinates and commands to start the High resolution jobs with the microscope (Leica Matrix Screener software) were implemented in python by Volker Hilsenstein (Tischer et al., 2014).

4.4 Correlation strategy (LM)

In the next step, the *CLEMSite LM Map builder* application reads the folder with the corresponding images. In the High resolution job, contextual images are saved with a low magnification objective (10x), which can be different from the objective used for prescan (e.g. 20x). In that case, the mechanical movement between the two objectives can cause a translational shift between images. Then, even if the stage coordinates stored as metadata are the same for both objectives, one of the images is shifted a few micrometers respect to the other. To prevent this problem, images from Prescan (20x) have to be registered to 10x by adding a translational shift. Translation shifts can be computed by cross correlation with subpixel accuracy. Thus, prescan images (20x) are scaled down to match the resolution of the 10x magnification images. With this, the organelle position in the prescan is now shifted to be accurate respect to the center of the 10x image.

A landmark is a distinguishing or prominent object that can serve as reference or a guide. Landmarks, in our application are extracted from reflected light images. In MatTek glass bottom dishes, the glass is patterned with a lattice grid formed by a repetitive sequence of 20 µm thick lines every 600 µm. The grid is formed by squares, each square containing a unique pattern of one letter and one number. Each corner of each square in the grid can be considered a landmark because, given the unique patter inside the square, is very straight to identify its position at the LM level with reflected light (Figure 4.5-B) and in SEM at the surface level with SE detectors. For convenience, square corners will be called crossings. Crossings can be identified with a line detection algorithm robust enough to not have a parameter dependency for each image, which I called LOD (Line Orientation Detector). Detected crossings are saved in pixel coordinates from the image. Since the stage coordinates of the optical microscope – saved in the metadata of the image – are known to match the center of

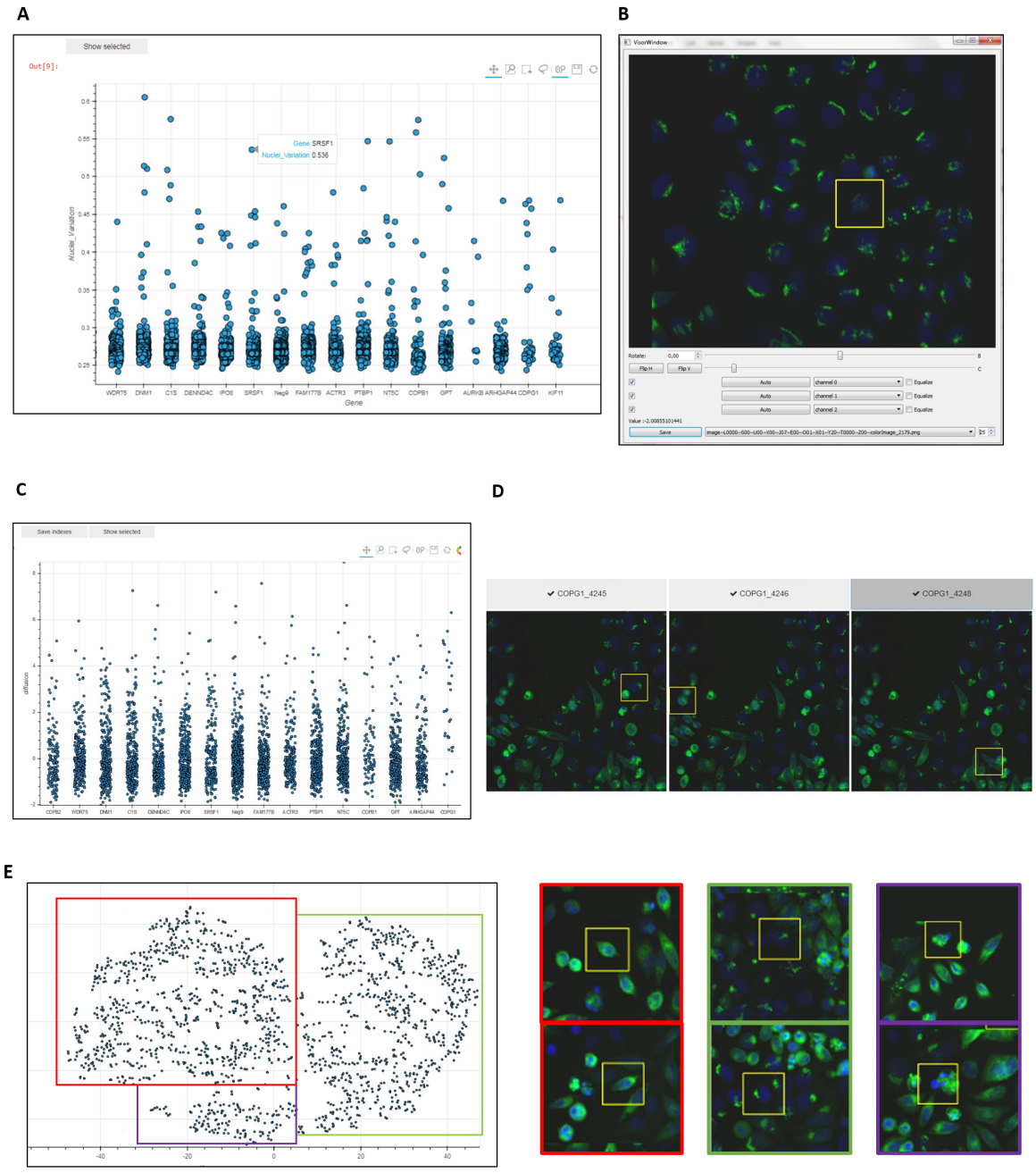

Fig. 4.2 **Interactive plots for quality control and cell selection.A.** A jitter plot shows each treatment on the x axis and its value in the y axis. The y axis depends on the quality control, in this case, coefficient of variation is shown. Each point is the value for one cell. **B.** If selected, a cell can be shown with detail in the viewer. The viewer has different options such as zoom in, brightness and contrast and transformation controls. It can show multiple cells simultaneously, if selected in group. **C.** In the same way, feature values can be plotted to select cells individually. In this case, the value of diffusion is plotted in the y axis. **D.** From the selected indexes, cells are shown to the user for quick selection of which cells will be acquired in high resolution and in EM. **E.** t-SNE plot using the four features referred in materials and methods. Perplexity value is usually 50. Each small cluster of the image shows cells grouped by similarity on features. With t-SNE, similar cells are close in space and form small clusters. For example, group 1 (red, left square in cluster plot) shows elongated cells with a diffuse Golgi apparatus, group 2 (green, right square in cluster plot), shows cells close to negative control and group 3 (purple, bottom square in cluster plot), shows aberrant cells, like under mitosis, dying or amorphous.

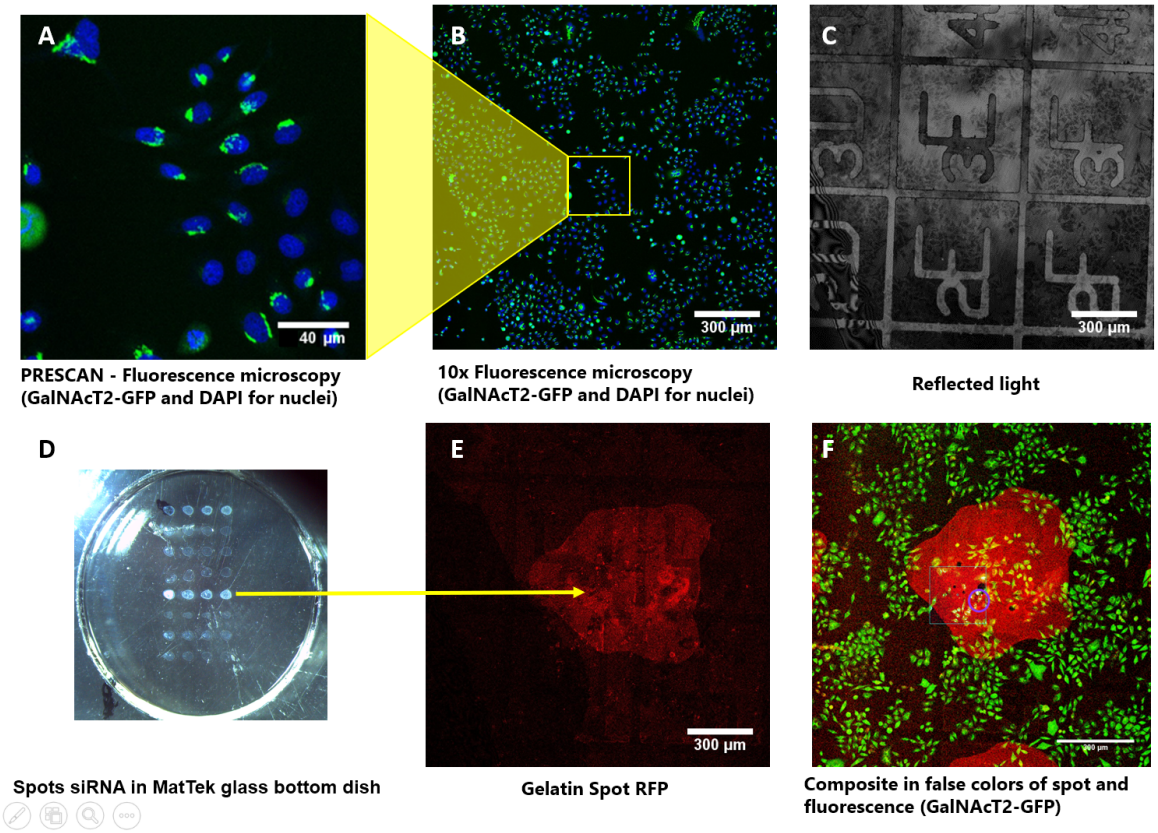

Fig. 4.3 4.3 **A.** Pre-scan image, GalNAcT2-GFP and DAPI for nuclei, objective 10x zoom factor 5. Rest of the images are from the high-resolution job, contextual part: at 10x Objective, (**B**) GalNAcT2-GFP and DAPI for nuclei,(**C**)reflected light and gelatin spot in RFP (**E**) . The correspondence with one of the siRNA spots of the real dish is shown (**D**). Final image (**F**) is a composite in false colors of the spot in RFP and the GalNacT2-GFP with the histogram equalized to stand out the cell bodies.

the image, the translation from pixel coordinates to stage coordinates is carried out by a simple linear transformation.

As explained, crossings are conveniently named after the two-character combination inside the nearest grid square [3] . To identify the characters inside the grid square, a Convolutional Neural Network (CNN) (Krizhevsky, Sutskever and Hinton, 2012; Bui and Chang, 2016) was trained using a mixture of real data and a synthetic dataset of the character patterns. The CNN architecture used 6 convolution layers in a sequential manner followed by two dense layers, resulting in a 98% accuracy on test data, very close to human performance in recognition.

Crossings are stored as stage coordinates followed by the pattern identified inside the square. Ideally, crossings follow a simple linear distribution (squares) which can be

[3] By our own convention, it was decided that given a grid square with the inner pattern straightly oriented, the top left corner point is named with the name of the inner pattern. See Figure 4.5-B.

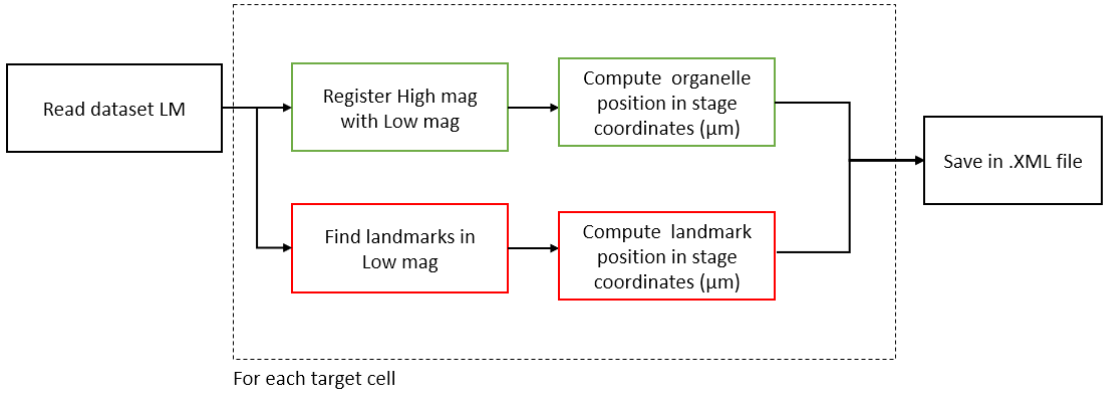

Fig. 4.4 Description of intermediate steps needed for obtaining LM stage coordinates. Each box represents an action to achieve the final coordinate files.

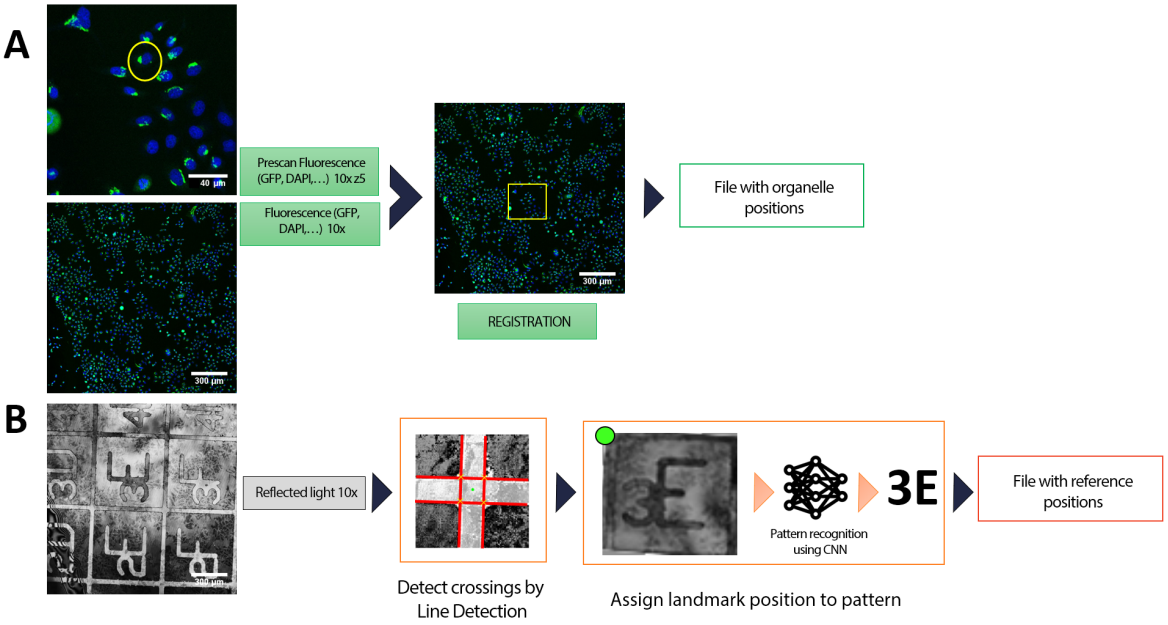

Fig. 4.5 A, prescan GFP images [10x zoom factor 5, 0.35 µm/pixel,1024 width,1024 height] are registered with fluorescent lower magnification, also GFP [10x , 1.7 µm/pixel,1024 width, 1024 height]. After registration, the coordinates of the cell of interest are stored relative to the low magnification image. B, First, line detection is applied on reflected light images to detect the crossings at the grid edges. Visible alphanumeric patterns in the image are cropped from the bounding box created by the intersection points and analyzed by a convolutional neural network, which recognizes the type of pattern, unique to each position in the grid. Each detected pattern is assigned to one crossing in the grid and both are stored as a couple of name-stage coordinates (e.g. 3E-(31.450 x, 72.567 y)) to define a crossing.

verified generating a linear model. For example, if coordinates belonging to 3E are (30,50), coordinates for 4E must be at (40,50) and 5E at (50,50). This is a simplified a map representation of the grid where the lattice pattern of the grid is ideal and is formed by perfect squares. However, the real stage coordinates are imperfect, with

an error depending on the imaging conditions and imprecisions of the image analysis algorithm used to extract them. Using least squares, crossings detected on real images can be correlated in a one to one relationship to the canvas coordinates. Then the error of the correlation can be used to dismiss potential errors from the real stage coordinates. Thus, when a new stage coordinate is detected, its validity is asserted comparing it against the predicted coordinate computed by the linear model. Crossings which error is less than an threshold can be discarded as wrongly detected, as shown in Algorithm 1 (Test positions).

Algorithm 1 Assess position

```
1:  procedure TEST POSITIONS(Landmarks_list)
2:      for landmark in Landmarks_list do
3:          Neigh_list = Get list of neighbors (maximum 20) from landmark
4:          if length(Neigh_list) >4 then
5:              H = Get Affine Transform (Neighs_list)
6:              Estimate landmark position using H
7:              error_estimate = |landmark − estimate|
8:              if error_estimate < 300 μm then
9:                  Add to map
10:                 Add error estimate to error_list
11:             else
12:                 Discard landmark
13:     Return Average(error_list), Standard Deviation (error_list)
```

Eventually, two independent files are stored, one with organelle centre stage coordinates and another one with crossing stage coordinates.

Line detection algorithm used for landmark finding

Several line detectors have been proposed over the years, being the most notable PHT (probabilistic hough transform) (Stephens, 1991) and LSD (Grompone von Gioi et al., 2012). Unfortunately, each time the images change in size, illumination or orientation, the algorithm parameters need to be adapted manually or by an extensive iterative parameter search. In order to keep a fixed set of parameters, a different approach was used.

LOD (Line orientation detector) applies a series of pre-processing steps in which pixel orientations are weighted with neighboring pixels by convolution with line morphological operators for each possible angle orientation. Hence, the main trend of a line inside the image can be detected. Calculating the line intersections for all the

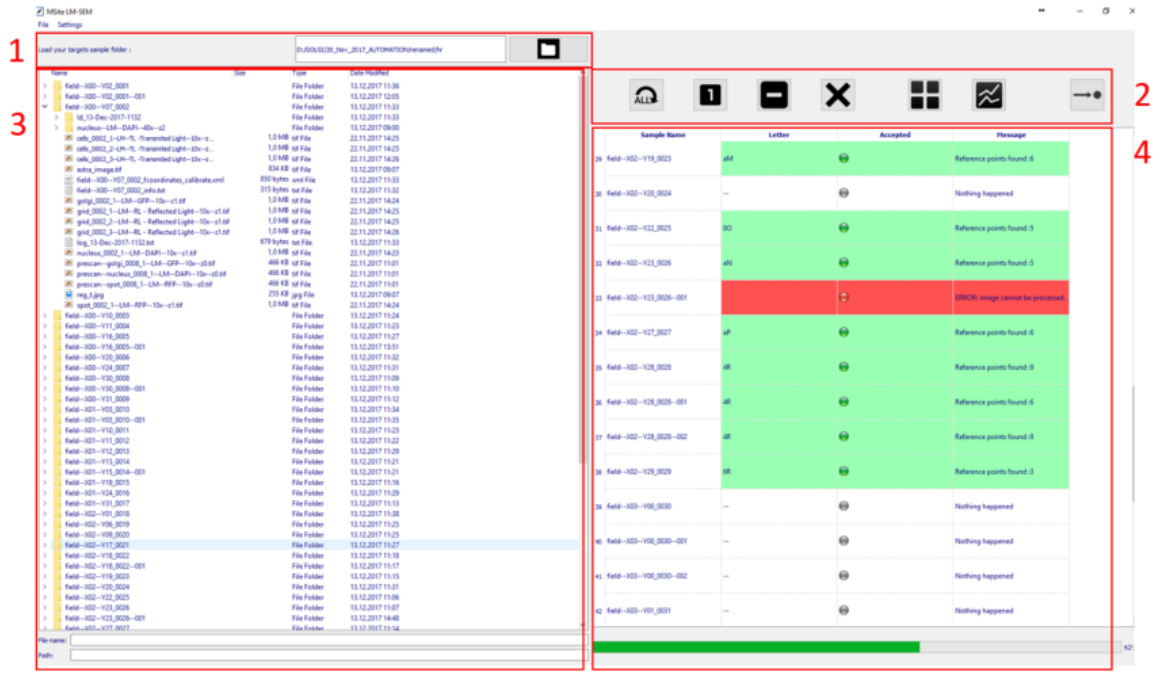

Fig. 4.6 GUI for LM Map Builder. 1. Dialog for experiment selection. Once the folder is selected the tree view (3) and list view display all the target cell samples present the folder. 2. Set of controls: Button [All] computes landmarks from reflected light (RL) images. One target is equivalent to one row in the list view. Button [1] computes landmarks from one cell, button [-] deletes all computations. Button [x] removes the selected cell from the list. Button [=>.] exports the results in .xml format. Other buttons show additional information: expected squared error and density distribution of targets. 3. Tree view, each folder contains all data generated for one targeted cell. 4. List view of cells. Green means the detection of the crossing has been successfully computed. Red means no crossings couldn't be detected. White means nothing has been computed.

lines detected inside one image results in a set of points defining the corners of the grid squares in image coordinates (pixel positions).

The algorithm starts with applying a Gaussian filtering (sigma = 1.5) and adjust for B&C unbalance (CLAHE (Heckbert and Karel, 1994)). Edges are extracted using an automatic version of Canny filter (Canny, 1986), which iterates until it finds a certain percentage of expected white pixels. In some exceptional cases where low frequency noise is present, a Laplacian filter is applied before edge extraction. Edges are enhanced and then a SWT (Stroke Width Transform) is used to fill the gaps between strokes (Epshtein, Ofek and Wexler, 2010).

After pre-processing, the image is filtered to obtain the Hessian from the image (Kovesi, 2000). Orientations are grouped using SLIC super pixels (Achanta et al., 2010) to get better homogeneity along large structures. The image of orientations is rotated on discrete steps from -90 to 90 degrees keeping a frame big enough to keep the full

image (maximum height is defined by the diagonal of the original image). Each rotated image is convolved with a directional filter. The "enhanced-edges" image obtained from the SWT is used as a mask and convolution with different orientation kernels is applied, similarly to what is shown in (Sandberg and Brega, 2007). The result is summed up by columns, so each 2D image with a rotation is represented with a 1D column (Figure 4.8).

The resulting matrix is called a sinogram, with degrees in the x axis and the diagonal length points in the y axis. Each local maximum can be assigned to a line in the image because it reflects the accumulation of neighboring pixels over a specific direction given by the angle. Non-maximum suppression can be used to find maxima and those are the lines belonging to the image. This method has the inconvenience that it provides lines but not segments. On the other hand, it is quite robust to noise and can find lines in one specific direction.

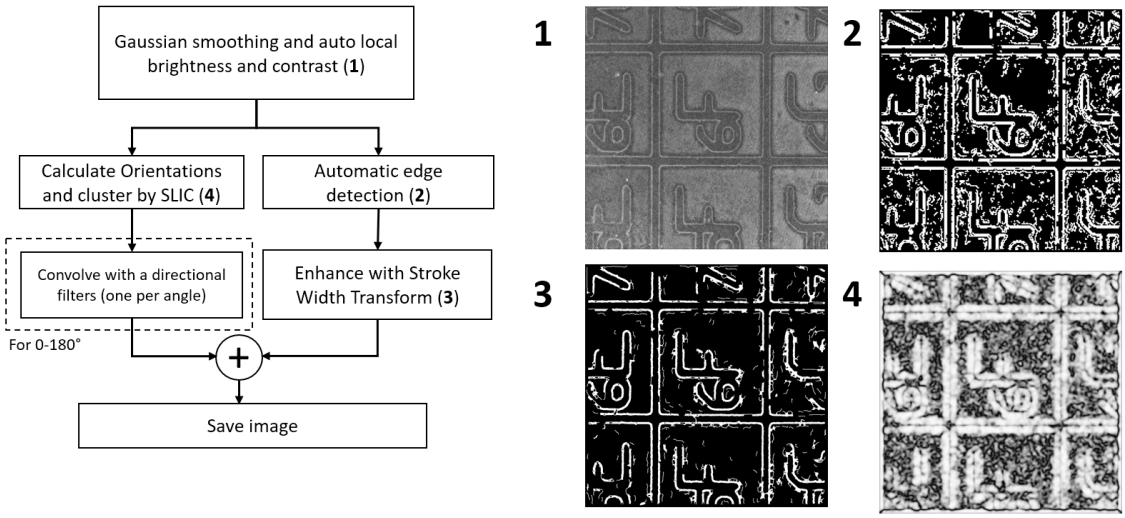

Fig. 4.7 **Line Orientation Detector part I:** Image 1 shows the image after gaussian smoothing and automatic local B&C. Image 2, is the result of the automatic edge detection and Image 3 after the SWT is applied (filling the gaps of close edges and cleaning the image). Image 4, reliability map of orientations. Gray image values are proportional to how reliable the hessian orientation is, so the whiter it is, the more reliable is the pixel orientation respect to the neighbors. A total of 180 directional filters are calculated (one per angle) and applied to image 4. Image 3 is used as a mask on each filtered imaged and stored for the next step.

After compute the orientations and projecting them, validation is required to find which lines belong to the glass bottom grid. First, we validate taking all maximum peaks over a minimum threshold (5% of the maximum value) and see if the distance between peaks in the diagonal is the same as the expected grid pattern. For example, with 600 µm spaced squares, a peak will be seen in two of the columns of the image in a periodic distance equivalent to the space. This regularity helps to discard any noise components.

In MatTek grids a thick line is 20 µm and a square width is 580 µm, that is why two peaks are observed in close proximity.

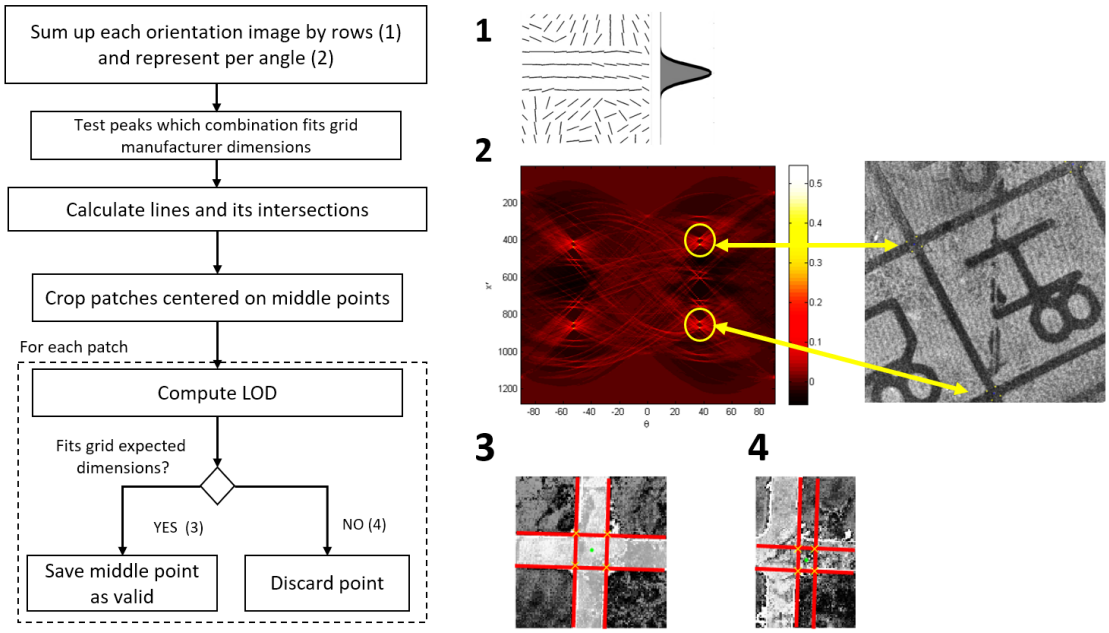

Fig. 4.8 **Line Detector algorithm Part II:** Orientation images (one per angle) are projected (1) and represented in a sinogram (2). Image 2 shows the result of projection, in the x axis the angles from -90 to 90 and in y the diagonal projection. Sinogram values are scaled between 0 and 1, with white/yellow having the highest values. After detection of all peaks, only combinations that fit the grid are kept (20, 580), in image 2 indicated by two peaks encircled with yellow that correspond to specific lines belonging to the grid patterns (arrows). Images 3 and 4 show patches of the crossings, with intersections in yellow and the middle point in green. Image 4 is a case that has been discarded because it does not fit the geometrical constraints, in this case, intersections must be separated 20 µm.

After this, intersections (middle points of two thick lines, in the case of MatTek) will provide a point in the image which is the crossing of one of the squares. This crossing of lines is cropped and stored in a patch. LOD is then applied again over the small patch, this time the angle of orientation is known and the image patch is small, so computations are fast. The middle point is computed again with higher precision and stored. This also helps to remove possible errors in detection. Positions are saved and translated to stage coordinates.

With this, all the necessary requirements for correlation with SEM are ready : stage coordinates from organelles inside cells and stage coordinates of crossings, which will be used as a reference in the next chapter .

4.5 Discussion

A key question about the LM pipeline here presented is how difficult would it be to adapt to any instrument and experimental conditions. A Leica SP5 was used for all the experiments presented in this manuscript. In principle, any other fluorescence microscope could be used for this application, providing that it can be controlled autonomously, and importantly, be endowed with a reflected light module. Even if the coordinate pattern detection could be adapted to DIC or transmitted light without difficulties, on a coverslip with cells with high confluency it will not be possible to read the imprinted glass patterns. Another requirement is to have a well calibrated stage where positions of at least one objective are saved in the metadata of the image. Every confocal and most fluorescent microscopes do this automatically. The final requirement is the possibility of executing online commands for automatic job execution. Fluorescent microscopes from almost any company can save sequences of commands in a job, for example, move to position (X,Y) and acquire a z-stack in the GFP channel. It is important to trigger these jobs iteratively given a list of coordinates. If these three conditions are met, adapting the pipeline to other microscopes should be straight forward.

Commercial microscopes are usually provided with software to not only control the acquisition but also to process images. The functionality of such programs can vary from simple filtering to advanced machine learning. Examples include *CellDiscoverer* (*Zeiss*), *Volocity* (*PerkinElmer*) or *Celleste* (*Thermofisher*). On their own, these packages are generally not enough to achieve a full analysis and require additional software for data exploration and machine learning. Thus, for analysis of data is preferred the use of open source software were code can be inspected with total transparency and there is freedom to modify any part of the pipeline. On the other hand, programming these softwares require considerable effort and expertise. Public institutions tend to use open software such as CellProfiler combined with software like R (HTM explorer), KNIME or Matlab for quality control and data exploration. Finally, classification of cells can be done by Cellcognition, CellProfiler Analyst or Ilastik. Although we opted for simplicity by manual selection of phenotypes, the presented pipeline can be modified to later include more sophisticated methods, like machine learning classification.

In this chapter I have described a workflow for processing light microscopy data that is a compilation of multiple modules with the aim to select cells within phenotypic sub-populations, and at the same time, provide spatial references for the consecutive

correlation in the FIBSEM. The LM workflow can be summarized as follows: low magnification image acquisition of cells, feature extraction, cell selection and high-resolution image acquisition of selected cells. In order to transfer this information to the EM, there are two essential images from the same position for each cell, one in LM with reflected light where the coordinate pattern of the glass bottom dish is clearly identifiable, and the other with fluorescence of the organelle of interest. After some post-processing of this data, a file is generated containing a list of stage coordinates for the ROIs that can be used later at the EM.

4.6 Acknowledgments and author contributions.

The experimental part corresponding to cell culture, gene selection, initial screening for phenotype characterization, siRNA solid phase transfection spotting on MatTek dishes and sample preparation was set up by Anna M. Steyer[1] with the help of Beate Neumann[2].

The feedback microscopy on the light microscope was developed by Volker Hilsenstein[2]. The image analysis pipeline with CellProfiler and the design of features for quantifying the phenotypes was developed by Christian Tischer[2].

The workflow presented has been refined successively during more than 35 experiments. In around 30 of them, the cell seeding for transfection, light microscopy and sample preparation was done by Anna M.Steyer during her PhD. In addition to the light microscopy imaging, she also did the sample preparation for EM. Nicole L. Schieber[1] and José Miguel Serra Lleti took over the light microscopy and sample preparation in the last 6 experiments.

José Miguel Serra Lleti designed, developed and tested the *Jupyter Notebook* for cell selection and the line detector for landmark extraction. Volker Hilsenstein gave valuable input about algebraic transformations and the best way to detect the grid by computer vision. He also provided some code snippets in python for the selection of cells with the *Jupyter Notebook* using *Bokeh*. Christian Tischer contributed with discussions about feature analysis and data representation.

Affiliations

(1) Cell Biology and Biophysics Unit, Schwab Team, European Molecular Biology Laboratory, 69117 Heidelberg, Germany

(2) Advanced Light Microscopy Facility, European Molecular Biology Laboratory, 69117 Heidelberg,

Germany

(3) Cell Biology and Biophysics Unit, Pepperkok Team, European Molecular Biology Laboratory, 69117 Heidelberg, Germany

References

Altan-Bonnet, N., Phair, R. D., Polishchuk, R. S., Weigert, R. and Lippincott-Schwartz, J. (2003) 'A role for Arf1 in mitotic Golgi disassembly, chromosome segregation, and cytokinesis.', *Proceedings of the National Academy of Sciences of the United States of America*. National Academy of Sciences, 100(23), pp. 13314–9. doi: 10.1073/pnas.2234055100.

Ayala, I. and Colanzi, A. (2017) 'Mitotic inheritance of the Golgi complex and its role in cell division', *Biology of the Cell*, 109(10), pp. 364–374. doi: 10.1111/boc.201700032.

Bray, M.-A., Fraser, A. N., Hasaka, T. P. and Carpenter, A. E. (2012) 'Workflow and Metrics for Image Quality Control in Large-Scale High-Content Screens', *Journal of Biomolecular Screening*. SAGE PublicationsSage CA: Los Angeles, CA, 17(2), pp. 266–274. doi: 10.1177/1087057111420292.

Bui, V. and Chang, L.-C. (2016) 'Deep Learning Architectures for Hard Character Classification'.

Canny, J. (1986) 'A computational approach to edge detection.', IEEE transactions on pattern analysis and machine intelligence, 8(6), pp. 679–98.

Chabin-Brion, K., Marceiller, J., Perez, F., Settegrana, C., Drechou, A., Durand, G. and Poüs, C. (2001) 'The Golgi Complex Is a Microtubule-organizing Organelle', *Molecular Biology of the Cell*. Edited by S. R. Pfeffer, 12(7), pp. 2047–2060. doi: 10.1091/mbc.12.7.2047.

Epshtein, B., Ofek, E. and Wexler, Y. (2010) 'Detecting text in natural scenes with stroke width transform', in 2010 *IEEE Computer Society Conference on Computer Vision and Pattern Recognition*. IEEE, pp. 2963–2970. doi: 10.1109/CVPR.2010.5540041.

Erfle, H., Neumann, B., Rogers, P., Bulkescher, J., Ellenberg, J. and Pepperkok, R. (2008) 'Work flow for multiplexing siRNA assays by solid-phase reverse transfection in multiwell plates.', *Journal of biomolecular screening*, 13(7), pp. 575–80. doi: 10.1177/1087057108320133.

Farhan, H., Wendeler, M. W., Mitrovic, S., Fava, E., Silberberg, Y., Sharan, R., Zerial, M. and Hauri, H.-P. (2010) 'MAPK signaling to the early secretory pathway revealed by kinase/phosphatase functional screening.', *The Journal of cell biology.* Rockefeller University Press, 189(6), pp. 997–1011.

doi: 10.1083/jcb.200912082.

Ferguson, S., Steyer, A. M., Mayhew, T. M., Schwab, Y. and Lucocq, J. M. (2017) 'Quantifying Golgi structure using EM: combining volume-SEM and stereology for higher throughput', *Histochemistry and Cell Biology*, 147(6), pp. 653–669. doi: 10.1007/s00418-017-1564-6.

Farquhar, M. G. and Palade, G. E. (1981) 'The Golgi Apparatus (Complex)-(1954-1981) from Artifact to Center Stage'. *The Journal of cell biology.* Rockefeller University Press. doi: 10.1083/jcb.91.3.77s.

Fujita, Y. and Okamoto, K. (2005) 'Golgi apparatus of the motor neurons in patients with amyotrophic lateral sclerosis and in mice models of amyotrophic lateral sclerosis', Neuropathology. Wiley/Blackwell (10.1111), 25(4), pp. 388–394. doi: 10.1111/j.1440-1789.2005.00616.x.

Gordon, D. E., Bond, L. M., Sahlender, D. A. and Peden, A. A. (2010) 'A Targeted siRNA Screen to Identify SNAREs Required for Constitutive Secretion in Mammalian Cells',*Traffic*, 11(9), pp. 1191–1204. doi: 10.1111/j.1600-0854.2010.01087.x.

Grompone von Gioi, R., Jakubowicz, J., Morel, J.-M. and Randall, G. (2012) 'LSD: a Line Segment Detector', Image Processing On Line, 2, pp. 35–55. doi: 10.5201/ipol.2012.gjmr-lsd.

Heckbert, P. S. and Karel (1994) Graphics gems IV, Graphics gems IV. AP Professional.

Huang, S. and Wang, Y. (2017) 'Golgi structure formation, function, and post-translational modifications in mammalian cells', *F1000Research*, 6, p. 2050. doi: 10.12688/f1000research.11900.1.

Jones, T. R., Kang, I. H., Wheeler, D. B., Lindquist, R. a, Papallo, A., Sabatini, D. M., Golland, P. and Carpenter, A. E. (2008) 'CellProfiler Analyst: data exploration and analysis software for complex image-based screens', *BMC Bioinformatics.* BioMed Central, 9(1), p. 482. doi: 10.1186/1471-2105-9-482.

Joshi, G., Chi, Y., Huang, Z. and Wang, Y. (2014) 'Alpha-Beta-induced Golgi fragmentation in Alzheimer's disease enhances Alpha-beta production.', *Proceedings of the National Academy of Sciences of the United States of America.* National Academy of Sciences, 111(13), pp. E1230-9. doi: 10.1073/pnas.1320192111.

Kimura, M., Takagi, S. and Nakashima, S. (2018) 'Aurora A regulates the architecture of the Golgi apparatus',*Experimental Cell Research.* Academic Press, 367(1), pp. 73–80. doi: 10.1016/J.YEXCR.2018.03.024.

Klumperman, J. (2011) 'Architecture of the mammalian Golgi.', *Cold Spring Harbor perspectives in biology.* Cold Spring Harbor Laboratory Press, 3(7). doi: 10.1101/cshperspect.a005181.

Kluyver, Thomas, Ragan-Kelley, Benjamin, Pérez, Fernando, Granger, Brian, Bussonnier, Matthias, Frederic, Jonathan, Kelley, Kyle, Hamrick, Jessica, Grout, Jason, Corlay, Sylvain, Ivanov, Paul, Avila, Damián, Abdalla, Safia, Willing, Carol and [Unknown], Jupyter development team(2016) Jupyter Notebooks – a publishing format for reproducible computational workflows. Loizides, Fernando and Scmidt, Birgit (eds.) In Positioning and Power in Academic Publishing: Players, Agents and Agendas. *IOS Press*. pp. 87-90. (doi:10.3233/978-1-61499-649-1-87 <http://dx.doi.org/10.3233/978-1-61499-649-1-87>).

Kovesi, P. D. (2000) MATLAB and Octave Functions for Computer Vision and Image Processing. Available at: http://www.peterkovesi.com/matlabfns/citesite.html (Accessed: 7 January 2018).

Krizhevsky, A., Sutskever, I. and Hinton, G. E. (2012) 'ImageNet Classification with Deep Convolutional Neural Networks'.

López-Sánchez, I., Sanz-García, M. and Lazo, P. A. (2009) 'Plk3 interacts with and specifically phosphorylates VRK1 in Ser342, a downstream target in a pathway that induces Golgi fragmentation.',*Molecular and cellular biology.* American Society for Microbiology (ASM), 29(5), pp. 1189–201. doi: 10.1128/MCB.01341-08.

Lucocq, J. (1993) 'Unbiased 3-D quantitation of ultrastructure in cell biology.', *Trends in cell biology*, 3(10), pp. 354–8.

Lucocq, J. M., Berger, E. G. and Warren, G. (1989) 'Mitotic Golgi fragments in HeLa cells and their role in the reassembly pathway.', *The Journal of cell biology.* The Rockefeller University Press, 109(2), pp. 463–74.

van der Maaten, L. (2013) 'Barnes-Hut-SNE'.

Marsh, B. J., Volkmann, N., McIntosh, J. R. and Howell, K. E. (2004) 'Direct continuities between cisternae at different levels of the Golgi complex in glucose-stimulated mouse islet beta cells.', *Proceedings of the National Academy of Sciences of the United States of America*, 101(15), pp. 5565–70. doi: 10.1073/pnas.0401242101.

Neumann, B., Walter, T., Hériché, J.-K., Bulkescher, J., Erfle, H., Conrad, C., Rogers, P., Poser, I., Held, M., Liebel, U., Cetin, C., Sieckmann, F., Pau, G., Kabbe, R., Wünsche, A., Satagopam, V., Schmitz, M. H. A., Chapuis, C., Gerlich, D. W., Schneider, R., Eils, R., Huber, W., Peters, J.-M., Hyman, A. A., Durbin, R., Pepperkok, R. and Ellenberg, J. (2010) 'Phenotypic profiling of the human genome by time-lapse microscopy reveals cell division genes.', *Nature.* Europe PMC Funders, 464(7289), pp. 721–7. doi: 10.1038/nature08869.

Otsu, N. (1979) 'A Threshold Selection Method from Gray-Level Histograms', *IEEE Transactions on Systems, Man, and Cybernetics*, 9(1), pp. 62–66. doi: 10.1109/TSMC.1979.4310076.

Palade, G. (1975) 'Intracellular aspects of the process of protein synthesis.',*Science* (New York, N.Y.), 189(4200), pp. 347–58.

Rios, R. M. and Bornens, M. (2003) 'The Golgi apparatus at the cell centre.', *Current opinion in cell biology*, 15(1), pp. 60–6. doi: 10.1016/s0955-0674(02)00013-3.

Russell, M. R. G., Lerner, T. R., Burden, J. J., Nkwe, D. O., Pelchen-Matthews, A., Domart, M.-C., Durgan, J., Weston, A., Jones, M. L., Peddie, C. J., Carzaniga, R., Florey, O., Marsh, M., Gutierrez, M. G. and Collinson, L. M. (2017) '3D correlative light and electron microscopy of cultured cells using serial blockface scanning electron microscopy.', *Journal of cell science.*The Company of Biologists Ltd, 130(1), pp. 278–291. doi: 10.1242/jcs.188433.

Sandberg, K. and Brega, M. (2007) 'Segmentation of thin structures in electron micrographs using orientation fields.', *Journal of structural biology*, 157(2), pp. 403–15. doi: 10.1016/j.jsb.2006.09.007.

Simpson, J. C., Cetin, C., Erfle, H., Joggerst, B., Liebel, U., Ellenberg, J. and Pepperkok, R. (2007) 'An RNAi screening platform to identify secretion machinery in mammalian cells', *Journal of Biotechnology*, 129(2), pp. 352–365. doi: 10.1016/j.jbiotec.2006.12.027.

Simpson, J. C., Joggerst, B., Laketa, V., Verissimo, F., Cetin, C., Erfle, H., Bexiga, M. G., Singan, V. R., Hériché, J.-K., Neumann, B., Mateos, A., Blake, J., Bechtel, S., Benes, V., Wiemann, S., Ellenberg, J. and Pepperkok, R. (2012) 'Genome-wide RNAi screening identifies human proteins with a regulatory function in the early secretory pathway.', *Nature cell biology.* Nature Publishing Group, a division of Macmillan Publishers Limited. All Rights Reserved., 14(7), pp. 764–74. doi: 10.1038/ncb2510.

Stephens, R. (1991) 'Probabilistic approach to the Hough transform', *Image and Vision Computing.* Elsevier, 9(1), pp. 66–71. doi: 10.1016/0262-8856(91)90051-P.

Sütterlin, C. and Colanzi, A. (2010) 'The Golgi and the centrosome: building a functional partnership.', *The Journal of cell biology.* The Rockefeller University Press, 188(5), pp. 621–8. doi: 10.1083/jcb.200910001.

Yadav, S., Puri, S. and Linstedt, A. D. (2009) 'A Primary Role for Golgi Positioning in Directed Secretion, Cell Polarity, and Wound Healing', *Molecular Biology of the Cell.* Edited by J. Lippincott-Schwartz, 20(6), pp. 1728–1736. doi: 10.1091/mbc.e08-10-1077.

Zaal, K. J. ., Smith, C. L., Polishchuk, R. S., Altan, N., Cole, N. B., Ellenberg, J., Hirschberg, K., Presley, J. F., Roberts, T. H., Siggia, E., Phair, R. D. and Lippincott-Schwartz, J. (1999) 'Golgi Membranes Are Absorbed into and Reemerge from the ER during Mitosis',*Cell*. Cell Press, 99(6), pp. 589–601. doi: 10.1016/S0092-8674(00)81548-2.

Zhang, X. and Wang, Y. (2016) 'GRASPs in Golgi Structure and Function',*Frontiers in Cell and Developmental Biology*, 3, p. 84. doi: 10.3389/fcell.2015.00084.

Wang, Y., Wei, J.-H., Bisel, B., Tang, D. and Seemann, J. (2008) 'Golgi cisternal unstacking stimulates COPI vesicle budding and protein transport.', *PloS one*. Public Library of Science, 3(2), p. e1647. doi: 10.1371/journal.pone.0001647.

5

Automated CLEM as a screening tool using the Golgi apparatus as example (II:EM)

5.1 Introduction

During the last years, volume EM techniques made possible high-resolution datasets of full cells (Briggman and Bock, 2012; Titze and Genoud, 2016; Russell et al., 2017; Hasegawa et al., 2018). So far this has only been applied to individual targets of one region. The most important technical development in this chapter is the application of the CLEM correlation to achieve unprecedent throughput of 3D volumes. Existent technologies in the market (*Shuttle and Find* from *Zeiss* and *CorrSight* from *FEI*), claim precisions of less than 5 µm, but in practice, require time-consuming manual intervention. In the method I developed, a precision below 5 µm can be achieved without manual intervention, opening the possibility to move automatically and perform multiple experiments in just one EM block. Multi-positioning is an innovation not existent in any other system commercially available.

As we have seen in the previous chapter, the first step is to do a careful selection of potential treatments by light microscopy. The light microscopy pipeline for cell selection was able to provide a good set of candidate cells classified by their phenotypic morphology. As described before, extracted landmark coordinates from the grid where the cells were seeded will serve as a transformation system between the LM and SEM

surface. In this chapter I will describe with details the algorithmic system used to locate precisely the selected cells in processed samples inside the FIB-SEM microscope.

A total of three experiments consisting in an array of solid phase transfection siRNAs (Erfle et al. 2008), with 14 different genes and controls in the same dish, were screened by EM. Tens of cells were acquired in EM for posterior ultrastructural analysis. It was decided that the most promising candidates were acquired in thin sections every 100 nm or 200 nm to apply stereological probes on them. However, instead of offering a detailed analysis of data, the purpose of this chapter is to introduce the multisite method and to prove the validity of it by targeting and acquiring cell volumes. For this reason, the analysis of results will be relegated to the discussion and a small example with cells transfected with COPB1 siRNA.

5.2 Materials and methods

Sample preparation for EM

One hour before processing, TCH (Thiocarbohydrazide, Sigma-Aldrich)was prepared at 1% concentration (0.1 g in 10 ml. in double distilled water (ddH2O)), put in the oven at 60 degrees, and agitated every 10 minutes until it is completely dissolved. Continuing the protocol from the previous chapter where cells were lightly fixed, cells were post-fixed with 4% OsO4, 3% $K_4Fe(CN)_6$ in cacodilate buffer 0.1M, pH 7.2. A Ted Pella Biowave Pro microwave was used, seven times two minutes vacuum at 100 Watts on-off cycles.

The sample was then rinsed three times with cacodylate buffer. Prepared TCH was filtered and added to the dish. After 10 minutes on bench, sample was rinsed three times with cacodylate buffer and one with ddH2O. After 10 minutes on bench, sample was rinsed three times with cacodylate buffer and once with ddH2O. A second post-stain of 1% OsO4 with cacodylate 0.1M pH 7.2 was added next to the sample, again using the microwave (same cycle program) before being rinsed 3 times with cacodylate buffer and 3 times with ddH2O. The final stain with 1% UA in water was applied, and after that rinsed 3 times with ddH2O.

Cells are then dehydrated in graded ethanol series. Dehydration was also accelerated by the use of the microwave at 250 Watts without vacuum, 40 seconds each step (50,70,90,100,100%). Final infiltrations were done sample with Durcupan (Sigma-

Aldrich) in progressive steps (50% ethanol-50% resin, 30% ethanol-70% resin and three times 100% resin).

Cells are left 72 hours in the oven at 60 degrees. After resin polimerization the sample was heat shocked (introduced in liquid nitrogen for 10 seconds, then in warm water) to remove the glass bottom dish. With the resin polymerized, the sample was mounted in a SEM stub, coated with gold (180 seconds,30 mA) and introduced in the FIB-SEM microscope chamber.

FIB-SEM preconditions

The microscope was operative, with SmartSEM software and EM server from Zeiss initialized. Atlas Engine (Fibics) was properly configured and connected to SmartSEM Server from Zeiss. As described in chapter 3, Atlas Engine had an authorization to use the API Atlas5 and it was installed in the same computer were the CLEMSite server (our software) was running.

EHT was set up at 1.5 kV. Sample was set in position with the following conditions: eucentric height is set and the sample tilted at 54°; WD at 5 mm; FIB current at 50 pA for imaging; focus, stigmatism and wobbler adjusted in the SEM at 2000x magnification; B&C set in FIB and SEM (50 B, 20 C) for SESI and SEM also with ESB (depending on the sample, usually around 48 B, 45 C). When imaging the sample surface, the grid lines had about 45 degrees rotation relative to the image frame and they were clearly visible. Coincidence point was done once at the middle of the sample.

Communication with the Electron Microscope

Two client software applications, called *CLEMSite Navigator* and *Multisite*, were developed with python 3.6 and Qt5 and connected to the CLEMSite Server. The application connects as a client to the CLEMSite server using the address 127.0.0.1 (local) and port 8098.

In the client application, after sending a connection request, a message from the server is received with the status of the microscope and a security key. If accepted, the program will continue as connected. Upon connection, the user must push “Save state” button to store all the initial set up conditions in the previous point (FIB-SEM preconditions) in the server. With this, the conditions established were restored before each new volume acquisition.The correlation strategy is explained in the Mapping system section of results.

Generation of setup file for volume acquisition.

As described in chapter 3, automation requires a setup file generated by the *ATLAS 3D* software from *Fibics*, indicating the measures and currents of the volume to be acquired. These are the parameters set up previous to automation: spacing

label Coarse trench (15 nA; 30x50µm), polish (3 nA; 30x2µm), FIB Setup with milling aperture (1.5 nA), minimum, with depth (20 µm), mill area (25x20 µm).

label SEM Setup with FOV (30x30µm), pixel size (5nm), dwell time (10µs), line Averaging (1)

label Slice thickness 200 nm

label Focus steps 15 nm with dwell time 20 µs, range 1 um, stigmators range 0.2

The same setup has been used for each cell, the volume acquired is 25x22x20 µm divided in 200 nm sections and 5x5 nm pixel size. The same is done for the ROI FOV, i.e., a rectangle marking the FOV width and height. The cross-section face is 25x20 µm and the region imaged inside the cross-section is 20x10 µm for a control Hela cell and 20x16 µm for cells with COPB1 knockdown phenotype. Restricting the FOV in this way, helps to speed up the acquisition by reducing imaging time.

Images were acquired at 1.5 kV with the energy-selective back-scattered electron (EsB) detector with a grid voltage of 1100 V, analytical mode at a 700pA current, setting the dwell time and line average to add up to 1.5-2 min per image.

Computational and image analysis

Obtained EM stacks were cropped to remove part of the black background, inverted, smoothed and brightness and contrast adjusted using Fiji. Fiji was also used to align the image stacks using SIFT features under the plugin 'Registration/Linear Stack alignment with SIFT'. It was indicated only translation in the transformation matrices, otherwise, default values of the plugin provided satisfactory results.

For volume estimation, a stereology approach was used (Ferguson et al. 2017). GA and vesicles bigger than 100 nm volumes were estimated using Cavalieri (Cruz-Orive et al. 1999; Gundersen 1986). A sample region of 12 µm in the z-direction was examined where the perinuclear region was included and, in all cases, most of the GA was present. The starting section was selected randomly and every 3 sections contacts with GA or vesicles were counted using a cycloid of 55 pixels. The formula used to

calculate the volume was P*A*k, where P is the total of counted touches, A is the area of each box of the grid and k the section distance (300 nm).

For the creation of 3D models, a python script was developed to crop only the cell and remove the background. The SLIC algorithm presented in chapter 3 was modified to perform a three-way thresholding and keep only the parts corresponding to the cell body on each section. The resultant stack was loaded into Drishti software. In Drishti, only the transfer function (gradient versus grey values) was manipulated to visualize different structures.

5.3 Results and discussion

Landmarks are automatically detected by machine learning and mapped to light microscopy coordinates.

In previous works (Gong et al. 2014; Kukulski et al. 2011) or commercially available solutions (*CorrSight* with *MAPS* from *FEI*, *Shuttle and Find* from *Zeiss*), one mathematical approach dominated, which consisted in to find common landmarks between LM and EM as punctual coordinates and then solve a least squares minimization problem. Landmarks can be found by identifying correspondences manually, like in *MAPS* and *Shuttle and Find* or by automatic detection of fiducial markers. Once positions are detected in both modalities, a linear model is usually enough to generate a mathematical transformation that predicts the ROI in EM with enough precision.

Fiducial markers are a good choice when using TEM sections (Kukulski et al. 2012; Arnold et al. 2016). They provide nanometer precision and their error can be quantified with respect to the fluorescent image of the section. Without fiducials, there is the option to rely on feature-based registration (Wang et al. 2015; Cao et al. 2014; Nam et al. 2014). However, in FIB-SEM the view is restricted to the sample surface of an embedded resin block with almost no features.

Another solution for correlation is to impose a grid with a pattern at the bottom of the cell culture. In the past, a variety of coordinate systems like metal grids, etched glass and sputter coated carbon layer were used in EM (Sartori et al. 2007; Jimenez et al. 2010). In (Beckwith et al. 2015), a home-made system grid based on Aclar substrates was created for targeting purposes. The method uses a silicon wafer micropatterned with the desired geometry. Aclar is placed on top of the wafer, and

after a thermomoulding process the film used as substrate for seeding the cells. The system is simple to reproduce and produces clean FIB-SEM images.

As commented in the introduction, some of the first papers doing CLEM used commercially available culture dishes endowed with a glass etched gridded coverslip (*CelLocate* coverslips from *Eppendorf-Netheler-Hinz GmbH*, used in (Stierhof et al., 1994; Mironov, Polishchuk and Luini, 2000)). In this thesis, we also decided to adopt commercially available culture dishes (P35G-1.5-14-CGRD-D from MatTek Corporation – see Figure 5.1). In the SEM surface, landmarks (crossings) belonging to this grid were successfully located and linked to their corresponding LM stage coordinates.

A mapping system was developed as backbone for the correlation software. A map is a table (similar to a database table) where each entry is associated to a position. Each position is a set of coordinates and a state tag associated to a unique identifier (UID). Coordinates of two different types,e.g. LM stage coordinates and SEM stage coordinates, have a bijective correspondence, where one set of coordinates is considered the source and the other the destination.

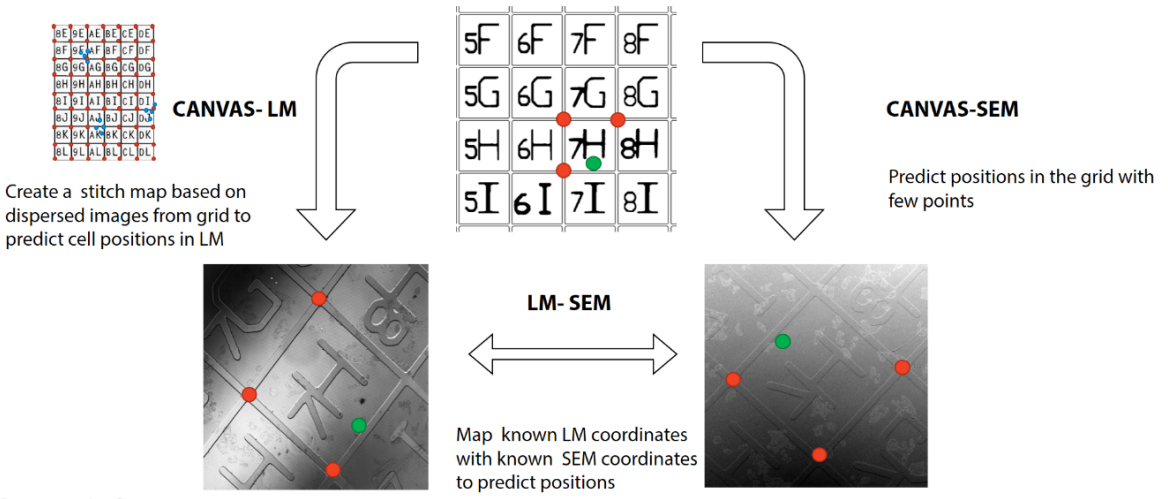

Fig. 5.1 CLEMSite uses 3 internal maps (Canvas-LM, Canvas-SEM and LM-SEM) between different types of coordinates. Each map uses a set of operators to query positions and predict coordinates. Position status are relative to what is defined as source and destination coordinates. For example, in the LM-SEM, LM stage coordinates are source and SEM stage coordinates are destination. Then, the green mark in 7H is a target position in SEM stage coordinates. The red marks corresponds to calibrated (reference) positions, because coordinates from source and destiny are known in both LM and SEM.

A set of operations can be used to query each map. There are two key operations in the library: coordinate prediction for new positions and querying for neighbors in a radius of 1200 µm. Neighbour positions, are used to compute local transformations close to a

position. Thus, a global homography is computed using all available positions from the map and used to predict unknown positions. On top of the global transform, one affine transformation is computed locally for each individual position with the closest neighbors taken in account. The implementation follows the idea from (Siklós & Kuhnt 1991) were features extracted were converted to points and used to compute local affine transformations with higher precision than a global transform. Implementation of the scripts used regular least squares to compute the transformation matrix and a kd-tree to find the closest neighbors, both from sci-python package.

Table 5.1 Relation between source and destination coordinates.

	SOURCE coordinates	DESTINATION coordinates
CALIBRATED	YES	YES
NON-CALIBRATED	YES	NO or not found
TARGET	YES	NO or predicted
ACQUIRED	NO	YES
NON-VALID (BLOCKED)	-	-

Positions can have states inside a map, which can be non-calibrated, calibrated, target or acquired. Calibrated and non-calibrated refer to landmarks, calibrated when coordinates of different types (e.g. LM and EM stage coordinates from the same landmark) are found and matched, non-calibrated when one of the coordinates is missing. Only positions that are present in both types of coordinates (e.g. LM and SEM) can be used for transformations. Targets are only present in the source coordinates (e.g. cell centroids in LM stage coordinates). They are predicted in the destination coordinates. Acquired positions are present in the destination coordinates but not in the source coordinates set (stored EM positions which don't have a correspondence with LM but are interesting to come back). Finally, non-valid positions cannot be used to generate transformations or to move to them, the position is then blocked. Map position states are summarized in Table 1.

Positions are stored in a total of 3 maps, as represented in Figure 5.1. Each map is used for different purposes, as it follows:

Canvas-LM: Light microscopy stage coordinates to Canvas representation. This was the map used in chapter 4. As explained then, a Canvas is an ideal representation of grid and is used to predict unknown positions in LM.

Canvas-SEM: Provides error detection and prediction of unknown positions of the grid, but using SEM coordinates. E.g.: Under the command move to 7H, the sys-

tem will translate canvas coordinate positions (70,80) to SEM stage coordinates (61988, 76543).

LM-SEM: Used to predict target positions based on correspondences between LM and SEM landmarks.

The map system is integrated in CLEMSite with an intuitive and easy-to-use GUI, called *Navigator*. The *Navigator* application (Figure 5.2) operates in two phases (Figure 5.3): first, it **maps** stage coordinates from LM to the canvas. The canvas represents an ideal grid generated with manufacturer specifications. Second, it **scans** the surface of the sample using SEM images and when a crossing is found, SEM stage coordinates and LM stage coordinates are associated right away in the LM-SEM.

In a first step, two files computed previously are loaded into the application: one containing the LM stage coordinates of the landmarks, and one containing the stage coordinates of the target cells. By looking at the SEM (Secondary Electrons detector), the field of view of the microscope is positioned at the center of one the grid squares. Then, a scan is initiated by pushing the bullseye button on the application (Figure 5.2-5).

The internal software logic is displayed in flowchart 1. First, a dialog is shown (Figure 5.4) to make the program aware of its initial position. If four crossings are detected by the line detector on the image of the grid square, they are mapped to the Canvas and a correspondence is established with SEM stage coordinates (Canvas-SEM map). The obtained positions are enough to predict the stage coordinates of a different crossing in the grid and move to it. This time the process is repeated automatically. The microscope moves to the predicted position of the next crossing and then the line detector software is applied again to detect the stage coordinates of the current crossing with higher precision.

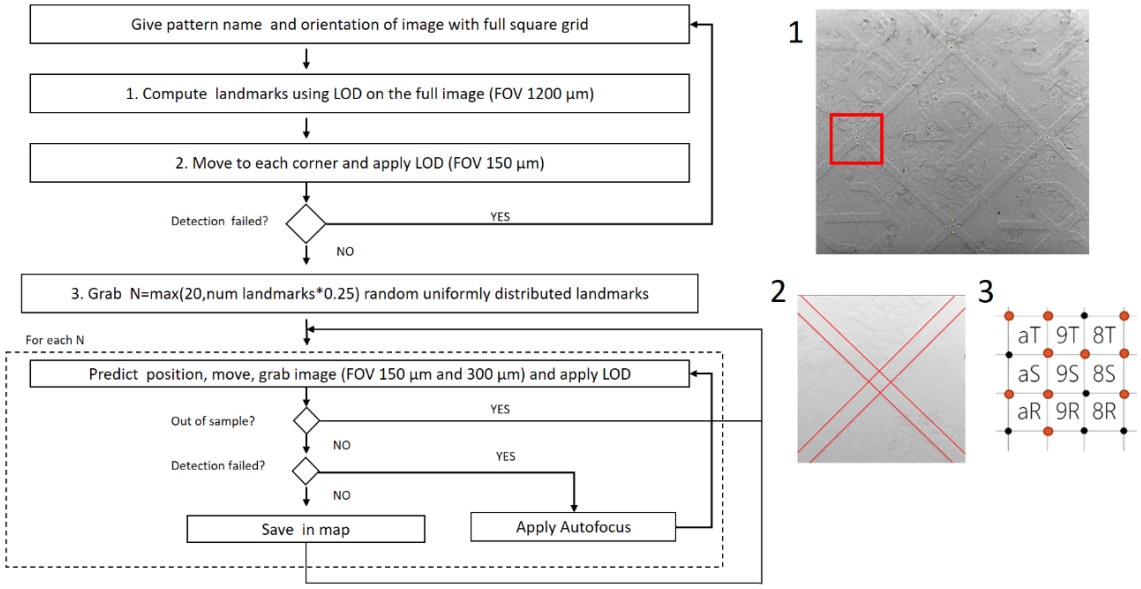

Flowchart 1. Scanning on CLEMSite Navigator. User drives the microscope stage to the center of one clearly identifiable grid square and provides information about its orientation and the alphanumerical identity. This square position is taken as reference, and landmarks are extracted for the 4 corners of the square. To avoid problems with magnification range, corners are re-imaged at higher magnification, with a FOV of 150 µm. Line detection is applied on the image, and using the intersection of the double orthogonal lines, the crossing of the grid at the corner is detected. If the detection fails, the FOV is changed to 300 µm and the process repeated. If the 4 corners of the grid square are successfully computed, the Navigator predicts the position of the closest crossing and repeats the process of imaging and detection. If the position is out of the sample, it is stored as blocked (non-available), and the software continues with the detection of the next landmark. If the detection fails, an autofocus is performed and the process repeated again. Autofocus is only applied once, if fails twice, the position is also discarded (not shown in chart).

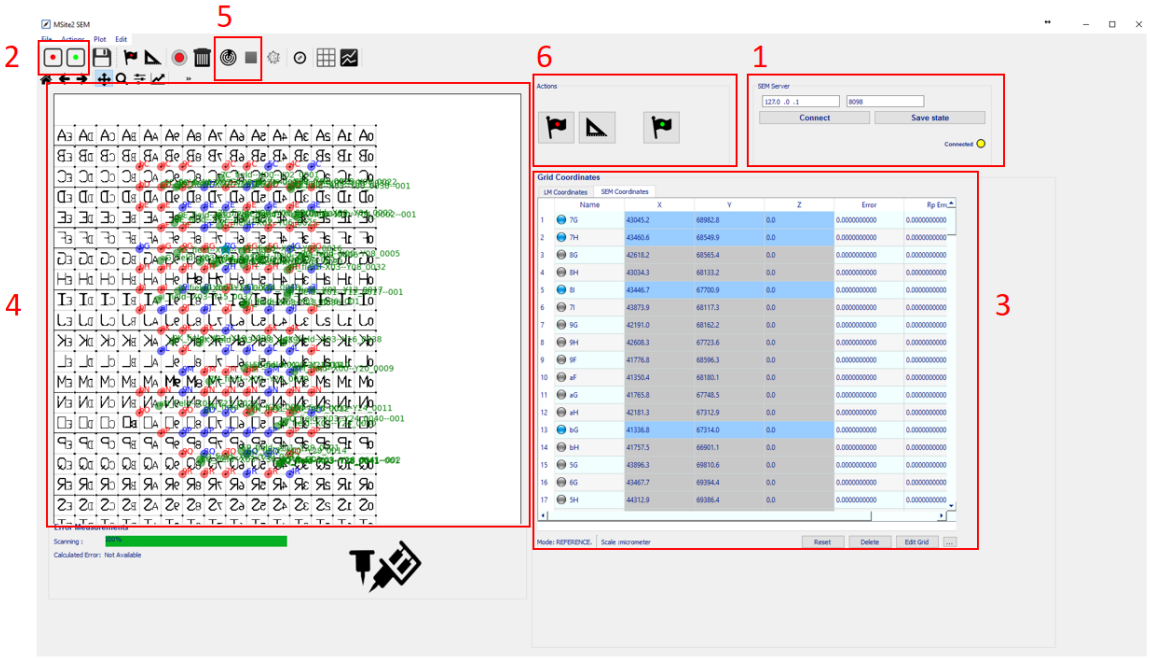

Fig. 5.2 CLEMSite Navigator GUI. 1. Connection form. Form to connect to FIB-SEM microscope. 2. Input file buttons. Red button to input the xml file with landmarks. Green does the same with target coordinates files. 3. List view with 2 tabs, one for LM stage coordinates and other for SEM stage coordinates, 4. GUI drawing representation. After input of LM file with coordinates, a representation of the grid (canvas) is displayed with the coordinates listed. 5. Scan buttons. Buttons used for starting the surface scan. Bullseye is used to start the process, square to stop it. 6. Flag buttons. Buttons used for manual assignment of positions. If a position from LM is found in SEM manually, the operator can assign the position with the red flag. If the user finds an interesting position, it can be stored using the green flag. The ruler can be used to correct a predicted or given position in the map.

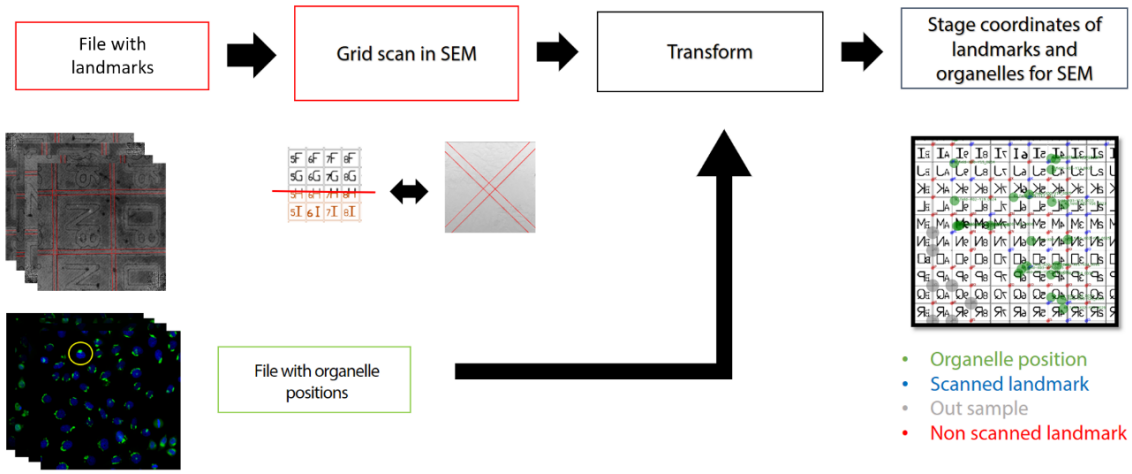

Fig. 5.3 **Simplified workflow of the automatic surface scan.** Landmark positions (crossings) collected from LM images are sent in a list to the Navigator. After the user filling the form from Figures 5.4, the SEM starts scanning the block surface, going from one predicted landmark position to the next, acquiring and image and performing line detection on it to determine the actual position in stage coordinates of the landmark. When enough landmarks are assigned (more than 30% of the total positions in LM and more than 20 points), an affine transform is computed with least squares. As a result, each cell target position is predicted in SEM stage coordinates.

LOD, the algorithm that was applied for detecting lines from the reflected light microscopy images, has a higher rate of failure when processing SEM images (2% instead of the 0.05% of LM). In SEM images, grid lines are very often blurry or erased. The system could be substantially improved if calculations were weighted by a probability map of the grid pattern. Recently, convolutional neural networks (CNN) have proved to be very resilient to noise in object detection (Qian et al. 2016; Zhu et al. 2018). Based on this, a neural network was trained to provide a probability mask were edges of the crossing could be found (Figure 5.5-B). The main difficulty when working with deep learning was to find enough training data to optimize the network. In this case, LOD with simple filters was used for more than a year and then errors curated manually. I extracted a total of 600 images from previous tests. In around 100 difficult cases, were LOD failed, I segmented manually the regions were the shadows of the corners were present. Data was augmented until 3000 images by variations in scaling, rotation, translation and intensity values. CLAHE (32x32 filter size) and gaussian blur (sigma 1, 5x5 filter size) were applied to images, which were normalized after augmentation.

Using as ground truth data 600 annotated images of grid crossings in SEM a convolutional autoencoder similar to U-Net (Ronneberger et al. 2015) was trained. Im-

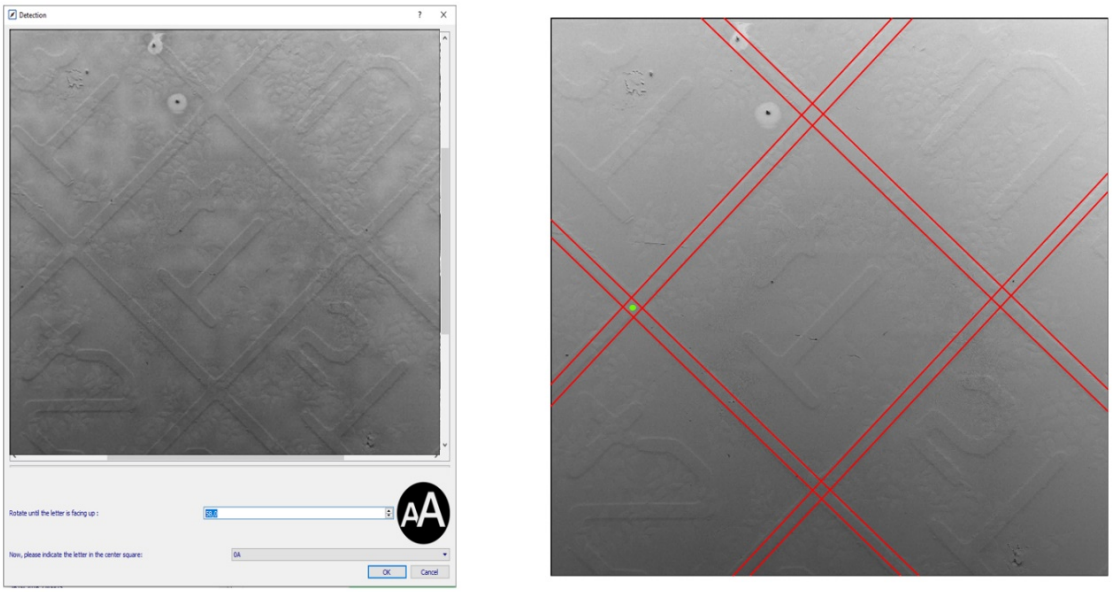

Fig. 5.4 A. Form shown before starting the scan procedure. The user has two controls, one to indicate which alphanumerical pattern is present in the center of the image (the user will select 4T for the present image in the combo box), and other to rotate the image until the pattern is straight. Thus, the general orientation of the grid can be obtained and used internally to narrow down the space search in the line detection algorithm. B. After clicking OK in the previous form, the line detection algorithm detects the lines forming the grid (lines in red). The landmark 4T is assigned to the proper square crossing (top right if image is straight, green spot).

plementation was carried out with Keras and Tensorflow [1] . The output provided a probability map for each pixel, which determines if grid borders could positively be found (Figure 5.5). The metric IOU was used to evaluate the progression (intersect over union, i.e., overlap between ground truth and results) but the function loss to train used was binary cross-entropy (sum of values that match ground truth). *Adam* optimizer was used with a learning rate of 1e-4. With the probability map computed, the last part of LOD algorithm was adapted to find the peaks based on the maximum probability of lines and provide results in the form of image coordinates. Using the detection system based on CNNs the rate of failure was reduced approximately to 0.06% (over 650 test images), a considerable improvement.

The scanning step is done for 30% of the grid corners (30-40 minutes), with a minimum of 20 points required, enough to generate a least-squares registration matrix with a targeting-accuracy of from 5 to 20 µm throughout a surface area of 1 cm². By computing the difference between each estimated position of a crossing and their real stage positions, the estimated error is 6.4±6 µm. This average was computed over 3

[1] Details about versions and implementation can be found in the Github addresses provided at the end of the thesis.

Table 5.2 Architecture of CNN trained for crossing detection.

Layer	Name	Layer	Name
Image, 256x256x1	Input	Transposed Convolution 64x2x2	T1
Convolution 8x3x3, Relu		Concatenate T1, C4	
Convolution 8x3x3, Relu	C1	Convolution 64x3x3, Relu	
MaxPooling 2x2		Convolution 64x3x3, Relu	
Convolution 16x3x3, Relu		Transposed Convolution 32x2x2	T2
Convolution 16x3x3, Relu	C2	Concatenate T2, C3	
MaxPooling 2x2		Convolution 32x3x3, Relu	
Convolution 32x3x3, Relu		Convolution 32x3x3, Relu	
Convolution 32x3x3, Relu	C3	Transposed Convolution 16x2x2	T3
MaxPooling 2x2		Concatenate T3, C2	
Convolution 64x3x3, Relu		Convolution 16x3x3, Relu	
Convolution 64x3x3, Relu	C4	Convolution 16x3x3, Relu	
MaxPooling 2x2		Transposed Convolution 8x2x2	T1
Convolution 128x3x3,Relu		Concatenate T1, C1	
C4 = Convolution 128x3x3,Relu		Convolution 8x3x3, Relu	
		Convolution 8x3x3, Relu	
		Convolution 1x1, sigmoid	Output

different scans: 9.18±7 µm, N = 15; 5.47±6.17 µm, N = 50; 4.53±4,39 µm, N = 54. More samples are needed for a real estimation of the error, which unfortunately is very dependent on the quality of the surface sample. Thermal drift due to sample and stage movement, irregular surface topology (the block surface is not a perfect 2D plane) and the large space between landmarks for this type of dishes (600 µm), makes difficult to improve the accuracy in a single scan.

Despite the efforts on having an accurate crossing detection algorithm, samples very often have regions that were accidentally scratched or fall outside the grid area. In best case scenario, the sample is scanned without errors, but often contain one or two regions with high probability to give 2 or 3 consecutive errors in detection.

Two corrective measures have been applied to prevent these cases. First, it can happen that not all the landmarks imaged in LM were present in the processed EM sample, for example, if the resin block is fractured or scratched on the block surface. To avoid this inconvenience, a machine learning system was trained to reject positions very close to the border or highly damaged. Images that are completely outside the sample are out of focus and easily discarded by a simple frequency analysis (images are completely homogeneous). Images from the borders or with damages (400 images) were collected and a CNN was trained for recognition (Simonyan and Zisserman, 2014). The network

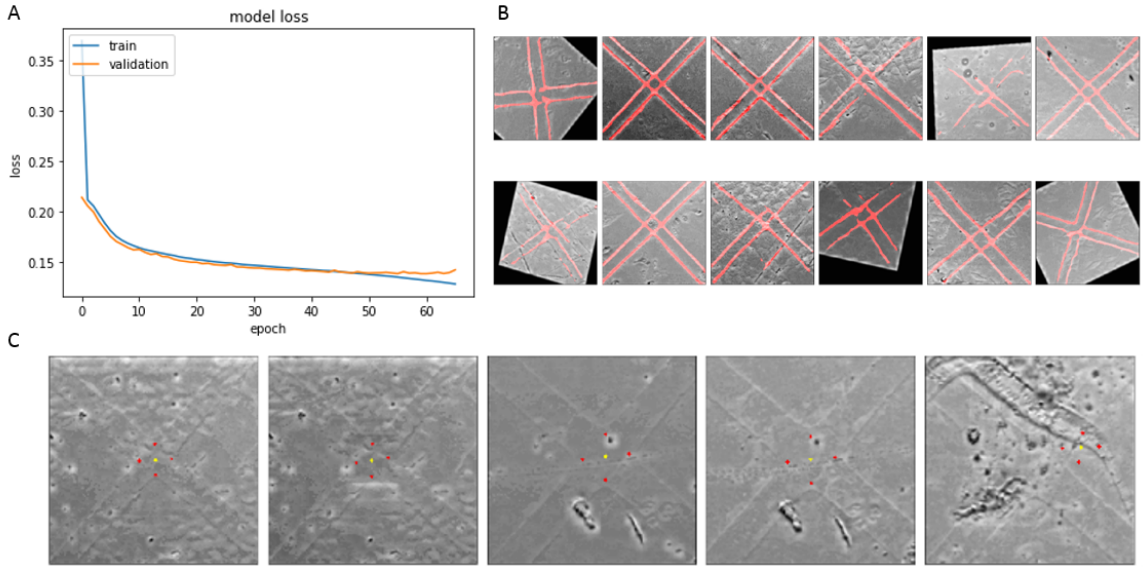

Fig. 5.5 **CNN + LOD on SEM images for image coordinates crossing extraction. A.** Loss function during training (loss value versus epoch. One epoch is when one entire training dataset is passed fully through the network). Batch size used was 24 and it was trained for 70 epochs with early stopping after 5 epochs without improvement. **B.** Overlay of probability (red) function with training input image. **C.** The probability map is processed using the last part of the LOD algorithm described in chapter 4: maximum values of backprojection extracted as lines and finding intersections that fit manufacturer constraints of grid. Intersections points are shown in red and the centre, the yellow point, is the final landmark used for transformation. In the last image, an example of bad detection is introduced. This can happen in one every 100 images, and additional mechanisms are needed to reject it (e.g., fitting between neighbour's prediction and position obtained).

classifies the images as acceptable or not before the line detection. The system blocks any position considered outside to prevent moving there. Due to high sample variability and the lack of enough training data, the accuracy for detecting outside regions is around 80%.

Second, precision can be increased using a similar algorithm to the one presented to validate light microscopy detection (chapter 4). For each position in SEM, the closest 20 neighbours are found. A linear model with minimum error is calculated using the RANSAC algorithm (Fischler & Bolles 1981) which takes as input the neighbours set and without including the position examined. The model is then used to predict the stage coordinates of the position. Thus, the prediction is judged successful if it is within less than a 30 µm radius of the position found in the detection [2]. Rejected points are then moved to a blocked status, which means, they will not be used for future transformations.

[2]The value of 30 µm is arbitrary and it is used to reject samples that are far away from predictions, it is not a measure of how precise the system is. It can be changed by the user.

As the scan progresses, each detected position is associated internally to the corresponding LM coordinate. With all coordinates at hand, transformation matrices are computed and cell stage coordinates in LM are predicted to the equivalent SEM coordinate stage positions. To finish with the *Navigator* program, a file is saved where all the maps and annotations are stored.

Correlation strategy by refinement of positions previous to acquisition achieves targeting precision below 5 µm.

For the acquisition of multiple volumes, the application Multisite presented in chapter 3 was used. Multisite can load the session stored by the Navigator and the coordinates of each individual target and crossing. The workflow proceeds as explained in chapter 3, with one difference (Flowchart 2). Usually, between two volume acquisitions at different positions, hours or days can pass, and during this time thermal and mechanical drift can change the precise location of a target. The current transformation, which initially had high precision, then has an error that must be adjusted.

To prevent this shift from the original position, the client application will perform a recalculation of the original position. First, it will extract a list of the closest crossings to the target position. Images of the 6 closest crossings are taken and a new affine transformation is computed. The original position is then overwritten by a new predicted position. Using a local transformation with points close to the region of interest (± 1100 µm) an average accuracy of 2±3 µm was achieved. Accuracy was estimated with 20 targeted cells over three different samples, always with precision enough to hit the cell of interest (Figure 5.6).

In theory, a transform using 6 landmarks has a bigger error than a transform using 20 landmarks. That is true if points are distributed in an ideal plane. However, MatTek dishes have a square grid with a side of 600 µm. Thus, acquiring 20 landmarks distributed as corners of squares, the area to be covered is around 2,4 mm in diameter. That implies moving to more distant positions which will increase the probability of finding a topological changes. The drop in precision could be solved using smaller grids.

Finer grids place crossings closer to the target, increasing the precision of the transformation. One example is the type of sapphire disk engraved grids used in high pressure freezing (figure 7). Unfortunately, sapphire disks have a small area to explore (2.5 x 2.5

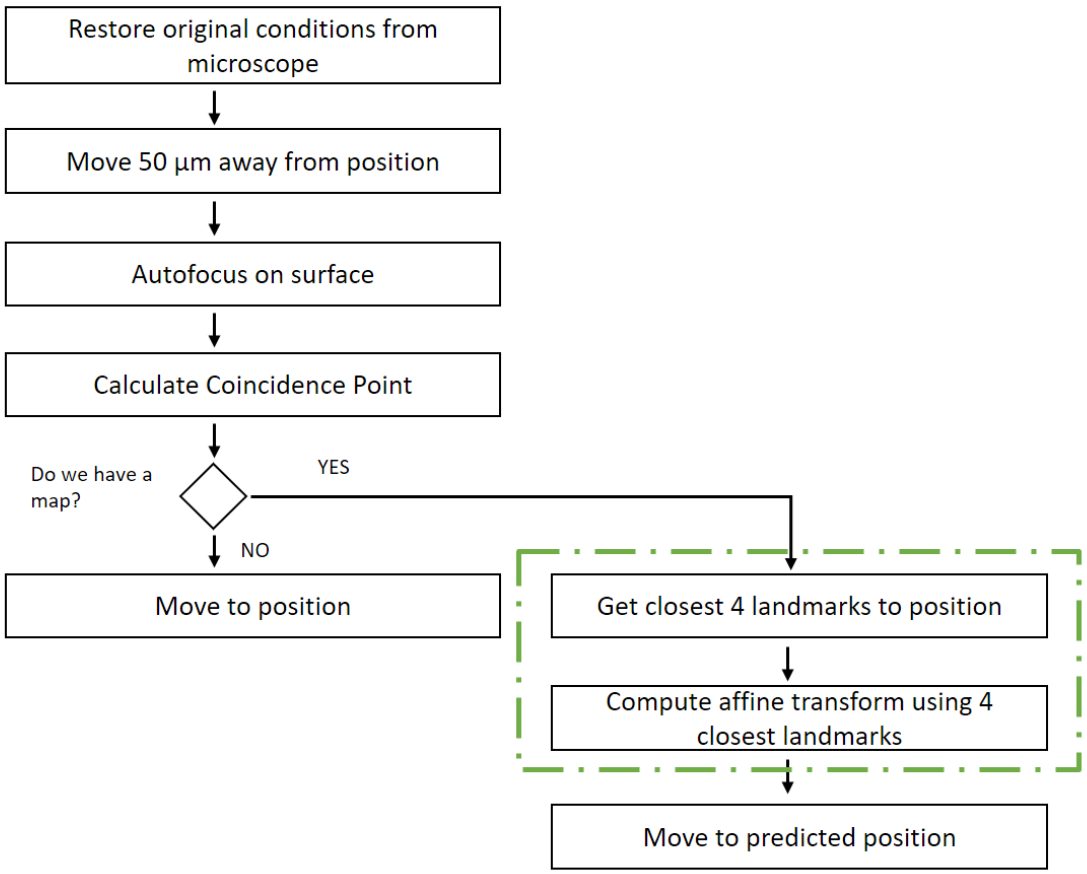

Flowchart 2. In step 1, SEM stage is moved to the precise position in stage coordinates of the target cell. This position will be the center of the region to be acquired. After restoring the original conditions, we have to move 50 µm in x direction. The coincidence point method will build a mark in the surface, thus, by moving away from the target, we avoid the mark affecting the coating of the target cell. After an initial quick autofocus on the surface and the coincidence point calculation, if a map is present in the client, the client will proceed to to recalculate the transform. The green marked square are extra operations are performed by CLEMSite to refine the position.

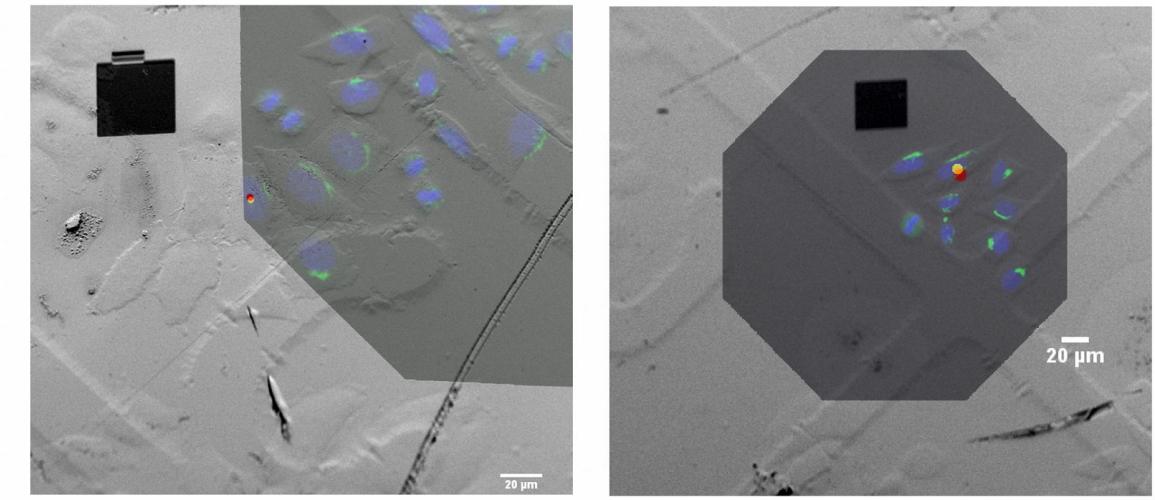

Fig. 5.6 Overlay of light microscopy and SEM targeted region. Red points mark the position targeted by CLEMSite and yellow points the original region of interest marked in light microscopy. The overlay was done by flipping horizontally the light microscopy image and rotating 45 degrees. Uniform scaling and translation was performed manually using as a reference the superimposed reflected light image against the SEM. Based on images, the estimated error for the first image is 2 µm and for the second image 3 µm.

mm) and there are no satisfactory grid systems available in the market [3] . If the system is changed, CLEMSite needs to be adapted by training different neural network models and simply indicate the new path with the new network model. CLEMSite reads the configuration of the grid (manufacturer measures and description of the embedded patterns) from an options file, which can be customized as long as the grid follows a squared or rectangular lattice.

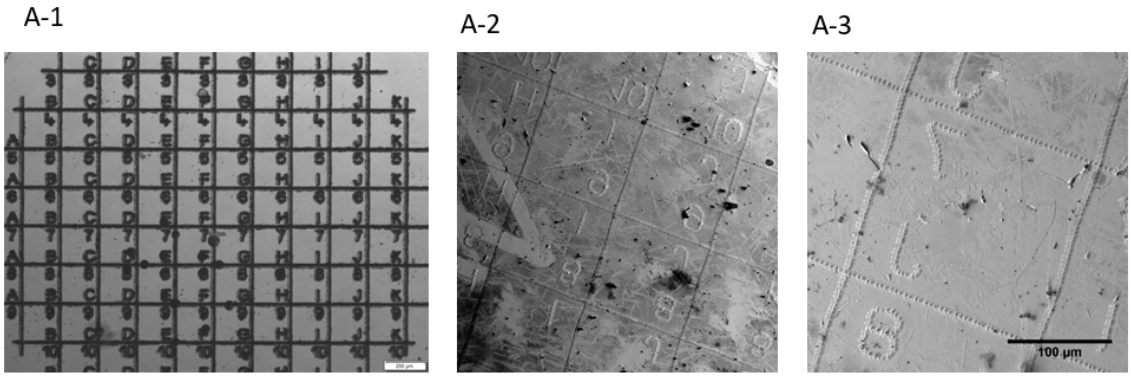

Fig. 5.7 Sapphire disc grid in transmitted light (A-1) and SEM (A-2 and A-3). The size of the squares (around 200 nm) could provide crossings closer to the real target, increasing then the precision.

[3] At the moment, the only manufacturer creating similar size grids is Ibidi (https://ibidi.com/content/157-clem). Due to the absence of engraved patterns in most part of the grid, our current system will need a more complex adaptation than the one described in this section.

Three automated executions successfully acquired more than 20 cell volumes per experiment.

The fully automated workflow was able to perform CLEM in multiple positions for several samples. CLEMSite moved to each position and triggered a new job in Atlas with pre-defined acquisition parameters. Automation steps involved milling the volume and update imaging parameters. For each position, a full cell volume was acquired and stored. Once acquisition was accomplished, CLEMSite moved the microscope stage to the next ROI, where a new acquisition started. The average time of acquisition per cell was around 4.5 hours.

In table 3 the number of cells targeted and successfully acquired for three of the solid phase transfection experiments is shown. It was counted if by any imperative reason, the current acquisition had to be stopped or the microscope manipulated for maintenance. Stops and other technical problems during a continuous run are listed with more details in table 4. One stop is always mandatory due to one the FIB voltage regulators (called suppressor), which is cannot maintain the ion beam flux for more than 3 consecutive days. To restore the ion beam, the process of recovery takes between 4 and 6 hours. This is counted in Table 4 as 'Out of suppressor'.

As discussed in chapter 3, it should be pointed out that the microscope is forced to do multiple acquisitions without stop and the commercial software and microscope hardware can fail in unexpected ways.

	Targeted cells	**EM datasets**	**Number of stops***
Exp I 13.04.	29	21	3
Exp II 19.10.	34	20	1
Exp III 20.11.	44	36	4

Table 5.3 **Automated screening datasets**.*Stop causes in table 5.4 marked with asterisk. Software errors fixed during the session are not counted as stop because the microscope was on hold until the problem was fixed.

In practice, as indicated in Table 5.5 (ROI incorrectly targeted), approximately 25% of the failures are cells incorrectly targeted. Incorrectly targeted entails that the precision expected was not achieved. The main reason was a failure in the automatic crossing identification in one of the positions, therefore providing an inaccurate transformation matrix. The causes are the poor manufacturing of MatTek grids and potential breaks or scratches in the block surface.

In a few cases of mistargeting, the cause of error was due to the relation between the central axis of the acquired cell and the volume acquired. Since the targeting is based

Cause	Sample 1	Sample 2	Sample 3	
*Out of suppressor**	1	1	1	
*Sample broken in two pieces**	1	0	0	
Unable to focus on sample surface	0	1	0	
CLEMSite bugs (e.g. trench not detected)	0	4	1	
*ESB detector failure (electronics) **	0	0	2	
Unexplained shutdown of ATLAS 5	0	0	1	
*FIB control failure (hardware)**	1	0	1	
	3	6	6	15

Table 5.4 **Causes of stop current acquisition.***Indicates that the microscope had to be stop, which means shut down and the full system had to be restarted. Otherwise, the system was paused and the problem was solved during the same acquisition.

	Sample 1	Sample 2	Sample 3	
ROl incorrectly targeted (partially acquired)	2	3	4	
ROI incorrectly targeted (missing)	0	1	1	
Incorrect sample from LM (mitotic, multinucleated, . . .)	4	1	4	
Outside sample	2	0	0	
Out of focus	2	7	0	
Scratches or accidents in sample	0	0	2	
	10	12	11	33

Table 5.5 **Causes of rejecting EM acquired volumes.**

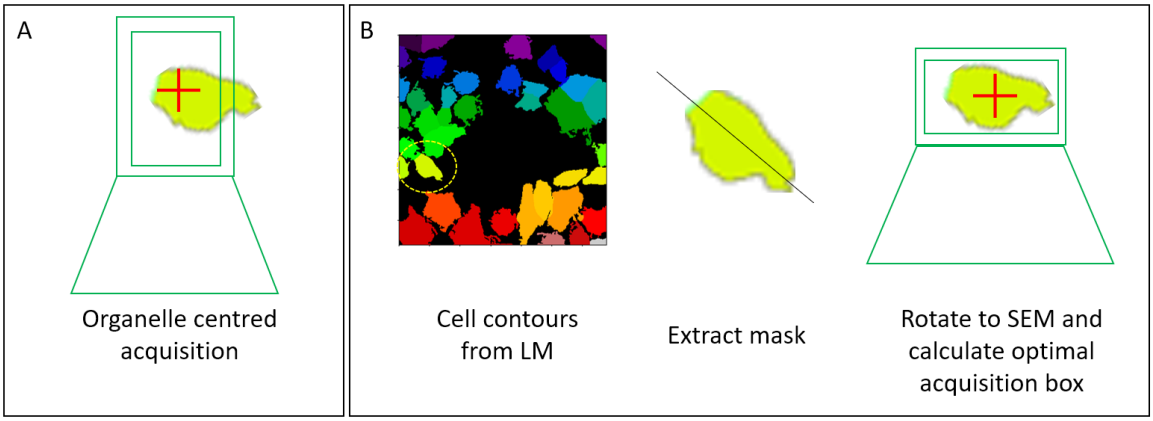

Fig. 5.8 A. A cell body contour and the boxes calculated for volume acquisition. If the organelle is not exactly in the gravity center or the cell, part of the cell body will be missed. B. In the suggested modification, cell contours can be extracted by traditional image analysis pipelines from transmitted light or cell body fluorescent dies (Meijering 2012) . The main axis of the contour can be used to fit an acquisition box. The cell is rotated as it is in the SEM sample and the box then fitted optimally.

on a single punctual position of the cell organelle and the cell can be oriented in any direction, the acquisition volume can miss part of the cell body (Figure 5.8-A).

A potential solution is to increase the size of the acquisition volume to fit the full cell. However, since cells can vary in width (e.g. Hela cells from 30 to 60 µm), there will be a lot of empty space imaged during the acquisition, which in consequence is a squander of beam time and storage space. A much better solution consists to analyze the cell contour of the cell using light microscopy images and place the volume of acquisition in an optimal position respect the centre of gravity of the cell. This has the advantage that the maximum volume of the cell body will be included (as illustrated in Figure 5.8-B). Thus, with a better grid system and an optimal acquisition box, the full workflow can be improved to obtain higher precision and optimal acquisition volumes.

Experiment with 14 siRNA treatments via solid phase transfection.

Following the classification of siRNA treatments according to their light microscopy phenotype (Appendix 1, Table 1), each phenotype presents the following similarities at the EM level:

Diffuse: cells present a distribution of vesicles (radius bigger than 100 nm) with no presence of GA stacks.

Tubular: The GA extends in a single connected ribbon along the nucleus. Usually no more than one stack is found per section. The ribbon can be tracked until a

perinuclear region with a high concentration of stacks- two or three together- can be found together with the MTOC.

Fragmented: Fragmentation can be presented at different degrees. Each fragment in the light microscopy corresponds to a stack or to a group of small stacks. Each fragment is apparently not connected with other stacks from other fragments. The MTOC can be found attached to one of the stacks.

Condensed: The Golgi ribbon is located in a confined volume in the perinuclear area. All stacks are interconnected or in very close proximity.

Except for diffuse phenotypes, if two treatments displaying the same phenotype are compared, they look very similar at the fluorescent and electron microscopy levels. The lack of differences at the ultrastructural level between treatments showing the same phenotype raises an interesting question about which mechanisms or circumstances are driving the morphology and disposition of the GA.

The next step is to quantify all the obtained data by stereology. As explained in the introduction, GA total volume, volumes of vesicles, number of cisternae and number of stacks can be measured for each volume. In the case of a solid phase transfection experiment with multiple phenotypes, the sample size is very small: two cells per phenotype in three different experiments, providing a total of 6 cells per phenotype. This means that after quantification only should be considered large effect sizes [4], which in the majority of cases, should be observable by visual inspection. To detect medium or small effect sizes, an increase of sample size is necessarily required (Krzywinski and Altman, 2013). Hence, any conclusion extracted from quantification, unless really remarkable, must be considered carefully.

The solid phase transfection experiment can be used as a fast screening method for electron microscopy of multiple phenotypes. Even if only large effect sizes should be considered, the benefit of EM is the observation of the full ultrastructure of the cell. Thus, if an interesting phenotype is found, a secondary screening can be done to obtain solid numbers and thorough analysis via EM. Then, tens of cells (60, three experiments with 20 cell volumes) should be enough to characterize further the phenotype and estimate smaller effect sizes.

In conjunction with sample size, there are specific considerations for quantification to be accounted for future experiments. Cells in a population can be at different stages of the cell cycle and present different phenotypes. Fragmented phenotypes can appear if

[4]The effect size is the difference between the negative control population and the examined population

(a) Diffuse

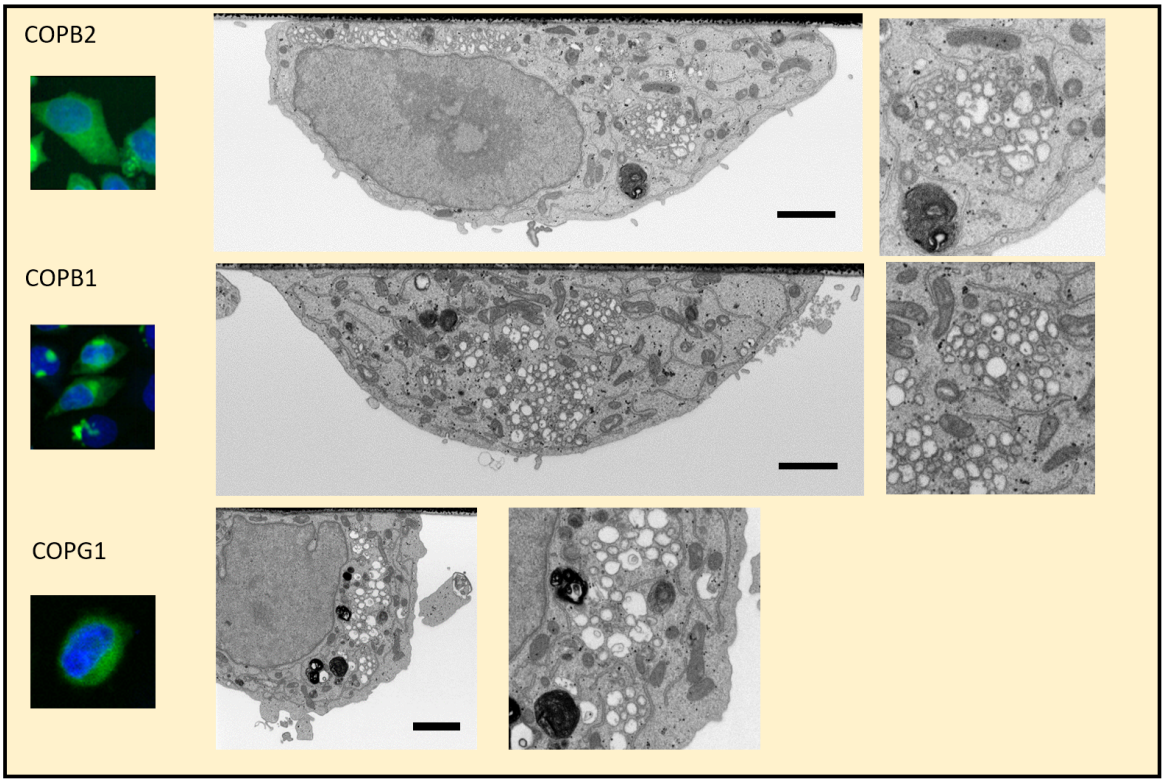

(b) Elongated

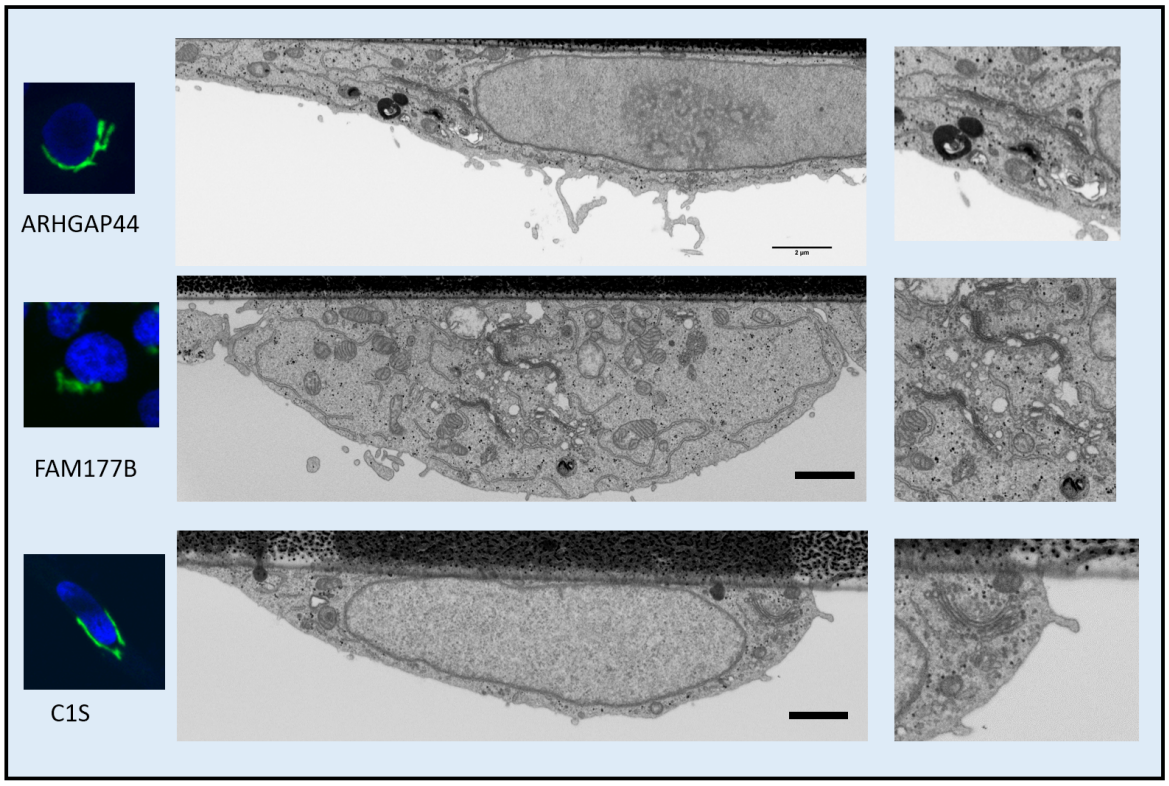

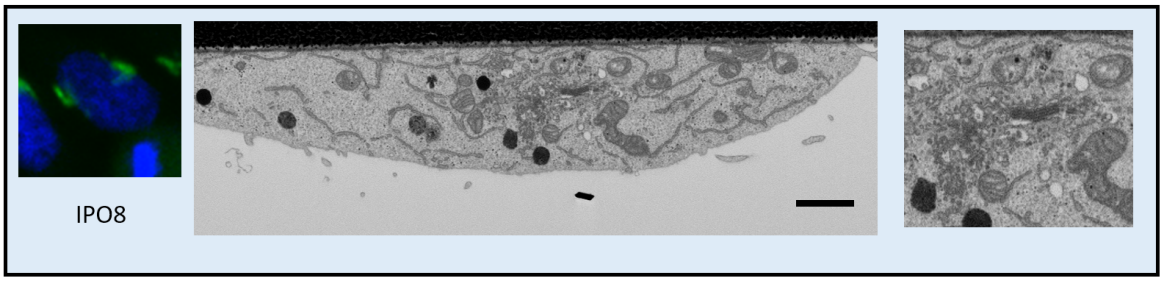

(c) Fragmented

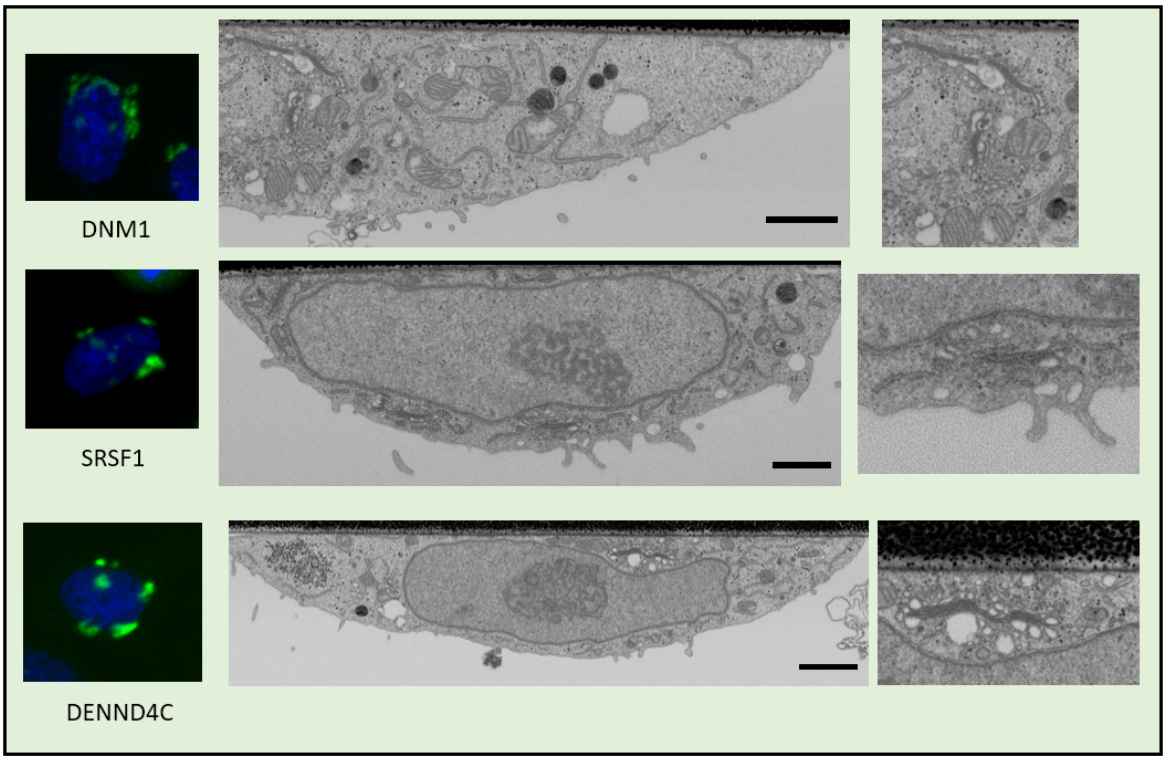

(d) Condensed

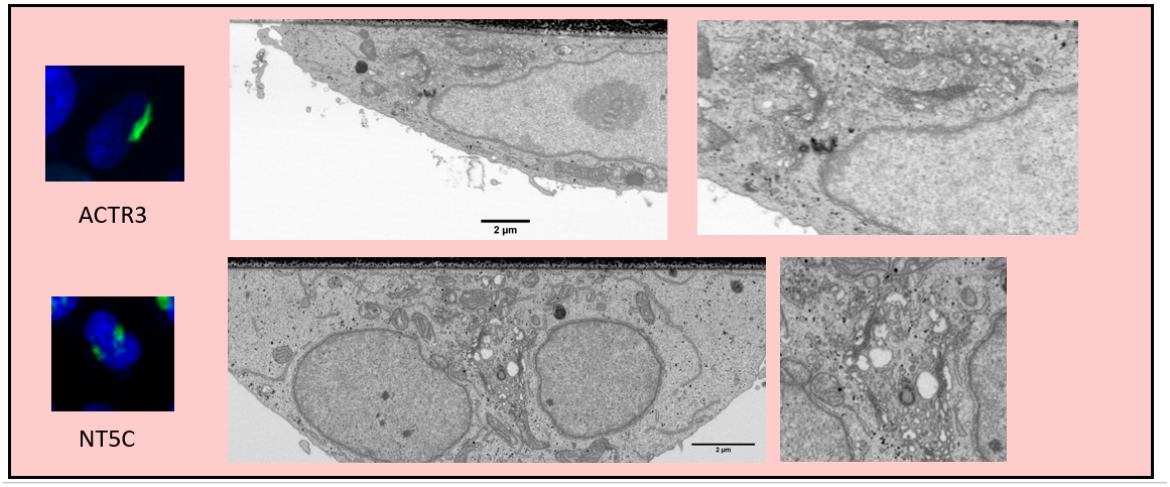

(e) Condensed

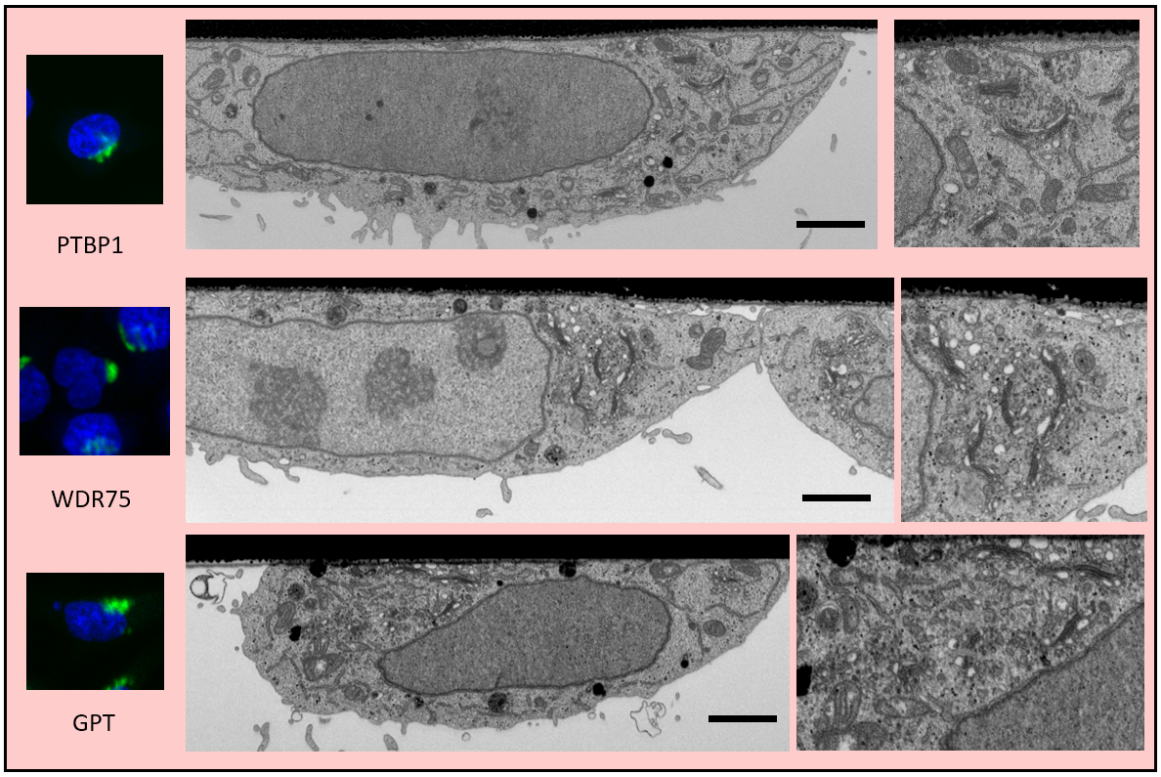

(f) Negative

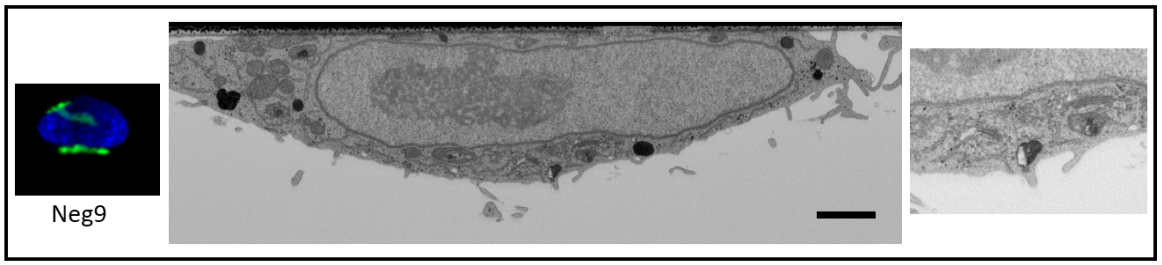

Fig. 5.9 Cells from the screening grouped by their expected phenotype. Each row with three pictures represents one treatment with a representative Hela cell acquired during the screening. All cell volumes have been acquired autonomously by the microscope and targeted via the CLEM strategy described in this chapter. Each cell has been cropped from the original fluorescence microscopy (10x zoomed by 5, DAPI nucleus, GalNACT2 for GFP) and then a random section in the volume where the GA can be observed. Brightness and contrast have been adjusted and the region of the GA cropped and scaled by 2x for visualization purposes. Scale bar: 2 µm.

a cell is in late S-phase or G2 (Lucocq, Berger and Warren, 1989; Ayala and Colanzi, 2017). In early G1, the Golgi starts to reassemble (Shorter and Warren, 2002) with the number and length of stacks continuously changing during a period of approximately one hour (Sourer, Pypaert and Warren, 1993). Besides, there is a growth in volume and length of the stacks during G1 which eventually doubles the GA volume in G2 (Sin and Harrison, 2016). Thence, parameters like cell volume and stack length may oscillate in a considerable range of values. To avoid this, there is the possibility of controlling the cell cycle stage using methods like thymidine arresting (Galgano and Schildkraut, 2006) or by PCNA immunolabelling and classification (Schönenberger et al., 2015).

Analysis of cells transfected with siRNA for COPB1

It was decided to perform a small-scale experiment where cells transfected with COPB1 siRNA were acquired in a small region (258 μm^2) (Figure 5.10). We will exemplify the data analysis process with the COPB1 gene KD, but for the rest of the genes screened, deeper analysis falls outside the main scope of this thesis.

Using GalNacT2-GFP fluorescent images as guidance, several cells were acquired and analyzed at the ultrastructural level in the same siRNA spot. Despite being in a very close proximity, some of the cells did not show the expected diffuse phenotype. The following paragraphs offer a concise analysis and description of these cells with the purpose of exemplify the type of analysis that could be applied to the full screening.

In the restricted area examined, cell 1, cell 2 and cell 3 presented a condensed, elongated and fragmented phenotype of the GA respectively. Their volume was estimated, taking into account the GA stacks and the surrounding TGN vesicles around it (Table 6). Cell 2 showed a higher state of fragmentation (approximately 4 different stacks in LM, confirmed by EM) and an abundance of tubular networks connecting them, which could be endosomal tubular networks as described in (Hierro et al. 2015, Lu & Hong 2014). Cell 2 is similar in GA volume to the negative control, but the fluorescent image indicates that a substantial part of GA was missing in the EM volume. The doubling in volume of the cells respect the negative control could indicate that they are at late S-phase or G2, where it has been shown the GA doubles in size (Sin & Harrison 2016) and the Golgi ribbon starts to fragment (Shima et al. 1997).

Cells 4 and 5 represented the expected phenotype, described morphologically as diffuse (Simpson et al., 2012). In EM, large amounts of vesicles bigger than 100 nm were observed (Figure 5.10, cells 4 and 5). A 3D model of this phenotype shows that big

vesicles form clusters in the regions where the GA should be present. All the vesicles were concentrated in a cell volume of 15x5x10 μm^3, approximately a third of the total cell volume.

Similar observations can be also found for other genes of the same family like COPBII and COPGI (Figure 5.9, Diffuse phenotypes). A possible explanation is that since anterograde transport is blocked, GA grows without membrane recycling and accumulates cargo. As some models suggest (Dmitrieff, Rao and Sens, 2013), the GA stack shape could be the result of an optimized cargo distribution along the cell. When the anterograde transport is blocked, like in the COPs case, Golgi stacks are disrupted in multiple vesicles.

Other possibility could be that blocking traffic generates a Golgi stress response which activates a signaling cascade that eventually leads to Golgi disruption. During the screen, a few cells undergoing cell death were accidentally found [5](Figure 5.9). They present vesicular clusters structures like in COP cells and darkened cytoplasm (Figure 8). When the cell starts an apoptotic process, individual cisternae divide into clusters of vesicles bigger than 100 nm. This process of Golgi disassembly during cell death has been well documented in (Hicks and Machamer, 2005; Landry et al., 2009). Wheter interfering with GA transport triggers an apoptotic signal that leads to a diffuse phenotype or the diffuse phenotype is the consequence of blocking transport, ultimately, generating an apoptotic signal, remains unclear. It would be interesting to compare time lapse light microscopy of the GA phenotype COPBI simultaneously

[5]Some cell death signs are disrupted mitochondria, absence of filopodia, cell shrinkage (round up of cell membrane), blebbing and nucleolar segregation, disrupted GA. In EM, a darkened cytoplasm is often seen in cells going under cell death. It indicates a chemical unbalance during sample preparation due to a change of pH or an alteration in cell membrane capabilities of permeabilization.

	Phenotype	**GA Estimated Volume (μm^3)**	**Golgi Vesicles $>$ 100 nm. (μm^3)**
Cell 1	Condensed	8.7	1.4
Cell 2*	Elongated	5.5	2
Cell 3	Fragmented	9.3	4.2
Cell 4	Diffuse	No presence of stacks	55
Cell 5	Diffuse	No presence of stacks	33.6
Negative control		5.4	2.3
Apoptotic cell		No presence of stacks	82.4

Table 5.6 Volumes measured from Figure 9 cells, and two additional cells from the screenings, one negative control and an apoptotic cell. (see materials and methods, data analysis). * In Cell 2, by looking at fluorescence, 1/3 of the GA is missing in the quantification.

with the appearance of several apoptotic markers. That could provide evidence that stress in the GA can ultimately generate apoptotic signals and that structural changes in GA would be the first ultrastructural signs of cell death before traditional apoptotic events start to manifest (chromatin condensation, blebbing,...).

Why other cells treated with the same siRNA displayed the expected phenotype and others do not, is a question that remains unclear. Possible causes are low transfection efficiency, the cell being in different part of cell cycle during the moment of imaging, heterogeneity in the effects of a cell population or a compensation mechanism able to bypass the canonical pathway of the gene affected. In any case, EM imaging of multiple cells could help to characterize the heterogeneous population of a treatment (siRNA knockdown, in this case) leading to new findings.

Discussion : stereology versus segmentation for quantification.

Stereology is a mathematical method that uses 2D information to estimate lengths, areas or volumes in the 3D space (Gundersen, 1986). With a good sampling strategy and only with a few sections, stereology can achieve 5 to 10% error in volume measures. Stereology has the advantage to provide a comparable quantitative measure faster than manual segmentation. On the other side, the numbers provided are averages and counts are executed manually. More complex probes require a good understanding in stereology principles and learning their right usage to avoid biases (Gundersen and Jensen, 1987).

Usually, around 100 sections are enough to quantify volumes of most part of the organelles inside the cell. In the FIB-SEM acquiring 100 serial sections, 200 nm apart, is performed by the FIB-SEM in about 4 hours. This provides enough information to inspect visually a phenotype for first time and by using stereology, it can serve as a valuable quantification.

Another approach is to obtain the full volume and shape by segmentation. Due to technical limitations of the FIB-SEM, a fully isotropic volume of 20 μm^3 with a pixel size of 8 nm requires about 2 days. This prevents us to scale the system and acquire multiple full volumes in a reasonable amount of time. In addition, manual modeling, which is, to paint manually labels for each pixel of the image, is tedious, prone to human errors and extremely time-consuming. Depending on the dataset, boundaries can be difficult to trace and quite often subjected to an interpretation of the person performing the tracing and generating the 3D model. On the other side, segmentation

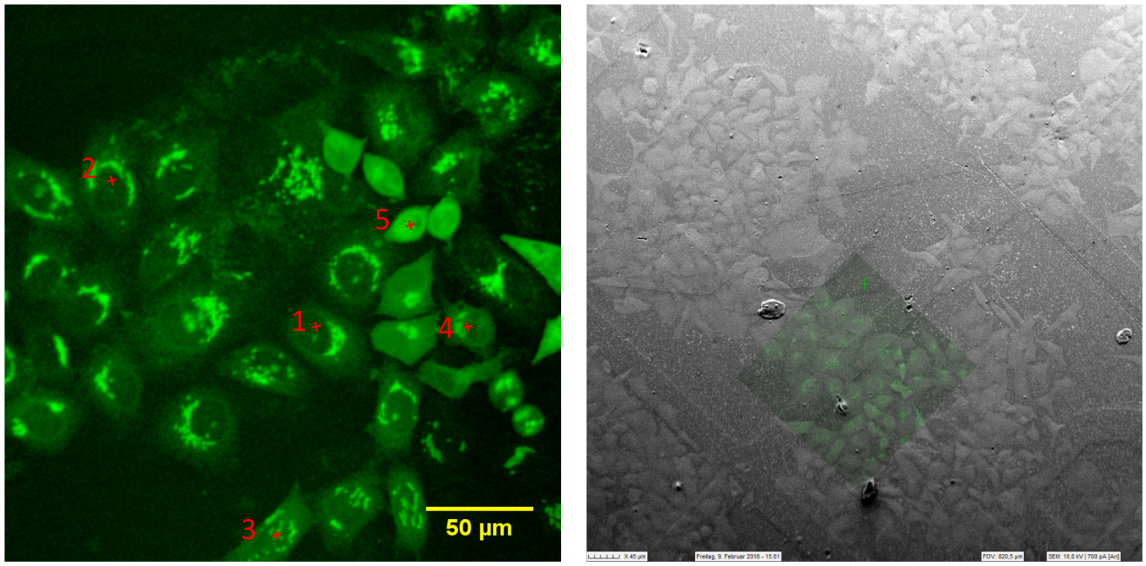

(a) GalNacT2 – GFP image of a region of 258 m^2. Cells selected for EM are numbered in red. Right image shows a superimposition of the green channel image with the SEM of the same correlated region. This region was specially selected for containing cells from a siRNA spot for COPB1.

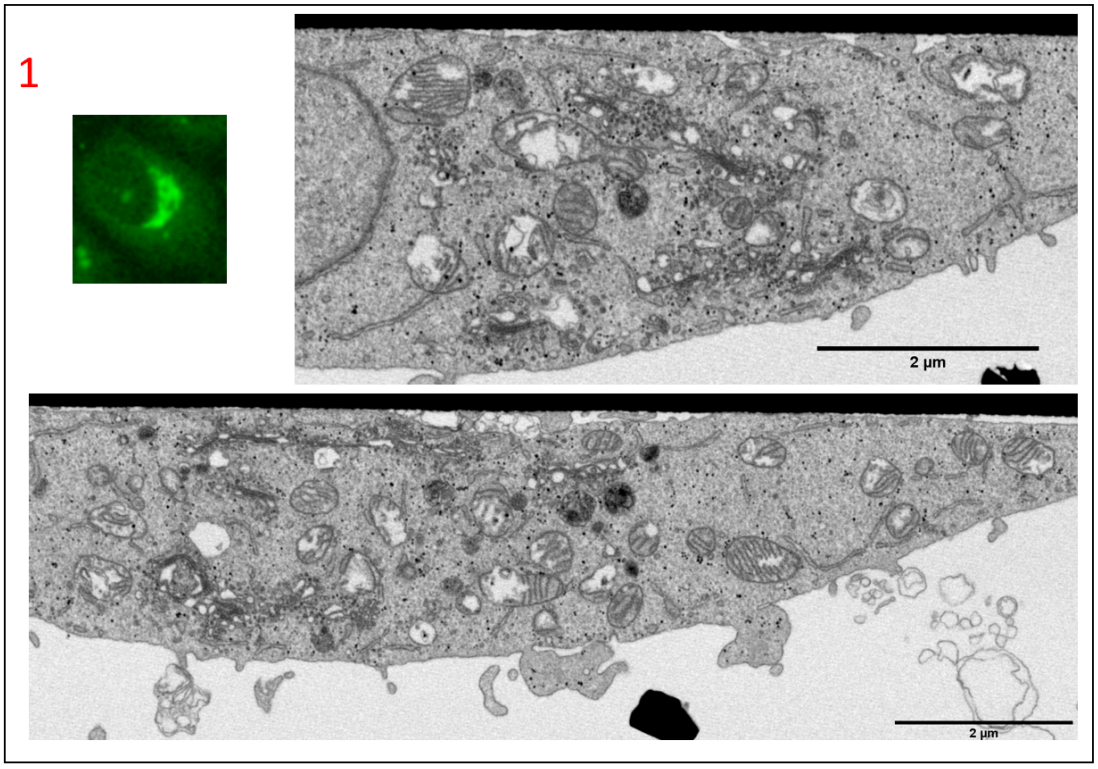

provides accurate volumes, with an error rate on isotropic volumes less than 1% (Liu et al., 2014) and a full 3D shape of the segmented object.

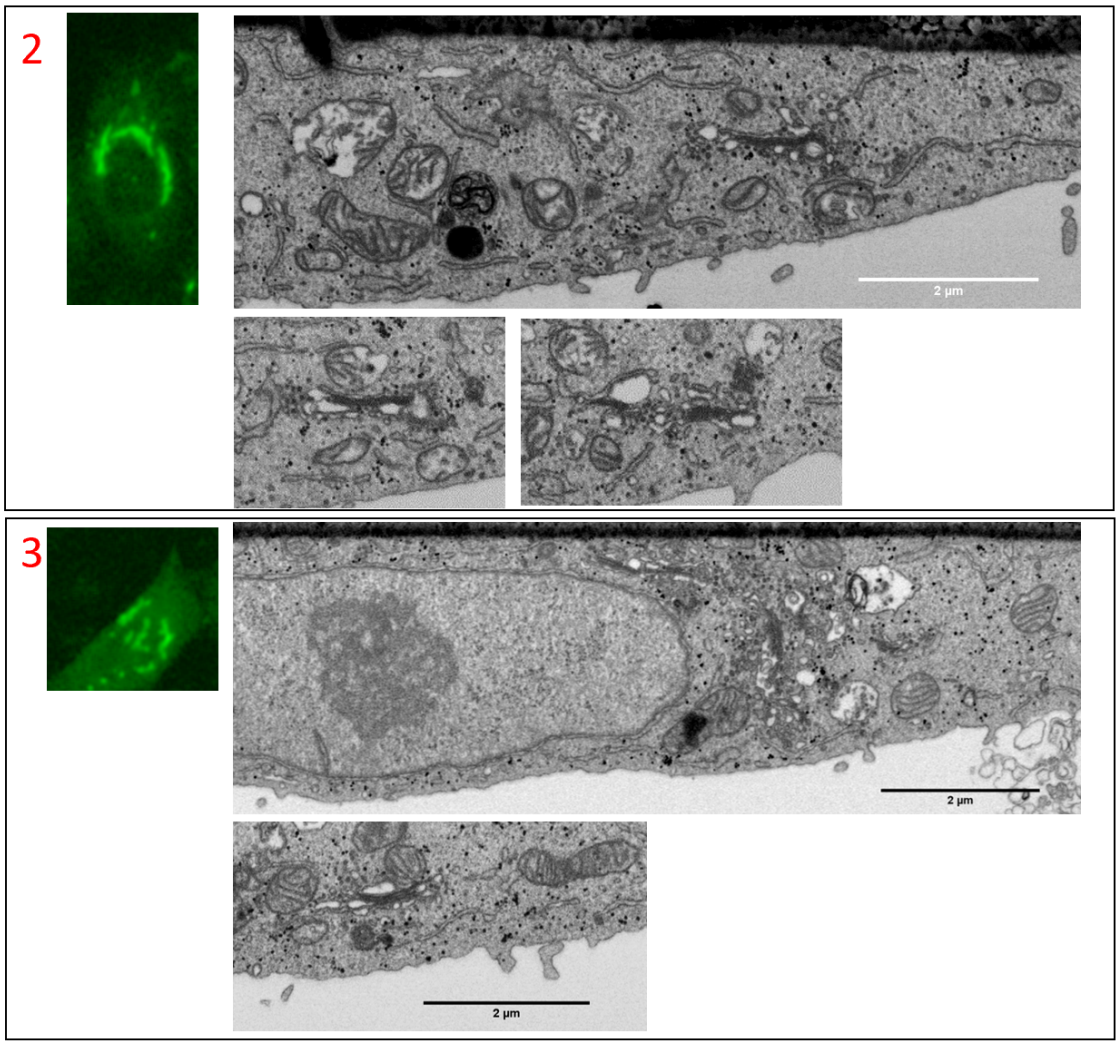
2
2 µm
3
2 µm
2 µm

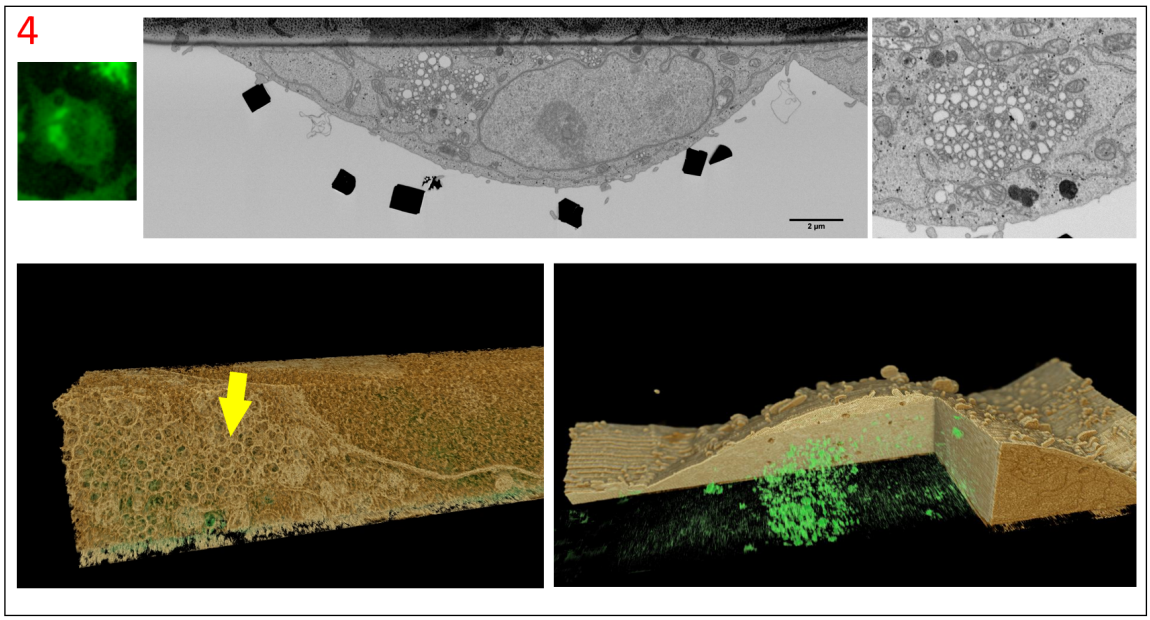
4
2 µm

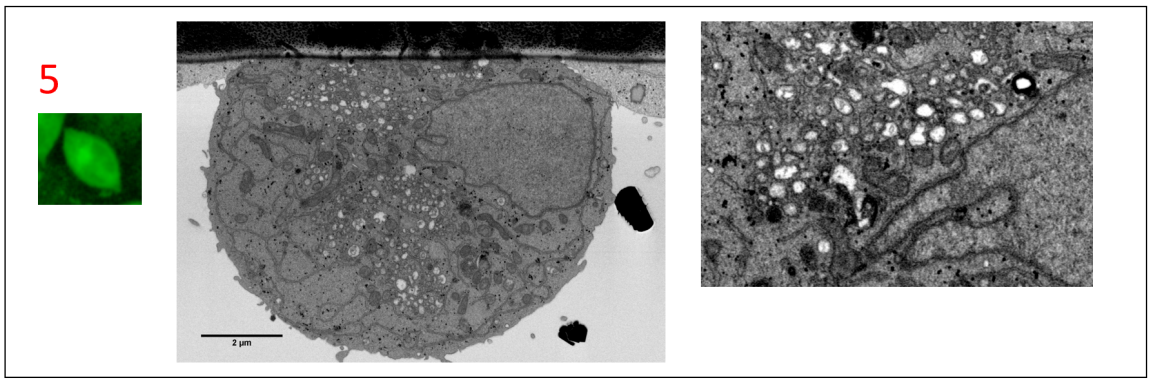

Fig. 5.10 Cell 1 phenotype can be described as condensed, cell 2 as elongated, cell 3 as fragmented and cells 4 and 5 as diffuse in different degrees. Cells are shown in GFP, then a section in EM and a crop of a region where the GA was present in another section. In Cell 4, bottom row shows a 3D model where the Golgi has been thresholded to show the density around big vesicles (yellow arrow). In the left image and the vesicle clusters (green blobs) in right bottom image. In cells 4 and 5, the GA region in EM of the right has been scaled to appreciate better the compacted vesiculated structure.

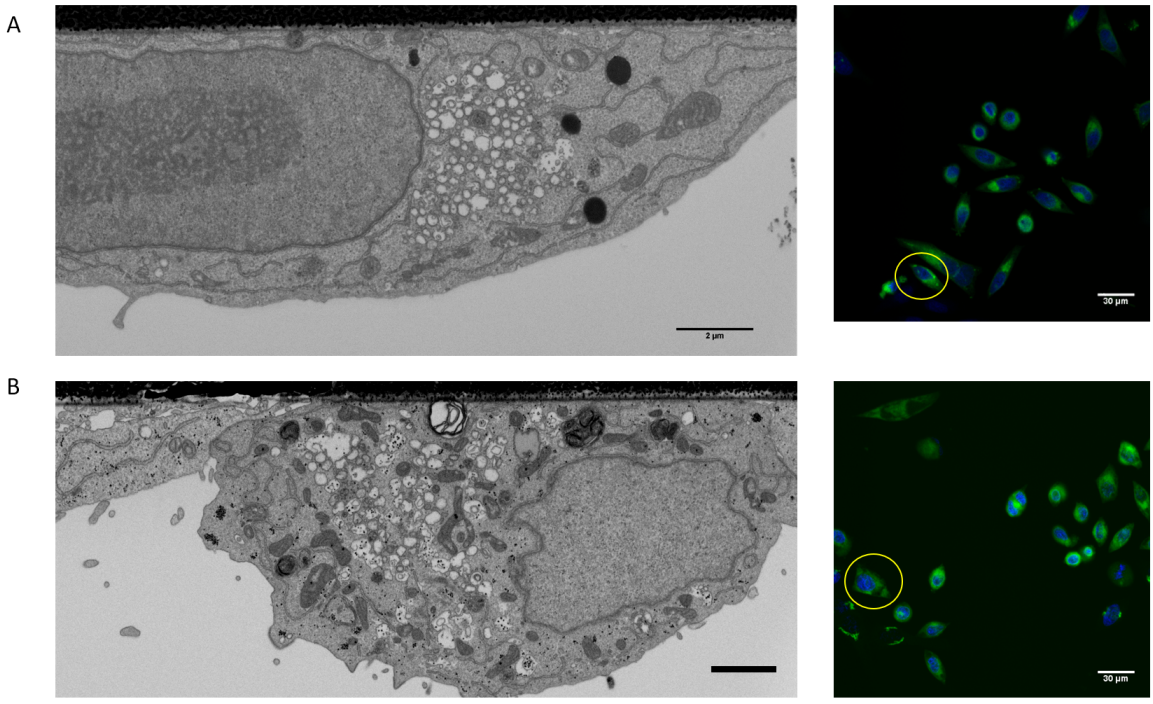

Fig. 5.11 COPB1 phenotype in A, AURKB in B.During one of the screenings, some cells were found with AURKB siRNA treatment under started apoptosis. It is known that under apoptosis, the GA matrix goes under proteolytic cleavage giving the appearance of clusters. Although the phenotype is not exactly the same as in COPB1, light microscopy images (GalNACT2-GFP for GA and DAPI for nucleus) and EM sections present similarities which could indicate a common pathway. Both A and B have the same scale.

Consequently, it has been the pursuit of many researches to achieve automatic image segmentation. Automatic segmentation has to deal with multiple problems. Here is a list of the most usual problems that every segmentation algorithm faces when dealing with electron microscopy volume data:

- **Data heterogeneity in shape and structure.** Biological data is known to be very heterogeneous. Stereotypical shapes are very rare and cells can show infinite varieties in morphology. Thus, heterogeneity usually poses a problem for supervised algorithms, which need to be versatile enough to handle variations in the same way as a human would do.
- **Continuity of contours.** Contours, like membranes, can be distorted by changes in contrast uniformity, almost to disappear or by other potential artefacts, like disappearance of the structure or bad alignments between sections. Cracks, occlusions or missing parts are problems that often need manual curation for algorithms to work properly.
- **Low signal to noise ratio.**
- **Discontinuities in non-isotropic data.**

Because of this, sophisticated methods usually require expert knowledge for parametrization and fail to succeed beyond academic circles. For example, variational segmentation, a type of physical modeling by minimization of energy functions was considered the future of automatic segmentation not so long ago (Chambolle, 1995). But time showed that defining the conditions for each data distribution was difficult and the hard parametrization conditions left its usage only to experts in the field.

Supervised methods, particularly known as machine learning, managed to overcome unsupervised methods. Instead of generating a mathematical model giving the probability of a pixel to belong to a class, the efforts are centered on obtaining training data to classify each image according to examples. Until 2012, most of the supervised methods were feature based. Features usually define a property of the object observed. After the tedious and non-trivial task of defining and calculating features, a general method called classifier can be used to weight if a pixel or set of pixels fulfills the conditions of belonging to a class. Random forests or support vector machines are popular methods used for classification. For example, a group of pixels with elongated shape, stripes and double membranes (two edges separate a few pixels) belong to the class defined as a mitochondrion.

In 2012, the ImageNet contest, which consisted in automatically label 15 million images into 22,000 categories, was won by a convolutional neural network by a large difference compared to typical feature classifiers (Krizhevsky, Sutskever and Hinton, 2012). Since then, the so-called deep learning methods have evolved and proved to be the ultimate technology for segmentation. They can be close to human performance in structure recognition and very good in segmentation. Some examples in cell biology are (Chen et al., 2017; Sadanandan et al., 2017; Haberl et al., 2018; Januszewski et al., 2018) and the number of publications reporting the usage of neural networks for segmentation keeps growing every month.

With the advent in the next years of fully automated segmentation tools, it is natural to wonder what is the best approach: thick sections on multiple datasets and get average measurements of selected descriptors, like volume, or thin sections on less than ten datasets and precise 3D models. The answer, depends on the biological question at hand.

A good starting point is to consider the number of treatments or conditions. With only two conditions, it is good enough to acquire one or two isotropic or thin sections and model them in 3D. If quantification is required, a stereological approach could be applied to a group of EM volumes acquired automatically. If the amount of conditions grows it would be better to start with a quick screening of the phenotypes, similar to what was presented in the 14 siRNA experiment via solid phase transfection. Quantification via stereology of multiple genes and their posterior comparison can lead to interesting discoveries. Once an interesting phenotype is discovered, a couple of full isotropic or thin section volumes can be acquired to generate a volume complete representation.

5.4 Summary and conclusion

Here I presented a method able to automatically acquire tens of cell EM volumes with the possibility to relate phenotypes at the fluorescence level with their ultrastructure. The novelty comes with a new CLEM system that allows the possibility to automatically target tens of datasets. After inspecting more than 50 EM volumes with 14 different siRNA treatments, only the knockdowns affecting COP components exhibited large effect sizes compared to negative control. When different treatments were grouped by phenotype, visual inspection of the EM volumes did not show any particular difference.

The study helped to set up a solid workflow for future experiments by acquiring multiple 3D volumes. By the practical application of the software in a real experiment, the developed software gained in robustness, a better experimental design was achieved together with ideas for future improvements (like reducing the glass bottom dish grid size).

Finally, the pros and cons of stereology and segmentation were examined. Even if the rapid progression of automatic segmentation during the last years foretells promising outcomes, stereology is still a tool to be accounted for. The combination of the new deep learning detection algorithms with stereology could potentially achieve rapid quantifications with non-isotropic data and to deliver solid numerical data comparisons.

We expect that comparison of phenotypes at the ultrastructural level can be used in the future to reveal new biological insights about the nature of GA and its relation with other organelles. Thus, the 3D EM volumes produced in this experiment can be a valuable source for the scientific community.

Acknowledgments and contributions

The correlation strategy was implemented by José Miguel Serra Lleti[1]. Analysis of data was also done by José Miguel Serra Lleti. Anna M. Steyer[1], Nicole L. Schieber[1] and José Miguel Serra Lleti prepared samples for EM. Yannick Schwab[1], Anna M. Steyer[1], Nicole L. Schieber[1], Beate Neumann[2], Volker Hilsentein[2] and Paolo Ronchi[3] contributed to discussions.

Affiliations

(1) Cell Biology and Biophysics Unit, Schwab Team, European Molecular Biology Laboratory, 69117 Heidelberg, Germany

(2) Advanced Light Microscopy Facility, European Molecular Biology Laboratory, 69117 Heidelberg, Germany

(3) Electron Microscopy Core Facility, European Molecular Biology Laboratory, 69117 Heidelberg, Germany

References

Arnold, J., Mahamid, J., Lucic, V., de Marco, A., Fernandez, J.-J., Laugks, T., Mayer, T., Hyman, A. A., Baumeister, W. and Plitzko, J. M. (2016) 'Site-Specific Cryo-focused Ion Beam Sample

Preparation Guided by 3D Correlative Microscopy', *Biophysical Journal*, 110(4), pp. 860–869. doi: 10.1016/j.bpj.2015.10.053.

Ayala, I. and Colanzi, A. (2017) 'Mitotic inheritance of the Golgi complex and its role in cell division', *Biology of the Cell*, 109(10), pp. 364–374. doi: 10.1111/boc.201700032.

Beckwith, M. S., Beckwith, K. S., Sikorski, P., Skogaker, N. T., Flo, T. H. and Halaas, Ø. (2015) 'Seeing a Mycobacterium-Infected Cell in Nanoscale 3D: Correlative Imaging by Light Microscopy and FIB/SEM Tomography.', *PloS one*. Public Library of Science, 10(9), p. e0134644. doi: 10.1371/journal.pone.0134644.

Briggman, K. L. and Bock, D. D. (2012) 'Volume electron microscopy for neuronal circuit reconstruction', *Current Opinion in Neurobiology*, 22(1), pp. 154–161. doi: 10.1016/j.conb.2011.10.022.

Cao, T., Zach, C., Modla, S., Powell, D., Czymmek, K. and Niethammer, M. (2014) 'Multi-modal Image Registration for Correlative Microscopy'.

Chambolle, A. (1995) 'Image Segmentation by Variational Methods: Mumford and Shah Functional and the Discrete Approximations', *SIAM Journal on Applied Mathematics.* Society for Industrial and Applied Mathematics, 55(3), pp. 827–863. doi: 10.1137/S0036139993257132.

Chen, M., Dai, W., Sun, S. Y., Jonasch, D., He, C. Y., Schmid, M. F., Chiu, W. and Ludtke, S. J. (2017) 'Convolutional neural networks for automated annotation of cellular cryo-electron tomograms', *Nature Methods*, 14(10), pp. 983–985. doi: 10.1038/nmeth.4405.

Cruz-Orive, L. M., Howard, C. V. and Reid, M. G. (1999) 'Unbiased Stereology: Three-Dimensional Measurement in Microscopy.', *Journal of Anatomy*. Wiley-Blackwell, 194(1), pp. 153–157. doi: 10.1046/j.1469-7580.1999.194101536.x.

Dmitrieff, S., Rao, M. and Sens, P. (2013) 'Quantitative analysis of intra-Golgi transport shows intercisternal exchange for all cargo.', Proceedings of the National Academy of Sciences of the United States of America. National Academy of Sciences, 110(39), pp. 15692–7. doi: 10.1073/pnas.1303358110.

Erfle, H., Neumann, B., Rogers, P., Bulkescher, J., Ellenberg, J. and Pepperkok, R. (2008) 'Work flow for multiplexing siRNA assays by solid-phase reverse transfection in multiwell plates.', *Journal of biomolecular screening*, 13(7), pp. 575–80. doi: 10.1177/1087057108320133.

Ferguson, S., Steyer, A. M., Mayhew, T. M., Schwab, Y. and Lucocq, J. M. (2017) 'Quantifying Golgi structure using EM: combining volume-SEM and stereology for higher throughput', *Histochemistry and Cell Biology*, 147(6), pp. 653–669. doi: 10.1007/s00418-017-1564-6.

Fischler, M. A. and Bolles, R. C. (1981) 'Random sample consensus: a paradigm for model fitting with applications to image analysis and automated cartography', *Communications of the ACM*. ACM, 24(6), pp. 381–395. doi: 10.1145/358669.358692.

Galgano, P. J. and Schildkraut, C. L. (2006) 'G1/S Phase Synchronization using Double Thymidine Synchronization.', *CSH protocols.* Cold Spring Harbor Laboratory Press, 2006(2), p. pdb.prot4487. doi: 10.1101/pdb.prot4487.

Gong, Z., Chen, B. K., Liu, J., Zhou, C., Anchel, D., Li, X., Ge, J., Bazett-Jones, D. P. and Sun, Y. (2014) 'Fluorescence and SEM correlative microscopy for nanomanipulation of subcellular structures', *Light: Science & Applications.* Nature Publishing Group, 3(11), p. e224. doi: 10.1038/lsa.2014.105.

Gundersen, H. J. (1986) 'Stereology of arbitrary particles. A review of unbiased number and size estimators and the presentation of some new ones, in memory of William R. Thompson.', *Journal of microscopy*, 143(Pt 1), pp. 3–45.

Gundersen, H. J. and Jensen, E. B. (1987) 'The efficiency of systematic sampling in stereology and its prediction.', *Journal of microscopy*, 147(Pt 3), pp. 229–63.

Haberl, M. G., Churas, C., Tindall, L., Boassa, D., Phan, S., Bushong, E. A., Madany, M., Akay, R., Deerinck, T. J., Peltier, S. T. and Ellisman, M. H. (2018) 'CDeep3M—Plug-and-Play cloud-based deep learning for image segmentation', *Nature Methods*. Nature Publishing Group, 15(9), pp. 677–680. doi: 10.1038/s41592-018-0106-z.

Hasegawa, T., Yamamoto, T., Hongo, H., Qiu, Z., Abe, M., Kanesaki, T., Tanaka, K., Endo, T., de Freitas, P. H. L., Li, M. and Amizuka, N. (2018) 'Three-dimensional ultrastructure of osteocytes assessed by focused ion beam-scanning electron microscopy (FIB-SEM)', *Histochemistry and Cell Biology.* Springer Berlin Heidelberg, 149(4), pp. 423–432. doi: 10.1007/s00418-018-1645-1.

Hicks, S. W. and Machamer, C. E. (2005) 'Golgi structure in stress sensing and apoptosis', *Biochimica et Biophysica Acta (BBA) - Molecular Cell Research.* Elsevier, 1744(3), pp. 406–414. doi: 10.1016/J.BBAMCR.2005.03.002.

Hierro, A., Gershlick, D. C., Rojas, A. L. and Bonifacino, J. S. (2015) 'Formation of Tubulovesicular Carriers from Endosomes and Their Fusion to the trans-Golgi Network',*International Review of Cell and Molecular Biology.* Academic Press, 318, pp. 159–202. doi: 10.1016/BS.IRCMB.2015.05.005.

Januszewski, M., Kornfeld, J., Li, P. H., Pope, A., Blakely, T., Lindsey, L., Maitin-Shepard, J., Tyka, M., Denk, W. and Jain, V. (2018) 'High-precision automated reconstruction of neurons with flood-filling networks', *Nature Methods*. Nature Publishing Group, p. 1. doi: 10.1038/s41592-018-

0049-4.

Jimenez, N., Van Donseelar, E. G., DE WINTER, D. A. M., VOCKING, K., VERKLEIJ, A. J. and POST, J. A. (2010) 'Gridded Aclar: preparation methods and use for correlative light and electron microscopy of cell monolayers, by TEM and FIB-SEM',*Journal of Microscopy*, 237(2), pp. 208–220. doi: 10.1111/j.1365-2818.2009.03329.x.

Krizhevsky, A., Sutskever, I. and Hinton, G. E. (2012) 'ImageNet Classification with Deep Convolutional Neural Networks'.

Krzywinski, M. and Altman, N. (2013) 'Power and sample size', *Nature Methods*, 10(12), pp. 1139–1140. doi: 10.1038/nmeth.2738.

Kukulski, W., Schorb, M., Welsch, S., Picco, A., Kaksonen, M. and Briggs, J. A. G. (2011) 'Correlated fluorescence and 3D electron microscopy with high sensitivity and spatial precision.', *The Journal of cell biology*, 192(1), pp. 111–9. doi: 10.1083/jcb.201009037.

Kukulski, W., Schorb, M., Welsch, S., Picco, A., Kaksonen, M. and Briggs, J. A. G. (2012) Precise, Correlated Fluorescence Microscopy and Electron Tomography of Lowicryl Sections Using Fluorescent Fiducial Markers. Academic Press. doi: 10.1016/B978-0-12-416026-2.00013-3.

Landry, M.-C., Sicotte, A., Champagne, C. and Lavoie, J. N. (2009) 'Regulation of cell death by recycling endosomes and golgi membrane dynamics via a pathway involving Src-family kinases, Cdc42 and Rab11a.', *Molecular biology of the cell*. American Society for Cell Biology, 20(18), pp. 4091–106. doi: 10.1091/mbc.e09-01-0057.

Liu, T., Jones, C., Seyedhosseini, M. and Tasdizen, T. (2014) 'A modular hierarchical approach to 3D electron microscopy image segmentation.', *Journal of neuroscience methods.* NIH Public Access, 226, pp. 88–102. doi: 10.1016/j.jneumeth.2014.01.022.

Lu, L. and Hong, W. (2014) 'From endosomes to the trans-Golgi network', *Seminars in Cell & Developmental Biology*, 31, pp. 30–39. doi: 10.1016/j.semcdb.2014.04.024.

Lucocq, J. M., Berger, E. G. and Warren, G. (1989) 'Mitotic Golgi fragments in HeLa cells and their role in the reassembly pathway.', *The Journal of cell biology.* The Rockefeller University Press, 109(2), pp. 463–74.

Meijering, E. (2012) 'Cell Segmentation: 50 Years Down the Road [Life Sciences]', IEEE Signal Processing Magazine, 29(5), pp. 140–145. doi: 10.1109/MSP.2012.2204190.

Nam, D., Mantell, J., Hodgson, L., Bull, D., Verkade, P. and Achim, A. (2014) 'Feature-based registration for correlative light and electron microscopy images', in 2014 IEEE International Conference on Image Processing (ICIP). IEEE, pp. 3567–3571. doi: 10.1109/ICIP.2014.7025724.

Nishita, M., Satake, T., Minami, Y. and Suzuki, A. (2017) 'Regulatory mechanisms and cellular functions of non-centrosomal microtubules', *The Journal of Biochemistry*, 162(1), pp. 1–10. doi: 10.1093/jb/mvx018.

Qian, Y., Bi, M., Tan, T. and Yu, K. (2016) 'Very Deep Convolutional Neural Networks for Noise Robust Speech Recognition', IEEE/ACM Transactions on Audio, Speech, and Language Processing, 24(12), pp. 2263–2276. doi: 10.1109/TASLP.2016.2602884.

Ronneberger, O., Fischer, P. and Brox, T. (2015) 'U-Net: Convolutional Networks for Biomedical Image Segmentation', in. Springer, Cham, pp. 234–241. doi: 10.1007/978-3-319-24574-4_28.

Sadanandan, S. K., Ranefall, P., Le Guyader, S. and Wählby, C. (2017) 'Automated Training of Deep Convolutional Neural Networks for Cell Segmentation', *Scientific Reports.* Nature Publishing Group, 7(1), p. 7860. doi: 10.1038/s41598-017-07599-6.

Sartori, A., Gatz, R., Beck, F., Rigort, A., Baumeister, W. and Plitzko, J. M. (2007) 'Correlative microscopy: Bridging the gap between fluorescence light microscopy and cryo-electron tomography', *Journal of Structural Biology*, 160(2), pp. 135–145. doi: 10.1016/j.jsb.2007.07.011.

Schönenberger, F., Deutzmann, A., Ferrando-May, E. and Merhof, D. (2015) 'Discrimination of cell cycle phases in PCNA-immunolabeled cells.',*BMC bioinformatics.* BioMed Central, 16, p. 180. doi: 10.1186/s12859-015-0618-9.

Shima, D. T., Haldar, K., Pepperkok, R., Watson, R. and Warren, G.(1997) 'Partitioning of the Golgi apparatus during mitosis in living HeLa cells.', *The Journal of cell biology*. The Rockefeller University Press, 137(6), pp. 1211–28.

Shorter, J. and Warren, G. (2002) 'Golgi Architecture and Inheritance', Annual Review of Cell and Developmental Biology. Annual Reviews 4139 El Camino Way, P.O. Box 10139, Palo Alto, CA 94303-0139, USA , 18(1), pp. 379–420. doi: 10.1146/annurev.cellbio.18.030602.133733.

Siklós, L. and Kuhnt, U. (1991) 'Algorithm for point-to-point correlation of geometrically nearly similar microscopic objects.', *Computer methods and programs in biomedicine*, 35(1), pp. 53–7.

Simonyan, K. and Zisserman, A.(2014) 'Very Deep Convolutional Networks for Large-Scale Image Recognition'. arXiv:1409.1556

Simpson, J. C., Joggerst, B., Laketa, V., Verissimo, F., Cetin, C., Erfle, H., Bexiga, M. G., Singan, V. R., Hériché, J.-K., Neumann, B., Mateos, A., Blake, J., Bechtel, S., Benes, V., Wiemann, S., Ellenberg, J. and Pepperkok, R. (2012) 'Genome-wide RNAi screening identifies human proteins with a regulatory function in the early secretory pathway.', *Nature cell biology.* Nature Publishing Group, a division of Macmillan Publishers Limited. All Rights Reserved., 14(7), pp. 764–74. doi: 10.1038/ncb2510.

Sin, A. T.-W. and Harrison, R. E. (2016) 'Growth of the Mammalian Golgi Apparatus during Interphase', Molecular and Cellular Biology, 36(18), pp. 2344–2359. doi: 10.1128/MCB.00046-16.

Sourer, E., Pypaert, M. and Warren, G. (1993) The Golgi Stack Reassembles during Telophase before Arrival of Proteins Transported from the Endoplasmic Reticulum.

Titze, B. and Genoud, C. (2016) Volume scanning electron microscopy for imaging biological ultrastructure, *Biology of the Cell.* doi: 10.1111/boc.201600024.

Wang, C.-W., Ka, S.-M. and Chen, A. (2015) 'Robust image registration of biological microscopic images', *Scientific Reports.* Nature Publishing Group, 4(1), p. 6050. doi: 10.1038/srep06050.

Zhu, B., Liu, J. Z., Cauley, S. F., Rosen, B. R. and Rosen, M. S.(2018) 'Image reconstruction by domain-transform manifold learning',*Nature*. Nature Publishing Group, 555(7697), pp. 487–492. doi: 10.1038/nature25988.

6

Elucidating causes of asymmetric nuclear damage in cancer cells after acute tetraploidy with CLEM

6.1 Introduction

During evolution, mammalian cells have developed a surveillance system against DNA lesions, the DNA damage response (DDR). DDR is a complex signaling network able to arrest the cell cycle and recruit the necessary components to repair the damaged DNA [1] . If the cell is considered beyond remediation, the DDR activates a cascade able to trigger senescence or apoptosis [2].

In the cell cycle, endogenous breaks, like double strand breaks, are common during S phase. They appear in loci where the replication forks are progressing slowly, especially in genome regions with high topological constraints or with particular structures (repetitive sequences, telomeres,...). These events put the cell under a condition known as replication stress (RS) and they are the main cause of DDR triggering. Many of the errors (double strand breaks) will be repaired during mitosis, but an important fraction is transferred to daughter cells where they become sequestered during G1 in 53BP1 bodies, a sort of repairing stations (C. Lukas et al. 2011).

[1] Some interesting related reviews on this topic are (Ciccia & Elledge 2010) , (J. Lukas et al. 2011) and (Hanawalt 2015).

[2] A conflict of signaling between p53 and Rb pathways will trigger and exit from proliferative state into a quiescence cell state. More details of this process can be read at (Ben-Porath & Weinberg 2005).

It is also known that primary mitotic errors can contribute to DNA breakage. Translocations during cytokinesis errors, dicentric chromosomes or mitotic delays caused by spindle alterations are some examples. What is the probability that mitotic aberrations increase DNA damage and vice versa? In (S Pedersen et al. 2016), the potential relationship between RS and mitotic aberrations was dissected in several experiments. By examining the temporal and spatial profiles of depleted cell cycle regulators by siRNA knockdowns, they were able to distinguish two main patterns.

From the 47 siRNAs selected, one cluster of genes showed an initial increase in mitotic aberrations, and afterwards, an increase in DNA damage. Similarly, but in inverse relationship, another cluster which was mostly formed by mRNA related to splicing factors, displayed high DNA damage during S and G2 phase and a consecutive increase in mitotic delays and segregation problems. These results confirmed that DDR and mitotic aberrations are correlated events but mechanistically different.

From the first cluster, where depletion of the proteins increased the probability of posterior mitotic aberrations, a certain fraction of cells was able to survive the first mitosis. However, survival was often accompanied with cytokinesis failure and an increase in ploidy. The most common phenotypic outcome is characterized by two complete and formed nuclei inside the same cell, a binucleated cell. Normally, binucleated cells remain in interphase without entering mitosis again, but some of them, showing high amount of DNA damage are likely to proceed mitosis and consequently,increase their polyploidy (Shi & King 2005).

One of the most penetrant phenotypes of the study showing this condition is due to KIF23 siRNA. KIF23 is a subunit of the centralspindlin complex, critical for microtubule bundling during cytokinesis. KIF23 levels are tightly regulated during cell cycle, with suppression in G1 phase and starting to increase in S phase to reach a maximum in G2/M (Fischer et al. 2013). Under KIF23 depletion, binucleated cells that enter G1 after the first aberrant mitosis do not yet show increased DNA damage. It is known that such mitotic aberrations leading to whole-genome doubling or tetraploidy activates the p53 pathway, which leads to cell cycle arrest in G1 in untransformed cells. However, the U2OS cancer model cell line used in this study, has a rather short G1 phase, which does not allow the build-up of p53 to sufficient levels. As a consequence, cells escape into S-phase, where some of them then encounter problems during DNA replication resulting in DNA damage. This probably leads an additional increase in DNA damage-mediated p53 activation. Most of these cells finally get arrested at G2, with a small part of them continuing with subsequent rounds of mitosis and accumulating errors until quiescence or cell death.

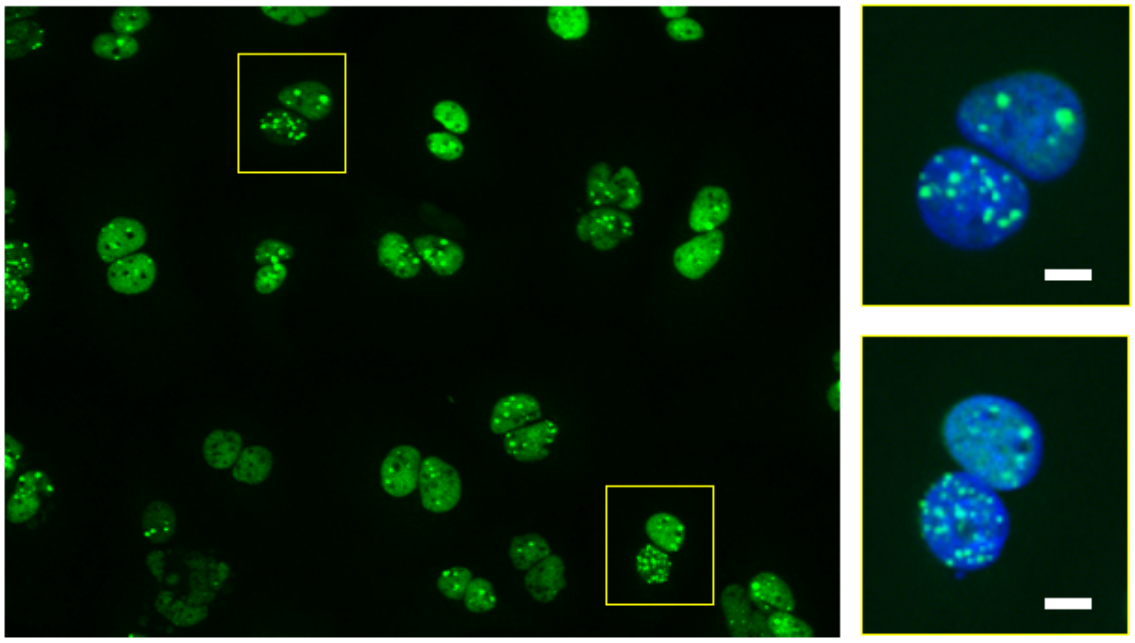

Fig. 6.1 Figure 1. U2OS cells treated for 72 hours with siRNAs against KIF23 and imaged for 53BP1-GFP (left image, 20x). Transfection leads to binucleated cells with a small subset of showing characteristic increase of DNA damage in one of the two nuclei (box and right images, DAPI added on top in blue channel).Scale bar 10 µm.

A percentage of these arrested cells (around 10%) show a distinct phenotype characterized by multiple DDR foci. The origin of this catastrophic DNA damage (CDD) remains unclear. Hypothetically, massive RS could be responsible to trigger signaling cascades that amplify DNA breakage to halt cell cycle progression. Deficient p53 cell lines[3]do not trigger the signaling for arrest and they do not develop CDD, indicating a potential implication of p53 upregulation. Even more intriguing, around half of the CDD cells show only damage in one of the two daughter nuclei (Figure 6.1). Such cells displaying asymmetric DNA damage do not continue into mitosis and it would be plausible to speculate that the DNA damage in one of the nuclei elicits and DNA damage checkpoint that arrests these cells in G2.

One hypothesis suggested by our collaborators is that physical contact between two nuclei in a binucleated cell can increase the signalling leading to the cell cycle arrest. In other words, mechanical transduction of the nuclear envelope might play a role in the signalling pathways leading to cell cycle arrest in binucleated cells. Thus, the region where nuclei are in physical proximity is of maximum interest to explore potential communications mechanisms between nuclei. For example, nuclear envelope contacts

[3]Hela is a p53 deficient cell line.

by membrane fusion could be an indicator of protein exchange. Defective nuclear pore structure and distribution in the damaged nucleus could indicate possible causes of a defective nuclear envelope assembly during mitosis.

In CLEM, as discussed in previous chapters, images from light and fluorescence microscopy are used to retrieve the region to be imaged with high-resolution in electron microscopy. The need of targeting is a constraint imposed by the selection of a few individuals inside a population, in the current work, the unusual event of asymmetric CDD nuclei. Thus, CLEM is applied over the selected group of adherent cultured cells, first imaged in light/fluorescence microscopy, found again in the resin block surface using SEM and imaged in 3D volumes via FIB-SEM technology. In addition, to complement the limits in resolution of FIB-SEM technology, sections of the binucleated cells intersection are examined by TEM tomography.

6.2 Materials and methods

Cell line and siRNA transfection

U2OS (human osteosarcoma) cells expressing 53BP1-GFP were cultured in DMEM Glutamax (Gibco) supplemented with 10% FBS (GE Healthcare) and 1% penicillin and streptavidin at 37°C in 5% CO2. KIF23 siRNA (Ambion-Thermo Fisher Scientific) with a concentration of 10 µM was prepared using a standard transfection protocol: 1 µl of siRNA was mixed with 62.5 µl of Optimem medium, and separated, 1.25 µl of RNAiMax from Termofisher was mixed with 62.5 µl of Optimem medium. After five minutes, both reagents were mixed together and incubated for 15 minutes at room temperature. Transfection mix was added to cells counted at 100.000 cells/ml and seeded in 35 mm glass bottom gridded dishes (MatTek P35G-1.5-14-CGRD-D).

KIF23 knowckdown has a highly penetrant phenotype and after 72 hours exhibited a population with 90% of binucleated cells, some of them with CDD. Two types of controls were used, SPL1 transfected cells and KIF23 binucleated without any CDD.

Light Microscopy and sample preparation

Light fixation. Prior to light microscopy imaging, cells were fixed with a mixture of 1% formaldehyde and 0.5% glutaraldehyde in 0.1 M Caco ph 7.2 buffer. Glutaraldehyde autofluorescence was quenched with 150 nM of glycine in PHEM buffer (240 mM

PIPES, 100 mM HEPES, 8 mM MgCl2, 40 mM EGTA in H2O, pH 6.9). Cells were transferred PHEM buffer for imaging.

Heavy fixation and sample preparation. Cells were immediately fixed after imaging with a mixture of 0.5% glutaraldehyde and 4% paraformaldehyde in Cacodylate (Caco) buffer (0.1 M, ph 7.2). Next day, cells were rinsed with Caco buffer and post-fixed with 4% OsO4, 3% KFe_4Cn_6 in Caco buffer. A microwave (Biowave Pro, Ted Pella) was used to accelerate processing, with a program of two minutes vacuum 100 Watts in on-off cycles seven times.

One hour before processing, Thiocarbohydrazide(TCH, Sigma-Aldrich) was prepared at 1% concentration (0.1 g in 10 ml. of double distilled water (ddH2O)) and warmed up to 60°C to accelerate dilution. Cells were rinsed three times with Caco buffer and TCH dilution was filtered and added to the dish. After 10 minutes on bench, sample was rinsed three times with Caco and once with ddH2O. Sample is further stained with 1% OsO4 in Caco. Microwave is used again (same cycle program) and the sample is rinsed 3 times with Caco and 3 times with ddH2O. Stain with 1% UA (Uranyl Acetate) in water is applied, and after that rinsed 3 times with ddH2O.

Cells are then dehydrated in a series of graded concentrations of ethanol. Dehydration was also accelerated by the use of microwave at 250 Watts cycles without vacuum, 40 seconds each step (50,70,90,100,100% for dehydration). Finally, samples are embedded in Durcupan (Sigma-Aldrich) in progressive steps (50 % ethanol- 50% resin, 30% ethanol- 70% resin and three times 100% resin).

After this, samples are left 72 hours in the oven at 60 degrees for polymerization. After 72 hours the samples are heat shocked to remove the glass bottom dish. With the resin polymerized, the samples are mounted in a SEM stub, coated with gold (180 seconds,30 mA) and introduced in the FIB-SEM microscope chamber.

FIB-SEM datasets

The microscope used was Crossbeam 540 from Zeiss. FIB current for acquisition 3 nA, SEM imaging at 1.5 kV using ESB detector with 10 µs dwell time.

- Cell number 1, sample 1. Treatment with KIF23 siRNA, with asymmetric CDD at a resolution of 5 x 5 x 5 nm (xyz) voxel size, comprising a total volume of 15x20x25 μm^3. Both nuclei were manually segmented using IMOD (Kremer et al. 1996). Inner walls of nuclei were segmented and exposed. Nuclear pores can

be seen using Volume rendering with MIP by setting up a right threshold function with Drishti (Limaye 2012).

- Cell number 2, sample 1. Treatment with KIF23 siRNA with asymmetric CDD at a resolution of 5 x 5 x 200 nm (xyz).
- Cell number 3, sample 1. Treatment with KIF23 siRNA with asymmetric CDD at a resolution of 5 x 5 x 20 nm (xyz). Cell 3D model created using Drishti (Figure 6.8).

TEM datasets

Cells processed with chemical fixation were found in the resin block using a stereoscope and using the MatTek grid pattern as guidance. 300 nm sections were collected by ultramicrotomy and post-stained using 2% uranyl acetate. Sections were imaged using SerialEM in an FEI Tecnai 30 transmission electron microscope operated at 300 kV. IMOD was used for further image processing and for the montage of the serial section images and serial tomography.

(a) Cells number 4 and 5, sample 2. Treatment with KIF23 siRNA with asymmetric CDD. Thick section 200 nm and tomography in specific regions along central region of nucleus.

(b) Cells number 6 and 7, sample 3. Treatment with ESPL1 siRNA binucleated cells with no damage.

6.3 Results and discussion

Correlation strategy by landmark clicking

Automatic landmark finding is suitable for multiple targets. But when the target is one or two cells, a different approach can be used with minimal input. The following set up is more practical for many applications, specially when the information from light microscopy is scarce (no stage coordinates and maybe just one transmitted light image with almost no reference).

Since a sample coming from a glass bottom dish can be relatively large (1.5 cm diameter), using a setup based on MatTek glass bottom grids can make easier the manual search for cell targets. A successful cell targeting requires the visible MatTek

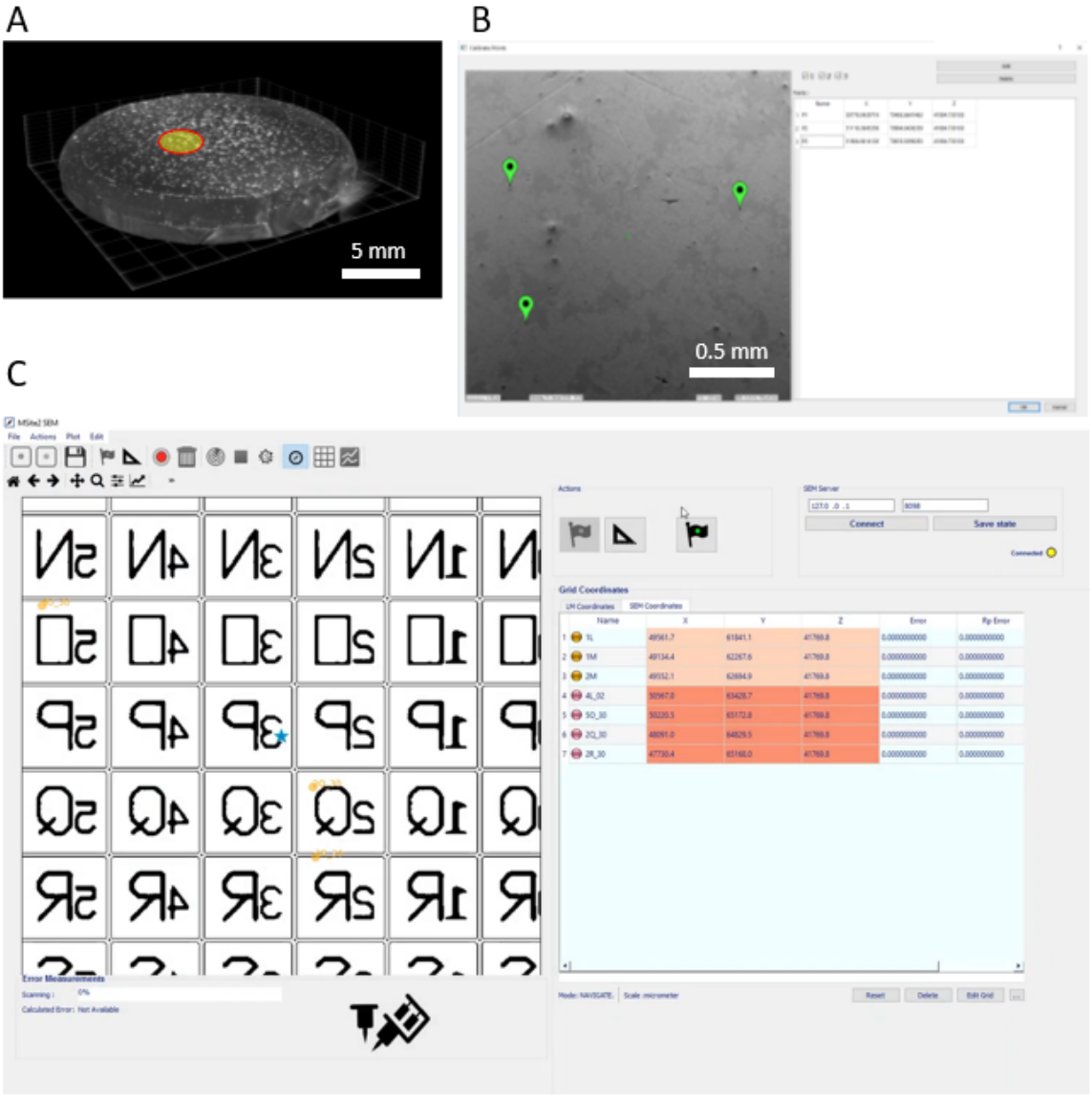

Fig. 6.2 **Manual navigational mode in CLEMSite Navigator.** A. 3D reconstruction of a typical sample block of cells, 1.5 cm in diameter. Image was obtained using an in X-Ray microCT and composed in Drishti using MPI only for illustration purposes of relative size. B. After moving to a square in the grid, the user clicks on the button (a compass in the GUI, C), then a form asks to select 3 orthogonal positions belonging to the crossings of the square in which the microscope FOV is centred. The user also has to indicate the alphanumerical name of the pattern imprinted on the square, bottom right relative to the crossing position. C. After 3 points, an affine transform is computed and the user can move around using the canvas. When a cell is located in the centre of the image, clicking on the green flag button will store the cell position on the map. Upon completion, the list of target positions can be exported or revisited for refinement.

grid imprinted onto the surface of the SEM resin block. Once the user has recognized a grid square with a distinctive alphanumerical pattern, he can move the stage on a grid crossing. Then, CLEMsite is used to select the alphanumerical pattern corresponding

to the stage position. This will associate the coordinates of the microscope of the current position with the pattern name inside the grid square. A total of 4 crossings can be manually assigned to compute an approximate transform used to predict SEM stage coordinates of any part of the grid (Figure 6.2)[4].

This transform is not very accurate and its only purpose is for the user to navigate in the SEM sample surface using the GUI representation display. Using a simple 4 points transformation, it is almost certain that the cell is within 20 µm range, but it is convenient to be as much precise as possible. A possibility is to visualize cell contours at higher kV on the surface of the sample (Figure 6.3-B). If the microscope is properly aligned and calibrated for positions between kVs, it is possible to move to higher kVs and store the position. However, often contours are diffuse and cells difficult to differentiate if they cluster in a group.

In a second step, each stage position can be refined previous to acquisition using a special plugin on CLEMSite, DCLEM. DCLEM is a simple interface able to show images from SEM surface in one side, and with the possibility to load composites of light microscopy in the other. Clicking in common landmarks between the two images, generates a close transform in 2D able to predict with high accuracy the position of a cell. DCLEM can be applied when the automation is not possible, for example, if the landmarks in the sample surface are not clearly visible. In addition, from the light microscopy side, it is not always possible to obtain reflected light images for the line detection presented (chapter 4) to work.

This software works very similarly to ecCLEM (Paul-Gilloteaux et al. 2017) and *Shuttle and Find* commercial software from *Zeiss*. The advantage of this small plugin in CLEMSite is the convenience of acquiring and image in SEM and find a new position that can be stored in CLEMSite without resorting to any extra additional software. Current version of the software only provides a position predicted for each clicked point in SEM stage coordinates, but newer versions can provide, without much effort, better integration with CLEMSite to transfer coordinates directly. Additional upgrade iterations could also involve typical image editing tools (brightness and contrast, alpha channel on each image) and an extra window to show a composite image with the final transformation (Figure 6.3-B).

[4]This process has the option of running fully automated in the same way as it was presented in chapter 5, but the manual process does not require of specialized libraries from *Carl Zeiss Gmbh*.

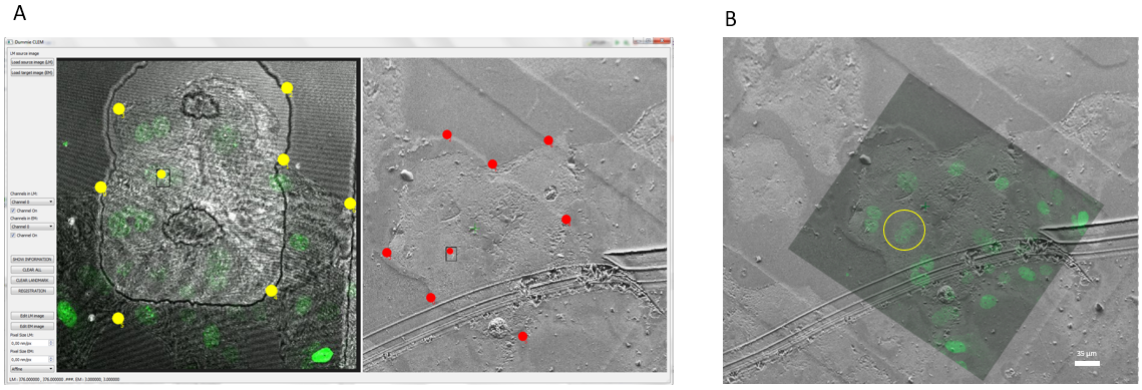

Fig. 6.3 A. DCLEM interface. The application displays two window ports, one on the left for light microscopy image and other in the right for SEM image. By clicking in landmarks and moving them around, a transformation is computed, so the next point clicked on the light microscopy image is predicted in the SEM side. B. Composite image of fluorescence microscopy (53BP1-GFP) and SEM surface at 5 kV (higher kV than acquisition, which is at 1.5 kV). In the SEM image, contours of cells can be observed, but individual cells cannot be distinguished. Yellow circle indicates the targeted cell.

Nuclear envelopes of binucleated cells are deformed in the contact region

In previous experiments reported from our collaborators, MIP (maximum intensity projection) of confocal images from binucleated U2OS cells stained for LAP2 (nuclear lamin), displayed an increased intensity close to the nuclei contact areas. NUP153 (nuclear pores) also showed peaks of increased intensity in the contact areas. A question was raised whether the increase in intensity could be explained by the presence of two adjacent membranes or if there was a membrane fusion. The first volume of EM data reconstruction (Figure 6.4-B and 6.5-A), instead of showing two flat walls opposing each other, one of the NE formed a big protrusion which went into the other nucleus. This type of deformation was confirmed with two more acquisitions of 3D volumes (cells 2 and 3). This could be evidence that nucleus in the region of contact can exert forces one each other, and then support the theory that mechanical forces can trigger different signals for each nucleus.

Nuclear envelopes are separated by a 50-250 nm space without showing contact or membrane fusion between them.

In the areas between the two nuclei appeared a narrow cleft which physically separated both nuclei by a distance between 50 and 250 nm. This space value was changing depending on the region measured. The length of the separation is very similar to the diameter of nucleoplasmic reticulum invaginations in other parts of the same cell. This

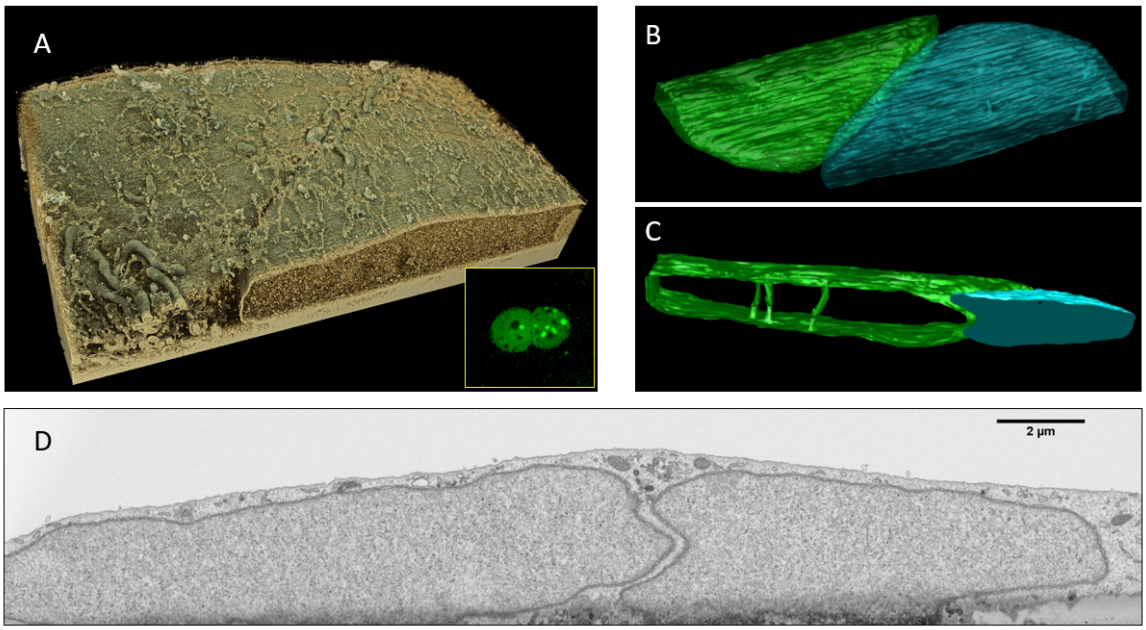

Fig. 6.4 **Cell 1. A.** Full volume reconstructed in 3D of binucleated UO2S (53BP1-GFP, small picture on the side). Nuclear envelopes are covered by a layer of tubular ER. Mitochondria can also be seen moving between NE and cell membrane, but other organelles are pushed to the side. **B-C.** Segmentation of the NE of both nuclei (damaged in blue, good in green). Deformation of NE forming an S pattern can be observed clearly in C. **D.** Section from FIB-SEM dataset, left intact nucleus, right, damaged nucleus. The space between the two nuclei is about 150 nm.

space indicates a possible 'exclusion zone' between the two synapsed nuclei. It would have been interesting to observe dark regions(densities) in the EM images of the space between membranes, which could belong to cytoskeletal structures forcing both nuclei to be apart (Jorgens et al. 2017). However, in FIB-SEM 3D volumes, only empty space was found without no hint of possible actin, microtubules or thin intermediate filaments. The absence of cytoskeleton was later confirmed by electron tomography of the space between NE.

The next step was to search for complex interactions between nuclear membranes, like protrusions or membrane contacts and fusions. NE from both cells seems to be side-by-side, with no invaginations or direct contact. Occasionally, with about 5 to 10 counted events per cell, external contacts seem to appear between the ONM of both nuclei (Figures 6.5 B, C, D). The contacts are distributed randomly, sometimes looking like an extension of the nuclear envelope outer membrane, sometimes as densities trapped between both nuclei. None of them is indicative of potential communication and no electron-dense heterochromatin can be seen close to them. The low frequency of these events indicates that they are rare, and could not be discarded as sample preparation

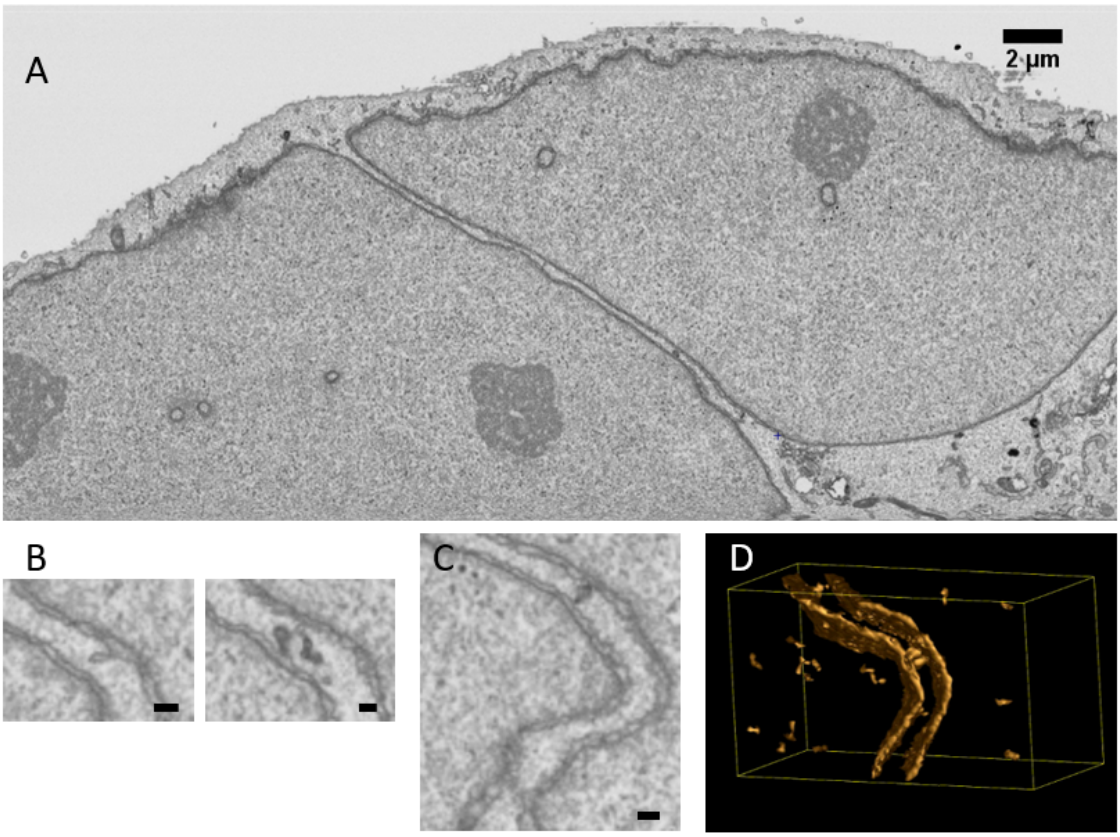

Fig. 6.5 **A.**XY perspective from a 3D volume of cell 1, were the two nuclei and the separation cleft between them can be observed.**B.** Separation showing a NE outer membrane protrusion, without any inner deformation. In the second image, one of the densities trapped between nuclei.**C and D** show the same contact density, the 3D surface reconstruction shows that the contact happens, but again, only in the outer membrane. Scale bar in B,C equivalent to 150 nm.

artefacts or accidents from the failed cytokinesis. This observation agrees with FRAP experiments performed by our collaborators which did not show an enhanced exchange of diffusible components between nuclei.

No chromatin differences between normal binucleated cells and asymmetric DNA damage cells.

Binucleated cells transfected with siRNA for ESPL1 (Extra Spindle Pole Bodies Like 1) results in single large tetraploid cells because chromosomes cannot segregate during the metaphase-anaphase transition. ESPL1 are used as another additional phenotype as a control. ESPL1 maintains a stable separation between sister chromatids before anaphase. Under a knockdown, cells grow in DNA but they are not able to divide even

if they increased their amount of DNA per cell. Transfected cells are easy to identify because their big nucleus. We use them as binucleated controls is that even if they double their DNA per nuclei, do not show CDD so often.

Examining thick sections by TEM allows observing potential differences between hetero and euchromatin (Figures 6.6. In both cells, nucleolus and high-density regions can be identified and correspond to dark areas in the nucleus of fluorescent images. By correlating fluorescent foci marking damage with EM images only can be observed a slight darkening respect usual euchromatin. Finally, examination of the nuclear envelope in the contact region between nuclei does not show an excess of heterochromatin. In other words, observation of chromatin domains by EM did not give any evidence of induced expression close to NE or in the regions with CDD.

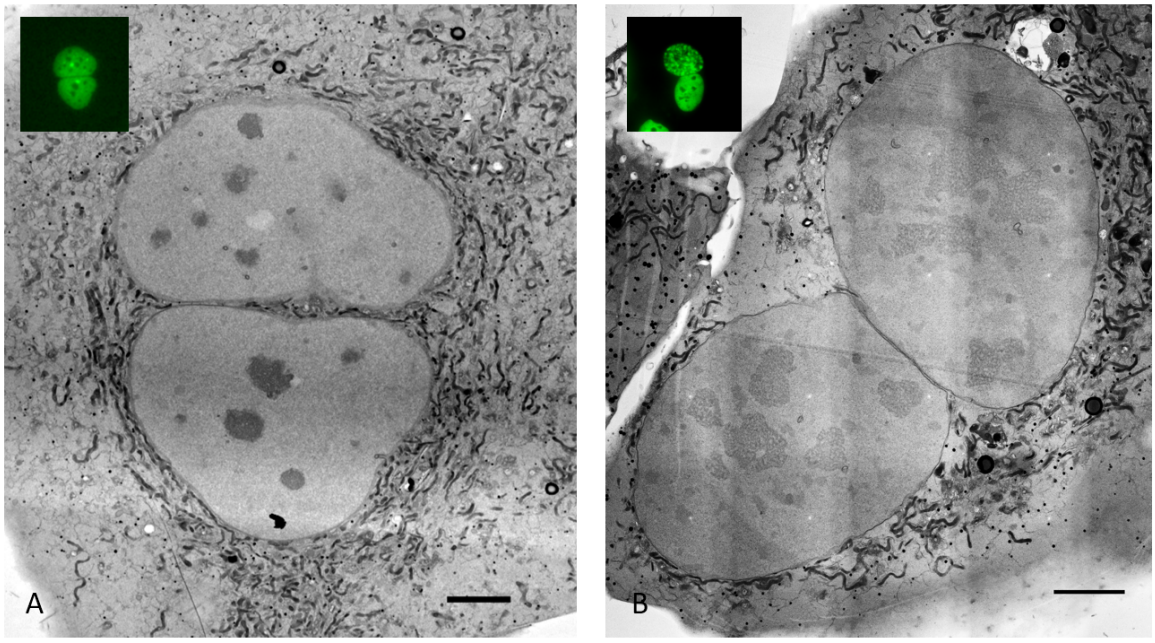

Fig. 6.6 Cells acquired by TEM, section taken in the middle of the cell. Upper corner shows fluorescence images, 53BP1-GFP. A. ESPL1 one control, without CDD. B. Cell with KIF23 knockdown, upper nucleus shows CDD. Scale bar 5 µm.

Nuclear pores in the space region do not show particular defects or changes in distribution.

In literature, is known that altered NPC (nuclear pore complex) composition can disrupt the relation with the nuclear envelope and affect the cell cycle progression. After segmentation of the nuclear envelope in cell 1 by FIB-SEM, Maximum Intensity Projection (MPI) was used to visualize the nuclear pore ring distribution (Figures 6.7-A

and B). Manual counting of nuclear envelope areas showed a typical distribution in mammalian cells of around 9-10 NPC per µm2 (Maul & Deaven 1977). No difference was observed between the CDD nucleus and the healthy one. In addition, to confirm any possible disruption of the NPC structure, tomography between ESPL1 controls and KIF23 cells was compared. Again, they did not show any particular difference in size (Figure 6.7-C).

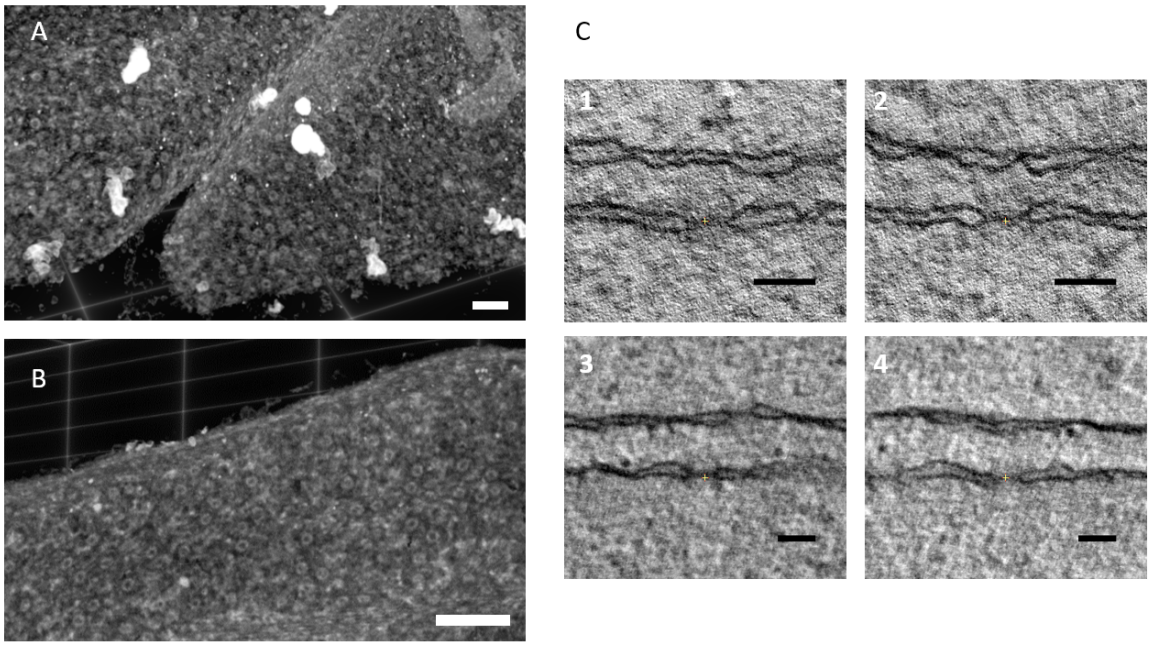

Fig. 6.7 A and B. Segmentation of the NE and Maximum Intensity Projection in a 3D rendered volume allowed to observed NPC (ring like structures), in A, the outer membrane and in B, the inner wall of the damaged nuclei. Scale bar 1 µm. C. NPC extracted from tomography sections. NPC have been aligned, so nucleoplasm is always in the bottom. 1 and 2 belong to ESPL1 siRNA treated cells, 3 and 4 to KIF23 siRNA treated cells. In both cases, NPCs have a hole diameter around 75-80 nm which agrees with literature measurements (Szymborska et al., 2013).

6.4 Conclusion

Manual workflow with CLEM. In the present chapter, I introduced a different way to do CLEM with cells. This mode can be particularly useful when the conditions of the sample surface are not optimal or the images from light microscopy are insufficient for automatic detection of landmarks. The CLEM experiment starts by giving some observed positions in SEM from the grid embedded in the glass bottom dish. Internally, the software matches with an ideal grid map, as explained in chapter 5. Although the

experiment used MatTek dishes, to extend the transform to other types of grids or patterns would require a minimum effort programmatically. In this case, machine learning approaches are not used, so implementation only requires to input the definition of the grid patterns and measures from the manufacturer. In practice, with this approach, the time necessary to localize a specific ROI is about 5 minutes, when it can easily take 30 minutes or more in fully manual workflows.

The second step showed *DCLEM*, a simple GUI plugin from *CLEMSite* to refine the position based on manual clicking on observed landmarks. The approach here presented has two advantages respect other competitors. First, images from light microscopy are not dependent from a specific microscope or format. DCLEM works in the image space of coordinates and produces a relative transform for the SEM stage position. Second, it is very simple and learning the operation requires few minutes, improving the usability for the EM microscope operator.

Other approaches over the years (Cao et al., 2014; Acosta, Bouthemy and Kervrann, 2016) tried to automatize the process of CLEM by registration approaches. They try to find common features on images and match them in a minimization procedure which results in an optimal transformation. This is possible in SEM surfaces displaying obvious topological features, but in some cases, finding the necessary features to register two images can fail for many reasons (brightness and contrast, type of cells, confluency, scratches, . . .) and parameter adaptation is required. As a result, takes more time to adapt parameters than to simply click on a few places easily recognizable by a human operator. Thus, the combined use of grid coordinates and manually selecting visible features is a good approach to achieve a fast correlation.

Binucleated cells with asymmetric CDD. The present work in binucleated cells has shown that there is no direct communication between close nuclear envelopes of both nuclei. Nuclei hold a separation cleft between 50 and 250 nm and nuclear envelopes fold between them. It would be interesting to compute if the compression forces are sufficient to allow this inter-space between nuclei to see if they are responsible for their deformation. Recent studies in nuclear mechanics indicate that the nuclear envelope is a powerful transduction system and there is the possibility that mechanical stress could regulate nuclear stiffness (affecting the nuclear lamina) and promote chromatin changes. This could influence nuclear signals and the outcome of the replication stress observed in some of the daughter nuclei.

If that is the case, it would be a considerable challenge to determine the molecular relationships involved in the signalling of the CDD. In that direction, our collaborators

are performing extensive proteomics to observe protein changes along the cell cycle combined with time lapse imaging studies. From the EM side, the contribution to determine the CDD culprit was rather small but provided evidence to disregard several hypotheses, namely possible fusions between the nuclear envelope or the direct contact between NEs. Potential findings like invaginations connecting nuclei, cytoskeletal filaments between the inter-nuclear space, changes in NPC distribution and shape, or massive heterochromatin changes close to the cleft between nuclei could have been indicators that the relationship between both nuclei is crucial for the development of CDD.

Besides, combination between TEM tomography and FIB-SEM proved that those techniques are complementary. Images like Figure 6.8 can only be obtained by 3D volume EM. They provide a full picture of the cell displaying all membranous elements and potential interactions. On the other side, only by tomography, the cleft between nuclei could be examined for precise contacts, cytoskeletal elements or NPC visualization. Thus, we have shown that delicate questions about biological structures can be efficiently addressed by CLEM with FIB-SEM and tomography.

6.5 Acknowledgements and contributions

This project was collaboration were Claudia Lukas[4] and Jiri Lukas[4] were leading researchers and provided the cells for the experiments. Yannick Schwab[1] and José Miguel Serra Lleti[1] contributed to decide what was the best EM approach for this project. Beate Neumman[2] helped with the siRNA treatment and with all the light microscopy experiments. Nicole L. Schieber[1] helped with the sample preparation for EM. Pedro Machado[3] sectioned and imaged the samples for TEM. José Miguel Serra Lleti did the cell culture, light microscopy, sample preparation and data analysis.

Affiliations

(1) Cell Biology and Biophysics Unit, Schwab Team, European Molecular Biology Laboratory, 69117 Heidelberg, Germany

(2) Advanced Light Microscopy Facility, European Molecular Biology Laboratory, 69117 Heidelberg, Germany

(3) Electron Microscopy Core Facility, European Molecular Biology Laboratory, 69117 Heidelberg, Germany

(4) Novo Nordisk Foundation for Protein Research. University of Copenhagen

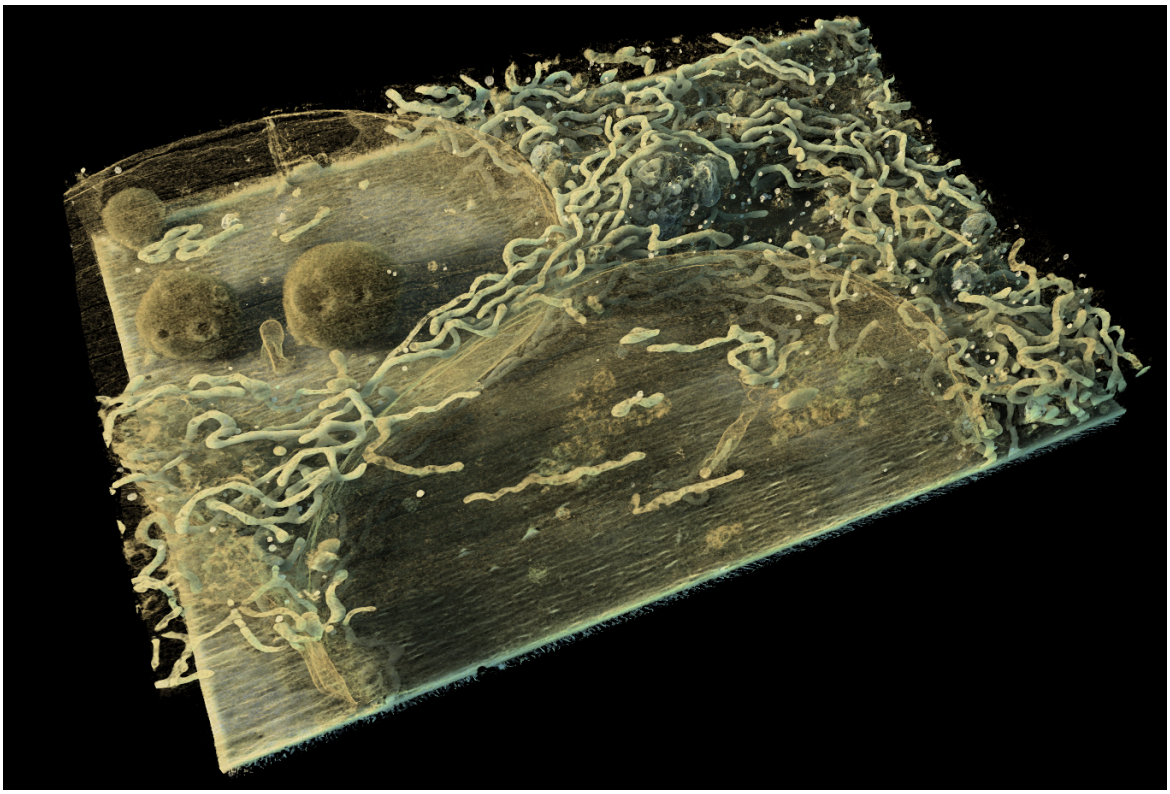

(a) A

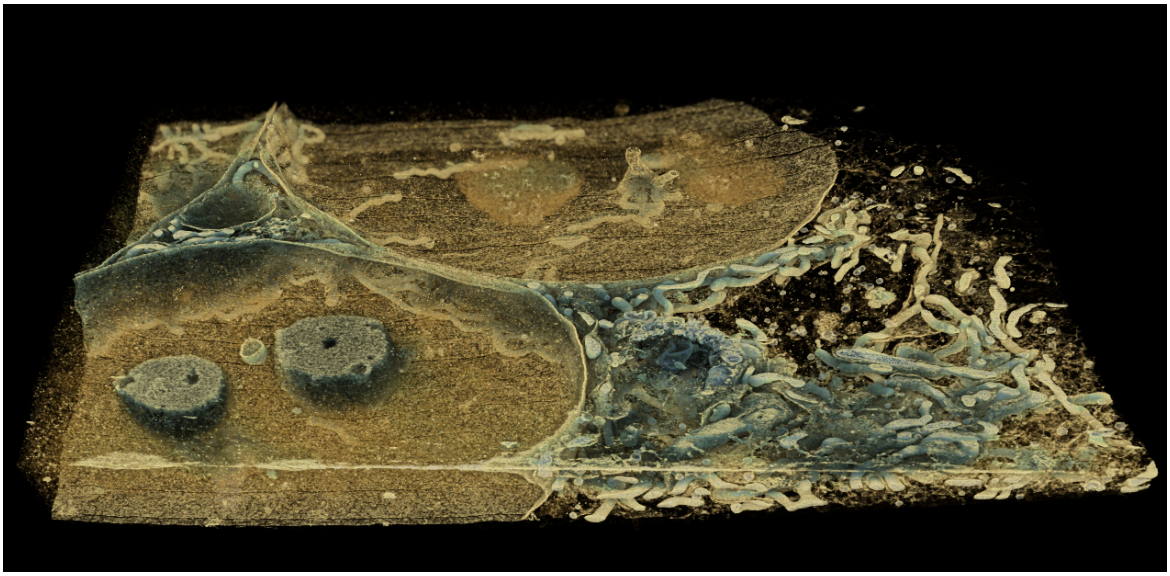

(b) B

Fig. 6.8 **3D model reconstruction of cell 3**, FIB-SEM (dataset adjusted to 20 nm pixel size, in addition from brightness and contrast, no modifications or modeling has been applied to this cell). This cell comprises a total of four nuclei, three nuclei with one small micro-nuclei in the middle. From the perspective of the first image, only two nuclei are visualized. The ball like structures in their middle are nucleolus. Nucleoplasmic reticulum (big nuclear envelope invaginations) can be observed, some of them crowded with mitochondria, the spaghetti like structures. In the cytoplasm extensive mitochondrial networks cover the full cell. The thin film that mixes with mitochondria, also in form of filaments is endoplasmic reticulum which, for visualization purposes has been done almost transparent. In the middle of the cytoplasm a ball like structure is a micro-nucleus being digested by a big lysosome.

6.6 References

Acosta, B. M. T., Bouthemy, P. and Kervrann, C. (2016) 'A common image representation and a patch-based search for correlative light-electron-microscopy (CLEM) registration', in 2016 *IEEE 13th International Symposium on Biomedical Imaging (ISBI)*. IEEE, pp. 257–260. doi: 10.1109/ISBI.2016.7493258.

Ben-Porath, I. and Weinberg, R. A. (2005) 'The signals and pathways activating cellular senescence', *The International Journal of Biochemistry & Cell Biology.* Pergamon, 37(5), pp. 961–976. doi: 10.1016/J.BIOCEL.2004.10.013.

Cao, T., Zach, C., Modla, S., Powell, D., Czymmek, K. and Niethammer, M. (2014) 'Multi-modal Image Registration for Correlative Microscopy'.

Ciccia, A. and Elledge, S. J. (2010) 'The DNA damage response: making it safe to play with knives.', *Molecular cell.* Elsevier, 40(2), pp. 179–204. doi: 10.1016/j.molcel.2010.09.019.

Fischer, M., Grundke, I., Sohr, S., Quaas, M., Hoffmann, S., Knorck, A., Gumhold, C. and Rother, K. (2013) 'p53 and cell cycle dependent transcription of kinesin family member 23 (KIF23) is controlled via a CHR promoter element bound by DREAM and MMB complexes.', *PloS one*. Public Library of Science, 8(5), p. e63187. doi: 10.1371/journal.pone.0063187.

Hanawalt, P. C. (2015) 'Historical perspective on the DNA damage response.', *DNA repair. NIH Public Access*, 36, pp. 2–7. doi: 10.1016/j.dnarep.2015.10.001.

He, G., Siddik, Z. H., Huang, Z., Wang, R., Koomen, J., Kobayashi, R., Khokhar, A. R. and Kuang, J. (2005) 'Induction of p21 by p53 following DNA damage inhibits both Cdk4 and Cdk2 activities', *Oncogene.* Nature Publishing Group, 24(18), pp. 2929–2943. doi: 10.1038/sj.onc.1208474.

Jorgens, D. M., Inman, J. L., Wojcik, M., Robertson, C., Palsdottir, H., Tsai, W.-T., Huang, H., Bruni-Cardoso, A., López, C. S., Bissell, M. J., Xu, K. and Auer, M. (2017) 'Deep nuclear invaginations are linked to cytoskeletal filaments - integrated bioimaging of epithelial cells in 3D culture.', *Journal of cell science.* The Company of Biologists Ltd, 130(1), pp. 177–189. doi: 10.1242/jcs.190967.

Kremer, J. R., Mastronarde, D. N. and McIntosh, J. R. (1996) 'Computer Visualization of Three-Dimensional Image Data Using IMOD', *Journal of Structural Biology*, 116(1), pp. 71–76. doi: 10.1006/jsbi.1996.0013.

Limaye, A. (2012) 'Drishti: a volume exploration and presentation tool', in Stock, S. R. (ed.). I*nternational Society for Optics and Photonics*, p. 85060X. doi: 10.1117/12.935640.

Lukas, C., Savic, V., Bekker-Jensen, S., Doil, C., Neumann, B., Sølvhøj Pedersen, R., Grøfte, M., Chan, K. L., Hickson, I. D., Bartek, J. and Lukas, J. (2011) '53BP1 nuclear bodies form around DNA lesions generated by mitotic transmission of chromosomes under replication stress', *Nature Cell Biology*, 13(3), pp. 243–253. doi: 10.1038/ncb2201.

Lukas, J., Lukas, C. and Bartek, J. (2011) 'More than just a focus: The chromatin response to DNA damage and its role in genome integrity maintenance', *Nature Cell Biology*. Nature Publishing Group, 13(10), pp. 1161–1169. doi: 10.1038/ncb2344.

Maul, G. G. and Deaven, L. (1977) 'Quantitative determination of nuclear pore complexes in cycling cells with differing DNA content.', *The Journal of cell biology.* The Rockefeller University Press, 73(3), pp. 748–60.

Paul-Gilloteaux, P., Heiligenstein, X., Belle, M., Domart, M.-C., Larijani, B., Collinson, L., Raposo, G. and Salamero, J. (2017) 'eC-CLEM: flexible multidimensional registration software for correlative microscopies', *Nature Methods.* Nature Publishing Group, 14(2), pp. 102–103. doi: 10.1038/nmeth.4170.

S Pedersen, R., Karemore, G., Gudjonsson, T., Rask, M.-B., Neumann, B., Hériché, J.-K., Pepperkok, R., Ellenberg, J., Gerlich, D. W., Lukas, J. and Lukas, C. (2016) 'Profiling DNA damage response following mitotic perturbations.', *Nature communications.* Nature Publishing Group, 7, p. 13887. doi: 10.1038/ncomms13887.

Shi, Q. and King, R. W. (2005) 'Chromosome nondisjunction yields tetraploid rather than aneuploid cells in human cell lines', *Nature.*Nature Publishing Group, 437(7061), pp. 1038–1042. doi: 10.1038/nature03958.

Szymborska, A., de Marco, A., Daigle, N., Cordes, V. C., Briggs, J. A. G. and Ellenberg, J. (2013) 'Nuclear pore scaffold structure analyzed by super-resolution microscopy and particle averaging.', *Science*(New York, N.Y.). American Association for the Advancement of Science, 341(6146), pp. 655–8. doi: 10.1126/science.1240672.

7

Conclusion and future perspectives

When this project started, it was not clear if the FIB-SEM could be automatized in the way that has been presented here. The machine was complex and the process of volume acquisition long and with multiple manual steps. There were two main tasks to accomplish. First, the CLEM task, the correlation of light and fluorescent images with the surface of the resin block imaged by SEM. Second, automate the acquisition and iterate over multiple regions of the same sample. The two tasks were clearly different, the first seeming one much easier to accomplish given the precedents in literature for TEM microscopes. In traditional EM ultramicrotomy sections, it is possible to apply image registration between fluorescence and stained EM sections (Kukulski et al., 2012).

Hence, the first task I embarked on was to analyze the images from light microscopy, get as much information as possible using computer vision analysis (via feature extraction, cross-correlation,...) and register them with the images from the SEM surface. But the SEM surface, same as a lunar landscape, does not have enough distinctive features. The scarcity of landmarks is still a challenge for current artificial intelligence algorithms, especially in biology where the landmarks can change from one sample to the next. A human is still able to delineate several similarities between transmitted light or DIC images and the SEM images from the resin block surface, but the same task was not possible for a computer program with the current technology.

To overcome the difficulties of image registration we used an embedded pattern at the bottom of the glass where the cells were cultured and we used it as a reference. This approach, as shown in the thesis, proved to be very successful for automatic detection. Once the principle of correlating the crossings from the grid was established, it was a matter of practical implementation. The current prototype was adapted to a single type

of commercial grids (MatTek), but it was a primary and necessary step to delineate the design of the application. With the prototype application working, different glass pattern designs are straightforward to adapt. In a future version of the solution, an extra software application can automatically read the patterns of a new glass bottom gridded dish and insert it into the system. This will allow, for example, to apply the correlation with high-pressure frozen samples, which due to their space limitation for freezing, require different carriers. High-pressure frozen cells are closer to their native ultrastructure compared to the chemically fixed cells used during this thesis.

The second task, the automation of a 3D Volume acquisition, required the internal control of the instrument. It was clear that a collaboration with Zeiss was needed to succeed. Zeiss refereed us to Fibics and their ATLAS Engine software, which simplified many tasks of the automation. By applying computer vision programs to solve tasks that usually a human will do, I developed a software able to successfully execute a single full 3D volume acquisition. After this, the next logical step was the integration with the correlation by simply indicating where the target cell was. And the final step was to integrate the software in a loop to iterate over several positions. The current prototype is functional, and we have already identified and planned the next development steps. Adding a protective coat for radiation before imaging, add a better online tracking of the FOV or the possibility to resume at any point a previously stopped acquisition are some the three main improvements to be followed up in further versions of the software

Since the Fibics API (Fibics programming library) provides all the control capabilities of the microscope, CLEMSite can be easily integrated into their ATLAS line of products as a plugin. The graphical interface will be different, but its functionality can be, in essence, the same as the prototype here presented. The plugin could be fully integrated with the feedback light microscopy at different extents, with the correlation principle working independently from the imaging pipeline design. Thus, any type of microscope providing reflected light images and stage coordinates should be able to be incorporated in our CLEM workflow. Besides, the application will benefit from new advances in FIB-SEM technology. For example, the *CrossBeam 550* from *Zeiss*, the successor of the microscope used for this thesis, claims to provide a more stable and durable FIB column for long-term experiments.

With the application running continuously, the flow of volume EM data will increase with a consequent demand in data storage and infrastructure. Many lessons can be learned from other fields, like light sheet microscopy. In fact, they produce raw datasets of the order of terabytes and they manage to store, compress without any loss

of information and access the data in real time (Amat et al. 2015, Pietzsch et al. 2014). If properly compressed, a cell volume isotropically acquired should not be bigger than 50 Gb. Recently, the EMPIAR initiative (https://www.ebi.ac.uk/pdbe/emdb/empiar/) started a process of standardisation to save electron microscopy datasets, including FIB-SEM and SBF-SEM volume data.

The future challenges will arise from the analysis of the data. Stereological probes, as we have seen, can have an advantagefor quantification with respect segmentation. They can be completed in less time because it only requires recognition of the structure at glance in a few sections. However, counting stereological probes manually, same as segmentation, is a repetitive and time-consuming task. Neural networks like Faster R-CNN (Ren et al., 2015), are able to recognize structures with high accuracy (Huang et al., 2018). This type of machine learning could be potentially used to automatize the process of counting hits on the structure of interest and thus, providing immediate quantifications.

On the side of segmentation, as discussed in chapter 5, with the new deep learning tools we head towards fully automated segmentation. One could envision a full pipeline where volumes recently acquired by the FIB-SEM are automatically pre-processed (aligned and cleaned for noise) and all the organelles of interest automatically segmented. Training data will come with time, and since EM data displays not only one organelle or molecule, but the full cell landscape, data from different studies can be reused as machine learning training data.

This data analysis and exchange will not only serve for training segmentation tools, but to develop new discovery tools. EM will form part of big data analysis, combining information from light microscopy, single cell genetics (sub-population based), proteomics and electron microscopy (with CLEM applied to cell sub-populations).

As an example application of the method, we already applied the automated collection of cell volumes to a siRNA experiment. We decided to target the Golgi apparatus and we observed differences between phenotypic morphologies. This is just one example of the possibilities of the method. siRNA knockdowns for any gene can be examined at the ultrastructural level for any membranous organelle, for example, nuclei (as seen in chapter 6), mitochondria, endoplasmic reticulum distributions or centrosomes.

Beyond the untargeted analysis of populations, the CLEM part of the project offers the possibility to pick the individuals, which increases the potential range of applications. One of these applications can involve, for example, the inspection of host-pathogen interactions by selecting specific infected individuals in a cell population. In the

biomedical field, it can help with the exploration of the heterogeneous response to a drug treatment, which can affect differently to a specific group of cells. In cell biology, it can help to examine the differences between cells at different stages of a process like a cell cycle or differentiation. And finally, we also have the possibility to select a sub-population of cells were a rare event is occurring. One example of this was shown in chapter 6 with the catastrophic DNA damage response in one of the nuclei, where only a small percentage of the population showed a particular phenotype.

In conclusion, we have successfully set up an automated CLEM workflow. The application of the workflow to different siRNA experiments demonstrated its potential for acquiring statistically relevant amounts of data from cell populations. We also have demonstrated that EM can help to support mechanistic models or discard some hypothesis. For example, in chapter 6, the nuclear envelope of binucleated cells are separated and not fused or showing signs of direct contact. Observations of the landscape of organelles at the ultrastructural level can certainly help to guide future experiments. If in addition, we can quantify the observations, we convert the EM data into valuable evidence for biological research. Applications like the one I developed for my thesis can help to make this true.

References

Amat, F., Höckendorf, B., Wan, Y., Lemon, W. C., McDole, K. and Keller, P. J. (2015) 'Efficient processing and analysis of large-scale light-sheet microscopy data', *Nature Protocols*. Nature Publishing Group, 10(11), pp. 1679–1696. doi: 10.1038/nprot.2015.111.

Huang, J., Rathod, V., Sun, C., Zhu, M., Korattikara, A., Fathi, A., Fischer, I., Wojna, Z., Song, Y., Guadarrama, S. and Murphy, K. (2016) 'Speed/accuracy trade-offs for modern convolutional object detectors'.

Kukulski, W., Schorb, M., Welsch, S., Picco, A., Kaksonen, M. and Briggs, J. A. G. (2012) Precise, Correlated Fluorescence Microscopy and Electron Tomography of Lowicryl Sections Using Fluorescent Fiducial Markers. Academic Press. doi: 10.1016/B978-0-12-416026-2.00013-3.

Pietzsch, T., Saalfeld, S., Preibisch, S. and Tomancak, P. (2014) BigDataViewer: Interactive Visualization and Image Processing for Terabyte Data Sets.

Ren, S., He, K., Girshick, R. and Sun, J. (2015) 'Faster R-CNN: Towards Real-Time Object Detection with Region Proposal Networks'.

Appendix A

Tables

GENE	FUNCTION	Morphology in GalNacT2, 72h. post transfection
COPB2	Coatomer complex subunit beta 2, required for budding from Golgi membranes and essential for the retrograde Golgi-to-ER transport.	DIFFUSE
COPG1	Coatomer complex subunit gamma 1, required for budding from Golgi membranes and essential for the retrograde Golgi-to-ER transport.	DIFFUSE
COPB1	Coatomer complex subunit beta 1, required for budding from Golgi membranes and essential for the retrograde Golgi-to-ER transport.	DIFFUSE
PTBP1	Involved in mRNA metabolism and transport	CONDENSED
ARHGAP44	GTPase-activating protein (GAP) that stimulates the GTPase activity of Rho-type GTPases.	TUBULAR
DNM1	Dynamin subfamily of GTP-binding proteins, involved in clathrin-mediated endocytosis and other vesicular trafficking processes	FRAGMENTED
WDR75	WD repeat domain 75, involved in ribosome biogenesis factor	CONDENSED
FAM177B	Family with sequence similarity 177, member B	TUBULAR
IPO8	Nuclear protein import 8	TUBULAR
C1S	Encodes a serine protease, which is a major constituent of the human complement subcomponent C1.	TUBULAR
DENND4C	Guanine nucleotide exchange factor (GEF) activating RAB10. Promotes the exchange of GDP to GTP.	FRAGMENTED
NT5C	Catalyzes the dephosphorylation of the 5' deoxyribonucleotides (dNTP) and 2'(3')-dNTP and ribonucleotides	CONDENSED
SRSF1	Ensures the accuracy of splicing and regulating alternative splicing.	FRAGMENT
ACTR3	ATP-binding component of the Arp2/3 complex	CONDENSED
GPT	Plays a key role in the intermediary metabolism of glucose and amino acids.	CONDENSED
AURKB	This gene encodes a member of the aurora kinase subfamily of serine/threonine kinases. These kinases participate in the regulation of alignment and segregation of chromosomes during mitosis and meiosis through association with microtubules. After an efficient siRNA knockdown, cells have aberrant nuclei (multinucleated).	Multinucleated
KIF11	This gene encodes a motor protein that belongs to the kinesin-like protein family. Members of this protein family are known to be involved in various kinds of spindle dynamics. After an efficient siRNA knockdown, cells become incapable of mitosis and die.	No cells

Table A.1 siRNA treatments, description of known function of the protein and the phenotype observed in light microscopy assays of GA with GalNACT2-GFP 72 hours of transfection. Gray rows indicate treatments used as positive controls.

Appendix B

Algorithms

Algorithm 2

```
1:  procedure SLIC_THRESHOLDING(image_section)
2:      width,height = image_section.size
3:      super_pixels_list = SLIC(image_section,n_super_pixels=1200)
4:      k_clusters = kMeans(k=3,medians_list)
5:      for super_pixel in super_pixels_list do
6:          if median(super_pixel) ⊂ max(k.cluster) then
7:              image_thresh[super_pixel] = white
8:          else
9:              if median(super_pixel) ⊂ min(k.cluster) then
10:                 image_thresh[super_pixel] = black
11:             else
12:                 if median(super_pixel) < mean(super_pixels_list) then
13:                     image_thresh[super_pixel] = black
14:                 else
15:                     image_thresh[super_pixel] = white
16:     Return image_thresh
```

Algorithm 3

procedure DETECT_FOCUS_POINTS(*image_section*)
stop_point = Compute_StopPoint(image_section)
width,height = image_section.size
x,y = Max_Orientations(image_section)
Cluster_centroids = kMeans(k=25,(x, y)) using euclidean distance
for *cluster* in Cluster_centroids **do**
if $cluster.x < 0.5 * width$ and $cluster.y > stop\_point$ **then**
Delete *cluster*
vx,vy,variances = removeLowVariance(Cluster_centroids,image_section)
nx,ny = $\frac{variance}{(vx-width*0.5)^2+(vy-height*0.2)^2}$
sorted_nx, sorted_ny = sort(nx,ny,order=descendent)
Return sorted_nx,sorted_ny

Algorithm 4

procedure TRACKING($dataframe$, $\beta = 0.8$, $gap = 0.5$)
last_section = dataframe[last,:]
shift_x = 0, shift_y = last_section.shift_y
track_done = False stop_point = Compute_Stop_Point($dataframe$)
if $length(dataframe) == 4$ **then** ▷ *Initialize, shifts are cumulative*
shift_y = stop_point
track_done = False
else
if $length(dataframe) > 4$ and last_section.track_done==False **then**
drift = stop_point - last_section.shift_y
if $stop\_point < 0.05$ **then** ▷ *Drifting upwards*
shift_y = last_section.shift_y + 0.25
shift_done = True
else
if $stop\_point > 2.0$ **then** ▷ *Drifting downwards*
shift_y = last_section.shift_y-0.25*stop_point
shift_done = True
else
if $abs(drift) > gap$ **then**
ashift =ASIFT(last_section.image,dataframe[current,image])
if $abs(ashift.x) < gap$ and $abs(ashift.y) < gap$ **then** ▷ *Control shift by using moving average*
shift_x = 0
shift_y = $\beta * last\_section.shift\_y + (1 - \beta) * (last\_section.shift\_y + ashift.y)$
dataframe[current,shift_done] = shift_done
dataframe[current,shift_x] = shift_x
dataframe[current,shift_y] = shift_y

Algorithm 5

procedure COMPUTE_STOPPOINT(*image_section*)
width,height = image_section.size
image = resize(image_section,1024,1024/width)
image = enhance_contrast_percentile(image, 0.1, 0.9)
signal = sum(image) by columns
stop_point_1 = max(derivative(signal))
thresh_image = SLIC_thresholding(image)
stop_point_2 = Min(Index($thresh\_image > 0$)) by columns
Return max(stop_point_1,stop_point_2)